1 2 9 0

UNIVERSIDADE Ð COIMBRA

Ana Francisca Henriques Parente dos Santos

BEHAVIOUR OF FRICTION JOINTS UNDER IMPACT LOADS

Setembro de 2019

Behaviour of friction joints under impact loads

University of Coimbra, Portugal
Department of Civil Engineering

PhD course in Steel and Composite Construction

University of Salerno, Italy
Department of Civil Engineering

PhD course in Civil Engineering, Building Engineering – Architecture, Environmental and Territorial Engineering

Ana Francisca Henriques Parente dos Santos

Supervisors:

Prof. Aldina Maria da Cruz Santiago

Prof. Gianvittorio Rizzano

Coimbra, September 2019

RESUMO

Resumo

O conhecimento do comportamento de estruturas porticadas em aço, quando solicitadas por uma ação excecional, como são exemplos os sismos, cargas de impacto e explosões, é fundamental para assegurar a integridade estrutural e prevenir o colapso progressivo das estruturas. Em particular, as ligações viga-coluna parecem ser um dos elementos críticos, visto que podem limitar a ductilidade e a resistência das estruturas. É assim fundamental, o conhecimento do seu comportamento quando solicitadas por este tipo de ações. Esta particularidade motivou o trabalho desenvolvido nesta tese doutoramento, que tem como objetivo principal o estudo do comportamento de uma ligação que funciona por fricção quando está sujeita a cargas estáticas e de impacto.

A ligação em estudo é a ligação viga-pilar desenvolvida pelo projeto Europeu FREEDAM "*Free from damage connections*". Esta ligação têm a particularidade de estar equipada por um dissipador por fricção "*friction dampers*", localizado no banzo de um esquadro que está, por sua vez, ligado ao banzo inferior da viga. Para além disso, o banzo do esquadro é furado com furos alongados de modo a permitir o seu escorregamento nas placas de fricção "*friction pads*", dissipando assim, a energia transmitida à estrutura em caso de um evento excecional. Esta tipologia de ligação foi primeiramente desenvolvida para assegurar um bom desempenho de estruturas porticadas quando sujeitas a sismos raros ou de grande intensidade, permitindo uma grande capacidade de dissipação de energia sem dano significativo para a estrutura, sendo o dano localizado apenas nas placas de fricção "*friction pads*". No entanto, o comportamento destas ligações no caso extremo de uma ação que provoque uma rotação superior à rotação máxima para qual os dissipadores por fricção foram dimensionados (impacto, explosões, etc.), era até aqui, completamente desconhecido. Por esta razão, a tese apresentada neste documento

dedicou-se ao estudo intensivo do comportamento desta ligação quando sujeita a ações extremas.

Para atingir este objetivo, foi desenvolvido um programa de trabalho dividido em três partes. A primeira parte consistiu no estudo da componente dissipativa quando solicitado à tração, enquanto que na segunda parte, foi estudada a ligação completa sujeita a momento fletor. Estes estudos confirmaram que a velocidade de aplicação da carga/deformação afeta o comportamento da ligação devido à ativação de taxas de deformação elevadas nos materiais que constituem os diferentes componentes da ligação. Posto isto, concluiu-se que é importante ter em consideração as mudanças no comportamento da ligação quando cargas consideradas excecionais são uma condição de dimensionamento. Pela razão acima indicada, foi de seguida desenvolvido um modelo de molas tendo por base o método das componentes. Este modelo teve em consideração o comportamento elástico e pós-elástico de cada uma das componentes da ligação, assim como, o efeito das taxas de deformação na resistência e ductilidade de cada uma delas. O modelo foi comparado com os resultados experimentais e numéricos, tendo sido concluído que é possível prever analiticamente as modificações no comportamento da ligação quando estas são sujeitas a cargas dinâmicas.

A terceira e última parte do trabalho dedicou-se à avaliação da robustez de uma estrutura porticada equipada com a ligação em estudo. Foram considerados diferentes tipos de análise, incluindo análises estática e dinâmicas não lineares, considerando a perda de um dos pilares externos (cenários independentes da definição da ação) e uma análise dinâmica na qual foi modelada a ação de impacto de um veículo colidindo no pilar externo da estrutura (cenário dependente da definição da ação). Os diferentes tipos de análise permitiram avaliar a sensibilidade da estrutura aos efeitos dinâmicos e a influência da consideração ou não da ação para a análise da robustez. Para além disso, os resultados foram ainda comparados com o comportamento da mesma estrutura, mas com uma ligação rígida. Foi possível concluir que a grande vantagem da utilização das ligações *freedam*, quando comparado com uma ligação mais comummente utilizada, é o deslizamento entre placas, que permite que parte da energia induzida à estrutura seja absorvida por fricção, não se verificando a plastificação dos elementos estruturais. Assim sendo, a estrutura poderá ser reutilizada, sendo necessário apenas a substituição das placas de fricção.

Palavras-chave: Ligações sem dano | Dissipadores de energia por fricção | Impacto | Robustez

Abstract

Predicting the behaviour of steel-framed structures subjected to unexpected extreme loads, such as seismic events, impact or even explosions, is necessary to ensure the integrity and to prevent collapse during such an event. In particular, beam-to-column connections are seen as the critical components limiting structural ductility and resistance of steel frames, thus their behaviour should be well known during such events. This consideration motivated this PhD thesis, which has the purpose to study the behaviour of a friction connection subjected to quasi-static and impact loading conditions.

The connection under investigation in this thesis is a beam-to-column connection developed within the European FREEDAM project: "*Free from damage connections*", which has the particularity of been equipped with friction dampers located in an additional haunch bolted to the lower beam flange. In this way, the energy dissipation is provided by the slippage of the haunch flange on the friction pads. Such connection typology was primarily designed to ensure a satisfactory performance of Moment Resisting Frames under severe seismic events, assuring a large energy dissipation capacity with negligible damage for the structure. However, their behaviour in case of extreme loading conditions (impacts, blasts, etc.) was completely unknown. Therefore, the response of such connections in case of extreme loading conditions was extensively studied in this thesis.

To accomplish the objectives of the proposed work, an extensive programme divided into three parts was carried out. The first part of the programme dealt with the individual behaviour of the friction damper under tension loads, whereas, in the second part, the behaviour of the whole connection was investigated when subjected to bending moment actions. These studies confirmed that the velocity of the application of the load affects the connection behaviour due

to the high strain rates induced in the materials composing the several components of the connection. It is therefore important to take this change of behaviour into to account if exceptional loading events is a design consideration.

For the abovementioned reason, an analytical spring model, based on the component method currently codified in Eurocode 3 part 1.8, was also developed in order to easily take into account the changes on the connection behaviour due to exceptional loading actions. These changes were considered in the resistance and ductility of each individual component of the connection. This model is able to predict the connection behaviour when subjected to different velocities by incorporating the strain rate influence in the individual components of the connection.

The third part of the work is devoted to the robustness of steel frames equipped with the studied connection. Different types of robustness analyses were used, with increased complexity, including static and nonlinear dynamic removal column loss analyses (threat independent scenarios) and a dynamic lateral impact analysis (threat dependent scenario). The different analyses showed the sensitivity of the structure to the dynamic effects and that the consideration of the impact action can lead to a quite different structural response when compared to those observed in the simple column removal analyses. Furthermore, the results were compared to the behaviour of the same frame equipped with one rigid connection. From this comparison, it was observed that the main advantage of using the *freedam* connection is the connection slip mechanism, which allows the dissipation of a great amount of the energy induced to the structure by the exceptional load, avoiding the plastic engagement of the beams and columns as well as the other steel components of the connections. In this way, the structure after the event can be reused, requiring only the replacement of the friction pads.

SOMMARIO

Sommario

La previsione del comportamento delle strutture in acciaio soggette ad azioni non prevedibili, come eventi sismici, impatti o persino esplosioni, è necessaria per garantirne l'integrità e soprattutto per prevenirne il collasso. In particolare, le connessioni trave-colonna rientrano tra i componenti critici il cui comportamento limita la duttilità strutturale e la resistenza dei telai in acciaio, pertanto il loro comportamento in caso di tali eventi dovrebbe essere ben noto a priori. Il lavoro presentato all'interno di questa tesi di dottorato è stato sviluppato proprio a partire da queste considerazioni, andando a studiare il comportamento di una connessione ad attrito soggetta a condizioni di carico quasi statico e a condizioni di impatto.

Nell'ambito di questa tesi è stata studiata la connessione trave-colonna sviluppata nell'ambito del progetto europeo FREEDAM: "FREEE from DAMage connections", che ha la particolarità di essere equipaggiata con dissipatori ad attrito situati su di un haunch aggiuntivo bullonato alla flangia inferiore della trave. In questo modo la dissipazione di energia avviene attraverso lo scorrimento della flangia dell'haunch sui piatti ad attrito. Tale tipologia di connessione è stata progettata principalmente per garantire prestazioni soddisfacenti dei telai a Momento Resistente (MRFs) in caso di eventi sismici severi, garantendo una grande capacità di dissipazione di energia con danni trascurabili per la struttura. Tuttavia, il loro comportamento in caso di condizioni di carico estreme (impatti, esplosioni, ecc.) era completamente sconosciuto. Pertanto, all'interno di questo lavoro di tesi è stata ampiamente studiata la risposta di tali connessioni quando soggette a condizioni di carico estreme.

Per raggiungere gli obiettivi del lavoro proposto è stato realizzato un vasto programma di analisi suddiviso in tre parti. La prima parte del programma è stata dedicata allo studio del comportamento individuale del dissipatore ad attrito sotto carichi di trazione, mentre, nella seconda parte è stato studiato il comportamento dell'intera connessione quando sottoposto ad

azioni di momento flettente. Questi studi hanno confermato che la velocità di applicazione del carico influenza il comportamento della connessione a causa delle elevate velocità di deformazione indotte nei materiali che compongono i diversi elementi della connessione. È quindi importante tenere conto di questo cambiamento di comportamento quando le condizioni di carico eccezionali vanno considerati nella progettazione.

Per la ragione sopra menzionata è stato inoltre sviluppato un modello analitico a molla basato sul metodo della componente, attualmente codificato nell'Eurocodice 3 parte 1.8, al fine di tenere facilmente conto delle modifiche del comportamento della connessione dovute ad azioni eccezionali. Questi cambiamenti sono stati considerati nella resistenza e nella duttilità di ogni singolo componente della connessione. Tale modello ha dimostrato di essere in grado di prevedere il comportamento della connessione quando sottoposto a velocità diverse tenendo conto dell'influenza della velocità di deformazione sui singoli componenti della connessione.

La terza parte del lavoro è dedicata alla robustezza dei telai in acciaio equipaggiati con la connessione FREEDAM. Sono stati utilizzati diversi tipi di analisi di robustezza, di complessità crescente, tra cui analisi di perdita della colonna, di rimozione dinamica statica e non lineare (threat indipendet scenarios) e un'analisi di impatto laterale dinamico (threat dipendet scenarios). Le diverse analisi hanno mostrato la sensibilità della struttura agli effetti dinamici e hanno portato a valutare che l'azione di impatto può portare a una risposta strutturale piuttosto diversa rispetto a quelle osservate nelle semplici analisi di rimozione della colonna. Inoltre, i risultati sono stati confrontati con il comportamento dello stesso telaio dotato di una connessione rigida. Da questo confronto, è stato osservato che il vantaggio principale dell'utilizzo della connessione FREEDAM sta nel meccanismo di slittamento della connessione, che consente la dissipazione di una grande quantità di energia che il carico eccezionale genera sulla struttura, evitando l'impegno plastico delle travi, delle colonne e degli altri componenti in acciaio delle connessioni. In questo modo la struttura dopo l'evento può essere riutilizzata, richiedendo solo la sostituzione dei piatti ad attrito.

Parole-chiave: Free from damage steel connections | dissipatori ad attrito | Impatti | Robustezza

ACKNOWLEDGEMENTS

Acknowledgements

This page is dedicated to those who, directly or indirectly, have helped me to reach the end of my PhD thesis. It was not always an easy path, but without them, it would have been much more difficult.

I would like to express my gratitude to my supervisor, prof. Aldina Santiago, for her continuous support and guidance during these years, and for sharing her experience and knowledge. Also to my supervisor of the University of Salerno, prof. Gianvittorio Rizzano, I have to thank for his support, guidance and for making me feel welcomed in Salerno. I would like to thank as well to prof. Luís Simões da Silva, for giving me the idea of enrolling in the PhD and working in the FREEDAM project, four years ago. I would not have remembered that by myself.

To the lab' technicians of the University of Coimbra, for all their help through my experimental campaigns.

I have to thank to my PhD colleagues, to those who I already had known from my Master course and to those I met along the way, in Coimbra and in Salerno, for making this journey more enjoyable.

Special and sincere thanks goes to Massimo Latour, for his constant help and enormous patience during all the tasks of this thesis - Grazie mille!

I will now switch to Portuguese to thank to my closest friends and family. Um muito obrigado às minhas amigas de sempre, Joana e Ângela, que me apoiam sempre em todos os aspetos da minha vida, independentemente da distância e do tempo que estamos sem nos vermos. Claro, também às minha amigas Rita e Sara, por todos os momentos bons e divertidos

que passamos todas juntas. Também tenho que agradecer ao meu grupo de amigas que conheci ainda durante o mestrado, pelas conversas e encontros de grupo "mensais".

Ao meu namorado Filip, por todo o apoio e amor que me deu e me dá diariamente, e por me relembrar todos os dias que o mais importante é, citando-o: "Aproveitar a vida". – Hvala puno ljubavi!

Por último, mas não menos importante, um agradecimento especial vai para toda a minha família, em especial para os meus pais e irmãs. À minha irmã Marta pelo companheirismo e amizade e às minhas irmãzinhas, Sofia e Madalena, pelas brincadeiras e por me fazerem esquecer do trabalho quando estamos juntas.

Aos meus pais, pelo apoio incondicional, não só durante estes quatro anos, mas desde de sempre, e por me terem ensinado que tudo é possível de ser alcançado. Este trabalho é essencialmente dedicado a eles.

TABLE OF CONTENTS

Table of contents

LIST OF FIGURES

List of Figures

LIST OF TABLES

List of Tables

Nomenclature

Uppercase Letters

C:　　　Strain rate constant

DF_{frict}　　Initial friction dynamic factor

DF_y　　　Elastic resistance dynamic factor

DF_u　　　Ultimate resistance dynamic factor

DF_S　　　Initial stiffness dynamic factor

$DF_{\delta u}$　　Ductility capacity dynamic factor

$F_A\,(t)$:　　Force at the application point of force in time [kN]

$F_I\,(t)$:　　Inertial forces in time [kN]

F_k　　　Kinetic friction resistance [kN]

F_p　　　Preload force [kN]

F_{slip}　　Initial friction resistance [kN]

F_u　　　Ultimate resistance [kN]

$F_{u,st}$　　Quasi-static ultimate Resistance [kN]

$F_{u,imp}$　　Ultimate resistance under impact loading [kN]

F_y　　　Elastic resistance [kN]

$F_{y,st}$　　Quasi-static elastic resistance [kN]

$F_{y,imp}$　　Elastic resistance under impact loading [kN]

$F_t\,(t)$　　Force in the tested specimen in time [kN]

I	moment of inertia about an axis parallel to the axis through the centre of mass [kgm^2]
I_{cm}	Moment of inertia about its centre of mass [kgm^2]
K_e	Elastic stiffness [kN/mm]
K_H	Horizontal spring representing the stiffness of the IAP [kN/mm]
L	Length of the "flying beam" [m]
L_{bolt}	Bolt length [mm]
$M_I(t)$	Moment of inertia in time, according to an axis parallel to the axis through the centre of mass [kN.m]
P	Stress applied to the bolt due to preload [MPa]
$R_p(t)$	Reaction force in the pivot in time [kN]
T*	Non-dimensional parameter based on melting
$X_2(t)$	Distance x_2 in time [mm]
$X_3(t)$	Distance x_3 in time [mm]
$X_4(t):$	Distance x_4 in time [mm]

Lowercase Letters

a_{cm}	Acceleration read by the accelerometer at the "flying beam" centre of mass [m/s^2]
a_f	Acceleration read by the accelerometer at the point of the application of the load [m/s^2]
d_f	Displacement read by the laser triangulation in the boundary of the application point of the force [mm]
d_p	Displacement read by the laser triangulation in the pivot [mm]
f_{ub}	Ultimate stress of the bolts [MPa]
f_p	Proof strength [MPa]
f_y	Yield strength [MPa]
f_u	Tensile strength [MPa]
k	Tightening factor
m	Number of surfaces in contact; Thermal softening fraction

n Number of the bolts; Constant that characterize the effect of strain hardening

s_0 Shear resistance of the weakest material employed in the friction interface

x_1 Distance between the pivot and the left end of the beam [mm]

x_2 Distance between the pivot and the centre of mass of the "flying beam" [mm]

x_3 Distance between the application point of the force and the centre of mass of the "flying beam" [mm]

x_4 Distance between the application point of the force and right end of the "flying beam" [mm]

x_{cm} Distance of the centre of mass to the pivot [mm]

Greek Letters

φ Ductility Index

δ Deformation [mm]

δ_{FD} Total ultimate deformation [mm]

δ_u Ultimate deformation of the bolt zone[mm]

$\delta_{u,st}$ Static ultimate deformation [mm]

$\delta_{u,imp}$ Ultimate deformation under impact loading [mm]

δ_y Yield deformation [mm]

δ_{max}:   Deformation at failure [mm]

ε Equivalent plastic strain [-]

μ Initial friction coefficient [-]

μ_k Kinetic friction coefficient [-]

σ Static strength

σ_{dyn} Dynamic strength

σ_0 Superficial Hardness of the softest material employed in the friction interface

$\ddot{z}_{cm}$ acceleration of the centre of mass of beam [m/s^2]

$\dot{\varepsilon}$ Strain rate [s^{-1}]

$\dot{\varepsilon}_0$ Reference quasi-static strain rate [s^{-1}]

$\dot{\varepsilon}^*$ Dimensionless plastic strain rate [-]

$\ddot{\theta}$ angular acceleration of the beam [rad/s^2]

Abbreviations

AFCS	Asymmetrical friction connections
DAP	Directly affected part
DIF	Dynamic increase factor
DST	Double Split Tee
EC	Eurocode
EP	End-plate joint
FEM	Finite element model
FEP	Flexible end plate joint
FIN	Fin plate joint
FREEDAM	Free From Damage Connections
IAP	Indirectly affected part
LVDT	Linear Variable Displacement Transducer
MRF	Moment resisting frame
NDA	Nonlinear dynamic analysis
SDOF	Single degree of freedom
SHJ	Sliding Hinge Joint
SLS	Service limit States
WC	Web cleat angles joint

Chapter 1   Introduction

1.1 General considerations

During their lifetime, structures can be subjected to accidental loading events, such as earthquakes, fire, impact, blast/explosions, terrorist attacks, among others, that can induce failure in the elements directly exposed to the event, or even cause the progressive collapse of the whole construction. The progressive collapse of a structure happens when the local damage caused by the initial event spreads to other elements of the structure, resulting in the collapse of the whole structure or a part of it, i.e. the final damage is disproportionate to initial local damage [1].

In the past, there are several examples of the consequences of these loading events on buildings. A good example of a progressive collapse induced by an explosion is the collapse of the Ronan Point apartment tower in 1968 (Fig. 1.1a). A gas explosion in the kitchen of one of the corner apartments of the 18th floor, led to the failure of the corner bay of the building, up to the roof and down to the base. Even though the entire building did not collapse, the damage was disproportionate to the initial damage. In fact, this event aroused the problem of robustness of structures subjected to accidental loads within the scientific community, and the UK in 1970 issued the first regulation on this topic.

Subsequences accidents leading to progressive failure increased the attention to this phenomenon and on how it would be reasonable to take it into account in the structural design of buildings. In particular, after the World Trade Centre terrorist attack, in 2001, the ductility of beam-to-column connections has been recognized as a key parameter to maintain the integrity of a structure. Since then, several research works started to appear in order to study the influence of beam-to-column connections on the robustness of steel structures, considering

the case of loss of a column [2–4]. However, most of these studies do not consider the influence of the strain rates induced by the extreme accidental actions on the behaviour of connections.

Currently, the design of beam-to-column connections is essentially addressed by Eurocode 3 Part 1-8 [5] using the component method, which only deals with the behaviour of connections under static loading conditions and does not provide any guidance concerning the design of such connections when subjected to extreme accidental loads. For this reason, in the last few years, many authors have performed experiments and finite numerical analyses in order to study the influence of such type of loading on the ultimate resistance, ductility capacity and failure mode of some typologies of steel connections and their typical components [6–9]. In addition, based on those results, some efforts to implement the influence of high strain rates in analytical models using the component method have also been made [10,11].

a. Ronan Apartment tower London   b. World Trade Center, USA

Fig. 1.1. Damage of structures subjected to extreme accidental loading events

Within the context of improving the knowledge on the behaviour of steel connections under extreme accidental actions, the response of a new type of friction beam-to-column connection subjected to quasi-static and impact loading conditions is investigated in this PhD thesis. This work is part of the European FREEDAM project and it follows the tasks of the project related to structural robustness when extreme loads are considered. The next sections present the main activities and objectives of this research work.

1.2 Scope and organization of the thesis

1.2.1 Motivation and objectives of the thesis

The research work presented in this thesis reflects the author participation in the FREEDAM project. The acronym "FREEDAM" derived from "*Free from Damage Connections*" and this

project had as a primary objective the development of a new type of beam-to-column connection. This new type of connection was designed in order to not suffer any damage when subjected to extreme seismic events, which is accomplished by equipping the connection with a friction damper device. Although the connection has been originally designed for seismic events, it was also an objective of the project to check if the dissipative mechanism could also improve the behaviour of structures under other extreme loading scenarios, such as impact loads.

This thesis was then motivated by this last topic of the project. The investigation is based on experimental, numerical and analytical work and it can be divided into four main tasks:

Task 1. Literature Review:

Available knowledge on the behaviour of steel connections subjected to rapidly applied loads and their influence in maintaining the robustness of structures subjected such loading events.

Task 2. Characterization of friction dampers under quasi-static and impact loading conditions:

The characterization of the friction damper was performed considering uniaxial tension loads since this device has the mechanism of a double shear lap connection. It consisted of three parts: (i) experimental campaign, (ii) numerical simulations and (iii) analytical modelling.

All the experimental tests were performed at the Civil Engineering Department of the University of Coimbra. The impact tests were performed using a layout specially designed for applying high loading rates [12]. Several configurations of the friction damper were tested to assess different failures modes.

The numerical simulations were performed using the ABAQUS software [13]. The results were calibrated against the experimental findings. Additionally, a parametric study was conducted to assess the influence of the loading rate on the behaviour of the device.

Finally, based on previous studies to assess the ductility capacity of shear lap joints [14], an analytical model was developed. The model is able to assess with enough accuracy the behaviour of these devices under quasi-static and impact loading conditions.

Task 3. Characterization of beam-to-column friction connections under quasi-static and impact loading conditions:

Following the same approach as for the friction damper, the characterization of the connection was done by means of experimental, numerical and analytical work. The experimental work was carried out at the University of Coimbra, while both the numerical studies and the analytical work were developed at the University of Salerno, in Italy.

The experimental tests were performed using the same layout as used for the friction damper but adapted to apply bending moment.

The numerical simulations were performed with the ABAQUS software [13]. The first part consisted in the simulation of the experimental tests. After the calibration of the model, parametric studies were carried out in which, the bending moment direction, the ductility of the bolt assembling to the ultimate resistance of the connection and the influence of the loading rate, were evaluated.

Finally, an analytical model was developed, following the bases of the Eurocode 3 part 1-8 [5]. The connection components at the friction damper zone were characterized according to the analytical model developed in task 2. Furthermore, for the components modelled as T-stubs, a theoretical model able to assess the non-linear force-deformation curves up to failure of this component was used [15]. For the remaining components, the formulations of the Eurocode and other literature suggestions were taken into account.

Task 4. Assessment of the robustness of steel frames with friction joints:

The robustness assessment of MRFs equipped with friction joints and subjected to a lateral impact was studied by means of numerical simulations on the ABAQUS software [13].

The lateral impact was applied at one of the external columns of the frame, simulating the impact of a car. The mass of the vehicle, dimensions and impact velocities were considered according to the recommendations of Eurocode 1 part 1-7 [16]. In addition, the robustness of this frame was compared to the behaviour of the same frame equipped with a more common bolted beam-to-column steel joint.

The connection behaviour was modelled by axial springs, in which the force-deformation F-δ curves obtained from the analytical approach developed for the friction joint in task iii) were implemented.

1.2.2 Organization of the document

This document is organized into 8 chapters. Chapter 1 presents the objectives and motivation of the study and its relation to the research project "FREEDAM", as well as the organization of the document.

In Chapter 2, an overview of the design and behaviour of steel beam-to-column connections when subjected to extreme loading events is presented. It also summarizes the current regulation concerning the design of structures to avoid progressive collapse when subjected to extreme events and the recent methodologies to assess the behaviour of a structure in a case of impact or column loss.

Chapter 3 describes the experimental campaign carried out in this PhD to assess the behaviour of friction dampers under different loading rates. The test arrangement, instrumentation, material characterization and the results are detailed explained through this chapter.

Chapter 4 describes the numerical and analytical work carried out to assess the behaviour of friction dampers under different loading rates. At first, the numerical modelling and all the results are fully reported and explained. Then, an analytical model is developed and the results compared with the numeric and experimental results.

Chapter 5 describes the experimental and numerical work carried out in one typology of the FREEDAM connection in order to understand the influence of different loading rates in its behaviour up to failure. The testing layout, instrumentation, numerical modelling and test results are detailed presented through this chapter.

Chapter 6 presents a component-based method to describe the whole connection behaviour under quasi-static and dynamic loads. Each component is described by its individual force-deformation curve taking into account both their static and dynamic behaviour. Afterwards, the components are assembled and the behaviour of the connection is obtained. The numerical simulations and experimental tests reported in the previous chapters were used to calibrate this model.

In Chapter 7, the robustness of a 2D MRF equipped with friction connections when impacted by a vehicle is studied. Different types of robustness analysis were used, with increased complexity, including static and nonlinear dynamic removal column loss analyses and a dynamic lateral impact analysis. The results from these analyses are presented and compared to the results of the same frame using a rigid connection. The analytical model developed in chapter 6 is used in the frame model to characterize the connection's behaviour.

Finally, in Chapter 8, the main conclusions, contributions and future works are presented.

Chapter 2   Steel structures subjected to accidental loading events

2.1 Introduction

Robustness is a property of a system that allows it to survive under an unexpected action. In structural engineering, robustness is considered as the ability of a structure to withstand without being damaged to an extent disproportionate to the original cause, when subjected to an accidental action. Accidental actions are actions with a low probability of occurrence, severe consequences of failure and are usually of short duration. Typical examples of these actions are fire actions, explosions, earthquakes, impact, floods, and others. However, even though all accidental actions are considered short-duration loads, some of them have shorter durations than others, which are usually called abnormal or extreme loads, such as impact loads and explosions. In particular, due to its particularly short duration (few milliseconds), these type of loads can induce high levels of strain rates in structures, which can lead to a completely different structural behaviour from the one predicted by the "normal" or even by the seismic actions. In Fig. 2.1, is reported the typically strain rates induced to a structure when subjected to different loading types. It is possible to observe that, impact loads can induce strain rates up to 1000 times higher than the most severe of the earthquakes. In fact, while in seismic actions the effects of strain rates can be often neglected (the induced strain rates are not higher than $10^0 \, \text{s}^{-1}$), when designing a structure to resist to a certain impact load, this is no longer true (. For this reason, the different accidental loading scenarios should be considered in robustness design of structures.
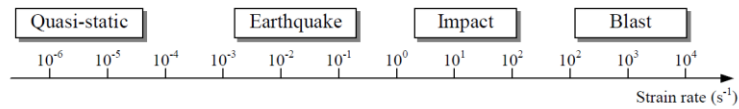
Fig. 2.1. Strain rate for different types of loading [17]

Historically, it was after the Ronan Point apartment tower incident (1968), that the first regulation on robustness of structures subjected to abnormal loads appeared in the UK (1970). However, it was after the World Trade Center disaster in 2001 that the scientific community truly awaken for this topic. Since then, several studies appeared related to this topic, some focused on the behaviour of a frame or building [18–23] and others focused on the performance of specific types of steel connections and their components under extreme loading [6,7,9,24–27].

When studying the robustness of structures subjected to accidental loading, different scenarios can be studied, as illustrated in Fig. 2.2. The first scenario, in Fig. 2.2a, is the most used by the researchers to assess the robustness of a structure and it simulates the loss of a column after some extreme event such as seismic events, impact or explosion. This method is a threat-independent alternate path method and based on it, several experimental, numerical and analytical studies can be found in the literature [3,4,19,20,22,28–31]. The two other scenarios presented in Fig. 2.2, are the impact on beams due to failing of the above floor (Fig. 2.2b) and lateral impact on a column due to a vehicle, flying debris or internal explosion (Fig. 2.2c). Concerning these two scenarios, fewer studies are found in literature due to the fact that contrarily to the first-mentioned scenario, both require a precise definition of the action. For example, case b) of Fig. 2.2 requires the definition of the masses of the falling stories and their impact points [32,33] while in case c), the velocity of the impact, the mass or the pressure of the vehicle and explosion, respectively, should be defined [18,31,34].

With reference to steel structures, beam-to-column connections are considered crucial to provide good robustness properties. Independently of the threat, beam-to-column connections should be properly designed in order to provide enough resistance and ductility capacities. In seismic design, the typically full-strength welded connection has been replaced by bolted semi-rigid connections, due to their good energy dissipation and rotational capacities. Following the same approach, recent studies on connection behaviour under short-duration loads are mainly

on bolted semi-rigid connections such as flexible end plates, web-cleats angles joints and fin-plates joints [6,9,24,25,27].

a. Column loss scenario[31]

b. Impact due to failing floor [33]

c. Lateral column impact [27]
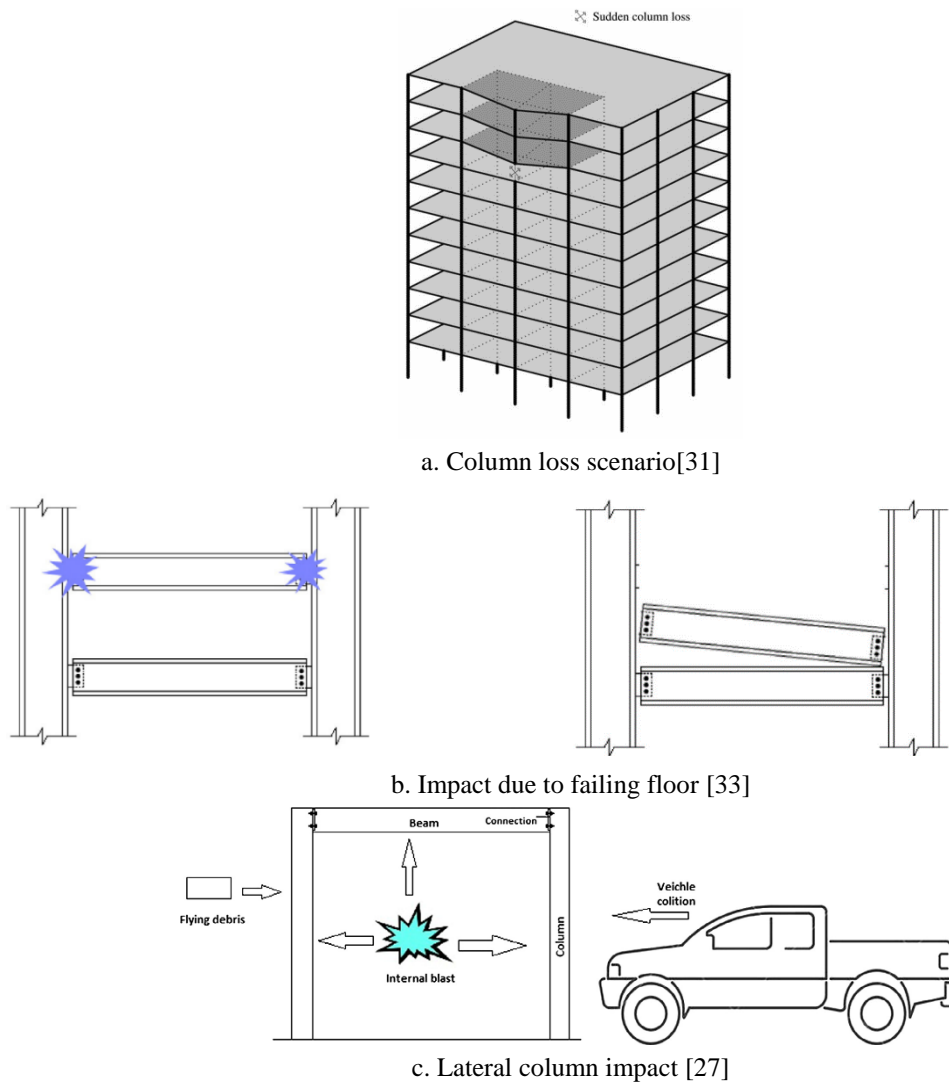
Fig. 2.2. Different robustness scenarios

The following sections are intended to present a review on the subjects of the design of steel structures and their connections, with respect to their robustness against progressive collapse. Therefore, a review on the evolution of connection design under accidental events is reported followed by a more detailed explanation of the beam-to-column connection studied in this thesis, i.e the FREEDAM connection. Concerning beam-to-column joint behaviour, a review on the available studies found in the literature regarding the behaviour of bolted steel connections under impact loading is also reported.

In addition, the main design recommendations and design concepts from the most used regulations with respect to the design against disproportionate collapse and impact loading are

reported. This chapter ends with a review of the most recent studies on how to assess the robustness of steel-framed structures subjected to accidental extreme loads.

2.2 Beam-to-column connections under accidental loading events

In the past, the use of full-strength welded connections was considered as the best practice to dissipate the input energy coming from extreme events, due to their good dissipative properties. Furthermore, the plastic engagement of the elements constituting the connection was avoided, since the dissipative zones were located at the beam-ends. However, after some extreme seismic events, such as the Kobe and Northbridge earthquakes, these connections showed a poor performance due to cracking of the welds. Therefore, new solutions that could provide the required combination of ductility, strength and stiffness, but avoiding the cracking of the welds were investigated. One of them is the RBS (reduced beam section) solution in which the beam flanges width are cut near the beam-to-column connection. In this way, the beam is designed as the dissipative member of the structure. Moreover, approaches to replace welds by bolts started to gain relevance.

Later, attention turned into the concept of partial strength connections. This concept rely on switching the dissipative member of connections from the beam-ends to the connection elements. Their behaviour has already been studied by several authors [35,36]. Within this framework, the DST (Double Split Tee) connections (Fig. 2.3) have been recognized as a promising solution to applied in MRFs frames because they can be easily repaired after an extreme accident [36], following the tendency of the scientific community in finding solutions that are easily fixed after an extreme event. However, experimental tests on these connections have shown a hysteretic behaviour significantly influenced by pinching, strength and stiffness degradation [36].
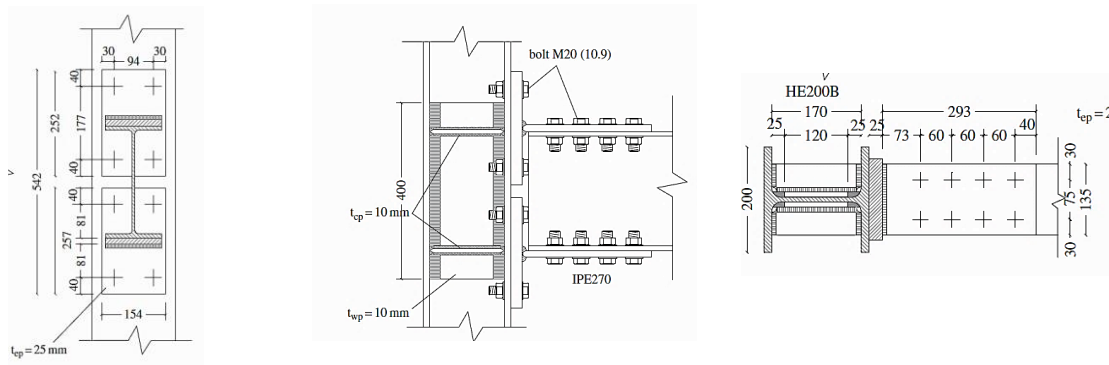
Fig. 2.3. Double Spit tee connection [36]

A more recent approach consists in introducing passive energy dissipation devices within the connections so that the devices work as the dissipative member of the structure. Several researchers have studied different solutions in this field.

One of the first solutions was introduced by Inoue *et al.* [37], who proposed a "weld-free system" (Fig. 2.4a). This system consists in bolting the top beam flange to the column so that the beams can rotate about the ends of their top flanges. At the beam flanges, buckling Braces (BRB) are installed to provide sufficient lateral resistance against seismic forces and to dissipate the input energy during the earthquake. The braces can be located only at the bottom flange or at both flanges. As the connection arrangement places the centre of rotation at the end of the beam top flange, the dampers can deform freely at the bottom of the beam without causing damage to the concrete floor slab when large story drifts occur. From cyclic tests on full scales connections, it was observed that this "weld-free system" provides connections with stable hysteresis behaviour under large story drifts with larger loops than those from conventional welded connections. In addition, the double angle geometry (Fig. 2.4a) provides ductile behaviour, large hysteresis loops and high lateral resistance.

Following the concept of Inoue, other solutions appeared, such as the ones proposed by Kishiki *et al.* [38] (Fig. 2.4b) and Oh *et al.* [39] (Fig. 2.4c). In both solutions, the centre of rotation is localized at the upper beam flange by a fixed T-stub, while the dissipation of energy is provided by dissipation mechanism systems at the lower beam flange. In the solution proposed by Kishiki *et al.* [38] (Fig. 2.4b), this system is composed by a T-stub with a dog-bone shape restrained by an additional plate in order to prevent its buckling in compression. Oh *et al.* [39] used a slit damper instead. Both solutions showed great dissipation energy capacities and the possibility of reparation/replacement of the dissipative system after an extreme event.

Furthermore, by placing the dissipative system only at the lower flange level, the damage of the concrete slab is avoided.

a. Inoue *et al.* [37]

b. Kishki *et al.* [38]

c. Oh *et al.* [39]
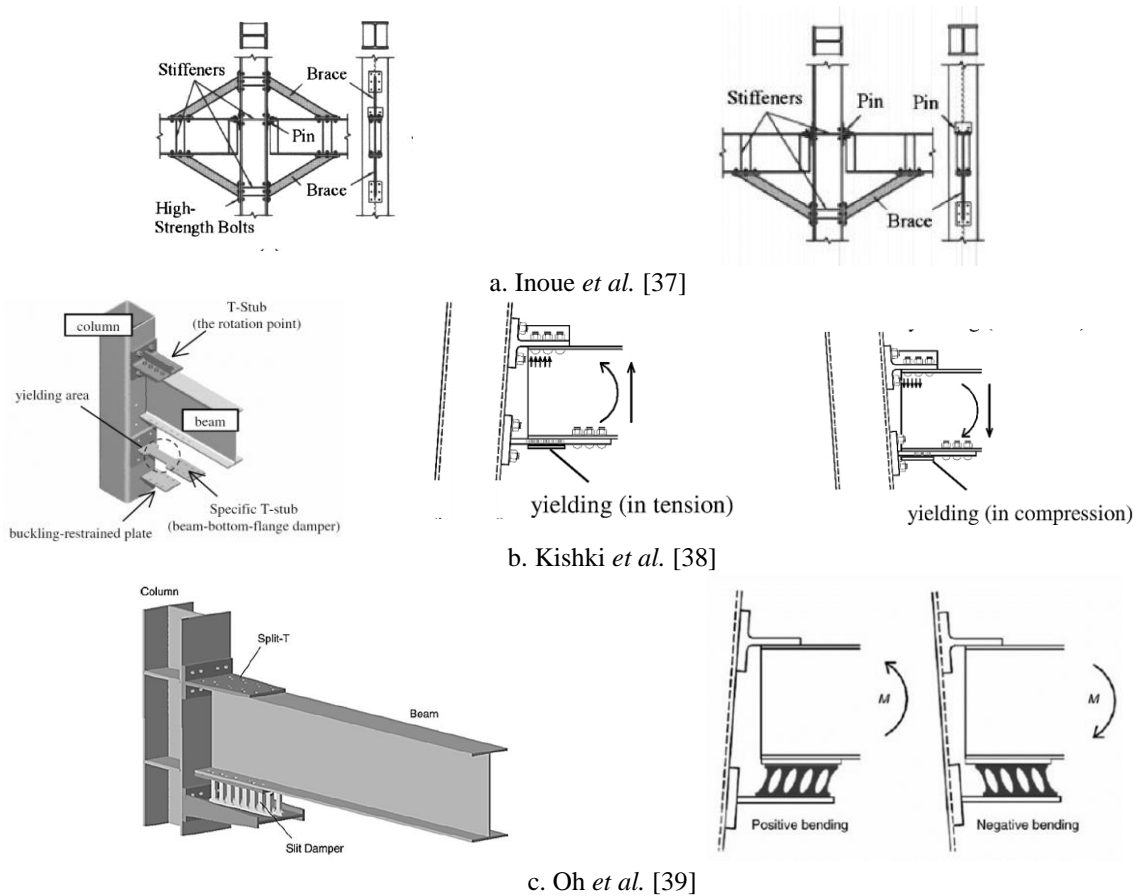
Fig. 2.4. Passive energy dissipation devices within connections

More recently, MacRae *et al.* [40] proposed a new typology of connection called *Sliding Hinge Joint* (SHJ), Fig. 2.5a. Similarly to the other approaches, the centre of rotation is situated at the upper beam flange by means of a top plate bolted to the beam flange and welded to the column. At the bottom beam flange and web, asymmetrical friction connections (AFCs) make the connection between the beam and column. Under gravity loads and serviceability limit state conditions (SLS), it works as a rigid connection while during a rare seismic event, it allows inelastic rotations. This configuration forces the beam to rotate about the top flange while the dissipation of the energy is done through the friction connections. The friction mechanism is reported in Fig. 2.5b; when the friction resistance of one of the surfaces is exceeded, the slip occurs between the bottom beam flange and the "bottom flange plate" (phase b) in Fig. 2.5b). As the deformations become greater, the bolts in the bottom flange move to such an angle that provide a sufficient shear force to initiate also the slip between the "bottom flange plate" and "bottom flange cap plate" (phase c) in Fig. 2.5b). The slip of these two surfaces doubles the

resistance. When the loading reverses, the connection works in the same way. The friction resistance is dependent on the shim material and of the force normal to the sliding surfaces.

Cyclic experimental tests on this typology of joints using brass, mild steel and sprayed aluminium as shims have been performed [40]. The experimental results have shown that the material brass is not appropriate to use as friction shims. The mild steel has a similar behaviour than brass but is cheaper. Conversely, the aluminium demonstrated a greater frictional resistance. However, this resistance degrades for repeated loading cycles. Nevertheless, in general, SHJ connection allows the dissipation of energy on the double friction surfaces and the hysteresis behaviour of these connections have shown a low possibility of large permanent displacements [40].
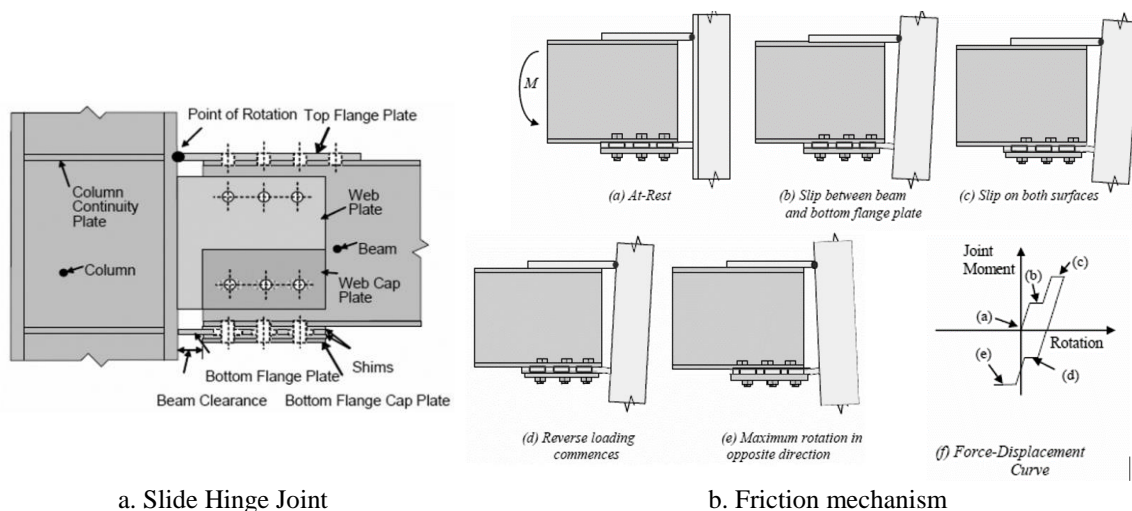
a. Slide Hinge Joint   b. Friction mechanism

Fig. 2.5. Sliding hinge joint (SHJ) [40]

Finally, a group of researchers from the University of Salerno in Italy developed a new type of Slide Hinge joint, called "*free from damage connections*" (FREEDAM). In general, this new beam-to-column connection consists in a modification of the classical DST joint by adding one or more friction dampers located at the beam flanges level or in an additional haunch connected to the lower beam flange. The friction damper is composed by a couple of angles and pre-loaded friction pads. The flange/s of the beam or haunch are provided with a slotted hole/s in order to allow the slip between plates.

The first tested configuration had friction dampers at both the bottom and upper beam flange [41](Fig. 2.6a). However, after experimental tests on full-scale joints under cyclic loading, it was noted that despite the geometrical symmetry of the connection, the behaviour and displacements were asymmetric. For this reason, the geometry of the connection has been

slightly changed and only one friction damper was placed at the bottom beam flange (Fig. 2.6b) or alternatively, in an additional haunch welded to the bottom beam flange, allowing the reduction of the tightening torque (increasing the lever arm, reduces the required horizontal slip resistance and therefore the required tightening torque, Fig. 2.6c). With these last proposed geometries, under bending actions, the connection rotates around the upper T-stub and the energy dissipation is provided by the slippage of the beam flange on the friction pads. Moreover, the fixed T-stub at the upper beam flange level can prevent the damage of the concrete slab.

a. Two friction dampers   b. Friction damper at the bottom beam flange

c. Friction damper at the bottom flange of an additional haunch welded to the beam
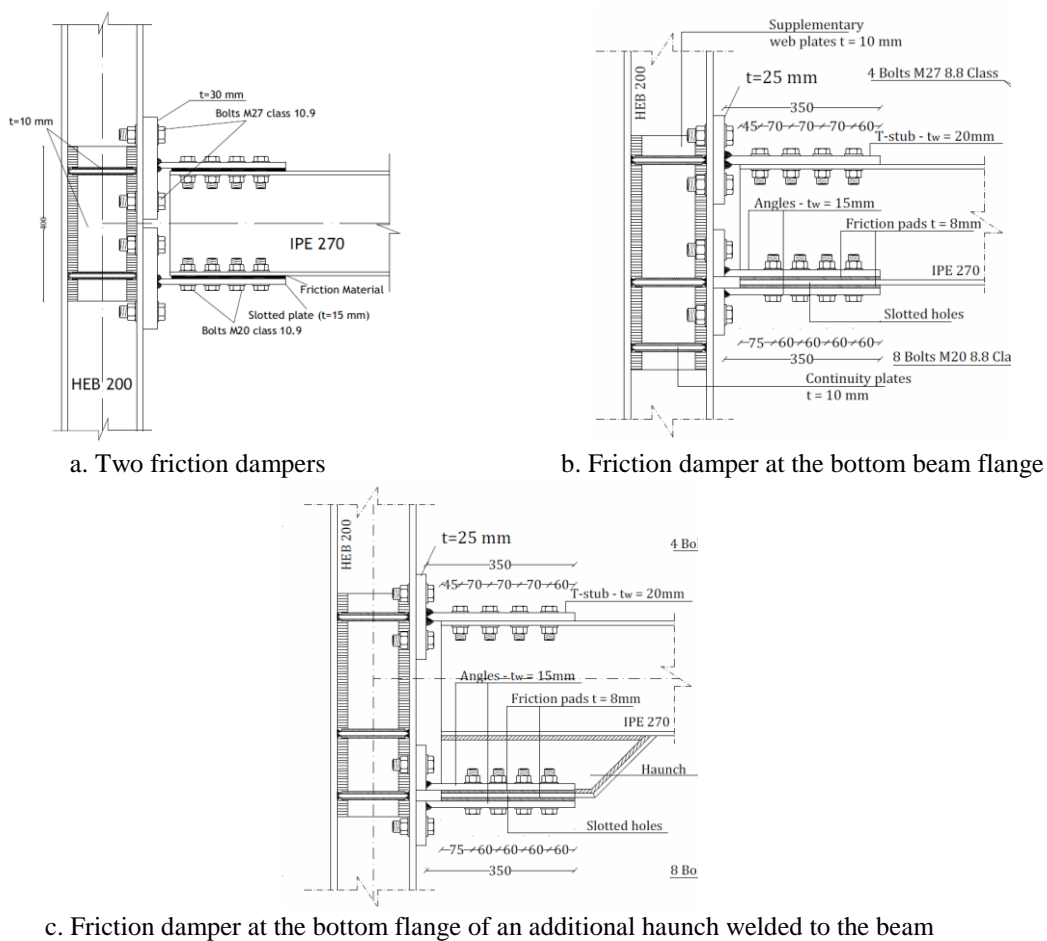
Fig. 2.6. Evolution of the FREEDAM connection [41,42] – Part I

In the last three years, this connection has been investigated within the European project FREEDAM. During the project, two configurations were used. The configuration I is the same as in Fig. 2.6c, but the haunch is bolted to the lower beam flange (Fig. 2.7a). In configuration II, the friction damper has a vertical configuration. The haunch has horizontal slotted plates while the L-stubs and friction pads have vertical slots (Fig. 2.7b). Furthermore, in both

configurations, the slotted flange of the haunch is made of stainless steel (to avoid the corrosion of the plates), while in the previous researches, all of the steel parts were from carbon steel S355.

| a. Horizontal friction damper | b. Vertical friction dampers |
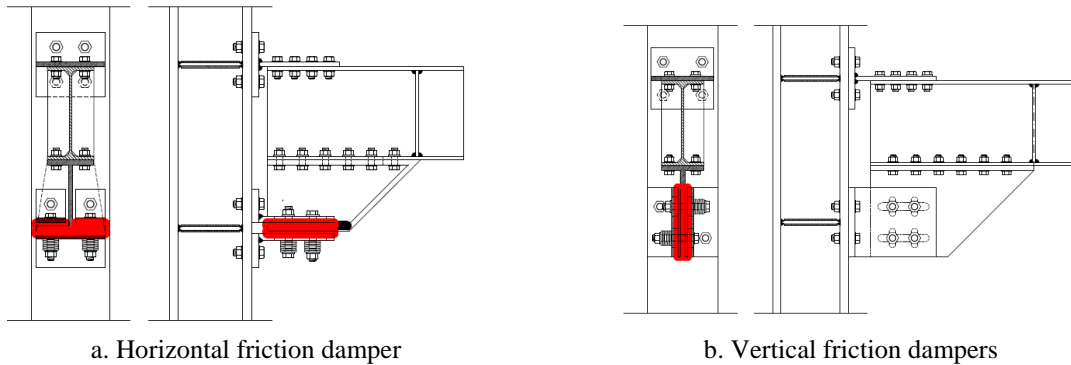
Fig. 2.7. Evolution of the FREEDAM connection [41,42]- Part II

2.3 The FREEDAM connection

As introduced in the previous section, the FREEDAM connection consists of an innovative design of beam-to-column connection for seismic resistant structures. Regardless of the configuration adopted for the connection (Fig. 2.7), it has as the main purpose to ensure that the structure and the components from the connection apart from the friction damper remain free from damage when subjected to frequent or extreme seismic events. Furthermore, under serviceability limit states, the connection has to behave as a rigid connection, i.e. slip not allowed.

The described behaviour is accomplished by a proper design of the friction damper. Moreover, the non-dissipative components have to be properly over strength in order to remain elastic. In this way, the flexural resistance of the connection depends on the friction resistance of the friction damper, which is given by the product of the friction coefficient between the friction pads and the beam μ, multiplied by the number of friction interfaces n_s and by the sum of the tightening torque applied to the bolts F_p. In addition, the length of the slotted hole/s is chosen in order to fulfil the rotation requirements coming from the seismic design.

However, the abovementioned design assumptions are true as far as the bolts of the friction damper do not reach the end stroke of the slotted hole/s. If that situation occurs, the resistance of the connection would not be anymore the friction resistance of the damper, but the resistance of the weakest steel component of the connection. Under this view, the project widened the studies to extreme accidental loading events that could lead to the achievement of the end stroke

of the slotted hole/s, such as impact loads. In particular, it is expected that due to its innovative design, the adoption of the FREEDAM connection could bring benefits to the structural robustness of MRFs frames when subjected to such loads. The first attempt to assess the behaviour of friction joints in case of a loss-of-a-column scenario has already been done by Milovanovic [43]. This preliminary study has evidenced that, owing to the possibility to calibrate the ductility of the friction connection by just increasing the size of the slot of the friction damper, these connections may have a high performance also in case of extreme loads.

Hence, the project was focused on the seismic and impact behaviour of this new connection. Furthermore, besides the connection behaviour itself, the robustness of MRFs structures equipped with these joints under seismic and impact loading conditions was also investigated. To accomplish all the objectives, the project was divided into several work packages, starting by investigating the possible coating material that could be used in the friction damper, following by study of the whole connection and ending with the assessment of the robustness of structures.

The project counted with the participation of several partners, namely, the University of Coimbra (Portugal), University of Salerno (Italy), University of Naples (Italy), University of Liege (Belgium) and two industrial partners: OFELIZ (Portugal) and FIP Industriale (Italy). The University of Coimbra participated in all the tasks related to the behaviour of the friction damper, connection and structural robustness of MRF under impact loads. Furthermore, it also participated in the experimental campaign to assess the cyclic behaviour of the connection together with the University of Salerno. In the following sections, a summary of the main findings of the projects is presented.

2.3.1 Characterization of the friction materials to be used on friction dampers

- **Frictional contact between metal surfaces:** Friction can be understood as the resistance to sliding motion of two bodies in contact. There are two basic laws of friction that are taken as true [44]:

1. The friction force is independent of the area of contact between the solids (Amontons' 1st Law);

2. The friction force is proportional to the load between the surfaces (Amontons' 2nd law).

In other words, it means that the ratio between the friction force F and the normal load N is a constant, which is called friction coefficient μ, Eq. (2.1)

$$\frac{F}{N} = cte = \mu \leftrightarrow F = \mu \cdot N \tag{2.1}$$

Furthermore, when two surfaces are in contact, very high pressures at their asperities are developed, creating a strong adhesion between them. When these surfaces slide over one another, the connections formed are sheared. Therefore, the necessary force to shear these surfaces is equal to the friction force F. Additionally, when the surfaces have very different hardness, the harder surface can plough out groves in the softer one. However, especially in the case of metals, this particularity is very small and therefore, can be neglected [44]. In this way, the friction force F is only given by the friction force due to adhesion F_A, which is proportional to the contact area A=N/σ_0 (Eq.2.2). According to equations (2.1) and (2.2), the friction coefficient can be determined by the Eq.2.3.

$$F = F_A = \frac{N}{\sigma_0} s_0 \tag{2.2}$$

$$F = \frac{N}{\sigma_0} s_0 = \mu \cdot N \leftrightarrow \mu = \frac{s_0}{\sigma_0} \tag{2.3}$$

where s_0 represents the critical shear stress of the weakest material and σ_0 is the hardness of the softest material. From the above relationship, in order to have high friction coefficients, the materials to be coupled have to have very different superficial hardness'.

The above friction force and corresponding friction coefficient represent the necessary force to initiate the sliding motion between two surfaces and are called static friction resistance and static friction coefficient. After the initiation of the motion, the force required to main the motion is generally different and it is normally referred to as kinetic friction force F_k. This force is generally lower than its corresponding static friction force, due to the lower adhesion of the contact surfaces after the initiation of the sliding.

Several parameters can influence the static friction coefficient, such as the normal load, the type of material, the sliding velocity, the temperature, stick-slip, among others. Among these factors, the normal load and the sliding velocity were investigated during the FREEDAM

project for the investigated contact pairs. Furthermore, in this thesis, also some observations on the influence of high velocities rates on the friction coefficient are reported.

With reference to the sliding velocity, the literature reports the study of Mohammad *et al.* [45] about the friction properties under different sliding velocities of stainless steel sliding on other metal surfaces (sprayed aluminium, brass, copper and gun-metal). In this study, the sliding velocity (1m/s, 1.5m/s and 2m/s), the normal load and the duration of the sliding were investigated. The results showed that, for all the sliding pairs, the friction coefficient increased when the sliding velocity increased, which was associated with an increase of temperature at the surfaces, which increased the adhesion between them.

- **Tests on friction materials:** Based on promising results of coating steel plates by means of thermally sprayed aluminum coming from past researches [46] and considering the low costs associated with the application of coatings on steel plates by means of thermal spray techniques, materials that could be employed with these techniques have been selected to be implemented in the friction damper. In the first phase of tests, the University of Salerno and FIP Industriale conducted cyclic tests at low and high velocities, respectively, in eight different materials. From this first phase of tests, the three best materials were chosen. Later, these materials were deeply investigated by means of cyclic tests, long-term tests and impact tests. The objective was to find materials, which allow (i) to achieve high values of the friction coefficient and (ii) to keep this value during the cycles associated to the seismic actions (i.e. ensuring a stable behaviour over time).

The first requirement, i.e. the achievement of high values of friction coefficient, can be achieved, according to Eq.(2.3), by selecting materials with a superficial hardness significantly different from the internal slotted plate. In these tests, the slotted plate is from stainless steel AISI 304. Therefore, the chosen materials were divided into two categories: category of "soft" materials (labelled as M1 to M5), in which the selected materials had a much lower superficial hardness than the stainless steel and the "hard" materials category (labelled as M6 to M8), where the selected materials had a much higher superficial hardness than the stainless steel. The former was composed of nonferrous pure metals or metal alloys with Vickers Hardness lower than 30, while the "hard" materials were carbide alloys materials produced as powder blends and electroless nickel friction shims produced by 3 M Deutschland GmbH [47].

The layouts used for the cycles tests at low and high velocities are reported in Fig. 2.8 and it is composed by a slotted internal plate from stainless steel AISI 304, a steel internal plate with normal holes with friction pads preloaded with M20 class 10.9 HV bolts. Both low-speed and high-speed cycles tests were performed.
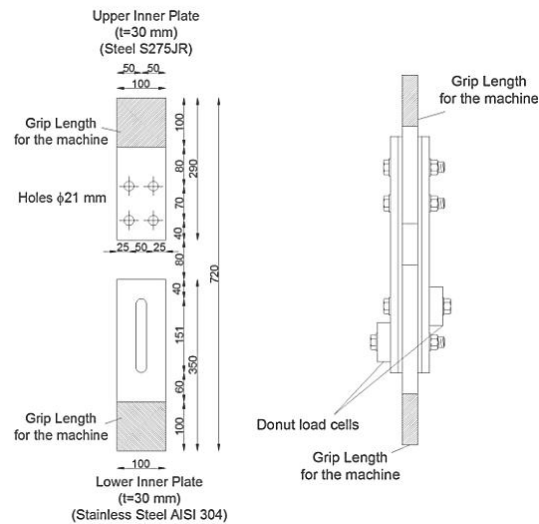
Fig. 2.8. Tested specimens under cyclic loading [48]

From the preliminary tests, three coating materials were chosen as possible candidates, namely, the "soft" materials labelled as M1 and M4, **Tin (Sn 99,9 %)** and **sprayed aluminium (AL 99 %)** respectively, and the "hard" material **Metco 70C-NS** (labelled as M6). In the second phase of tests, the influence of the preload level, the velocity of the tests and the washer configuration on the friction coefficient as well as bolts' force degradation and the effective damping deterioration were evaluated [48], considering the three materials selected in the preliminary tests. Additional, the long-term tests were carried out aiming to investigate the creep behaviour of the different coatings and to assess the long-term loss of preload.

The results from the experimental tests made possible to reach the following conclusions:

- All three materials can provide a stable cyclic response;

- At high velocities, the materials M1 (Tin) and M6 (Metco 70C-NS) were characterized by stick-slip phenomena, which may induce problems to the structure. Furthermore, the material Metco 70C-NS developed high temperatures and strong vibrations;

- The material M4 (sprayed aluminium) had the most stable response, even though under cyclic loading presented degradation of the friction resistance due to wearing of the plates;

- The tests at variable values of preload made possible to limit the preload to an upper bound value equal to 60% of the proof load for the three materials. For the material M6 due to its better hysteretic response for lower pressures (without stick-slip phenomena). For the other two materials, this value is justified because the energy degradation is lower for lower pressures.

- The Disc-Springs are effective in maintaining the preload over the friction interface;

- The tests on the evaluation of the randomness of the friction coefficient made possible to create a regression analysis in order to apply in the design and modelling of friction devices. In addition, Table 2.1 provides values of the friction coefficient that can be used in the design. For the design of the friction damper (number of bolts and their tightening torque), should be considered the 5% fractile of the dynamic coefficient, whereas, for the non-dissipative parts (beams, columns and the other elements of the connection), the 95% fractile of the static friction coefficient should be considered;

- The long-term tests showed that the loss of preload occurred in the first 12h after tightening and that the use of Disc springs only affect the specimens with the "soft" materials (M1-Tin and M4-sprayed aluminium).

- Finally, the University of Naples performed FEM modelling to simulate the cyclic tests at low speed. Since the experiments showed an increase of temperature due to the friction mechanism, a temperature-dependent friction coefficients model was used in the numerical analyses. The numerical analyses were able to show the same experimental reduction of friction through the cycles (Fig. 2.9).

Table 2.1. Design values for the friction damper [48]

Material M1		Material M4		Material M6	
Design *FC*	$\mu_{0,design}$	Design FC	$\mu_{0,design}$	Design FC	$\mu_{0,design}$
Static 5% fractile	0.62	Static 5% fractile	0.69	Static 5% fractile	0.52
Static 95% fractile	0.81	Static 95% fractile	0.84	Static 95% fractile	0.68
Dynamic 5% fractile	0.43	Dynamic 5% fractile	0.53	Dynamic 5% fractile	0.49
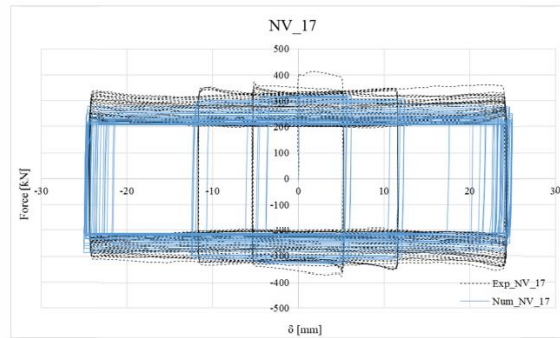
Fig. 2.9. Sliding force vs displacement: Exp. vs numerical [49]

2.3.2 Design rules for friction joints

With the information on the friction damper component reported in the above section, a design procedure for the connection under study was proposed. These design guidelines follow the two principles of capacity design. In a first step the dissipative component, i.e. the friction damper is designed while, in a second step, attention is focused on the non-dissipative zones.

Step 1: Determination of the friction resistance $F_{friction,Rd}$ of the dissipative component, i.e. the friction device.

Knowing the actions acting on the beam it is possible to provide the slip force needed to design the damper. This action is the maximum value above the one provided by seismic actions and gravity loads. In a first step, the beam section is designed to support vertical loads. The haunch height can be assumed equal to the beam height d_b and, if needed, progressively increased to reduce the action on the friction damper. The sum of the beam and haunch height is the lever arm h needed to determine the slip force acting on the device, $F_{slip,Ed}$ (Eq.2.4). In turn, the slip force can be also obtained by Eq. (2.5), where μ is the friction coefficient, which can assume two values: $\mu_{dyn,5\%}$ and $\mu_{static,95\%}$ (see Table 2.1 for the design values), F_p is the bolt preload force computed according to EC3, n_b is the number of bolts, n_s is the number of the surfaces.

$$F_{slip,Ed} = \frac{M_{b,Rd}}{h} \tag{2.4}$$

$$F_{slip} = \mu \cdot F_p \cdot n_b \cdot n_s \tag{2.5}$$

The purpose is to define the minimum number of bolts to achieve the required slip resistance of the friction damper, which can be obtained from Eq. (2.5) using the lowest expected friction dynamic friction coefficient $\mu_{dyn,5\%}$, Eq.(2.6).

$$n_{b,\min} = \frac{F_{slip,Ed}}{\mu_{dyn,5\%} \cdot F_p \cdot n_s} \tag{2.6}$$

This number is rounded up and fixed. Then, it is used to obtain a new preload force $F_{p,red}$ (Eq.2.7). Also this value of preload is rounded up and a new friction resistance $F_{slip,Rd}$ and the corresponding bending moment $M_{slip,Rd}$ are found (Eq.2.8 and Eq.2.9).

$$F_{p,red} = \frac{F_{slip,Ed}}{\mu_{dyn,5\%} \cdot n_b \cdot n_s} \tag{2.7}$$

$$F_{slip,Rd} = \mu_{dyn,5\%} \cdot n_b \cdot n_s \cdot F_{p,red} \tag{2.8}$$

$$M_{slip,Rd} = F_{slip,Rd} \cdot h \tag{2.9}$$

Step 2: Calculation of bending moment $M_{cf,cd}$ at the column flange and check of the resistance of the beam in bending.

After the design of the dissipative component, the non-dissipative components have to be designed in order to transmit the maximum force that the dissipative component is able to exhibit, $F_{slip,Cd}$. The maximum bending moment at the column flange $M_{cf,Cd}$ can be obtained from Eq. (2.9), using the maximum value of friction resistance of the damper $F_{slip,cd}$ which is obtained from Eq. (2.10).

$$F_{slip,Rd} = \gamma_b \cdot \mu_{dyn,5\%} \cdot n_b \cdot n_s \cdot F_{p,red} \tag{2.10}$$

Where γ_b is the expected over strength factor, obtained from the ratio between the 95% fractile of the friction coefficient and the 5% fractile dynamic friction coefficient (see Table 2.1 for the design values).

The bending moment at the axis of the beam plastic hinge $M_{b,Ed}$ cannot be greater than the plastic bending moment of the beam $M_{b,Rd}$. Therefore, it is necessary to evaluate the bending moment at the axis of the beam plastic hinge to each corresponds the applied bending moment at the column flange. Assuming a triangular distribution of the bending moment along the beam length, this can be checked according to the following inequality:

$$M_{b,Ed} = M_{cf,Cd} \frac{L_e - a}{L_e} \leq M_{b,Rd} \tag{2.11}$$

Where L_e is the shear length of the beam and a is the horizontal extension of the joint. If the above inequality is satisfied, the reduced preload force $F_{p,red}$ can be used. If not, there are two possible solutions: i) reducing the preload force through a coefficient $\overline{m}$, obtained from the ratio between the beam plastic moment and the column face design moment or ii) increasing the beam section. In addition, on the basis of the experimental tests on the friction damper reported in the previous section, the range of the applied preload force should be in between 50%-60% of the preload value recommended by the Eurocode 3 part 1-8 [5], in order to limit the relaxation of pre-loading due to creep phenomena and to prevent the yielding of the bolt shank under bending.

After defining the preload force to be applied, the non-dissipative components are designed according to Eurocode 3 part 1-8 [5], to resist the maximum value of friction resistance of the damper, $F_{slip,Cd}$.

2.3.3 Friction connection behaviour

The assessment of the connection behaviour was quite similar to the friction damper, in the sense that the connection behaviour was investigated under cyclic loads (seismic behaviour) and impact loads. Furthermore, from the results of the work on the behaviour of the coating materials, the sprayed aluminium (M4) was selected as the preferred coating material.

The cyclic tests were performed by the University of Salerno (external joints) and by the University of Coimbra (internal joints) [42]. The configurations showed in Fig. 2.7d and e) were used for this purpose. The influence of scale effects was also evaluated adopting two different beam sizes (IPE 270 and IPE450). Furthermore, in some tests, disc springs were used instead of flat washers.

Fig. 2.10 depicts the cyclic behaviour of the tested connections obtained in 4 tests. The label code used to identify each assembly is, as follows: "FD" means friction device, the first number corresponds to the joint configuration (1 for the assembly with the horizontal friction device, Fig. 2.7a, and 2 for the configuration with the vertical friction device, Fig. 2.7b) and the second number is related to the size of the assembly (1 for small beam or 2 for large beam). In addition, the term "DS" identify the use of disc springs. The experimental tests showed that the cyclic

behaviour of these connections is similar, independently of the friction damper configuration and assembly size and that they are characterized by stable hysteretic behaviour. Both assemblies behave as rigid up to the activation of the slip. Furthermore, both show asymmetric behaviour under sagging and hogging moment, being this difference larger for the connections with the horizontal friction damper (configuration 1). In addition, a loss of strength is always observed, especially in the cases where a higher beam section is used, which was explained by the use of longer bolts and a higher applied bolt preload.

The higher asymmetric behaviour was stated to be related to the local deformation of the T-stubs and L-stubs elements. While the upper T-stub is the same for both assemblies and thus the gap opening of this element under hogging moment is of the same value for the different assemblies, the lower L-stubs were different depending on the friction damper configuration. In fact, under hogging moment, the gap opening of the T-stub elements was of the same value for the different configurations and thus, the difference under hogging moment is not significant. On the other hand, under sagging moment, the lower L-stubs in the case of connections with the horizontal friction damper showed a larger gap opening which explains the difference in terms of flexural strength under sagging moment. Furthermore, negligible plastic deformations were observed in the beam and T-stub/L-stubs elements, at a rotation demand of 0.05rad.
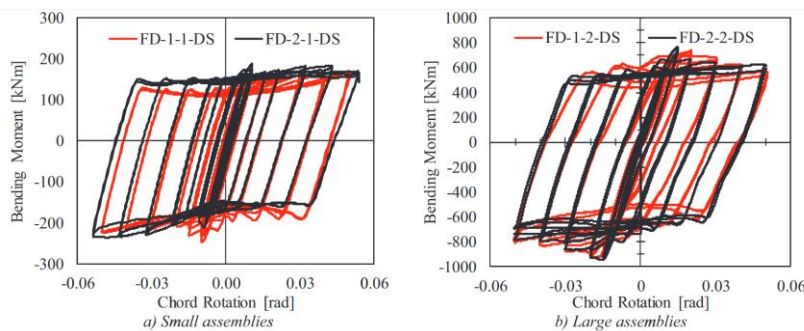
Fig. 2.10. Comparison of the responses of the 2 device configurations [42].

Additionally to the experimental tests, FEM simulations using ABAQUS software were carried out in order to simulate the cyclic tests on the external joints and to perform parametric analysis on the influence of the preload force and of the friction coefficient on the cyclic behaviour of the investigated connections [42]. Fig. 2.11 shows the comparison between the numerical simulations and the experimental tests already showed in Fig. 2.10, for the cases where a lower beam section is used. The numerical simulations can generally simulate the

global and local behaviour of the joint. Only the first cycles are not accurately simulated because the transition between the static friction coefficient and the dynamic was not modelled. However, this accuracy increases with the increase of the number of cycles. As in the experiments, some plastic deformation some plastic deformations in the bolts and in the connecting L-stubs and T-Stubs. In addition, in accordance with the experiments, the simulations also showed that the joints equipped with the vertical friction damper exhibit lower plastic deformations than the corresponding device with the horizontal friction surface. However, it should be noted that these plastic deformations are negligible and that they happened at a large rotation demand (0.05 rad).

Finally, the parametric studies highlighted the importance in controlling the preload force applied to the bolts as well as the randomness of the friction properties of the friction pads, since the bending capacity of the connections is directly proportional to these two parameters.
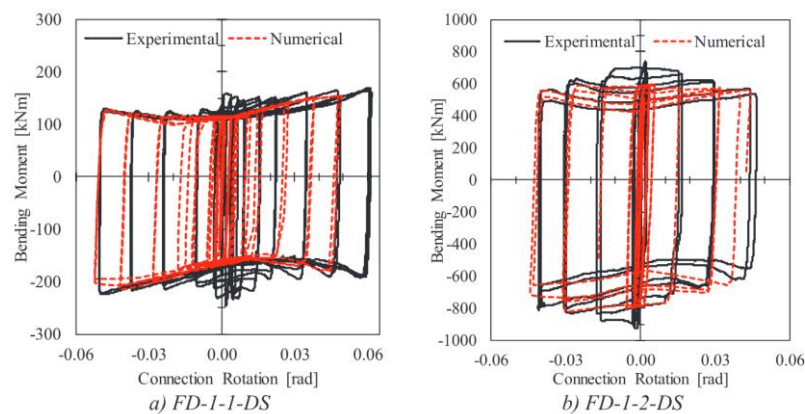
Fig. 2.11. Numerical vs experimental [42]

2.4 Design of structures against progressive collapse

2.4.1 European and American regulations for progressive collapse

The Ronan Point Tower incident, in London 1968, led to the released of the UK Building Regulation, which provided requirement to ensure a minimum level of structural integrity, and led also to some changes to American and Canadian codes. However, only after the Oklahoma City bombing in 1995 and the World Trade Center disaster in 2001, were progressive collapse assessment method guidelines introduced by the Us General Service Administration (GSA) [50] and the US Department of Defence UFC [51]. Eurocode 1 part 1-7 [16] only appeared in 2006 and it contains the rules of the UK Building Regulations of 2000. Rules between European and

American codes are similar. However, the American codes had evolved and improved their robustness requirements considerably. In Table 2.2 is reported the main differences and similarities between the Eurocode and the American UFC code, where it can be observed that the American code provides some additional points such as the consideration of the dynamic effects (by the implementation of dynamic amplification factors) and some provisions on connection ductility in progressive collapse.

Table 2.2. Differences between European and American regulation [52]

	Eurocode 1 Part 1-7	UFC
Alternative load Path method	●	●
Notional element removal	●	●
Key element design	● (34 kPa)	● (Ductility Requirements)
Horizontal damage extension limit	● (less of 15% storey area or 100 m^2)	● (no failure of floors)
Horizontal Tying	●	●
Vertical Tying	●	●
Systematic risk assessment	●	●
Building classes/ Buiding risk classification	●	●
Consideration for dynamic effects		●
Provisions for ductility of connections		●
Applicability	All buildings	All buildings

2.4.2 Design methods for robustness

There are two primary design methods when designing a structure to avoid progressive collapse, **indirect** and **direct design methods**. The **indirect method** is a prescriptive method in which certain design rules are applied to structures in order to assure its robustness. Examples of design rules can be a good plan layout, an integration of a system of ties (**tie force method**), load-bearing interior partitions, catenary action of the floor slab, ductile detailing and additional reinforcement for blast and load reversal if the designer must consider explosive loads [51]. It is the most basic and easiest method to improve the robustness of a structure and does not rely on the assessment of the structural response to abnormal loading. This method results in a reinforcement of the structural elements in order to develop more their capacity either in flexural or membrane action when subjected to abnormal loading conditions [1].

Direct methods however rely strongly on the calculation of the structural response to abnormal loading and the enhancing of the structures strength is provided by designing key

structural elements to resist failure under abnormal loading (**specific load resistance method)** or by designing the structure so it can bridge across the local failure zone (**local alternative path method**). Irrespective of the chosen method, it requires more sophisticated analyses when compared to the usual gravity or/and lateral load analyses commonly used in the design of structures.

The specific load resistance method (key element design) is a threat specific approach, in a sense that the designer designs the critical load-bearing components to resist a specific threat such as impact or blast pressures. On the other hand, the local alternative path method does not require the definition of a specific threat. In this method, the capability of the structural system to resist the removal of a primary load bearing component is checked by means of the activation of alternate loading paths after the loss of the element. This method is still the most used method to assess the robustness of a structure after an abnormal event leading to the loss of one of its loading bearing components because it promotes structural systems with ductility, continuity, and energy absorbing properties that are desirable when preventing progressive collapse.

In the following subsections, the previous design methods will be described in detail.

2.4.2.1 Tie force method

The tie force method is a prescriptive method or indirect method with the intention of providing some minimum requirements of robustness on buildings. The different types of ties typically incorporated in a structure are schematized in Fig. 2.12. Horizontal tying allows the floors to carry loads to the undamaged zones of the structure through large displacement membrane or catenary actions, activating alternative load paths. In turn, vertical ties are considered to provide continuity between structural members, for the cases where reverse load happens exerting vertical upwards pressure upon the slabs.

In general, this method provides a contribution to structural robustness because it ensures a minimum level of strength and continuity between the structural elements. On the other hand, it does not provide a quantification of the increase in robustness. Furthermore, in the cases where the elements adjacent to the directly affected zone are unable to resist the new distribution of internal forces, the tying method can produce a "*drag-effect*" where the local damage zone drags the rest of the structure into collapse, creating a disproportionate collapse. However, this last drawback can be avoided using alternative load path analyses together with the tie force method, in order to ascertain adjacent member resistance.
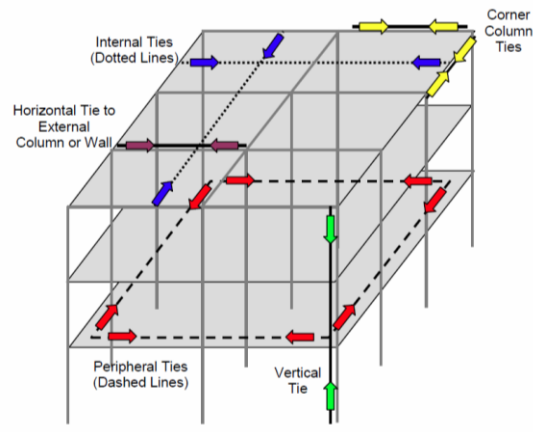
Fig. 2.12. Tie force method [1]

In Eurocode 1 Part 1-7 [16], the calculation of the design horizontal tying forces depends on the dead and live loads acting on the floors and on the span, using the expressions of Table 2.3, while for the vertical design tie forces, the code requires that the columns and walls carrying vertical actions should be capable of resisting a tensile force equal to the largest design accidental vertical load from any upper storey. These rules are required for medium-low and medium-high consequences classes 2a and 2b. For the former, it allows only the provision of horizontal tying, while for the medium-high consequences classes, it recommends that effective horizontal ties should be provided together with vertical ties in all supporting columns and walls.

Together with the tying provisions, notional element removal analysis can be carried out, removing one bearing element at a time. However, it is important to state that although suggested, Eurocode does not provide any guideline procedure for element notional removal analysis.

Table 2.3. Horizontal ties forces

Internal	$T_i = \max\left(0.8(g_k + \psi \cdot q_k) \cdot sL; 75\right)$
Perimeter ties	$T_p = \max\left(0.4(g_k + \psi \cdot q_k) \cdot sL; 75\right)$

Ψ – Live load factor which depends upon the considered type of accidental action; g_k – dead load; q_k – Live load; s – ties spacing; L span of the tie; A – cross-section area; H – Height; t - thickness

2.4.2.2 *Alternative path method*

The alternative load path is a quantitative threat-independent method in which the structural robustness is assessed by removing a load-bearing element of the structure. By removing a load-bearing element, the structure's ability to redistribute internal forces by means of alternative

loading paths is evaluated. In this way, all the elements of the structure can be designed in order to have sufficient residual capacity in terms of strength and ductility, avoiding disproportionate collapse. This method is the most used by the researches, due to its simplicity and accuracy. In fact, the main advantage of this method is the possibility of using several different types of analysis, with different types of complexity, while the main disadvantage is that only one bearing element is removed at a time. Both the partial collapse of the Alfred Murrah federal building in 1995 and the World Trade Centre disaster in 2001, where more than one bearing element was instantaneously destroyed by the attack, highlight this disadvantage.

There are several procedures that can be used in the alternative path method, as summarised in Table 2.4. The linear procedures are the easiest to employ but are limited to small displacements and lead to a conservative design since it requires that the elements should remain elastic and that second-order effects (P-Δ) and instabilities should be ignored. For these reasons, these methods are not often used. On the other hand, the nonlinear methods, although more complex, are able to account for geometric nonlinearity and allow the development of alternative load path mechanisms.

Table 2.4. Alternative path method procedures [53]

	Linear static DLF[1]	Non-linear static DLF	Non-linear static pushover	Linear dynamic	Non-linear dynamic
Include material plasticity		●	●		●
Account for strain hardening		●	●		●
Include P-Δ effects		●	●		●
Negates the use of dynamic load factors			●	●	●
Accounts for strain-rate material effects					●
Account for damping					●
Allowable in GSA	●	●	See note [a]	●	●
Allowable in Us DoD	●	●	See note [a]		●

[a] The non-linear static pushover method has been developed since US DoD and GSA guidelines were published and at the time of writing is not currently included. This may change as new version of the guidance are produced.
[1] DLF – Dynamic Load Factor

As mentioned before, although Eurocode and the UK regulation suggest the use of the alternative load path method, neither provide a specific procedure to conduct such analysis. On the other hand, the American standard GSA [50] recommends that this analysis should be done

considering the removal of a middle column of the long side of the building, a middle column on the short side and corner column at the first storey ground level. UFC [51] suggests the removal of the columns at each floor level for the same locations as indicated by GSA. Both codes approve four approaches for this method: i) linear static DLF, ii) nonlinear static DLF, iii) linear dynamic and iv) nonlinear dynamic analysis.

All the static procedures have to account for the dynamic inertial effects in the collapse. The easiest way to do it is to increase the dead and live loads of the static analysis by dynamic load factors (DLF), which is given by the ratio of the dynamic to static load required to achieve the peak vertical displacement of the structure. This factor can vary from 2 (elastic system) to 1. However, when using material nonlinearity the calculation of this factor is complicated due to the achievement of significant plastic rotation and deformations.

A static nonlinear procedure, which does not require the estimation of DLFs to predict the dynamic response, has been developed by Izzuddin *et al.* [23]. This procedure is an energy balance method, which compares the energy released by the column removal against the energy absorption capacity of the structure. Due to its simplicity, it can be applied to structures with different levels of idealisation, from a simple double span beam scenario to multi-storey structures, using simplified or detailed models to account for the material nonlinearity and connection response. The nonlinear static response of the damaged structure is calculated considering the structure loaded only with vertical loads, which are gradually applied to the structure. The column loss is simulated by pulling the structure down, at the node representing the removed column. The nonlinear static load-displacement curve resulting from this analysis accounts for elastic and plastic phases before hardening or softening in case of failure. Once the response is established, a dynamic assessment is conducted, assuming that the response has a single dominant deformation mode. This assessment allows the determination of the maximum dynamic displacement to which the structure achieves the equilibrium in its damaged state ($F_{y, damaged}$ in Fig. 2.13a), considering the energy balance between the work done by the external load and the internal energy stored within the structure (Fig. 2.13b). At the time of column loss, the resistance is lower than the applied gravity load (F_{st} in Fig. 2.13a), leading to an acceleration of the structure. At this point, the difference between the work done and the internal energy is the kinetic energy. At the time when the resistance becomes greater than the work done, the kinetic energy is reduced and the structure can eventually be brought back to rest. The displacement at which this happens is calculated such that the internal energy and

work done are equal ($F_{y,\,damaged}$ in Fig. 2.13a). In the cases where this balance is not reached, the progressive collapse of structure is likely to happen. If the equilibrium is achieved, a ductility assessment should be performed to ensure that the damage deformation remains within the limit state.

a. Force-displacement curve   b. Energy balance method
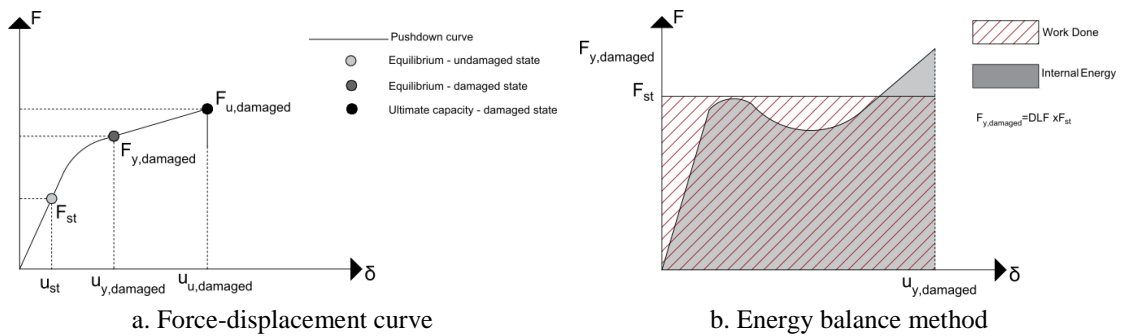
Fig. 2.13. Pushdown analysis – energy balance [23]

A dynamic analysis allows the complete time history response of the structure to be obtained. Contrary to the static procedures, there is no need to define dynamic load factors or calculate the pseudo-static response first, since the dynamic effects are already accounted for. Furthermore, in addition to the material nonlinearity and connection response, the strain rate effects should also be considered in this type of analysis. Another important factor when performing a dynamic analysis is the removal time of the column since it can influence the time history response of the structure [52,54]. GSA guidelines suggest that this time should not be higher than 1/10 times the period associated with the structural response mode for the vertical element removal.

To conclude, all of these analyses have their advantages and disadvantages. Simpler procedures generally lead to conservative designs but are easier to verify. On the other hand, more complex design procedures require higher computational effort and engineering expertise.

However, all of the procedures abovementioned require the definition of a structure model and a static and stability analysis prior to the progressive collapse analysis. In this way, a progressive analysis method, as suggested by Marjanishvili [55] can be implemented, i.e. several analyses are performed, with increased complexity. In this way, the results coming from more complex analyses can be compared with those obtained in the simpler methods, decreasing the probability of analysis errors.

2.4.2.3   Key element design

The key element design method is a direct design method with a different philosophy than the tying and alternative path method. While the tying and alternative path method are focused on limiting the spread of damage after an incident that leads to a loss of a member/s, the key element design method prevents the damage of the supporting element to an extent that it can no longer provide the required support. Contrary to the alternative path method, this method is a threat dependent design approach where the "key elements" that can lead to failure of the structure are designed to withstand a specific threat, such as explosions, impact, fire or others.

In the Eurocode framework, the use of this method is recommended for medium-high consequences class buildings, for supporting members to which an unstable structural behaviour or damage spread above the limit stabilise by the code was obtained in the alternative load path analyses. These members should be checked for an accidental action equal to 34 kPa, applied in both vertical and horizontal directions. It is worth to mention that, this action was estimated from the Ronan Point collapse and it corresponds to a rounded estimation of the explosion pressure to have cause failure of the load bearing corner wall of the building [56].

2.4.3 Impact loads on building according to Eurocode 1 Part 1-7

Eurocode 1 part 1-7 [16] covers the definition of impact loads due to road traffic, train traffic and ships in its Section 4 and Annex C.

Regarding the determination of the impact actions, the Eurocode allows the use of a dynamic analysis or the representation of impact actions by means of equivalent static forces. The model with static equivalent forces can be used for verifying the static equilibrium, strength and deformations of the structure. In addition, it also recommends the determination and consideration of the mechanical properties of both structure and colliding object, as well as the strain rate effects, when relevant. However, no further guidance is given, leaving it for the designer to decide how to model these parameters.

With reference to the definition of the impact actions, the code gives the designer two options: i) design the impact action as a "*hard impact*", where the energy is completely absorbed by the impact body, while the structure remains rigid (Fig. 2.14) or ii) design the impact action as a "*soft impact*", where the energy is absorbed by the elastic-plastic deformations of the structure. In both cases, the general expression to obtain the static equivalent impact force is

presented in Eq. (2.12), where v_r is the velocity of the colliding object, k is the elastic stiffness of the colliding object or the structure in case of "*hard impact*" and "*soft impact*", respectively, and m the mass of the colliding object. The duration of the action can be obtained by Eq.(2.13), if the force is considered as a rectangular pulse applied on the structure surface (Fig. 2.14).

$$F = v_r \cdot \sqrt{k \cdot m} \qquad (2.12)$$

$$\Delta_t = \sqrt{m/k} \qquad (2.13)$$
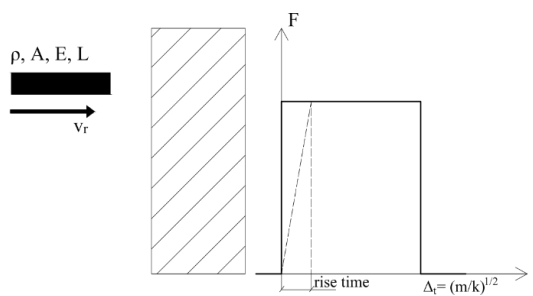
Fig. 2.14. Hard impact model of Eurocode 1 Part 1-7 [16]

With reference to loads from vehicle collision on structures, the code suggests that the velocity of the collision object v_r of Eq.(2.12) can be determined by Eq. (2.14), where v_0 is the velocity of the vehicle leaving the trafficked lane, a is the average deceleration of the lorry after leaving the trafficked lane, s is the distance from the point where the vehicle leaves the trafficked lane to the structural member, d is the distance from the centre of the trafficked lane to the structural member and d_b is the braking distance $d_b = (v_0^2/2a)\sin\varphi$, where φ is the angle between the trafficked lane and the course of the impacting vehicle (Fig. 2.15a). In Table 2.5 is reported the code suggested values for the required parameters to the calculation of the collision force of Eq. (2.12). In addition, the code gives recommendations about the dimensions of the applicable area of the resulting collision force F, as shown in Fig. 2.15b.

$$v_r = \sqrt{v_o^2 - 2as} = v_o \cdot \sqrt{1 - d/d_b} \qquad (2.14)$$

Table 2.5. Table C.1 Eurocode 1 Part 1-7 [16]: Indicative data for probabilistic collision force calculation

Variable	Designation	Probability distribution	Mean value	Standard deviation
v_o	Vehicle velocity			
	highway	Lognormal	80 km/h	10 km/h
	urban area	Lognormal	40 km/h	8 km/h
	courtyard	Lognormal	15 km/h	5 km/h
	parking garage	Lognormal	5 km/h	5 km/h
a	Deceleration	Lognormal	4 m/s^2	1.3 m/s^2
m	Vehicle mass - lorry	Normal	20 000 kg	12 000 kg
m	Vehicle mass - car	----	1500 kg	----
k	Vehicle Stiffness	Deterministic	300 kN/m	----
φ	Angle	Rayleigh	10º	10º

Vehicle type	Area of application force F
Lorry	h = 0.5 to 1.5 m a = 0.5 m by min (1.5 m; member width)
car	h = 0.5 m a = 0.25 m by min (1.5 m; member width)

a. Definition of the parameters *s*, *d* and *φ*   b. Application of the force surface
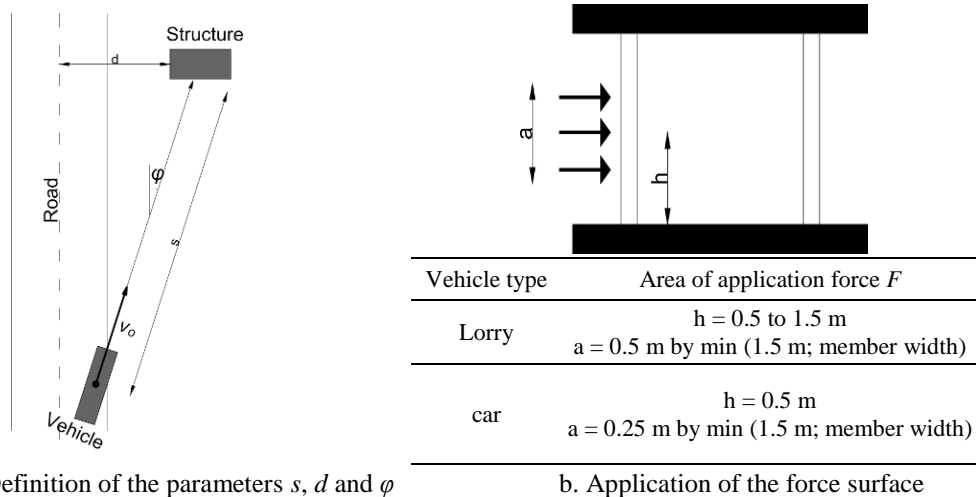
Fig. 2.15. Lateral impact from a vehicle in a building [16]

2.5 Strain rate sensitivity of steel materials

2.5.1 Introduction

Strain rate defines the strain deformation per unit of time to which a material is subjected, d_ε/d_t. Strain rate sensitivity implies that some of the properties of the material are a function of the strain rate. Generally, the strength properties increase for high strain rates, this increase being more pronounced for steels with high ductility, while the ultimate strain decreases [57,58]. This considered, it is easy to understand that connections, being, in general, the assembly of different steel grades (typically high strength steel for bolts and mild steel for plates), can exhibit a dynamic response strongly different from the static one, depending on the strain rate sensitivity of the materials constituting plates and bolts.

Usually, the experimental characterization of the behaviour of steel under different strain rates is performed by the Split Hopkinson bar test. The test arrangement normally used is shown in Fig. 2.16 and it consists on a loading bar (or incident bar), which is impacted through a striker bar (this striker bar can be a hammer, pneumatic cylinder or others). The specimen is in between the input and the output bar. When an impact occurs, it generates a wave-pulse that travels through the loading bar to the specimen, where it is partly transmitted to the transmitter bar and partly reflected to the loading bar. The stresses in both bars are measured by strain gauges.
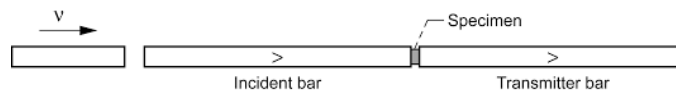
Fig. 2.16. Hopkinson bar test

In the next sections, the available literature concerning the behaviour under different strain rates of the materials used in the FREEDAM connection is presented. All steel elements are from mild steel (S275 JR), except the lower flange of the haunch which is from stainless steel AISI 304. The bolts are all carbon bolts of class 10.9 HV.

2.5.2 Mild steel

When it comes to the behaviour of mild steel under high strain rates, there are assumptions that are considered to be true, as follows:

(1)   The yield and ultimate stress increase. This increase is normally more pronounced for the yield strength than for the ultimate strength;

(2)   The ultimate and fracture strain decreases;

(3)   The initial stiffness remains unchanged.

Several works on the characterization of the tensile behaviour of mild steel under high strain rates can be found in the literature [58–60]. One of them is the work of Saraiva [59], who tested mild steel S355 specimens at an average rate of $600s^{-1}$ using the Hopkinson bar test. From the stress-strain curves shown in Fig. 2.17a, the three above assumptions can be observed, i.e. increase of the yield and ultimate strength, the decrease of the ultimate strain and the initial stiffness remained almost unchanged. Furthermore, it can also be noticed that, at high strain rates, mild carbon steel does not show its characteristic yield plateau. From these tests, Saraiva found an increase of 1.5 of both yield and ultimate strength at $600s^{-1}$, when compared to the

static values. Also Vedantam *et al.* [58], observed an increase between 1.5 and 1.6 for mild steel at strain rates ranging from $10^{-3}s^{-1}$ to $1800s^{-1}$ (Fig. 2.17b). However, here, the yield strength increased much more than the ultimate strength, while in the tests performed by Saraiva [59] this difference is not so visible.

| a. Saraiva [59] | b. Vedantam [58] |
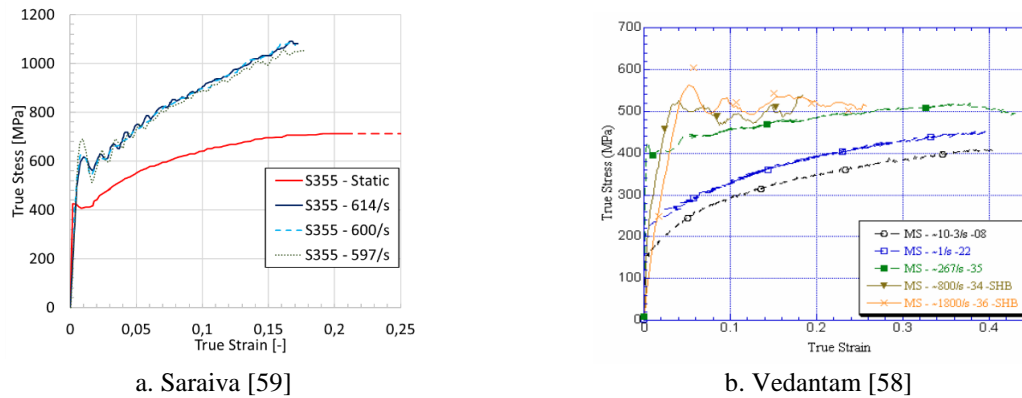
Fig. 2.17. True stress-true strain relationships for mild steel under high strain rates

2.5.3 Austenitic stainless steel

Concerning the behaviour of austenitic stainless steel at different strain rates, the works of Albertini and Montagni [61] and Lee *et al.* [62] can be highlighted. In Fig. 2.18 the stress-strain curves for austenitic stainless steel type 304L are reported. In both works, an increase of the strength is observed while both ultimate and fracture strains decrease, with the increase of the strain rates. For instance, for a strain rate equal to $50s^{-1}$, Albertini and Montagni observed an increase of 1.4 and 1.1 of the yield and ultimate strength, respectively, while the ultimate and fracture strains represented values around 0.6 of the strains observed under static strain rates (Fig. 2.18).

Lee *et al.* [62] also evaluated the behaviour of stainless steel AISI304L for strain rates between $10^{-3}s^{-1}$ and $4800s^{-1}$ as reported in Fig. 2.18b. The behaviour of the steel tested here is in agreement with conclusions made from the work of Albertini and Montagni, i.e. an increase of both yield and ultimate strength. In addition, also a decrease in the ultimate stress is observed.

a. Albertini and Montagni [61]　　　　　b. Lee *et al.*[62]
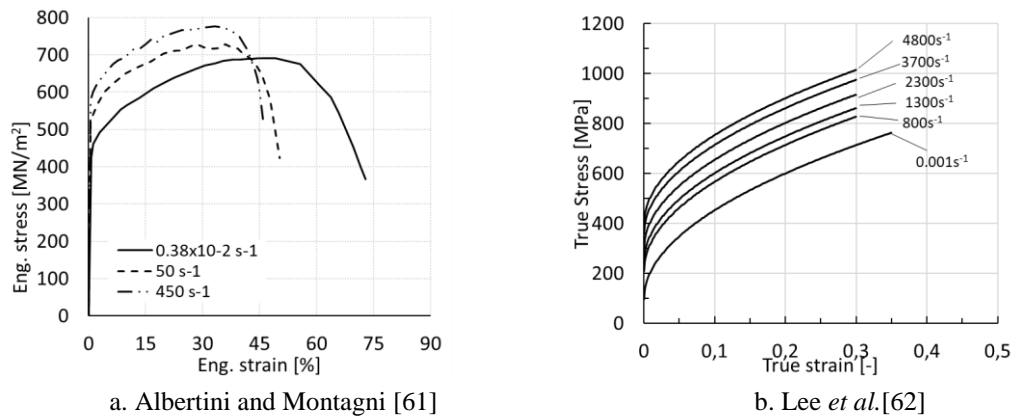
Fig. 2.18. Behaviour of stainless steel 314L under different strain rates [61,62]

2.5.4 Bolts

Bolts are normally characterized by less sensitivity to strain rates when compared to mild or stainless steel due to their significantly higher strength. In any case, their behaviour under different strain rates should not be disregarded. Conservatively, some authors suggest that the DIF for this component should not be considered more than 10% [63].

Munoz Garcia *et al.* [64] carried out the first studies on the influence of strain rates on tensile behaviour of bolts. Bolts of different grades such as 8.8 and 10.9 and different types (black bolts, galvanized and stainless steel) with diameters ranging from M12 to M16 were tested. The objective of the work was the study of the resistance, ductility and failure mode of the bolts under different strain rates. In addition, the influence of using more than one nut on the failure mode was also evaluated.

Under quasi-static loads, they found that the carbon steel bolts were characterized by nut stripping failure when using one nut and by shank failure at the threaded part between the nut and the unthreaded shank when two nuts were used. In any case, 8.8 or 10.9 carbon bolts (galvanized or black) showed a brittle failure. On the contrary, the stainless steel bolts always failed by shank necking, showing a much higher ductility than the carbon bolts.

Under dynamic loading, the failure modes did not change. Carbon bolts showed a reduction of strength and ductility as the rate increased. On the other hand, the stainless steel bolts showed an enhancement of their properties under high strain rates.

In contrast to the findings of Munoz Garcia *et al.* [64], Fransplass [65] observed always an increase in the tensile stress when high strain rates were considered, independently of the failure

mode (nut stripping or shank failure at the threaded part between the nut and the unthreaded shank). Furthermore, he also observed a reduction of the ductility of the bolts.

The findings of Fransplass [65] are also in agreement with the most recent research of the University of Sheffield carried out by Culache *et al*. [26]. They experimentally tested carbon and stainless steel M12 8.8 bolts and observed that, for carbon steel bolts, the failure happened by nut stripping with an enhancement of the ultimate strength and reduction of ductility as the strain rate increased (Fig. 2.19a). In the case of stainless bolts, as in [64] the failure happened by shank failure with necking deformation. Furthermore, for higher strain rates, the tensile strength increased and ductility decreased.
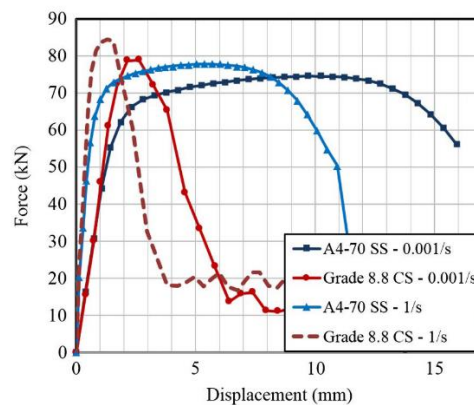
Fig. 2.19. Behaviour M12 class 8.8 carbon and stainless bolts under different strain rates [26]

Concerning the shear behaviour of high strength bolts under dynamic loading, much less information can be found in literature. In fact, only the research of Kim *et al.* [66] was found. They study the sensitivity M30 bolts under quasi-static and dynamic shear loading. The bolts had grooves cut into them to create a shearing plane of 20 mm and 22 mm of diameter and a high-speed crash machine with a maximum velocity of 9.5m/sec has been used. From the tests, an enhancement of 20% of the ultimate strength was found for the specimen with 20 mm. However, no information about the ultimate shear deformation is provided.

2.5.5 Methodologies to account for strain rate effects in FEM and analytical models

The effects of the strain rates are usually implemented into models considering a "dynamic increase factors" (*DIFs*), which promotes the increase of the yield and ultimate strengths based on the ratio of the strengths observed dynamically and statically, Eq. (2.15). Models to represent

the yield and ultimate dynamic increase factor are available in the literature [57,60] and are based on laboratory tests.

$$DIF = \frac{\sigma_{dyn}}{\sigma_{static}}$$

(2.15)

One of them is the model of Malvar and Crawford [57]. The study included a detailed literature review on the effects of high strain rates. The results indicated that there was a greater dynamic effect on the yield stress than on the ultimate stress and that higher strength steels were less affected. Equations to calculate the DIF for both yield and ultimate stress from the strain rate and static yield stress were proposed.

Yield DIF: $\phi = \left[\dfrac{\dot{\varepsilon}}{1 \times 10^{-4}} \right]^{\alpha_y}$

(2.16)

Ultimate DIF: $\Omega = \left[\dfrac{\dot{\varepsilon}}{1 \times 10^{-4}} \right]^{\alpha_u}$

(2.17)

where: $\alpha_y = 0.074 - 0.040(f_y/414)$ and $\alpha_u = 0.019 - 0.009(f_y/414)$ in which f_y is the yield strength in MPa and $\dot{\varepsilon}$ is the strain rate in s^{-1}. However, the model has some shortcomings since it is only valid for materials with yield strengths between 290 and 710 MPa and for strain rate between 10^{-4} and 225 s^{-1}.

Another model widely used to compute the increase of the yield strength is the Johnson-Cook model [60]. This model is described by the Eq.2.18. The first term of the equation gives the stress in function of the equivalent plastic strain rate ε at the quasi-static reference strain rate $\dot{\varepsilon}_0$, whereas the second and third term represent the effects of strain rates and temperature on material behaviour, respectively. In this way, the increase of strength due to strain rates (*DIF*) can be obtained from the second term of the equation where $\dot{\varepsilon}$ is the strain rate and *C* is a strain rate constant (Eq.2.19).

$$\sigma = \left[A + B\varepsilon^n \right] \times \left[1 + C \ln \left(\frac{\dot{\varepsilon}}{\dot{\varepsilon}_0} \right) \right] \times \left[1 - \left(T^* \right)^m \right]$$

(2.18)

$$DIF = \left[1 + C \ln \left(\frac{\dot{\varepsilon}}{\dot{\varepsilon}_0} \right) \right]$$

(2.19)

Recent research works [67–69] showed that this model can predict the enhancement of strength to strain rates up to 10^3 s^{-1}, which includes the strain rates that can be induced by impact loads (Fig. 2.1). On the other hand, for loads inducing strain rates above this value (for instance blast loads), many materials (especially the more ductile) have a sudden increase of the yield strength and the logarithmic form of the equation 2.19 cannot predict this increase (Fig. 2.20a).

This thesis is focused on situations when a structure is subjected to impact loads such as vehicle collision. Therefore, Equation 2.19 can be used to assess the effects of the strain rates on the material behaviour. It is also worth to notice that the last term of Equation 2.18, which concerns the effects of temperature, was neglected in this work since all tests were carried out at ambient temperature.
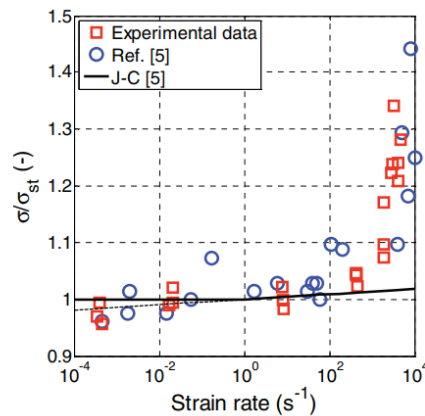
Fig. 2.20. Johnson-Cook model [69]

2.5.5.1 Evaluation of the C parameter of Johnson-Cook model to apply in the FEM and analytical models

Based on the aforementioned researches, the C parameter of the Johnson-Cook law was derived for the steel grades composing the plates and bolts and used afterwards in the numerical and analytical models, presented in the following chapters of this thesis (Table 2.6). For mild steel, the value used by Ribeiro *et al.* [7] was assumed, which is based on the results of Saraiva [59] (C = 0.039). In case of stainless steel, a C equal to 0.0093 and 0.045 was extrapolated for the ultimate and yield strength respectively, based on the work of Lee *et al.* [62] (Fig. 2.18b). Finally, the ultimate strength of bolts was characterized by the value of Culache *et al.* [26] (Fig. 2.22). Considering the enhancement of yield strength, according to Ribeiro *et al.* [7], it can be slightly higher than the enhancement of ultimate strength with a maximum of 10% (Fig. 2.22).
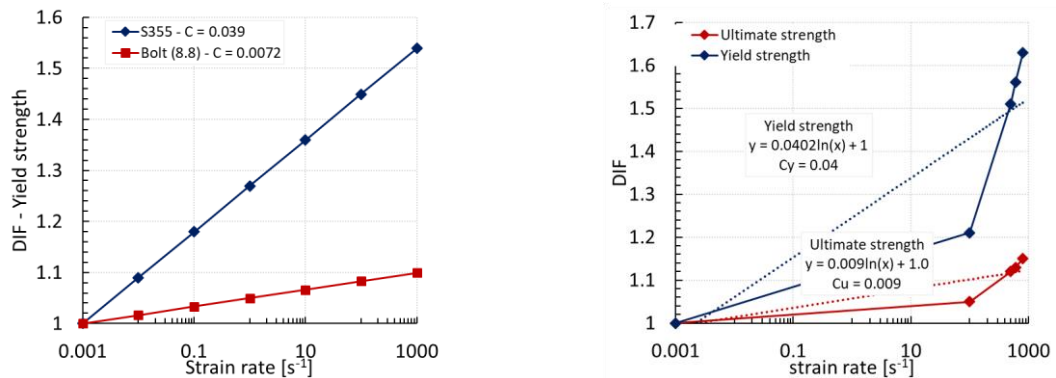
a. Work of [7] based on the true-strain curves of [59] b. DIF at yield (0.2% strain) and the ultimate strength (30% strain)[62]

Fig. 2.21. Johnson-Cook parameters C for mild steel and stainless steel [7,62]
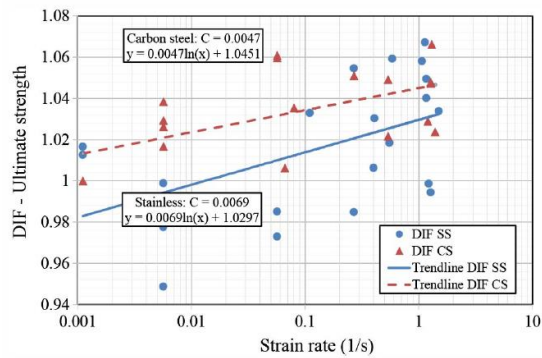
Fig. 2.22. Parameter C for bolt M12 class 8.8 [26]

Table 2.6. C parameters from literature

Material	Carbon steel [7]	Stainless steel 304 [62]	Bolts
C_y	0.039	0.040	0.0072 [7]
C_u	0.039	0.009	0.0047[26]

2.6 Beam-to-column connections and buildings under extreme loading events

2.6.1 Impact loading on beam-to-column connections

The avaiable literature dealing with the effect of impact loading on steel beam-to-column connections is quite recent. From the relevant research works avaiable, the work conducted by the Pennsylvania State University, the University of Shedfield, the University of Coimbra and the Norwegian University of Science and Technology was found relevant for this thesis.

The work conducted by Sabuwala *et al.* [70] in 2005, is one of the first studies that can be found concerning the effect of exceptional loads on the behaviour of beam-to-column connections. They developed 3D FE models capable of assessing the behaviour of fully restrained joints exposed to blast loads. The behaviour was later verified based on the criteria specified in TM5-1300 [71]. The connections studied were a part of the *AISC Northbridge Moment Connection Test Program*, which was performed after the Northbridge Earthquake in order to determine the causes of the failure of steel connections and to provide guidelines for their retrofitting increasing their performance under seismic loads. From this study, one unreinforced (Fig. 2.23a) and one reinforced connection (Fig. 2.23b) were selected. The FE models were developed using the ABAQUS software and validated against the experimental results. After the calibration of the model, the behaviour of the connections under blast loads was assessed. The characterization of the blast load was made using SHOCK and FRANG codes, while the strain rate influence on the mechanical properties of steel has been taken into account by the use of a dynamic yield increase factor (DIF) equal to 1.12 and 1.29 for steel Grade 50 and Grade 36, respectively, as suggested in TM5-1300.

The results showed that according to the TM5-1300 criteria, the structural members of both connections were over-designed for blast loads as the peak values of displacements and rotations from the numerical models were lower than the limiting criteria given in TM5-1300. For this reason, it has been concluded that these criteria are inadequate for blast-resistant design.

a. Unreinforced connection   b. Reinforced connection
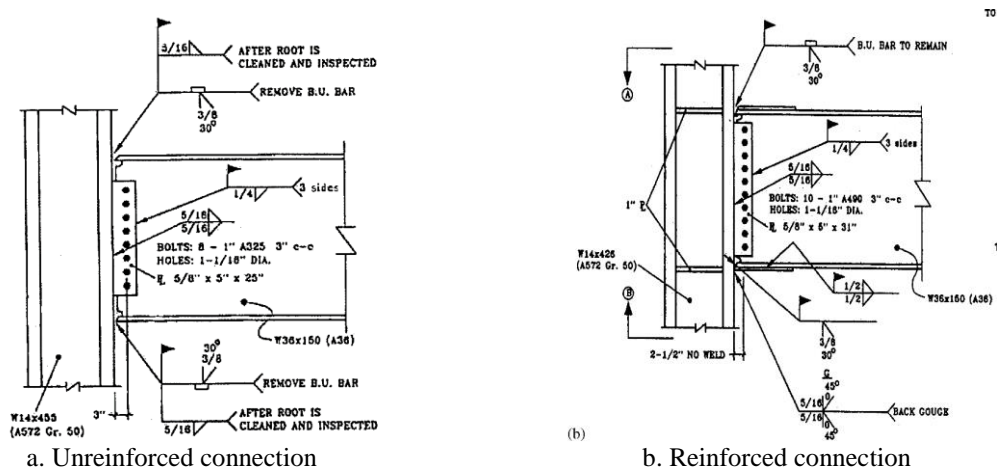
Fig. 2.23. Studied connections [70]

Since 2011, the University of Sheffield has been conducting an extensive programme on the dynamic behaviour of single-sided bolted steel connections, including experiment tests, FEM

modelling and the development of analytical based models to account for the influence of the strain rates.

Starting from the experimental campaign, a test rig capable of applying high loading rates was developed (Fig. 2.24). The load is applied laterally in the column of the connection, simulating loading cases such as vehicle impact, flying debris or internal explosion. The experimental test rig can apply axial tension load, using both of the loading rams simultaneously, or a combination of moment and tension, using only one of the loading rams. In addition, the opposite end of the column can be left free to rotate, producing a high rotation/tension ratio, or restrained by a pivot, producing a lower ratio. The loading rate is governed by the flow-rate of gas loading the rear face of the loading rams [72].
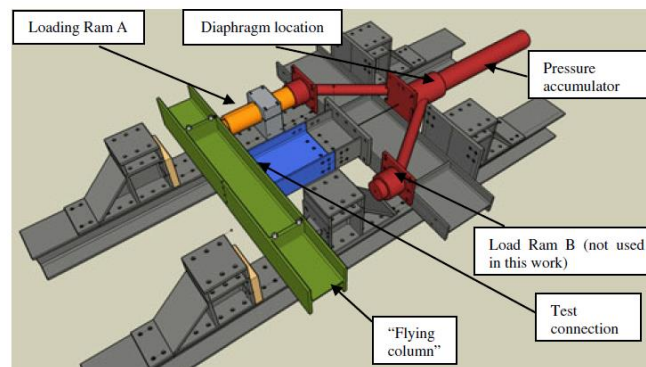
Fig. 2.24. Rig scheme [72].

In the first experimental campaign, three types of connections were evaluated: flexible end-plates joints (FEP) with 10 mm or 8 mm thickness, web-cleats angles joints (WC) with leg angles thickness equal to 8 mm or 10 mm and fin-plates joints (FIN). All bolted with M20 8.8 carbon bolts. More recently, extended and flush end-plates were also evaluated using both M20 8.8 carbon (CS) and stainless steel bolts (SS) [26]. All the connections were tested statically and dynamically, considering a combination of moment and tension loads. The summary of the results is reported in [25] for FEP and FIN connections, in [9] for the web-cleat connections and in [26] the tests on extended and flush end-plates with CS and SS bolts is reported.

From the tests, it has been concluded that the response of end plates and fin plates connections become stiffer and the failure modes less symmetric as the loading rate increased, as demonstrated by the moment-rotation curves depicted in Fig. 2.25. Contrarily, web cleat connections (WC) response were not affected by the loading rate (Fig. 2.26)

a. Flexible 8 mm end plates   b. Fin plate connections
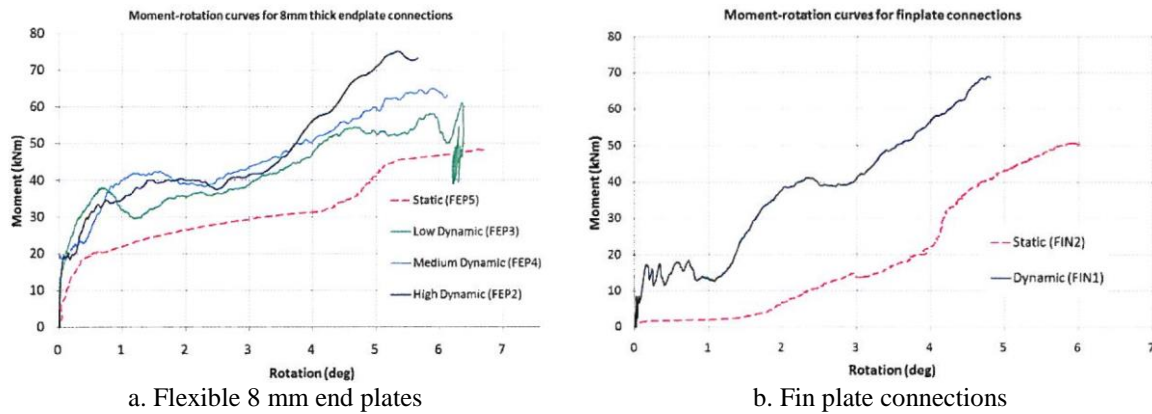
Fig. 2.25. Moment vs rotation curves [25]

Test	Peak connection resistance		Time to reach 6 degree rotation (s)	Failure mode	Post test beam web	Post-test angle deformation (from load ram end of connection)
	Tensile (kN)	Moment (kNm)				
WC6 10 mm cleat static	72	48	185	Beam web block shear		
WC7 10 mm cleat dynamic	65	43	0.035	Beam web block shear		

Fig. 2.26. Summary of the results: Test WC6 and WC7 [9]

In the last experimental campaign, the quasi-static and dynamic behaviour of extended and flush end-plates with carbon and stainless steel bolts were performed. The main point was to observe the advantages of using stainless steel bolts instead of the typical carbon bolts. From the quasi-static tests in Fig. 2.27, it was observed that the use of stainless steel bolts allowed a ductility almost 4 times higher, changing the T-stub failure mode from mode 3 (bolt failure without significant deformation of the plate) to mode 2 (bolt failure with yield of the plate). In the dynamic tests, the connections with carbon bolts rapidly lose their strength due to thread stripping, not showing the enhancement of strength observed in bolt testing (see Fig. 2.19). In the connections with stainless steel bolts, only the flush end-plate connections showed an enhancement of strength due to strain rates. Furthermore, a decrease in ductility was also observed. In the extended end plate, the dynamic ultimate strength decreased due to the asymmetric buckling of the compression flange.

a. Extended end-plate   b. Flush end plate
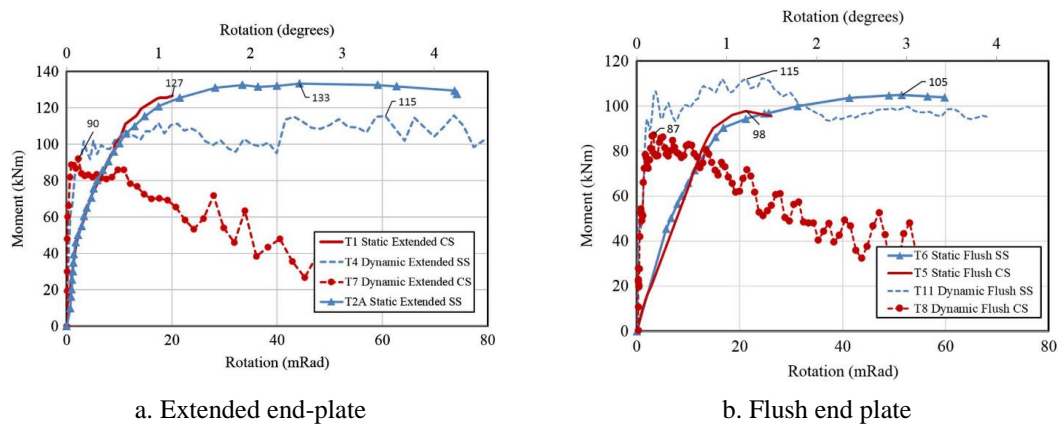
Fig. 2.27. Quasi-static and dynamic moment-rotation curves of the tests in [26]

Following the experimental campaign, the *LS-DYNA* software was used to simulate the experimental tests on web-cleat angle connections [9], see the numerical model presented in Fig. 2.28a. Furthermore, in the parts of the connection in which high deformations and failure were expected, the rate dependent simplified Johnson-Cook model was implemented (Eq.2.19), taking into account the work hardening and strain rate effects on the material. The model was first calibrated against the experimental results (Fig. 2.28b) and then the effects on the load-carrying and the failure mechanisms by varying the loading rate, material strength and size of the connecting elements were studied.

The parametric studies indicated that the loading rate does not influence the failure mode nor the resistance and ductility of web cleat connections, as already observed in the experimental campaign. Furthermore, changing the thickness of the legs of the web cleat angles affects significantly the ductility of the joint (thicker angle legs reduced the ductility).

| a. Model | b. Moment vs rotation and failure modes |
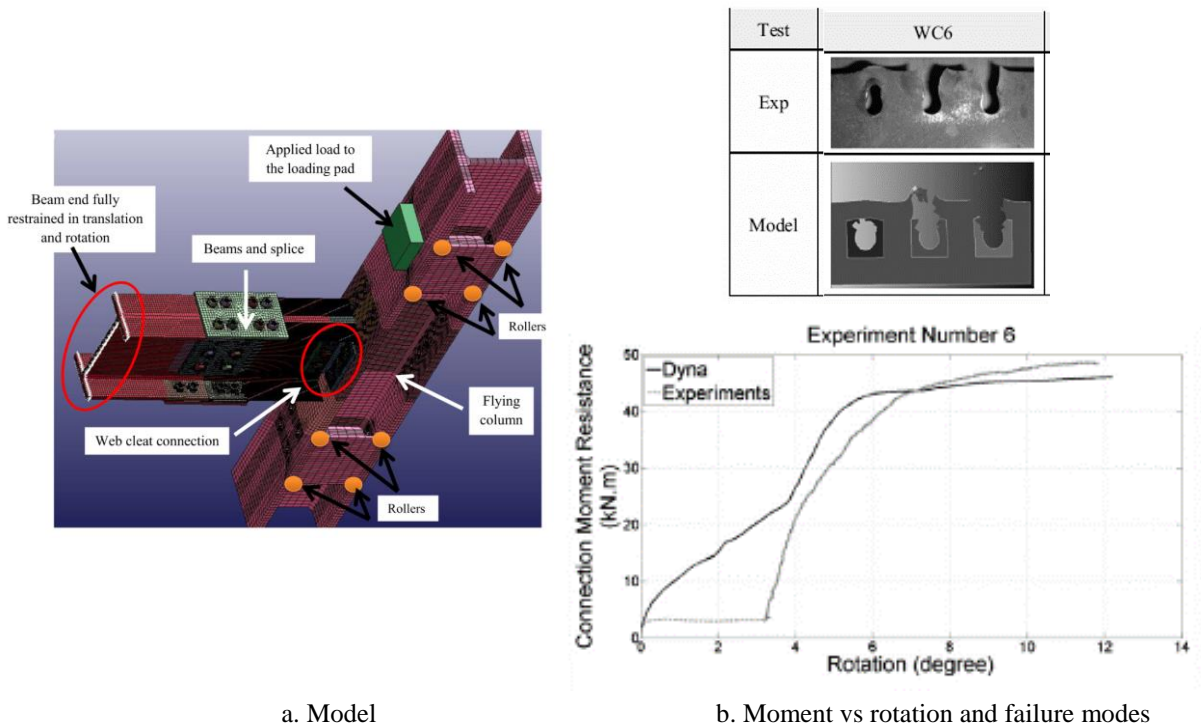
Fig. 2.28. Calibration of the numerical model [9]

A component-based model was developed in order to assess the dynamic behaviour of flexible end-plate and fin-plates connections [11,73]. The dynamic behaviour of the connections was assessed introducing dynamic increase factors (*DIF*) into the material behaviour, using the method of Malvar and Crowford [57] (Eq.2.16-17).

With reference to the end-plate joints, the component end plate in bending was calculated as a T-stub (Fig. 2.29a), considering a tri-linear force-displacement relationship (Fig. 2.29b). Strain-hardening and plastic stiffness were obtained as the ratio of the elastic stiffness (K_e in Fig. 2.29b) based upon experimental data and both yield and ultimate capacity were calculated in terms of the applied force (F_{ep} in Fig. 2.29a). Moreover, the approximate strain-rate was calculated during the elastic phase for a defined deformation velocity at the centre of the end-plate, and it was found dividing the strain at the surface of the plate at the yield displacement by the time it would take to reach it.

With reference to the bolt in tension component, its force-displacement curve was calculated using the Hook's law, assuming the bolt subjected to a direct tensile force equally distributed over the tensile bolt area. It has been considered that, after yielding, the bolts presented very little ductility and no dynamic enhancement was included in the model.

a. End-plate idealization   b. Tri-linear force-displacement response for the end-plate
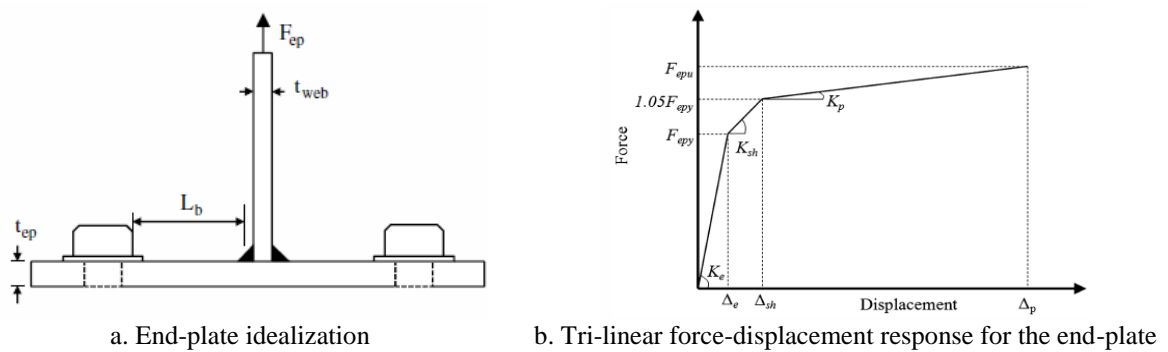
Fig. 2.29. Analytical model for end-plate in bending [73]

For the fin-plates connections, the model of Sarraj [74] for fin-plate connections in fire, was used as a base model. Dynamic increase factors for the plates in bearing and shear response of the bolts were applied. For the bolt in shear, the model adopted is adapted from the parametric studies of finite element models used to study the shear behaviour of M20 class 8.8 bolts. In addition, it was assumed that the yield strength and strain is achieved over an initial deformation of 1/40 of the bolt diameter. Therefore, this value was used to approximate the strain rate by diving the yield strain by the time that takes to reach that strain at a certain shear rate. Concerning the plate in bearing, the analytical model was developed based on experimental work on the behaviour of a single bolt bearing against a single plate.

Fig. 2.30 compares one experimental curve with the analytical prediction for each connection. From the moment-rotation curves, can be observed that the analytical model predicted well the initial stiffness and yielding. In addition, the dynamic enhancement in the strength of the connection can be predicted with accuracy. Only for the fin-plate connection, the post-elastic stiffness is overestimated which was related to an overestimation of the material strength at the considered loading rate or to the fact that the model does not account for web buckling or crushing of the lower flange.

a. End-plate plate, 8mm [73]   b. Fin-plate connection [11]
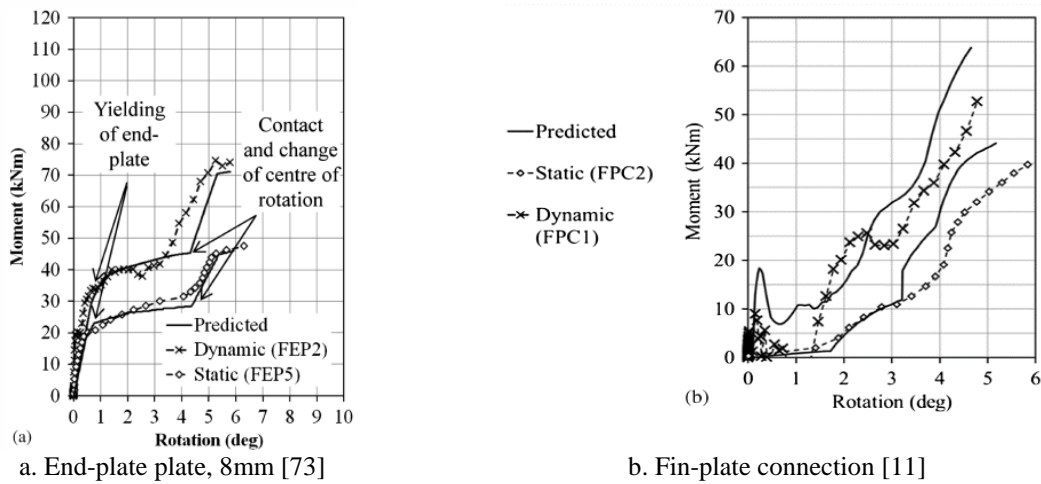
Fig. 2.30. Analytical and experimental moment-rotation [11,73].

At the University of Coimbra, a similar test rig was developed [12], and an extensive experimental campaign comprising T-stub components and single-sided end plate joints under impact loading conditions was carried out. The same test rig was also used in the experimental part of this thesis. A complete description of the experimental system and the procedure used for analyzing the data is reported in Chapter 3, but a summary is presented here. The layout used is schematically presented in Fig. 2.31. The test rig was designed following the requirements of Eurocode 3 part 1 [75] and Part 1-8 [5] and it is composed of two beams connected to each other, forming a very stiff structure. The yellow beam (flying beam) is loaded at one end by a pneumatic cylinder (red coloured in Fig. 2.31), thus, loading the specimen. At the opposite end of the application of the force, the beam can be restrained by a pivot or free to rotate. For the T-stub component, the beam was restrained by a pivot and the specimen was connected by means of two hinges, only allowing the transmission of axial forces. For the connection tests, the beam was free, thus, the centre of rotation of the system was the connection.
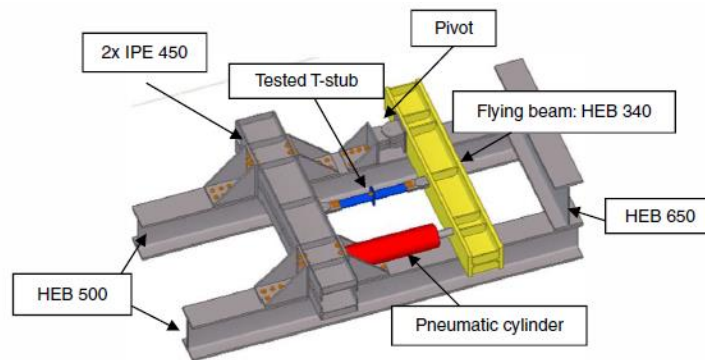
Fig. 2.31. Test rig for dynamic testing [12]

Starting from the experimental tests on the T-stub component [76]. The experimental campaign comprised a T-stub with plates of 10mm thickness, welded by means of a continuous 45° fillet (a_w=7mm). The flange was bolted to the "flying beam" by means of four M20 class 8.8 bolts, fully threaded.

In Fig. 2.32a) is reported the force-displacement curves for the impact tests and the reference quasi-static test. From the results was possible to drawn some observations: (i) the loading rate does not have influence the elastic stiffness of the T-stub; (ii) both yield and ultimate resistance increases for higher loading rates, being this difference higher for the yield strength and (iii) the global ductility decreases compared to the reference static test. Concerning the failure modes, in all tests, the T-stub failed according to the mode 1 of Eurocode 3 part 1-8, i.e. deformation of the T-stub flange without bolt failure.
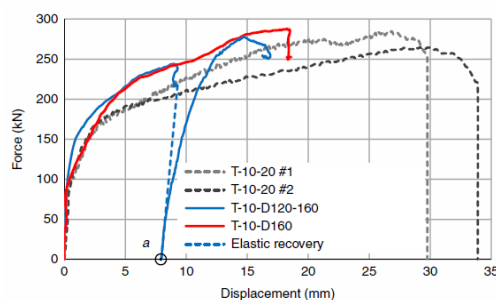
a. Force-displacement curves for impact tests vs quasi-static test
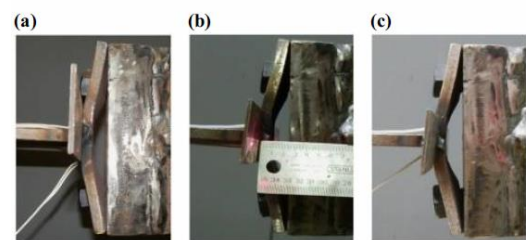
b. Failure modes

Fig. 2.32. Experimental results of T-stubs under impact loads[76]

Concerning the tests on end-plate joints, two different connections were tested: an end plate with 10 mm thickness (EP-10) and other with a thickness equal to 15mm (EP-15), subjected to both quasi-static and impact loads.

The results from the dynamic impact tests were compared to the reference static ones, as reported in Fig. 2.33a) and b), for the EP-10 and EP-15 specimen, respectively. In both situations, an increase of the plastic resistance moment and of the ultimate resistance moment of the connections was observed. For the EP-10 specimen, a reduction of the ultimate rotation was observed, while for the EP-15 specimen, the ultimate rotation was close to the one observed in the quasi-static test. For both specimens, the failure modes were the same as in the quasi-static tests: weld fracture near the beam flange and bolt fracture, for EP-10 and EP-15 respectively.

a. EP-10   b. EP-15
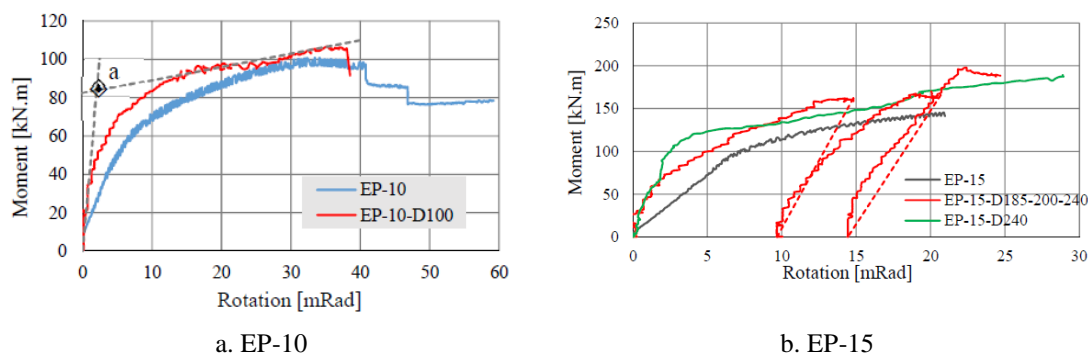
Fig. 2.33. Curves moment vs rotation for end-plate under impact loads [6]

Both the T-stub component (Fig. 2.34a) and end plate joint Fig. 2.34b) behaviour was simulated by means of FEM modelling, using ABAQUS software. In the model, the real behaviour of the materials obtained from coupon uniaxial tests were introduced. Furthermore, the sensitivity of the materials to strain rates was implemented considering the Johnson-Cook model [60]: for the steel plates the work of Saraiva [59] was used (see Fig. 2.17a) and a parameter C equal to 0.039 was considered (DIF =1.5 at 600 s^{-1} with $\dot{\varepsilon}_0$ =0.001 s^{-1}). For the bolts, DIF equal to 1.1 was assumed, obtaining a C equal to 0.0072. Finally, the prediction of the failure modes was modelled by the ductile failure mode criteria included on ABAQUS software.

In the same way as the previous authors, the experimental tests were used to calibrate the FEM models and then, parametric studies were carried out. The influence of the load application, load application time and thickness of the plates were considered.

For the T-stub component, as for the experimental tests, an improvement of the force-displacement response under dynamic loading was observed. In addition, from the parametric studies, it was concluded that increasing the dynamic loading has a minor effect in the response

of the T-stub, while different load application times changes the T-Stub response. On the other hand, increasing the flange thickness leads to less ductile failure modes, i.e. bolt fracture, and so the enhancement of the force-displacement response is less pronounced (T-stub cannot take advantage of the increase in the strength of the flange steel due to higher strain rates).

The end-plate connection models made possible to observe the enhanced capacity of the connection in the experimental tests. In a similar way as for the T-stub models, increasing the dynamic loading has a minor effect on the response and under dynamic loadings, end plate connections seem to tend to less ductile failure modes.

| a. T-stub[7] | b. End plate connection [77] |
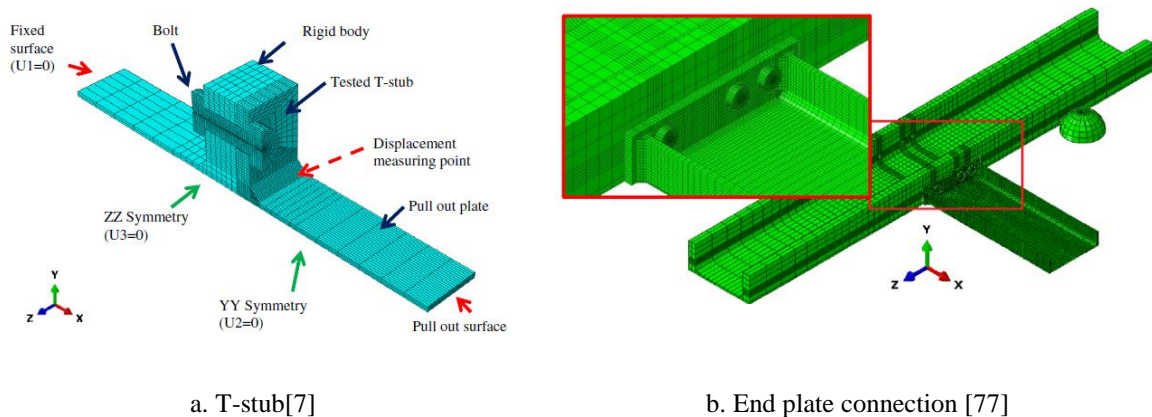
Fig. 2.34. Geometry of the numerical models of [7,77]

Additionally, Ribeiro *et al.* [10] assessed analytically the behaviour of T-stub under rapidly applied loads, in two ways. In both ways, the effects of the elevated strain rates of the steel materials were incorporated into the model, considering dynamic increase factors (*DIF*). In order to derivate these factors, the John-Cook model was used and the same values of the parameter *C* used in the numerical studies were also used here. In addition, both methodologies were calibrated against the experimental and numerical studies.

A first estimation of the resistance of T-stub under impact loads was assessed considering an approach based on the methodology of the component method [5]. The *DIFs* considered for the plates and bolts were approximated based on the global velocity of the T-stub flange observed in the numerical simulations. In this way, a strain rate equal to 225 s^{-1} was found, resulting in a *DIF$_{steel}$* = 1.5 for the steel plate Fig. 2.21a. For the bolt, a maximum *DIF*=1.1 was assumed, according to [63].

In the second approach, the model of Yu *et al.* [78] was used and modified to incorporate the effects of the strain rates. Briefly, the analytical procedure developed by Yu *et al* consists in deriving the behaviour of simple yield-lines where the plastic hinges are usually developed, allowing to take into account the material hardening. In this way, the non-linear behaviour of a T-stub can be captured. Here, it was considered a time dependent strain rate. The maximum deformation δ occurring in a total time Δt is divided in a "step by step analysis" in which the displacement δ_i occurs in an amount of time Δt_i, obtained by a linear discretization of δ and Δt in a number of increments, n. In this way, the strain rate is calculated in each step and thus, different DIFs for each increment can be applied.

The results of the application of the developed analytical methods are reported in Fig. 2.35a) and b). For the monotonic responses, the simplified model from the Eurocode provides conservative values while, the non-linear approach, allows the prediction of approximate values of the F-δ T-stubs curves. For the dynamic responses (Fig. 2.35b) the simplified approach predicts that the dynamic response of the T-stub should be 50% higher than the static one, whereas for the non-linear approach the enhancement of the T-Stub resistance is 24%, closer to the experimental and numerical values.

a. Monotonic F- δ response: T-10 and T-15   b. T-10 static (blue) vs dynamic (red)
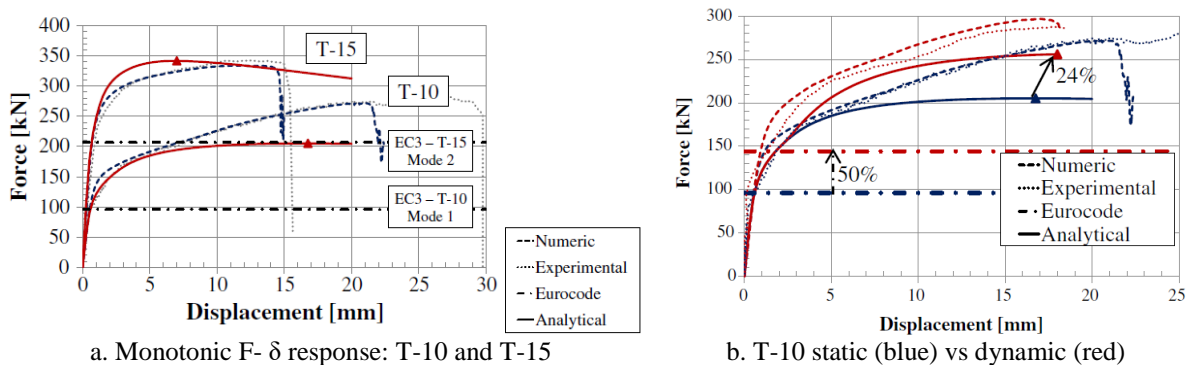
Fig. 2.35. Results of the analytical model for T-stub components [10]

End-plate joints under quasi-static and dynamic loading were also studied by Grimsno *et al.* [79]. Here, double-sided joints were considered and an axial load was applied to the column simulating the loading conditions in case of column loss.

The beams and columns of the tested specimens were HEA180 and HEB220 rolled steel sections, respectively, connected by end-plates with 12 mm welded to the beams and bolted to the column by means of six partially threaded M16 bolts of class 8.8. Two different geometries were considered, as reported in Fig. 2.36a. and b. The first loading configuration represents the

loading direction of the connection in practical applications (design loading direction), inducing two rows of bolts in tension, while in the second configuration only one row of bolts is induced in tension and is related to loading conditions in a case of column-loss scenario (reverse load direction).

Four quasi-static and eight dynamic tests were performed, using the tests set-ups reported in Fig. 2.37a. and b., respectively. In the quasi-static tests, the column was gradually pulled by a hydraulic actuator under displacement control until failure, while the dynamic tests were carried out with a pendulum accelerator. From the eight dynamic tests performed, four were with what was considered low speed with approximately 5 m/s (two tests in each specimen) and the others four were performed at high speed at a velocity of 12 m/s.

The first quasi-static test was performed using only one nut in the bolt of the end-plate, which led to an earlier failure of the connection due to nut stripping failure, as in the previous research work [26]. For this reason, two nuts were used in all the following tests in order to exploit the full plastic resistance and ductility of the connections. The application of two nuts changed the failure mode from nut stripping failure to shank failure, increasing the maximum joint moment in 10% and the maximum joint rotation in 130%.

The experimental tests showed that the resistance of the joint increased for higher dynamic loads, which is stated to be associated with more symmetrical deformation modes, enhanced strain-rate hardening and larger local deformations of the joints. Furthermore, the failure mode was not influenced by the velocity, being always by bolt fracture in tension with yield of the end-plate. In both previous research, the same conclusion was drawn for the end-plate joints [6,25]. In addition, an increase of the displacement of the column at fracture was observed for higher impact velocities, which has been interpreted as an increase in the ductility of the joint.

FEM modelling using ABAQUS software was also performed by this author [8]. The real behaviour of the materials was introduced in the model in the same way as in [7]. The numerical studies were first validated against the experimental tests, and then parametric studies were conducted, studying the influence of the end-plate thickness on the energy dissipation capacity of the connection, the influence of the axial forces in the beam and the inertial forces of the floor slab could influence the response of the connection.

From the parametric studies, the following conclusions could be made: (i) the reduction of the end-plate thickness allows for higher deformation of the end plate before bolt fracture, i.e.

the energy dissipated by the joint increases. In fact, this conclusion was also made by Ribeiro *et al.* [77]; (ii) considering tensile axial forces in the beams does not affect significantly the response of the joint and (iii) the additional mass from structural elements as floor slabs can affect the failure mode. In the simulation in which additional inertia of the beams was considered, was observed a different failure mode, pointing out that the inertia effect can significantly alter the response of connections.

a. Design load Direction (DLD)   b. Reverse load Direction (RLD)
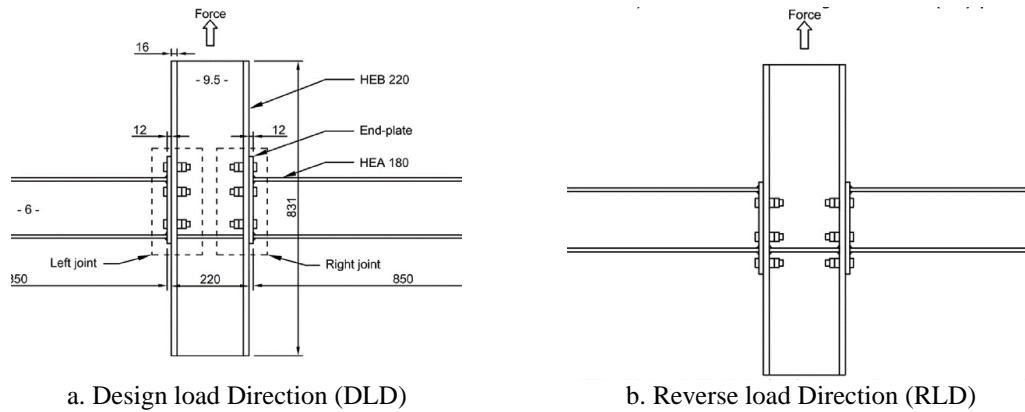
Fig. 2.36. Configuration of the specimens tested in [8]

a. Quasi-static tests;   b. Dynamic tests
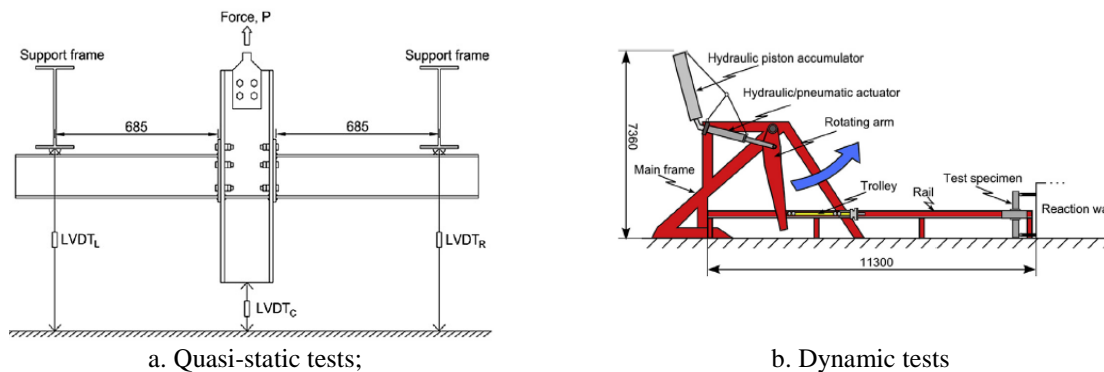
Fig. 2.37. Scheme of the tests Set-up performed in [8]

2.6.1.1 General conclusions

From the research mentioned in this section, it is possible to make some observations regarding the behaviour of steel bolted connections under high loading rates. First, from the three types of steel connections reported, (end plate, fin plate, web-cleat angle connection and T-stub component) the only one that did not show any sensitivity to strain rates was the web-cleat angle connection. This lack of sensitivity is believed to be due to the flexible nature of the connection that can rapidly dampen the applied deformation, thus limiting the strain rates

induced in the components [9]. All the others typologies presented changes when high strain rates were considered. In general, the following conclusions can be drawn:

- The yield and ultimate resistance increase with the increase of strain rates. In general, the enhancement of strength is higher when the failure is by a ductile component. For example, in the tests of [26], the flush end plates only showed an enhancement of strength when stainless steel bolts were used, due to their high ductility;

- The ultimate deformation/rotation decreases with the increase of strain rates. This parameter depends on the ductility of the failing components. For example, Barata *et al.* [6] observed a reduction of the ultimate rotation on the end-plate with 8 mm of thickness, while the ultimate rotation of the end plate with 15 mm was not affected by the strain rates. This is probably due to the different failure mechanism. While in the 8 mm plates, the failure is by the plate, with 15 mm plates the failure is by the bolts, which have a brittle failure. On the other hand, the tests carried out by Grimsno *et al.* [8] showed an increase of ductility for higher strain rates;

- For the cases considered, the failure mechanism does not change due to the increase of strain rates.

2.6.2 Robustness of structures subjected to extreme loading

2.6.2.1 *Column loss scenario – threat independent scenarios*

In the event of a loss of one vertical bearing element, alternative load paths must be available to redistribute the loads to the adjacent intact members of the structure, avoiding the progressive collapse. Structures can resist collapse through different mechanisms, such as Vierendeel action, arch effect of beams and/or catenary or membrane effect of beams through large rotations and inelastic deformations.

In general, when a structure is subjected to a column loss, two main parts of the structure can be identified (Fig. 2.38a): (i) the directly affected part (*DAP*), which is the part of the structure right above the considered lost column, and (ii) the rest of the structure (indirectly affected part –*IAP*). The evolution of the force versus the vertical displacement *u* at the point where the column was removed (column AB in Fig. 2.38a) can be divided into three phases (Fig. 2.38b). Phase one in Fig. 2.38b describes the situation before the event, i.e. the column supports the loads coming from the upper storeys. When the event that led to the loss of the column occurs, there is a progressive loss of the axial resistance of the column and up to the

development of a plastic mechanism (point 4 in Fig. 2.38b). After, when the full plastic mechanism is formed, the phase 3 starts. The vertical displacement u at the top of the lost column increases and, as a result, catenary actions start to develop in the beams of the directly affected part of the structure providing a second-order stiffness to the structure. The rest of the structure (IAP), provides lateral stiffness to these actions; the stiffer the *IAP* is, the higher the catenary actions will be in the *DAP*.

(a) Frame description   (b) Behaviour description
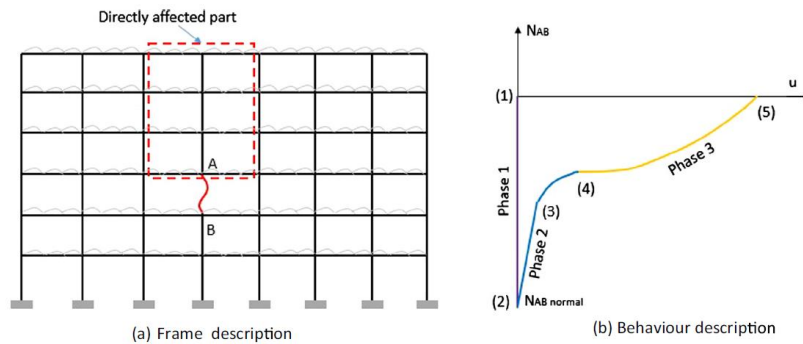
Fig. 2.38. Behaviour of a frame submitted to a column loss.[20]

A great effort to study this extreme loading events in steel and steel-concrete composite buildings has been made by the University of Liège. Within the European RFCS "Robust structures by joint ductility" project [80], they developed an analytical procedure able to predict the building behaviour after such an event. From the activities of this project, two PhD theses were developed. The first, presented by Jean-François Demonceau [19], was focused on the local response of a frame when the membrane effects associated with significant second-order effects appeared within the beams directly above the damaged column. The second thesis, presented by Hải [81], was dedicated to the investigation of the global behaviour of a frame following a column loss, taking into account the redistribution of the internal forces and considering the influence of the development of catenary actions on the structure. Joining the work from these two theses, a first analytical model able to predict the response of frames following a column loss was developed.

The Demonceau model [19] predicts the P-u curve during phase 3 (Fig. 2.38b) when a 2D frame loses one column under static loads. It is based on the study of a substructure containing only the lower beams of the *DAP*. The surrounding structure is simulated by a horizontal spring with a stiffness K_H (Fig. 2.39), assuming an elastic behaviour of the *IAP* during all phase 3. During phase 3, additionally to bending moment, the plastic hinges are also subjected to tension forces. For this reason, there was a need to define M-N interaction curves in the plastic hinges

that can develop in the beam or in the joints. The axial stiffness of the plastic hinges K_N is necessary to defined the relationship between the normal force N and the plastic hinge elongation δ_N. Further details of the application of this analytical model can be found in [19]. In addition, as demonstrated in Demonceau's work, this model is only able to give accurate results if the parameters K_N and K_H are well estimated. However, no analytical procedure to estimate these two parameters is given.

Later, Huevelle *et al.* [20] improved the Demonceau model by coupling the DAP with the IAP by defining an appropriate substructure (Fig. 2.40). In addition, the local phenomena occurring in the yield zones was considered by defining a multi-layer spring model at the beam ends.
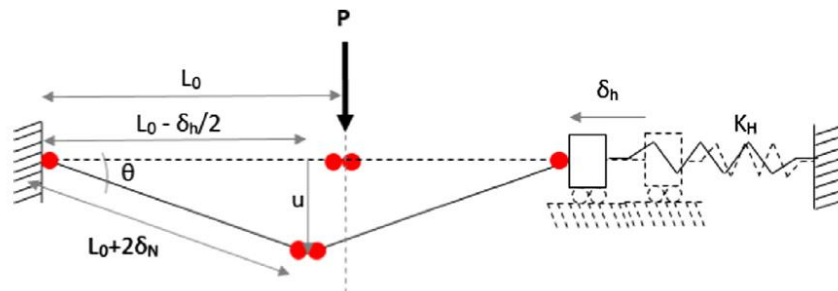
Fig. 2.39. Demonceau substructure [19]

New generalized substructure
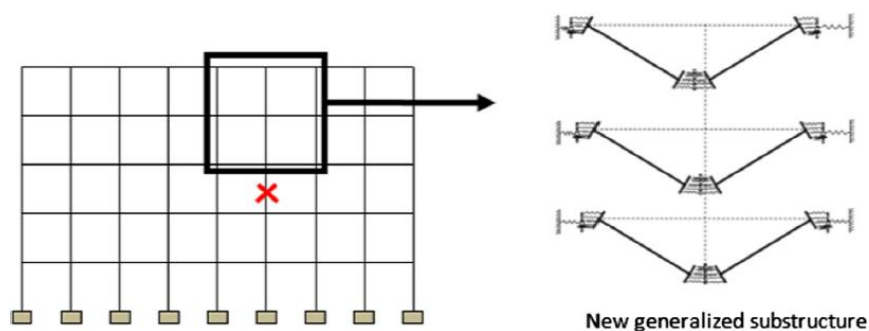
Fig. 2.40. Huevelle *et al*. substructure [20]

Recently, within the FREEDAM project, the model was extended to the case of structures with FREEDAM connections [43]. In particular, the friction connection with one friction damper at the lower flange level of an additional haunch welded to the beam (Fig. 2.7c) was chosen for this study and both hogging and sagging moment behaviour were considered. For this study, the following steps were considered: i) the component method was applied in order to assess the full monotonic behaviour of the joint (Fig. 2.41), ii) a 2-spring model to be

implemented in the analytical model routine was developed and iii) the behaviour of a simple frame under column loss scenario was investigated. It is worth to note that neither the dynamic effects nor the post-elastic behaviour of the joint were considered. In addition, the rotational capacity has been arbitrarily chosen since no limitation on the ductility of the component was introduced in the model.

The analytical model was run using a Matlab routine [43]. The stiffness of the horizontal spring K_H representing the indirectly affected part (IAP) was varied considering a range of possible values. Fig. 2.42 presents some of the results obtained from the analyses in terms of applied load vs vertical deflection at the top of the removed column. The results showed that a higher stiffness of the IAP, led to an increase of the forces before the formation of the plastic beam mechanism, which was related to the slip effect of the connection. In fact, when the plastic mechanism is formed (phase 3 in Fig. 2.42), part of the load is already redistributed within the structure i.e., an alternative load path has already been activated. Therefore, the required plastic deformation capacity at the joint level is much smaller when friction joints are implemented due to the additional flexibility that the slip of the connection provided to the system, allowing the activation of an alternative load path for the load redistribution prior to reaching the plastic resistances in the system.
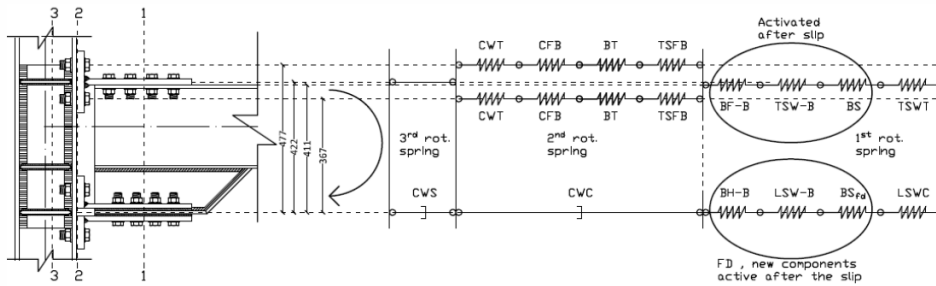
Fig. 2.41. Mechanical model under hogging [43]
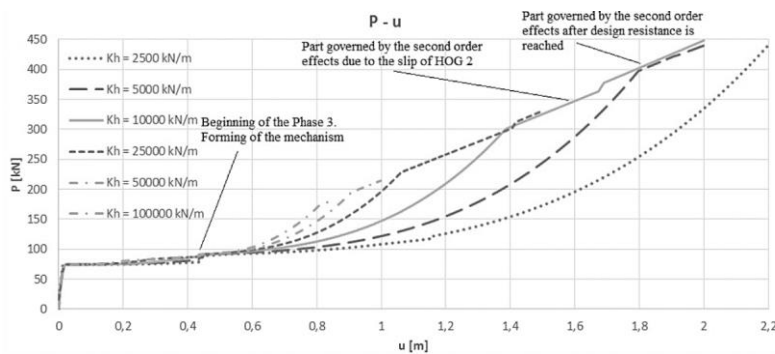
Fig. 2.42. Parametric analyses [43]

Simultaneously, other authors have also studied the behaviour structures with composite and steel beam-to-column connections under column loss, using both experimental and FEM approaches [3,4,28–30].

Yang *et al*. [3,29] used their experimental and FEM findings to develop component-based methods to predict the behaviour of several types of composite and steel beam-to-column connections under middle column removal scenarios. In their studies, the typologies of connections evaluated included composite and steel web cleat connections, composite and steel flush end plate connections, steel top and seat angle connections, top and seat with web angle (TSWA), end-plate connections and extended end plate connections. The experimental tests showed that all the selected connections could deform in a ductile manner and develop catenary actions prior to failure and that the addition of the concrete slab increases the load-carrying capacity of the connections at both flexural and catenary actions phases [30]. The additional FEM simulations underlined the influence of the number of bolt rows and bolts arrangement on the load carrying capacity, stiffness and ductility under catenary actions (Fig. 2.43).

a. Effect of bolt rows for flush end plate connections   b. Effect of bolt arrangement for flush end plate connections.
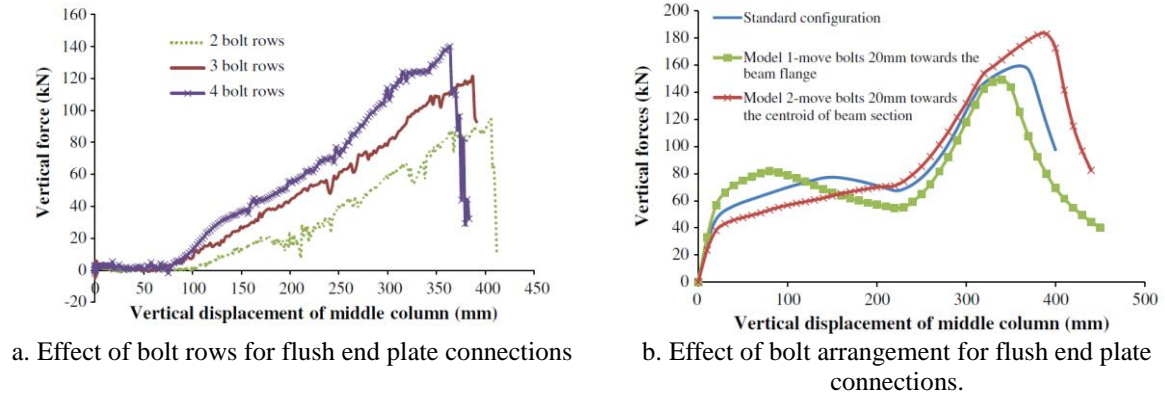
Fig. 2.43. Parametric numerical studies on the robustness of end plate and flush end plate connections [4]

The analytical model developed by Yang *et al* [3] is based on the component method and takes into to account: i) the interaction between bolts and angles; ii) a failure criteria to determine the deformation capacity of all the components constituting the connection; iii) load limits due to bolt fracture. As an example, in Fig. 2.44 is shown the considered components for a TSWA connection. A more detailed description of this model can be found in [3]. The main purpose of these analyses was to: i) identify the difference in the structural performances between the simplified joint model and frame modelling (Fig. 2.45a), ii) the influence of the

type of load applied to the beam, concentrated force (CPL) and uniformly distributed load (UDL) on the behaviour of steel frames and iii) the effect of the horizontal restraint. In Fig. 2.45b the results from the frame modelling, the experimental and joint model are compared. The frame model predicts the same load-displacement curves as the proposed joint model, which indicates that the joint tests can represent with accuracy the behaviour of the steel frame. In addition, the parametric study on the influence of the horizontal restraint stiffness indicates that this parameter can significantly influence the behaviour of steel frames when the horizontal restraint stiffness is smaller than the frame stiffness under tension loads.
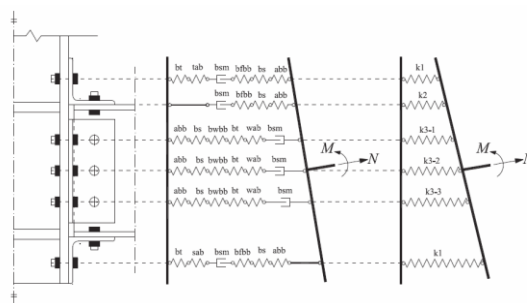
Fig. 2.44. Component-based model of TSWA connections [3]

a. Frame model and joint model

b. Comparison of frame models with test results and joint models for TSWA-12
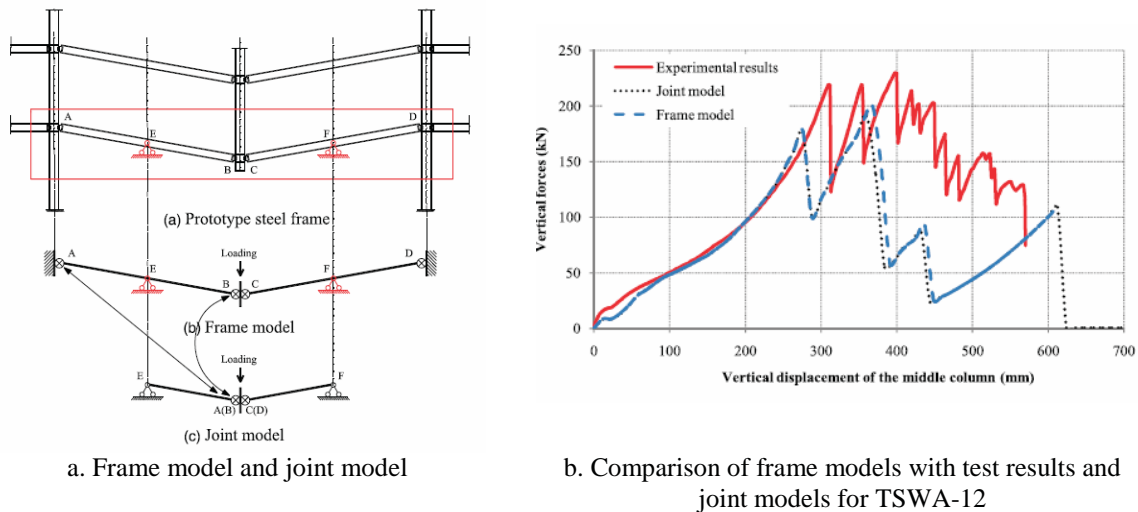
Fig. 2.45. Frame modelling and results of [3]

The University of Sheffield studied the behaviour of structures subjected to exceptional loading events, where a simple beam subjected to blast was investigated, by employing the component-based models reported in section 2.5.1 [73] Contrary to the models previously described, the influence of strain rates on the behaviour of the connections were considered. The investigation of the blast behaviour of the considered beam has been carried out considering

different degrees of impulsiveness, measured by the ratio of the duration of the blast t_d to the natural period of the member, t_n. In addition, different supports conditions were analysed and compared, namely: (i) pinned supports; (ii) Component model representing fin-plate connections; (iii) Component model representing 8-mm end-plate connections and (iv) component model representing 10-mm end-plate connections.

Using ABAQUS/Explicit software, the component-based models were incorporated into FE models as axial connector sections and discrete rigid elements. In order to transmit the shear load from the beam to the supports, a shear spring was added at the centre line of the connections. In addition, the response obtained by the FE models was compared against the use of an equivalent single degree of freedom (SDOF) method. Fig. 2.46 shows the FEM beam response normalized against the SDOF results. The mid-span displacement values show that the beam model with fin-plate connections is in agreement with the SDOF predictions. Conversely, the beam with end-plate connections showed reduced deflections in all cases. These results highlighted the importance of including the real connection behaviour. In addition, the results show that the increase rate of rotation as a result of the dynamic loading caused an increase in the rotational stiffness of the connections. This behaviour changes the response of the system, which leads to an increase in the dynamic shear forces.
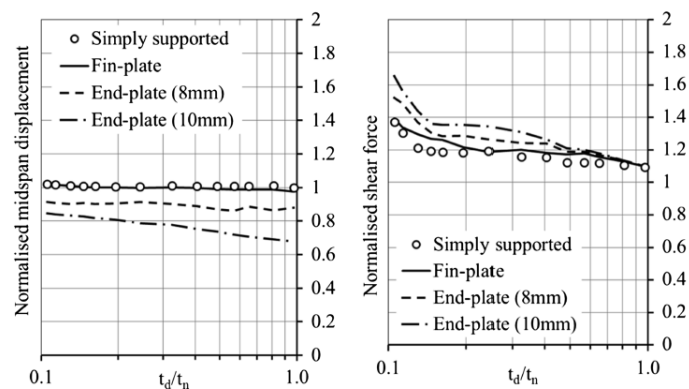
Fig. 2.46. FE beam response normalized against SDOF results [73]

Another very interesting study on robustness of structures under extreme loads was carried out by Jeyarajan *et al* [21,22]. Contrary to the works mentioned previously, these authors considered 3D structures instead of sub-frames and apart from the joint spring model, a spring model to simulate the slab effect was also developed. In the slab model, the profile metal deck is represented by rows of rebars and the profile concrete is converted into an equivalent uniform concrete section. The semi-rigid composite joints were represented by spring connectors

describing their force-displacement and moment-rotation relationships. Both joints and slab models were validated against experimental test results (Fig. 2.47). A nine storey 3D building frame was considered for the numerical investigation, using ABAQUS software. Beams and columns elements were modelled as beam elements B31 to reduce the computational time. In the analysis, several parameters were studied, namely, i) type of analysis (linear static –LS, linear dynamic – LS and nonlinear dynamic -ND), ii) consideration or not of the slab and iii) removal column position – corner column or perimeter column.

From the analysis, some conclusions were drawn. With reference to the contribution of the slab, its consideration reduces about 50% the frame vertical deflection under column loss and contributes favourably to resist progressive collapse (Fig. 2.48). Concerning the position of the removed column, it has been found that corner column loss is more critical than the loss of a perimeter column, which is associated with the lower number of members connecting the corner column to redistribute the load (Fig. 2.48).

a. Semi rigid joint web-cleat connection   b. Slab model
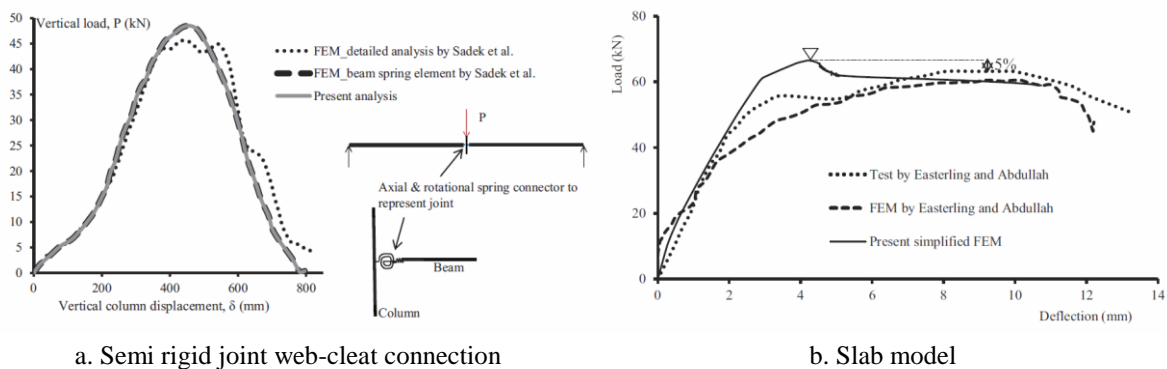
Fig. 2.47. Validation of the spring models [21]

a. Perimeter column   b. Corner column
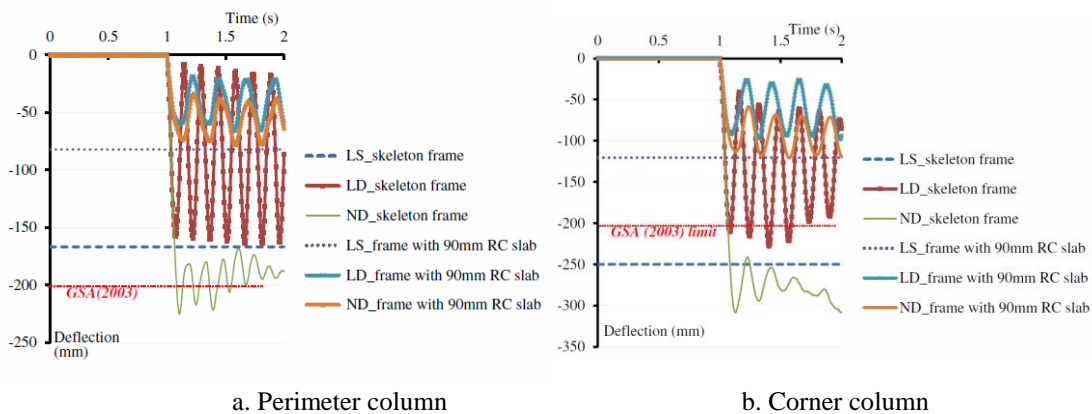
Fig. 2.48. Moment frame deflections at column removed position [22]

2.6.2.2 Robustness evaluation using threat dependent scenarios

Research work on robustness of structures where the threat is completely characterized are few due to its complexity. Here two recent works will be presented. The first is the work of Jeyarajan *et al* [21]*,* who used a 10 storey building frame to perform robustness analysis under blast loading. The blast load was characterized according to the suggestion of UFC [51] and it was applied in the front surface of the building as a uniform surface at a stand-off distance of 20 m.

The results showed the importance of considering the strain rate effects in the material model – the deflections of the frame when considering strain rate effect were significantly lower than those without the strain rate effect. Furthermore, the force demands in the members increase due to the increase of strength and stiffness caused by higher strain rates. The nonlinear dynamic analyses have shown that blast loads can severely damage several columns at the ground floor, induce high shear forces at the 1st storey columns and caused large lateral drifts as well as axial forces on the ground floor columns. Finally, comparing the blast analysis with the alternate path approach, the study concludes that, scenario-dependent analysis can capture better the behaviour of structures. The authors suggested the use of an alternate path approach as a preliminary design check of building robustness.

Concerning robustness [18,82] analysis on steel-framed structures under vehicle impact, the work of Kang *et al.* can be highlighted. The authors carried out impact analysis on 3D steel building frame, using the LS-DYNA software. The vehicle model was provided by the *National Crash Analysis Centre* and it has a total mass equal to 8 ton. Fig. 2.49a shows the building and vehicle modelling. Impact velocities of 40km/h, 80 km/h and 120 km/h were considered for the impact analysis and two impact positions were considered: external column (Fig. 2.49a) and corner column (Fig. 2.49a). Furthermore, prior to impact analysis, nonlinear dynamic analyses (NDA) using alternate path method were performed, where it was considered: i) single column removal – exterior (A3) or corner column (A4) and ii) double column removal – exterior and adjacent column (A3 and B3) and corner and adjacent column (A4 and B4). These first analyses had the purpose to investigate the potential progressive collapse of the structure and the results were compared afterwards with the impact analysis.

From the alternate path method analysis, the authors concluded that the investigated structure is capable to survive the loss of a critical bearing element/s. On the other hand, the impact analysis showed that the structures remained stable when the vehicle collided at the speed of

40 km/h, while at speeds of 80 km/h and 120 km/h the structure was severely damaged by the impact, followed by progressive collapse. These results highlight the fact that the alternate path approach is sometimes not enough to prevent the progressive collapse of a structure exposed to a possible impact of a vehicle under high speed, which is related to the fact that besides from the vertical deformation of the structure originated by the loss of a bearing member, the lateral vehicle collision can also imply a significant lateral deformation of the structure not accounted in the alternate path approach. This fact results in a quite different structural behaviour, especially when very high collision velocities are considered.

With reference to the collision position, the damaged caused by a collision in the corner column was far greater than the damage observed in a collision to the exterior column.

a. Building and vehicle model
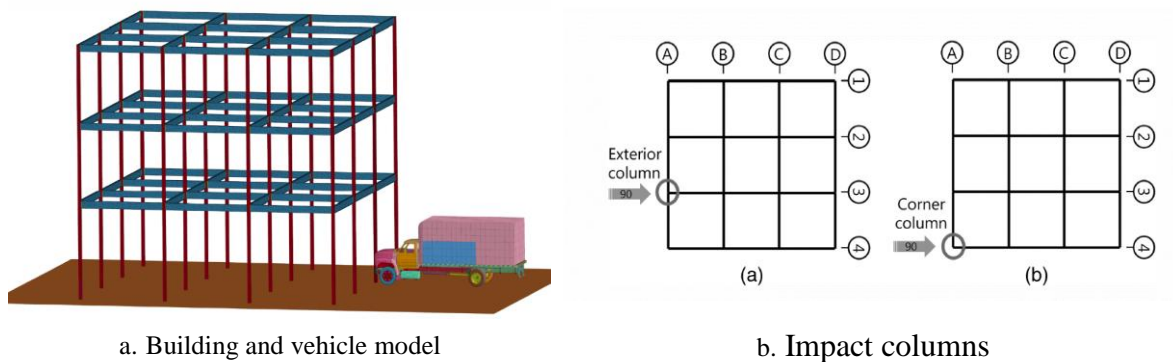
b. Impact columns

Fig. 2.49. Model and impact columns [18]

a. Alternate load path (NDA)

b. Impact analysis
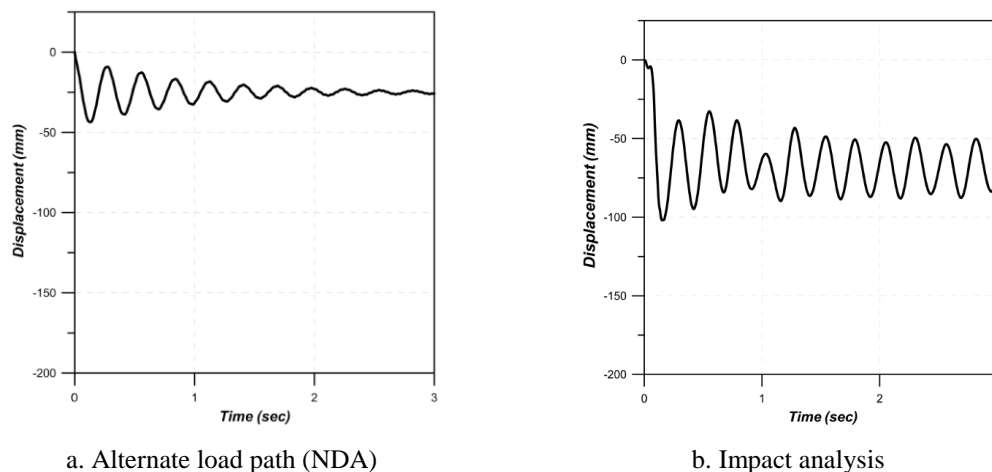
Fig. 2.50. Vertical displacement at the exterior column (B3) [18]

2.6.2.3 General conclusions

In this subsection, some of the available research works concerning the robustness analyses of structures which were used as base material for this thesis were reported. From these works, some remarks can be made on the topic of robustness of structures, as follows:

- Different types of analysis can be used to assess if a structure is susceptible or not to progressive collapse [18,21,22,82].. The most used is the alternative load path analysis due to its simplicity. This method can give a good estimation about the ability of a structure in finding alternative load paths after a loss of a bearing elements (such as a column) and it can be performed considering different complexity levels (static linear, static nonlinear, nonlinear dynamic…). However, it has as a main disadvantage the fact of not considering explicitly the event that originated the loss of the bearing member which can be quite unsafe for instance, in cases where can be other sources of deformation rather than the vertical displacement of the structure due to the loss of the member, as reported previously for impact loads on structures coming from a vehicle collision at a high velocity. In such cases, alternative load paths can always be performed as preliminary analyses to have a first estimation of the structural robustness and/or check and eliminate modelling error that are easily noticeable when simpler methods are used.

- The works reported in this subsection underlined the importance of considering the real behaviour of the connections instead of the rigid or pinned assumption [3,73]. This is important because since connections are elements connecting the structural members of the structures (beams, columns…), their stiffness, ductility and resistance influence the ability of the whole structure when a bearing element is lost, specifically connections behaviour have a great influence on the ability of a structure in developing catenary actions.

- Besides from the connection behaviour there are other aspects that can also play an important role in the robustness of a structure, such as, the consideration of the composite behaviour (slab behaviour) [22] and a correct lateral stiffness when a substructure is used in the analyses [3,20,43]

- Finally, another aspect highlighted when impact analysis are considered is the influence of the strain rates induced by the impact load on the structural robustness. In fact, strain rates can influence both members (beam, columns) and connection behaviour [21,73]. Therefore, strain rates should be considered in all cases where it expected to have significant strain rates induced to the structures.

Chapter 3   Friction   dampers   under   different loading rates: experimental characterization

3.1 Introduction

In this chapter, the experimental campaign devoted to the assessment of the response of the friction damper to be implemented into the FREEDAM connection under different loading rates, is presented.

The impact tests were performed using a test rig previously designed at the University of Coimbra [12], whereas the quasi-static tests and tensile coupon tests for material characterization were conducted using a Universal Walter Bay LFV-600 machine.

3.2 Tested specimens and experimental programme

The tested specimens are basically double shear lap connections with a couple of additional 8 mm steel plates (made of steel S275JR) coated by means of thermal spray (friction pads), pre-stressed with M20 bolts (Fig. 3.1). Two distinct parts composed the specimen. The first is the "slip part", in which the internal plate (made of AISI304 stainless steel) is slotted in order to simulate the slotted haunch flange of the FREEDAM connection. The second part is the "fixed part", where an internal steel S275JR plate is used to connect the specimens to the experimental layout. In addition, two external steel plates with a thickness of 15 mm are placed between the bolt heads and the friction pads in order to reproduce the spreading effect of the bolt forces at the interface.

Three different modifications from the "standard" configuration of Fig. 3.1 were designed according to Eurocode 3 [5], so that different failure modes of the friction damper could be assessed (Fig. 3.2).

The entire experimental programme is summarized in Table 3.1 and it is divided into three groups. In the first group (Group A), the specimen configuration *a* (Fig. 3.2) was used, which has two slotted holes with a total length equal to 41 mm, internal plates with a thickness equal to 30 mm and preloaded M20 10.9 HV bolts. In Group B, bolts M20 8.8 SB were used in all eight tests. In these tests, the specimen *a* was used for the static tests while, the specimen *b* was used in the impact tests, differing from the specimen *a* in the length of the slotted hole (it has only one longer slotted hole, Fig. 3.2). Finally, in Group C, the specimen *c* was used, that differs from the configuration *a* in the thickness of the internal plates (here a 10 mm thickness was adopted), so that a plate in bearing failure mode could be tested. Additionally, the width of the internal plate at the fixed part was also enlarged in order to assure the failure mode at the slip part of the specimen. Furthermore, the three different coatings materials referred in the section 2.3.1 (M1- Tin, M4- sprayed aluminium and M6 – Metco 70C-NS) were used in each group test.

A total of 8 static tests and 32 impact tests were performed. Before each test, the bolts were tightened by means of a calibrated torque wrench in order to introduce a preload force F_p equal to $0.5 \cdot f_{ub} \cdot A_s$ (f_{ub} is the ultimate strength of the bolt and A_s is the tensile stress area of the bolt). The magnitude of torque applied to each bolt is dependent on the design preload value F_p, the diameter of the bolt *d* and of the bolt *k-factor*.
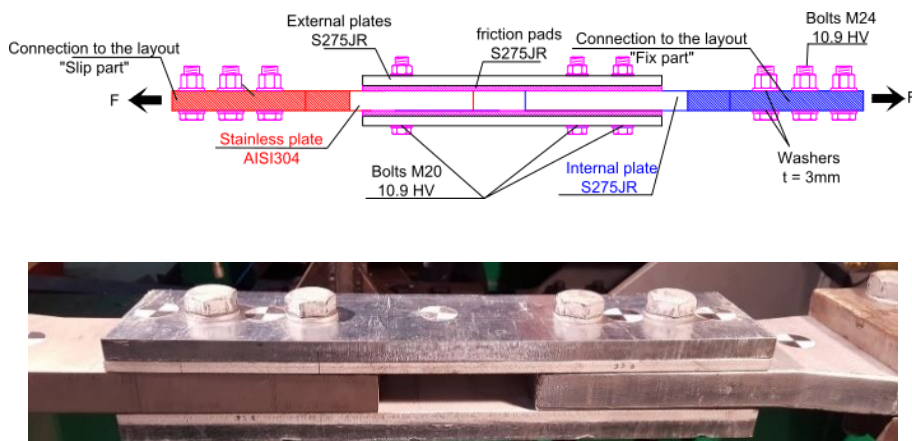
Fig. 3.1: FREEDAM specimen - Lateral view
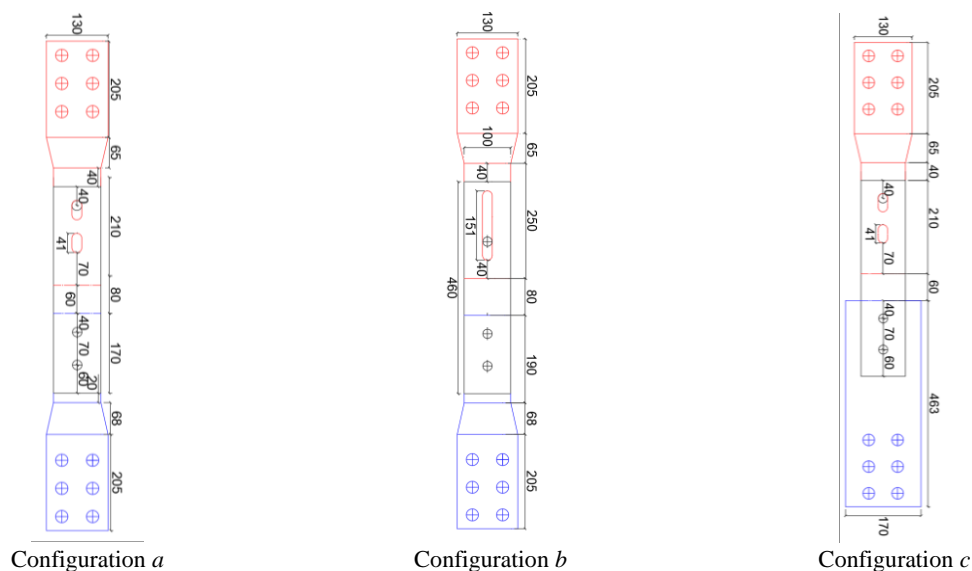
Fig. 3.2. Tested specimens – Front view (dimensions in mm).

Table 3.1. Experimental programme

[1]ID	Conf.	Bolt	Preload	[2]Test Type
Group A				
T3- M4/M1/M6-SI-30	a	M20 10.9 HV	122.5 kN	4 Impacts. 20Bar; 50Bar; 75Bar; 100Bar
T4- M1/M6- FI-30				100Bar
T8-M4/M6/M1-St.-30				Monotonic FC: 0.2KN/s
T10/11 –M4–St. 30				Monotonic DC: 0.01mm/s
Group B				
T1-M1- SI-30	b	M20 8.8 SB	98 kN	3 Impacts: 40Bar; 60Bar; 80Bar
T2-M1- FI-30				80Bar
T1-M6- SI-30				3 Impacts: 20Bar;40Bar; 60Bar
T7-M1/M6-St.-30	a			Monotonic FC: 0.2kN/s
Group C				
T5-M4- SI-10	c	M20 10.9 HV	122.5 kN	5 Impacts: 50Bar; 80Bar; 100Bar; 120Bar; 150Bar
T5-M1/M6- SI-10				3 Impacts:50 Bar; 100 Bar; 150 Bar
T9-M1-St.-10				Monotonic [2]FC: 0.2kN/s

[1]ID-Test: Tn°- X- Tt – Pt: Tn°=Test number- X=ID Coating Material (M4, M1, M6) – Tt=Test type: Sequential (SI), Full Impact (FI), Static (St.) – Pt=Internal plate thickness [mm])
[2]FC – force control; DC- displacement control

3.3 Mechanical properties

A material test series, consisting of quasi-static uniaxial tension tests, were performed in order to determine the material properties of the different materials composing the friction damper. Therefore, two steel grades were tested namely, the carbon steel S275JR composing the external plates, the friction pads and the internal plate at the "fix" part of the friction damper, and the stainless steel grade 304 composing the internal plate with the slotted hole. Afterwards, the same type of tests considering the same steel grades were repeated for each part composing the whole connection, described in chapter 4 of this thesis. However, all the tensile coupon tests are presented here for the sake of simplicity.

The tests were performed according to the ISO 6892-1 [83], adopting the method A (method based on strain rate control), considering a strain rate equal to $0.00025 \mathrm{s}^{-1}$ up to the lower yield strength (range 2a and *ReL* in Fig. 3.3c) and a strain rate equal to $0.0067 \mathrm{~s}^{-1}$ up to the ultimate tensile strength (range 4a and *Rm* in Fig. 3.3c). The specimens were of standard flat type with the thickness of the product (Fig. 3.3a and b). Fig. 3.4 depicts the test arrangement.

Fig. 3.5 shows the engineering stress-strain curves obtained from the different materials tested. Table 3.2 set out the average characteristics of the materials. In this table, the values of the Young's modulus E, the yield strength f_y (taken as an offset of the slope of E at 0.2% proof strength), the ultimate strength f_u and ultimate and fracture strain (ε_u and ε_f) are given. It is worth to mention that the stress and strain values indicated in the table correspond only to the static values, i.e. when the strain rate is not relevant.

Friction damper	Connection	Range 2: $e = 0.00025$ s^{-1}; range 4: $e = 0.0067$ s^{-1}
a. Specimen geometry (dimensions in mm)		b. Method A of ISO 6892-1 [83]
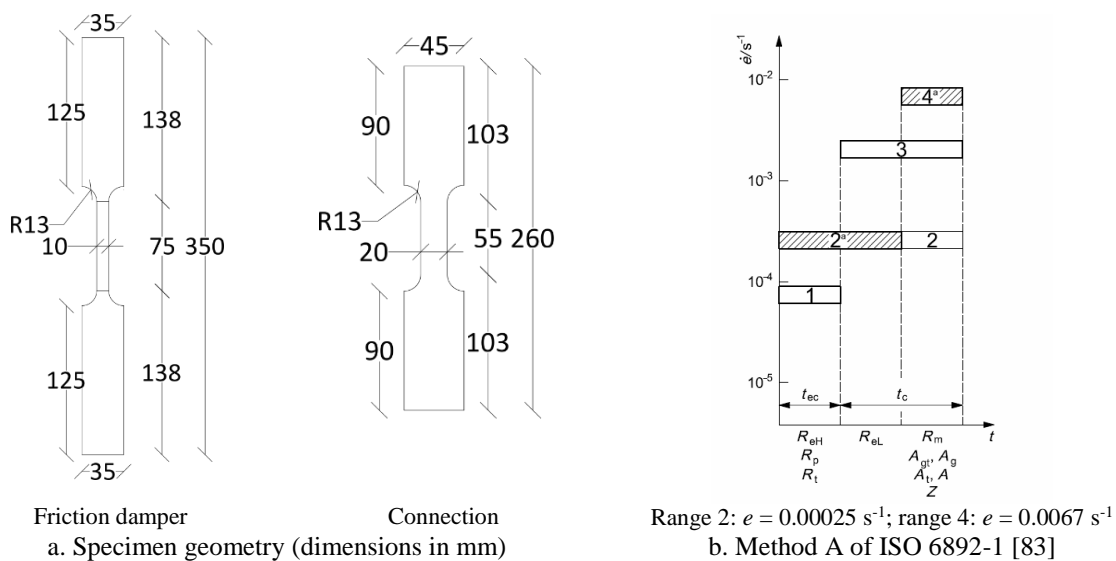
Fig. 3.3. Coupon test specimens and testing method

Fig. 3.4. Extensometer used for material characterization
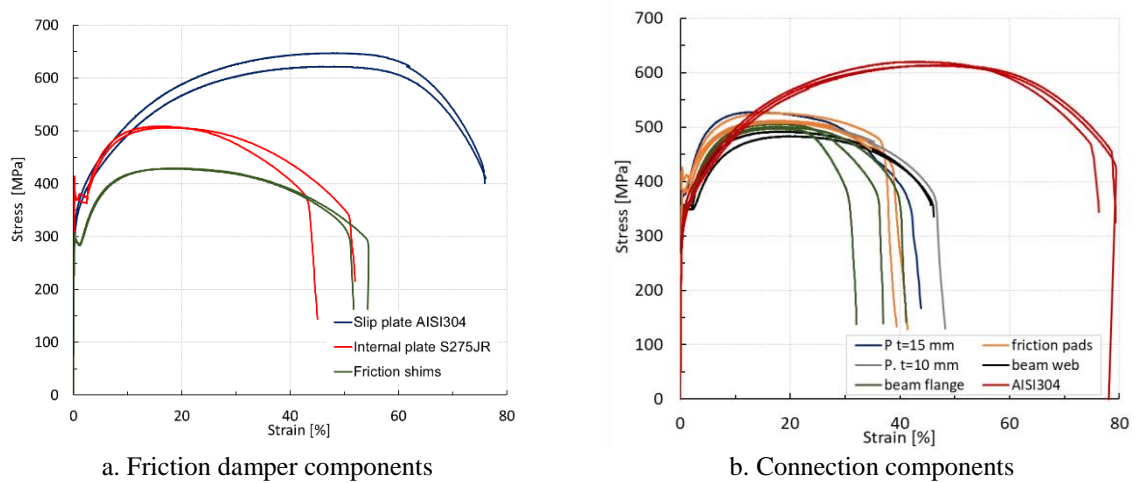
a. Friction damper components   b. Connection components

Fig. 3.5. Engineering stress-strain curves

Table 3.2. Material proprieties from uniaxial coupon tests

	ID	Mat.	t [mm]	E [GPa]	f_y [MPa]	f_u [MPa]	ε_u [%]	ε_f [%]
Friction damper	Slip plate (SP)	AISI 304	30	181.76	302.83	617.9	45.80	73.82
	External plate (EP)	S275JR	15	205.75	291.7	431.31	18.58	53.79
	IP – Internal plate (IP)	S275JR	30	203.3	377.9	508.7	16.52	43.19
Connection (chapter 4)	P.15mm	S275JR	15	202.89	369.6	524.5	13.67	43.79
	P.10mm	S275JR	10	208.48	328.03	488.71	16.91	48.28
	Friction damper (FD)	S275JR	8.08	207.72	392.97	515.56	17.38	40.45
	Beam flange (Bf)	S275JR	8.8	211.37	319.21	458.36	17.47	36.73
	Beam web (B_w)	S275JR	6.1	212.48	356.89	487.53	20.23	45.86
	AISI 304 (Friction damper)	AISI 304	15	195.5	304.76	615.68	45.6	77.88

3.4 Preliminary design

The components of the friction device activated under static and dynamic loading condition are the **plate net section in tension**, the **bolts in shear** and the **plate holes in bearing**. The initial elastic stiffness and design resistance of these components have been evaluated according to part 1-3 [75], part 1-8 of [5] and part 1-4 [84] of Eurocode 3 (Table 3.3). The mean values of the mechanical properties of the used materials, obtained by the tensile tests, were considered (Table 3.2). All the partial safety coefficients have been considered equal to 1.

Table 3.3. Formulation of the Eurocode 3 for the design resistance and initial stiffness

Component	Bolt in shear	Plate in bearing	Net section in tension
F_{Rd} [kN]	$F_{y,s} = n_s \cdot \alpha_v \cdot f_{ub} \cdot A$	$F_{y,b} = k_1 \cdot \alpha_b \cdot f_u \cdot d \cdot t$	$F_{y,T} = 0.9 \cdot f_u \cdot A_{net}$
S_{ini} [kN/mm]	$S_{ini,s} = 8 \cdot d^2 \cdot f_{ub} / d_{M16}$	$S_{ini,b} = 12 \cdot k_b \cdot k_t \cdot d \cdot f_u$	$S_{ini,T} = E \cdot A / p$

Table 3.4 summarises the values of the design resistance F_{Rd} and initial elastic stiffness S_{ini} of the three tested typologies of the friction damper. Following the recommendations of the Eurocode for shear lap joints, the design resistance is equal to the resistance of the weakest component of the bolt zone, while the initial elastic stiffness is equal to the reciprocal sum of individual stiffness of each component of the bolt zone. From the results, it is expected that the failure of the specimens tested in Group A and B is by the bolt in shear at the slip part, while the specimens tested in Group C are expecting to fail by bearing of the slotted hole.

Table 3.4. Design initial elastic stiffness and ultimate resistance of the friction dampers according to the codes

Specimen	Design Resistance, F_{Rd} [kN]	Design initial stiffness, S_{ini} [kN/mm]	Failure mode
a	377	146	Bolt in shear (slip part)
b	196	134	Bolt in shear (slip part)
c	174	82	Slotted hole in bearing

3.5 Experimental set-up and test procedure for quasi-static tests

The specimens were subjected to a monotonic uniaxial tensile force, using the Universal Walter Bay LFV-600 test machine (maximum tests load 600 kN). The specimens were clamped to the testing machine at both ends by the internal plates, as shown in Fig. 3.6a. The force was applied at the internal plate with slotted holes, while, at the opposite end, the other internal plate was fixed.

The force applied to the specimen was read directly by the machine's load cell, while the displacements were read with three LDVT's (Fig. 3.6). Two LVDT's were placed on each side of the specimen and fixed to the internal fixed plate so that the displacement of the sliding plate could be read. The third LVDT was placed between the claws of the machine, in order to check if there was any global movement of the specimen due to slipping between the specimen and the machine's claws.

a. Photo   b. Scheme
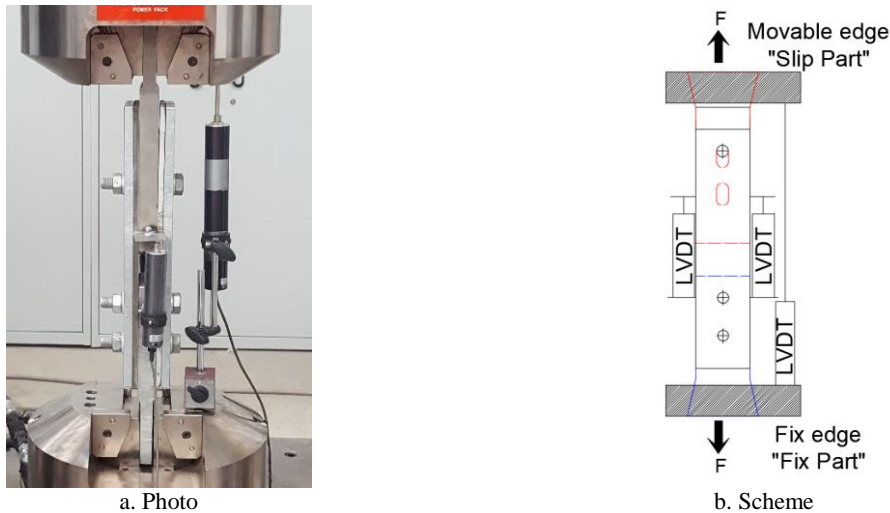
Fig. 3.6. Test set-up for the quasi-static tests

3.6 Experimental set-up for impact tests

3.6.1 Test procedure

The test set up used for the impact tests is schematically presented in Fig. 3.7. It comprises two HEB 500 beams placed horizontally and fixed to the reaction slab of the lab. At one end, these beams are orthogonally bolted to a rigid reaction frame built from two IPE450s whereas, at the other end, are connected to an HEB650. All the steel parts of the layout were of structural steel grade S355. In this way, a very stiff structure was built, which can accommodate impacts without deformations or rotations. Furthermore, the column to which the impact force is applied ("*flying beam*") is placed in parallel to the rigid reaction frame and it is made from a cross-section with very high stiffness (HEM340), in order to not suffer significant deformations when the impact force is applied. In addition, this beam is restrained by a pivot at the opposite end of the application of the load.

Finally, the specimen to be tested is connected to the flying beam and to the reaction frame. The boundary conditions of the specimen depends on the type of loads to be transmitted. In this

case, the specimen was connected by two hinges in order to transmit only tension uniaxial forces (Fig. 3.8).

The impact force is applied by a pneumatic cylinder, which is composed by an accumulator, a barrel and a valve between them (Fig. 3.9). The internal diameter of the barrel has approximately 125 mm and it was designed to work with pressures up to 300 Bar, resulting in a maximum design load of about 360 kN. Before each test, the accumulator is filled with the predefined pressure and then, the valve is open allowing the air to flow from the accumulator to the barrel, inducing the impact force. In this way, the system produces approximately deformation controlled rate tests in a sense that the deformation rate is mainly dependent on the applied initial pressure [12]. However, it should be noted that the real deformation rate of the specimen depends on its stiffness. Instrumentation is used to find the forces and moments applied to the specimen.

Two types of impact tests can be performed using this layout - full and sequential (FI or SI). In a sequential test, the same specimen is loaded and unloaded multiple times, with higher pressure in each sequence, up to failure (red lines in Fig. 3.10). In this way, it is possible to determine the approximate value of pressure needed to achieve failure. Moreover, from the unloading phase of the specimen, an approximation of the elastic stiffness of the specimen can be obtained. For a full impact test, the collapse pressure from the sequential test is used.
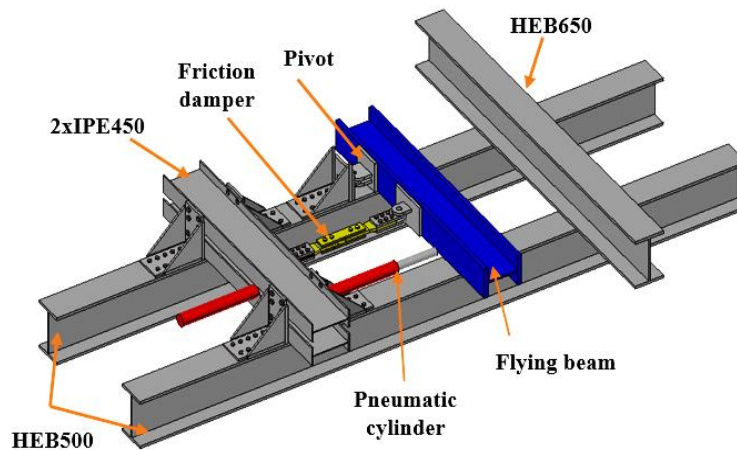
Fig. 3.7. Sketch of the experimental layout used for impact tests – Friction damper tests
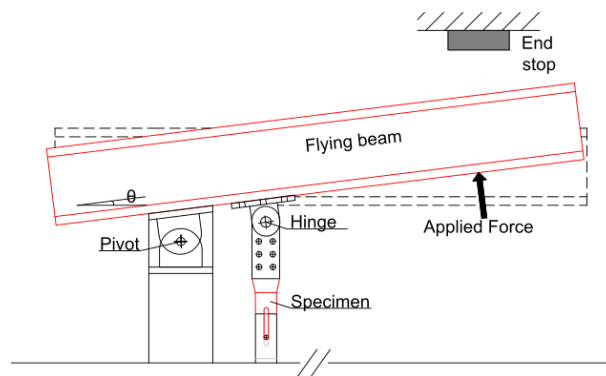
Fig. 3.8. Loading arrangements – Impact tests on the friction damper (top view)
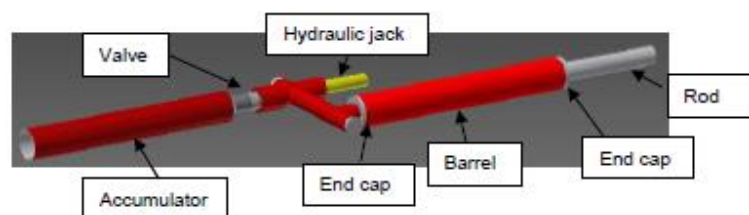
Fig. 3.9: Scheme of the pneumatic cylinder
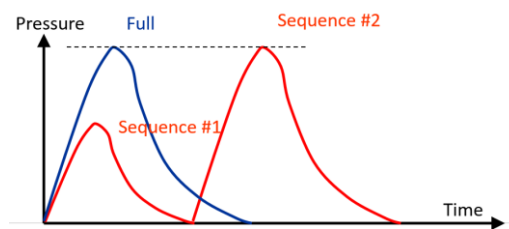
Fig. 3.10. Types of impact tests – Force history scheme

For testing the specimens under impact loads, the instrumentation needed is not as simple as for the quasi-static tests due to the dynamic nature of the loads. Firstly, the inertial forces of the system can no longer be neglected and secondly, the instrumentation used has to be specific to read short-duration tests. It is then necessary to read, besides from the force and displacements, also accelerations and velocities. In Fig. 3.11, is shown the instrumentation system used. A NI Compact DAQ 9172 chassis system and an HBM MX408 system were used for data acquisition.

The force was read by a load cell specially built to perform the impact tests (Fig. 3.12a). This load cell is located at the end of the rod of the barrel (see Fig. 3.9). The deformation of the specimen and "*flying beam*" were measured by laser triangulation sensors (Fig. 3.12b). These sensors have a high accuracy (+/-0.5mm) and a very fast reaction time (frequency rate of 9.4 kHz). The main requirement for using them is to ensure that they are fixed in a position

perpendicular to the target surface. In addition, a Photron high-speed camera was used (Fig. 3.12d), which recorded the tests and provided displacements, velocities and accelerations during the tests on specific points of the specimen (Fig. 3.13).

To take into account the inertial forces of the beam, two accelerometers from Brüel & Kjær model 4370 (Fig. 3.12c) were used to record the accelerations at the centre of mass of the "flying beam" a_{cm} and at the point of the application force a_f.
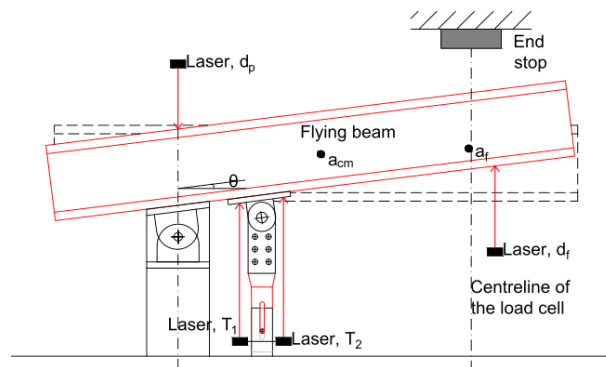
Fig. 3.11. Position of the instrumentation used for impact testing (top view)

a. Load cell

b. Laser sensor triangulation – Riftek RF603/500

c. Accelerometers

d. Photron high-speed camera

Fig. 3.12. Instrumentation used during the impact tests
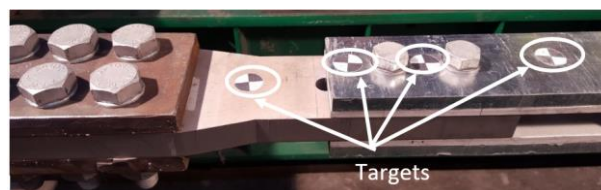
Fig. 3.13. Points to be read by the high-speed camera

3.6.2 Calculation of the force transmitted to the friction damper

Fig. 3.14 shows the diagram of the forces/moments and displacements/rotations acting on the "*flying beam*", assuming that the friction at the hinges and at the bearing supports is negligible.

The rotation of the beam is restrained by the pivot (point *A*), the impact force F_A, is applied at point *C* and the tested specimen is subjected to the force F_t, at point *B*. Furthermore, the inertial resistance moment of the beam has to be taken into account in the assessment of the force transmitted to the friction damper, since impacts tests are in the field of dynamic tests.
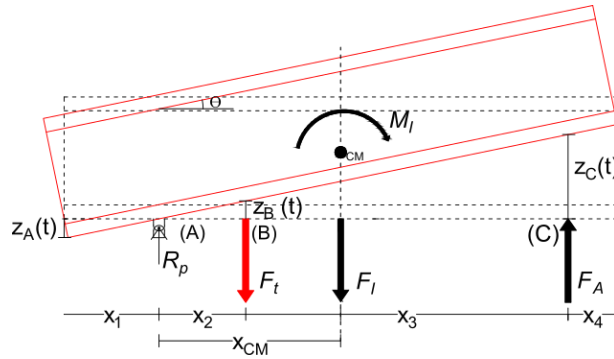
Fig. 3.14. Free body diagram

The assessment of the force applied to the specimen is obtained from the dynamic equilibrium of bending moments around the pivot (point *A*). Eq. (3.1)-(3.2) represent the equilibrium of dynamic forces and the dynamic equilibrium of bending moments around the pivot, respectively.

$$F_t(t) = F_A(t) - F_I(t) + R_p(t) \tag{3.1}$$

$$F_t(t) \times X_2 = F_A(t)\left(X_2(t) + X_3(t)\right) - F_I(t) \times X_{cm} - M_I(t) \tag{3.2}$$

$$F_I(t) = m \times \ddot{a}_{cm} \tag{3.4}$$

$$M_I(t) = I \times \ddot{\theta}(t) \tag{3.5}$$

$$I = 1/12\, mL^2 \tag{3.6}$$

where $X_2(t)$ and $X_3(t)$ are the distances X_2 and X_3 in time, respectively [m], $F_I(t)$ is inertial force in time [kN], X_{cm} is the distance from the centre of mass to point (A) [m], $M_I(t)$ is the

inertial resistance moment of the flying beam in time, [kN.m], $\ddot{a}_{cm}$ is the acceleration of the centre of mass of the beam [m/s^2], I is the inertia of the beam at its centre of mass [kg.m^2] (Eq.(3.6)), $\ddot{\theta}$ is the rotational acceleration of the beam [rad/s^2], m is the mass of the beam [kg] and L is the total length of the beam [m].

The rotation of the beam θ can be obtained by the laser displacement at the point d_f, (Fig. 3.11) or by double integration of the acceleration at the point a_f (Fig. 3.11) using Eq. (3.7) or Eq.(3.8), respectively. In turn, the rotational beam acceleration $\ddot{\theta}$, can be obtained by double differentiation of the laser displacement data, Eq. (3.9), or by using the accelerometer reading at the application load point, a_f, Eq. (3.10).

$$\theta(t) = \tan^{-1}\left(Z_c(t)/X_2(t) + X_3(t)\right) \tag{3.7}$$

$$\theta(t) = \tan^{-1}\left(\iint a_f\,dtdt \Big/ X_2(t) + X_3(t)\right) \tag{3.8}$$

$$\ddot{\theta}(t) = d^2 Z_c(t)\big/dt^2 \tag{3.9}$$

$$\ddot{\theta}(t) = a_f(t)\big/(X_2(t) + X_3(t)) \tag{3.10}$$

where $Z_C(t)$ is the displacement measured by the laser at the application load point in time [m] and a_f is the acceleration measured by the accelerometer at the application load point [m/s^2].

3.7 Experimental results

3.7.1 Quasi-static response of the friction damper

The behaviour of the friction damper is evaluated in terms of its friction resistance and behaviour after slip. Specifically, the friction resistance of the damper was evaluated in terms of its slip resistance F_{slip}, initial friction coefficient μ, friction resistance at the end of the slip (kinetic friction resistance, F_k) and the corresponding friction degradation given by the ratio between the kinetic friction force and slip resistance F_k/F_{slip}. The initial friction coefficient μ has been calculated as the ratio between the slip resistance force and the sum of the nominal values of the pre-loading force applied by the bolt (preload value in Table 3.1), Eq.(3.11).

The behaviour of the friction damper after the complete slip of the slotted plate has been evaluated in terms of its ultimate resistance F_u, ductility capacity δ_u and failure modes.

Furthermore, an approximation of the initial elastic stiffness after slip S_{ini} and design resistance F_y is also measured, by a bilinear approximation of the slopes of the elastic and post-elastic stiffness, as proposed by Jaspart [85].

$$\mu = \frac{F_{slip}}{n_s N_b} \tag{3.11}$$

Group A

Five quasi-static tests were performed: three under force control (0.2KN/s) using each one of the selected coating materials and two under displacement control (0.01mm/s) using the coating material M4. The reason for using both procedures was to study their influence on the variation of the slip force during the slip of the plate. The force-displacement curves of the quasi-static tests are reported in Fig. 3.15 and the main results summarized in Table 3.5 and Table 3.6.

From the force-displacement curves, different phases of the friction damper's behaviour can be observed. Initially, the force increases with no significant movement until reaching the friction resistance (F_{slip} in Fig. 3.15). At this stage, the slip of the slotted plate on the friction pads starts. Immediately after this, the force decreases due to the damage occurring in the friction shims and simultaneous loss of the initial bolt pre-loading (here called as "preload degradation" phase) and then, it continues to decrease until the bolt reaches the end stroke of the slotted hole (δ_{slip}, corresponding to the force F_k). This degradation may be due to some loss the initial preload and wearing of the friction pads.

Finally, the plates and the bolt are subjected to shear and bearing until reaching the failure, which always occurred due to the **bolt shank in shear**, as predicted by the preliminary design (Table 3.4). Furthermore, before achieving the ultimate resistance, a second slippage branch is usually observed (reported in Fig. 3.15 as Slip_2), due to the clearance of the cap plates holes.

Regarding the friction resistance of the specimens of this group, from Table 3.5, it can be recognised that the material M1 provides a higher initial value of the friction coefficient, followed by the material coating M4 and then M6. In general, the friction coefficient ranges between 0.45 and 0.65. After the initiation of the slip, all materials exhibit an evident force degradation. Concerning the influence of the tested method, i.e. force or displacement control, the results on material M4 highlight that, it does not influence the static friction coefficient. More significant it is the influence on the degradation during the slip, as under force control,

due to instantaneous slip, according to the results shown in [86], a greater friction degradation has been recognised.

The design resistance was measured by a bilinear approximation of the slopes of the initial stiffness and post-elastic stiffness [85]. An example is shown for one test in Fig. 3.15. From the results, an average value equal to 360 kN and 116 kN/mm was found for the design resistance F_y and initial stiffness S_{ini}, respectively (Table 3.6).

Finally, with reference to the ultimate behaviour of the friction damper, in all the tests a similar behaviour is observed. The ultimate load presents an average value of 441 kN (15% higher than the value given by Eurocode, Table 3.4). This testifies that the influence of the typology of the coating material, the method of the test control and of the initial friction coefficient is negligible, which is in line with the findings of Fisher and Wallaert [86,87]. In Table 3.6, the values of the ductility capacity of the friction damper are also reported. In particular, two values are given: the total deformation of the damper δ_{max} and the deformation of the bolt zone δ_u, which is obtained deducting the deformations corresponding to first and second slip to the total deformation. An average value of 6.4 mm was observed for the shear deformation of the bolts. The bolts after failure are shown in Fig. 3.16. Shear deformation of the bolts with a small bending effect can be observed.
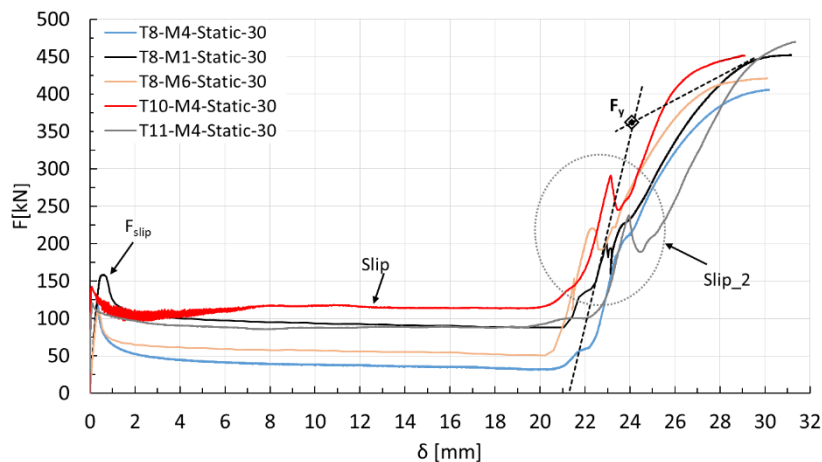
Fig. 3.15. Quasi-static tests Group A

| a. T11-M4-St-30 | b. T8-M1-St-30 | c. T8-M6-St-30 |

Fig. 3.16. Bolts after failure – Quasi-static tests Group A

Group B

The force-displacement curves of the quasi-static tests of Group B are shown in Fig. 3.17. These curves show very similar behaviour to those of the previous group. The major difference is in the slip phase. The calculated friction coefficient was significantly lower than expected (0.33 and 0.38. for materials M1 and M6) due to the use of SB bolts rather than HV or HR bolts. Concerning the degradation of the slip, it presents similar values to the test carried out under force control of the previous group (Table 3.5).

After the complete slip, the failure happens due to the **bolt in shear** in both tests (Fig. 3.17) with an ultimate resistance equal to 290 kN and 297 kN, around twice the ultimate resistance that is given by the Eurocode (Table 3.4). In addition, a ductility capacity slightly higher than found in the previous group (Table 3.6). On the other hand, a lower initial stiffness was observed compared to one found in the previous group, which is due to the lower strength of the bolt and the fact that the bolt was fully threated (Table 3.6).
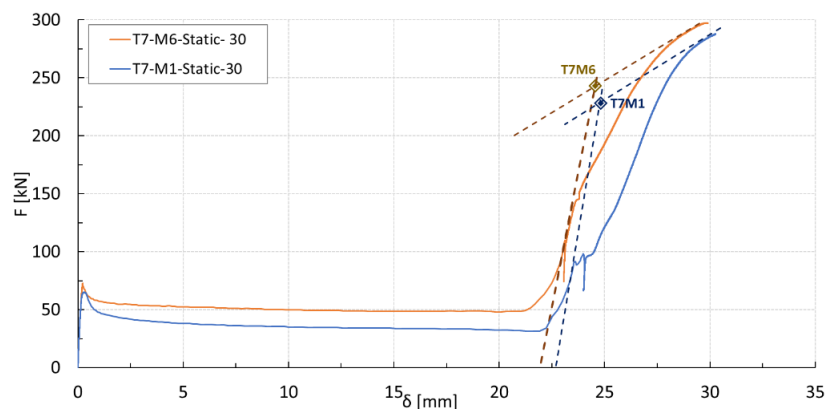
Fig. 3.17. Force-displacement curves for the quasi-static tests T7-M1-Static-30 and T7-M6-static-30

Fig. 3.18. Bolt shearing: Quasi-static test Group B

Group C

The quasi-static test on the specimen with the configuration *c* (Fig. 3.2) was performed only with the coating material M1. The whole force-displacement curve is presented in Fig. 3.19 and the main results from the test are reported in Table 3.5 and Table 3.6

The force-displacement curve shows two hardening branches due to the particular configuration of the slip plate which is characterized by two separate holes. When the bolt reaches the end of the hole' stroke (see Fig. 3.20b), the plate deforms in bearing, reaching the adjacent hole (failure by shear tear-out between the two slotted holes, Fig. 3.20c: $F_b = 406$ kN, $\delta_b = 62.5$ mm). Immediately after this failure, the bolt reached the edge of the adjacent hole and the plate failed (failure by plate net section in tension, Fig. 3.20d: $F_u = 416.9$ kN, $\delta_u = 106.3$ mm). It should be noted that in the impact tests it was only possible to reach the first failure mode due to the attainment of the maximum rotation of the layout. From the practical point of view, only the first hardening branch is of interest, therefore, only the force-displacement response up to the bearing of the plate hole (first failure of the curve Fig. 3.19) will be considered for the comparison with the results of impact tests.

Concerning the initial stiffness, this specimen has the lowest stiffness of all the test groups, since the behaviour is governed by the bearing behaviour of the slip plate (Table 3.6).

Finally, Fig. 3.21 shows the conditions of the stainless steel plate, friction pads and bolt after the test. The tear-out between the two holes caused by excessive bearing and the plate net section failure can be easily observed. Furthermore, significant necking of the plate, shear deformation and bending of the bolt and wearing of the friction pads are noticed.
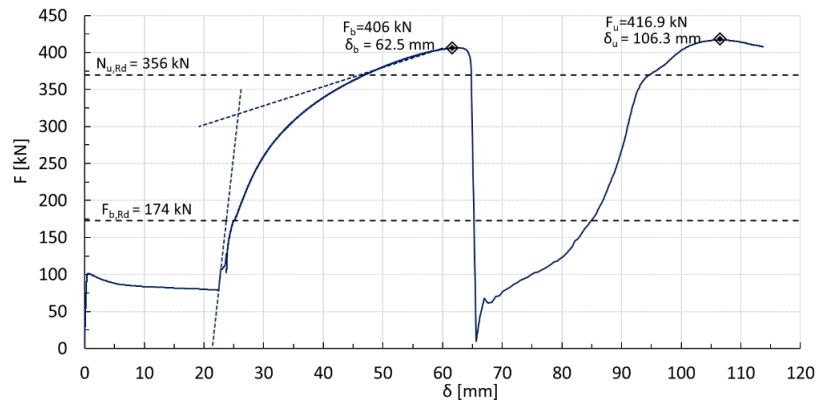
Fig. 3.19. Force-displacement curve of the quasi-static test T9- M1-Static-10
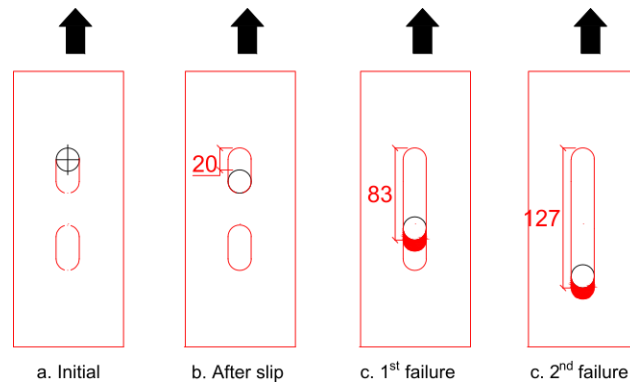
Fig. 3.20. Position of the bolt during the test- Quasi-static test Group C (dimensions in mm)

a. Slip plate   b. Bolt 10.9 HV   c. Friction pads

Fig. 3.21. Plates and bolt after the test - Quasi-static test Group C

Table 3.5. Results from quasi-static tests– Friction properties

Group	Mat.	Test Type[1]	ID	F_{slip} [kN]	μ	F_k [kN]	F_k/F_{slip}
A	M1	FC	T8-M1-St.-30	156	0.64	87	0.6
	M4	FC	T8-M4-St.-30	118	0.48	35	0.3
		DC	T10-M4-St.-30	142	0.58	113	0.8
		DC	T11-M4-St.-30	120	0.49	100	0.8
	M6	FC	T8-M6-St.-30	110	0.45	50	0.5
B	M1	FC	T7-M1 St.-30	65	0.33	31	0.48
	M6	FC	T7-M6-St.-30	75	0.38	50	0.67
C	M1	FC	T9-M1St.-10	100	0.41	80	0.8

[1] see bottom reference of Table 3.1

Table 3.6. Results from quasi-static tests– behaviour after slip

Group	Mat.	Test Type[1]	ID	S_{ini} [kN/mm]	F_y [kN]	F_u [kN]	δ_{max} [mm]	δ_u [mm]	Failure Mode
A	M1	FC	T8-M1-St.-30	126	362	450	31	7.4	BS[2]
	M4	FC	T8-M4-St.-30	128	339.6	410	30.17	6.4	BS[2]
		DC	T10-M4-St.-30	106	360.8	452	29.08	5.4	BS[2]
		DC	T11-M4-St.-30	113	352.9	470	31.3	6.3	BS[2]
	M6	FC	T8-M6-St.-30	105	345	450	30.28	6.3	BS[2]
		Mean		116	352	441		6.4	-
B	M1	FC	T7-M1 St.-30	108	228.7	290	30.6	7.6	BS
	M6	FC	T7-M6-St.-30	92.8	242.6	297	29.9	7	BS
		Mean		100	235.7	294	-	7.3	-
C			T9-M1St.-10	60	286.7	406	62	38.4	SP[3]

[1] see bottom reference of Table 3.1; [2] BS –Bolt shear; [3]SP – sliding plate in bearing

3.7.2 Impact response of the friction damper

For the sake of simplicity, only the impact tests performed on the specimens with the coating material M1 are presented in detail. For the specimens tested with the other coating materials, the main results are reported in tables throughout the subsections, while the force-deformation curves can be found attached to this document (Annex A).

In order to evaluate the influence of the strain rate on the behaviour of the friction damper, a dynamic factor "*DF*" is used, which corresponds the ratio between a certain behavioural parameter under impact loading conditions and under quasi-static loading. In fact, as mentioned in Chapter 2, this parameter is normally called dynamic increase factor "*DIF*" and is used to translate the increase of strength or resistance of elements when subject to high strain rates. However, in this work, some of the parameters under evaluation presented a decrease under high strain rates. Therefore, this parameter is here called dynamic factor "*DF*". Six parameters are under evaluation (Eq.3.12-3.16), namely: the static friction coefficient μ, the design and ultimate resistance (F_y and F_u), the initial elastic stiffness after slip S_{ini} and the ductility capacity of the damper after slip δ_u.

$$DF_u = \frac{F_{u,imp}}{F_{u,st}} \tag{3.12}$$

$$DF_{frict} = \frac{\mu_{imp}}{\mu_{st}} \tag{3.13}$$

$$DF_\delta = \frac{\delta_{u,imp}}{\delta_{u,st}} \tag{3.14}$$

$$DF_S = \frac{S_{imp}}{S_{st}} \tag{3.15}$$

$$DF_y = \frac{F_{y,imp}}{F_{y,st}} \tag{3.16}$$

Group A

With reference to the coating material M1, in Fig. 3.22, the impact tests, both sequential and full tests, performed with specimen *a* are reported and compared with the reference quasi-static test. In Table 3.7 and Table 3.8, the main parameters concerning the friction resistance and behaviour after slip of the devices under impact loads are summarised.

Starting from the sequential test (blue lines in Fig. 3.22), four sequences were performed. First, 20 Bar pressure was applied. During this sequence, the friction resistance was exceeded by a force equal to 150 kN and then, the slotted plate slipped on the friction pads until the bolt reached the end of the stroke of the slotted hole. From the unloaded slope of the specimen, a value of 166 kN/mm was found for the initial stiffness after slip, corresponding to an increase of 30% ($DF_S = 1.3$) of the value of the reference quasi-static test. In the following three sequences (#50 Bar, #75 Bar and #100 Bar), the specimen was loaded and unloaded up to the failure. The failure was reached for a force equal to 465 kN, representing an increase of 3% ($DF_u = 1.03$) of the ultimate resistance when compared with the reference quasi-static test. Furthermore, the design resistance was approximately measured as in the quasi-static tests, obtaining the same dynamic factor as obtained for the ultimate resistance ($DF_y = DF_u = 1.03$).

After the sequential test, a single impact was performed (green line in Fig. 3.22). The pressure of 100 Bar was applied, as this pressure led to the collapse in the aforementioned sequential test. Both the friction resistance and the ultimate resistance showed slightly higher

values than the ones obtained in the quasi-static tests. A friction resistance of 170 kN was achieved with DF_{fric} =1.09. Furthermore, in contrast to the static tests, the degradation of the force during the slip is less significant, which is in agreement with the observations of Block [88], who stated that for higher velocities, the initial friction coefficient is closer to the kinetic coefficient and, therefore remains more stable during the slip. The failure was reached for an ultimate resistance equal to 479 kN, to which corresponds a DF_u=1.06.

Regarding the ductility of the friction device, in sequential and full impact tests the values of the ultimate deformation were 4.6 mm and 4.9 mm, respectively, to which correspond to a DF_δ equal to 0.62 (SI) and 0.66 (FI), evidencing an average of 37% loss of the ductility capacity observed in the quasi-static test (Table 3.8).

In Fig. 3.23, the bolts and the stainless steel plate after the test are shown. It may be observed that a certain bearing of the stainless steel plate occurred. With respect to the deformation of the bolts, as observed in the quasi-static tests, the bolts show deformation by shear while the bending deformation is not as significant as observed in the quasi-static tests.

For the specimens with the other two coating materials (M4 and M6), the main results concerning the ultimate capacity and friction resistance are reported in Table 3.7 and Table 3.8, respectively. In all tests, the friction damper shows a more brittle behaviour under impact loads, i.e. greater initial stiffness and ultimate resistance and lower ductility, but the failure mode remained the same as in the quasi-static tests, i.e. failure by bolt shearing. Finally, it may be concluded that the coating material M1 always provides the highest initial friction coefficient, even at a high loading rate (Table 3.7)
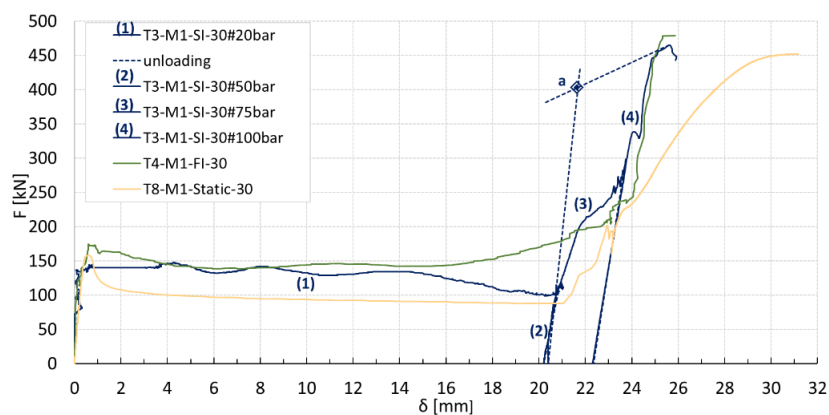
Fig. 3.22. Force displacement curves – Group A: quasi-static test T8-M1-Static-30 and impact test T3-M1-SI-30 and T4-M1-FI-30

Fig. 3.23. Bolt and stainless steel plate after the tests- Group A, specimens with coating material M1

Group B

The force-displacement curves of two impact tests (SI and FI) performed on specimen B with the coating material M1 are shown in Fig. 3.24. In the case of the SI test, the slip occurred when the force reached a value of 100 kN, whereas this value was significantly higher in the case of the FI test (150 kN).

After slip, the measurements of the unloading phase of the test, showed an increase of the initial stiffness of the specimen, in a similar way as in the previous test group (Table 3.8). Unfortunately, due to the lack of a post-elastic branch in the impact tests of this group, the design resistance F_y could not be assessed.

The collapse, as expected, occurred by failure of the bolt in shear in both tests for a force equal to 309kN and 315kN in the sequential and full impact, respectively, to which corresponds an increase of the ultimate force of 6.5% and 8.6% compared to the quasi-static test (Fig. 3.25).

An additional sequential impact test was performed, this time with the coating material M6. A friction resistance force equal to 77 kN was obtained and the collapse, once again, occurred due to the failure of the bolt in shear for a force equal to 318 kN, to which corresponds an increase of the ultimate force of 7% compared to the quasi-static test.

Concerning the ductility, in the same way as observed in the previous test group, the ductility of the specimens decreased by approximately 30% when dynamically loaded (see Table 3.8).
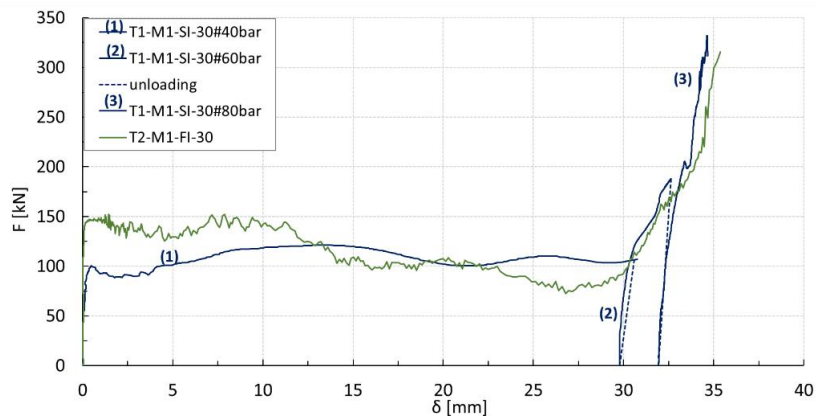
Fig. 3.24. Force-displacement curves for T1-M1-SI-30, T2-M1-FI-30.

Fig. 3.25. Bolt failure – Group B: impact

Group C

The force-displacement response of the quasi-static and sequential impact test on the specimens with the coating material M1 is reported in Fig. 3.26. Three sequences of impact were considered. In the first sequence ((1) in Fig. 3.26) the friction resistance was exceeded for a similar force to the one achieved in the quasi-static tests (F_{slip} = 100 kN). After the slip of the slotted plate on the friction pads, the bolt is engaged in shear and the plates in bearing up to the failure, where an initial stiffer behaviour is observed when compared to the quasi-static test (DF_S =1.28).

The failure was then achieved by an excessive bearing of the slotted plate, with an ultimate load equal to 450 kN and a deformation of 40 mm (sequences (2) and (3) in Fig. 3.26). Compared to the quasi-static test, an increase of the ultimate strength in the impact test (DF_u = 1.11) is observed (Table 3.8). In addition, with the bilinear approximation of the initial and post-elastic stiffness, a design resistance equal to 374.7 kN was obtained, representing 1.2 times the static design resistance (DF_y = 1.2). This higher increase of the design resistance compared to the ultimate resistance was also observed in [6,7] for the both T-stub and end-plate joint., which is related to the behaviour of the steel grades composing the plates under dynamic loading, in which the increase of the yield strength is higher than the increase of the ultimate

strength [59,61,62]. Furthermore, a decrease in the friction damper ductility of about 50% is observed (Table 3.8).

The bolt and the stainless steel plate after the quasi-static and the sequential impact test are shown in Fig. 3.27. It can be observed that the bolt, used in the sequential impact test, did not experience a bending and shear deformation as significant, as observed in the quasi-static test. As for the stainless steel plate, before the tear-out of the steel between the holes, a minor necking and high bearing deformation is noticed.

Two other sequential impact tests were performed, using the coating materials M4 and M6 and the main results are indicated in Table 3.7 and. In these tests, the bearing collapse of the plate was not achieved due to the prior attainment of maximum rotation of the assembly. Nevertheless, high deformation by bearing of the holes was observed (Fig. 3.28) and with a maximum force that exceeded the ultimate resistance of the corresponding quasi-static test.
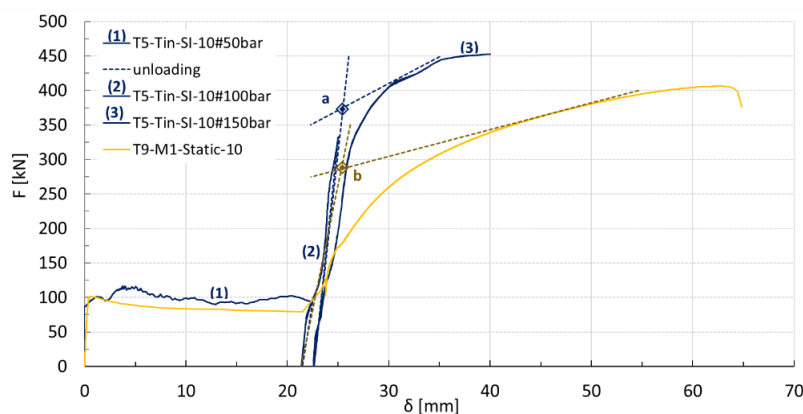
Fig. 3.26. Force-displacement curves – Group C: quasi-static test T9-M1-Static-10 and impact test T5-M1-SI-10.

Table 3.7. Results from impact tests– Friction properties

Group	Mat.	Test Type[1]	ID	F_{slip} [kN]	μ	F_k [kN]	F_k/F_{slip}
A	M1	SI	T3-M1-SI.-30	150	0.61	100	0.66
		FI	T4-M1-FI.-30	175	0.71	150	0.86
	M4	SI	T3-M4-SI.-30	143	0.58	120	0.84
	M6	SI	T3-M6-SI-30	109	0.44	150	1.37
		FI	T4-M6-FI-30	143	0.58	120	0.84
B	M1	SI	T1-M1-SI-30	100	0.51	100	1
		FI	T2-M1-FI-30	150	0.77	100	0.67
	M6	SI	T2-M6-SI-30	77	0.39	100	0.83
C	M1	SI	T5-M1-SI-10	100	0.41	91	0.9
	M4	SI	T5-M4-SI-10	123	0.5	110	0.89
	M6	SI	T5-M6-SI-10	150	0.6	150	1

[1] see bottom reference of Table 3.1

Table 3.8. Results from impact tests– behaviour after slip

Group	Mat	Test Type[1]	ID	S_{ini} [kN/mm]	F_y [kN]	F_u [kN]	δ_{max} [mm]	δ_u [mm]	Failure mode
A	M1	SI	T3-M1-SI.-30	166	403.9	465	25.6	4.6	BS[2]
		FI	T4-M1-FI.-30	-	-	479	25.85	4.85	BS[2]
	M4	SI	T3-M4-SI.-30	159	380.5	457	26.9	4.9	BS[2]
	M6	SI	T3-M6-SI-30	154	356.7	444	25.9	4.4	BS[2]
		FI	T4-M6-FI-30	-	-	453	25.7	4.2	BS[2]
		Mean		**160**	**380.4**	**460**		**4.6**	**-**
B	**M1**	SI	T1-M1-SI-30	135	-	332	34.6	4.6	BS[2]
		FI	T2-M1-FI-30	-	-	316	35.4	5.4	BS[2]
	M6	SI	T2-M6-SI-30	121	-	318	33.4	3.4	BS[2]
		Mean		**128**	**-**	**321**	**-**	**4.2**	**-**
C	M1	SI	T5-M1-SI-10	93.6	374.7	453	39.7	20	SP[3]
	M4	SI	T5-M4-SI-10	107	-	[3]433	[3]39.17	[3]18.2	No failure
	M6	SI	T5-M6-SI-10	111	-	[3]427	[3]42.55	[3]20.6	No failure
		Mean		**103.9**	**-**				**-**

[1] see bottom reference of Table 3.1; [2] BS –Bolt shear; [3]SP – sliding plate in bearing

Fig. 3.27. Bolt and stainless steel plate after the tests: T5-M1-SI-10

a. T5- M4-SI -10   b. T5-M6-SI-10

Fig. 3.28. Stainless steel plate after the test (group C)

3.8 Discussion of the results

On the basis of the experimental results under quasi-static tests, sequential impact test and full impact tests discussed in the previous sections, it can be recognised an influence of strain rates on the behaviour of the devices. In Table 3.10 and Table 3.9, the values of the dynamic factors evaluated in all the examined cases, are summarised.

With reference to the friction behaviour, it can be recognised that for the specimens with bolts of class 10.9 (group A and group C) and for all typology of coating materials, the impact load leads generally to an increase of the friction resistance with a DF_{fric} ranging between 1.00 and 1.11. The use of SB bolts rather than HV or HR in specimens of Group B leads to a different influence of the strain rate due to the low value of the friction coefficient under static loading conditions. In this case, the DF_{fric} is characterised by a great variability for the different materials ranging between 1.03 and 1.94.

With reference to the ultimate force of the friction device, the influence of the strain rate is similar for the different materials and for the different specimen configurations. The impact load leads generally to an increase of the ultimate resistance exhibited under quasi-static loads with a DF_u ranging between 1.03 and 1.12.

Regarding the influence of the strain rate on the ductility of the friction damper, from Table 3.9, it can be recognised that the strain rate leads in all cases to a significant reduction of the ultimate displacement of the friction devices with DF_δ ranging between 0.48 and 0.77. More precisely, it can be observed that when the failure mode is the bolts in shear (Group A and Group B), the average value of the DIF_δ provided by all coating materials is equal to 0.64 while when the failure mode is the plate in bearing (Group C), the DIF_δ reaches its minimum value equal to 0.5. This reduction of ductility was also observed by Ribeiro and co-authors [10] when studying the behaviour of T-stubs subjected to impact uniaxial tension loads. They found that the increase of the loading rate activates less ductile failure modes, which happens, due to the high sensitivity to high loading rates of the steel grade composing the plates.

Finally, concerning the initial stiffness, also an increase is observed under impact loading, with values of DF_S between 1.3 and 1.5. In literature, this parameter is generally not evaluated. However, some authors had reported general comments about this parameter. In [25,72], it was reported that the tested connections present an initial stiffer behaviour under impact loads. On the contrary, Barata and co-authors [6,12] did not observe any changes on the stiffness of T-stubs and end-plate joints. One of the reasons for the different observations on the same parameter can be related to the active components of the specimens. While in Eurocode, the coefficients of stiffness for the components bolt in shear and plate in bearing depend on the ultimate strength of the material and on the elastic Young's modulus E, for the particular case of the T-stub or end-plate joints, the stiffness of the involving components (T-stub in bending and bolt in tension), depends more significantly on the geometrical parameters of the

components. Therefore, assuming that Young's modulus E remains unchanged and the ultimate strength increase according to DF_u, it is logic that also the stiffness of the tested specimens increase for higher loading rates.

Table 3.9. Summary of the values of the Dynamic factors after slip

	Test Type	Group		
		A	B	C
S	Static	116	100	60
	Impact	160	128	103.9
	DF_S	**1.37**	**1.28**	**1.44**
F_y	Static	352	235.7	317
	Impact	380.4	-	374.7
	DF_y	**1.08**	**-**	**1.3**
F_u	Static	441	294	406
	Impact	460	321	452
	DF_u	**1.04**	**1.09**	**1.11**
δ_u	Static	6.4	7.3	41
	Impact	4.6	4.2	18
	DF_δ	**0.72**	**0.57**	**0.44**

Table 3.10. Summary of the values of the friction dynamic factors and degradation of the friction resistance

Material	Bolt class	Test type		F_k/F_{slip}	μ_{avg}
M4	10.9 HV	Static	FC	0.3	0.51
			DC	0.8	
		Impact		0.84	0.54
		DF_{fric}			1.06
M1	10.9 HV	Static		0.7	0.56
		Impact		0.9	0.58
		DF_{fri}			1.04
	8.8 SB	Static (FC)		0.48	0.33
		Impact		0.84	0.64
		DF_{fri}			1.9
M6	10.9 HV	Static		0.5	0.45
		Impact		1.15	0.51
		DF_{fri}			1.13
	8.8 SB	Static (FC)		0.67	0.38
		Impact		0.83	0.39
		DF_{fri}			1.03

Based on the previous results, the main conclusions that can be drawn regarding the behaviour of this type of friction devices are:

- When subjected to impact loads, the resistance of the friction damper increases and the ductility decreases compared to what was observed when statically loaded;

- The influence of the loading rates on the ultimate resistance and ductility of the friction damper was more significant when the specimen failed by the plate in bearing rather than the bolt in shear (an increase of resistance of 11% vs 5% and a decrease of ductility of 50% vs 30%). This is due to the fact that the stainless steel used in plates have higher sensitivity to different strain rates than the high strength steel used in bolts [62,63].

- For the tested specimens, the failure modes observed in the static tests did not change in the presence of high loading rates. In fact, the changes in the static failure mode of connections due to impact loading is still not completely understood since it seems to depend on several aspects such as the mechanical and geometric properties of the parts constituting a connection (as the thickness of plates and/or bolt grade), the rate of the test and the experimental boundary conditions. For example, the parametric study carried out by Ribeiro *et al.* [10] showed that the T-stub component with the increase of the loading rate, show brittle failure modes. On the other hand, other authors such as [6,24], observed always the same failure mode, independently of the plates' thickness or the applied loading rate.

- During the slip, degradation of the slip force was observed in both impact and quasi-static tests. However, independently of the coating material, this degradation was less significant in the impact tests, probably because, at high loading rates, the initial friction coefficient is closer to the kinetic coefficient. In addition, an increase of the initial friction resistance was generally observed under impact loading. From this perspective, the application of friction dampers within connections can increase their performance under loads rapidly applied since their friction resistance is increased by the presence of elevated strain rates.

- Finally, the elastic initial stiffness after the slip also increased for higher loading rates, which was related to the increase of the ultimate strength of the materials composing the components of the friction damper.

Chapter 4 Friction dampers under different loading rates: numerical characterization and analytical developments

4.1 Introduction

Following the experimental campaign described in the previous chapter, a numerical study has been carried out to widen the knowledge on the friction damper behaviour. At first, the model was calibrated against the experimental results. After calibration, a parametric study was performed considering: i) four internal plate thickness, namely, 8 mm, 10 mm 15 mm and 30 mm, in order to activate different failure modes, ii) variation of the initial bolt preload and iii) different velocity rates. All the numerical analyses were carried out with ABAQUS software, using the dynamic implicit solver [13] with the quasi-static procedure to capture the quasi-static behaviour and the moderate dissipation procedure to capture the dynamic behaviour of the specimens.

Finally, an analytical component-based model was developed to characterize the non-linear behaviour of this component. The developed analytical model is based on the model recently developed by Henriques *et al.* to predict bolted shear lap connections subjected to tension loads [14], with some modifications in order to take into account the changes on the resistance and ductility when strain rates are relevant.

4.2 Numerical study

4.2.1 Model geometry, boundary and loading conditions and model discretization

The model has the same geometry as the specimens experimentally tested in the previous chapter (Fig. 4.1). Comprises five parts: i) external plate, ii) friction pad, iii) fixed internal plate (fixed end), iv) internal plate with slotted holes (free end) and v) bolts (head and shank as a single piece).

With reference to the boundary conditions, a rigid body constraint was applied to each edge of the internal plates to provide the required boundary conditions (Fig. 4.1). No restraint was provided in the sliding plate, and on the other end, the fixed internal plate was restrained in the direction of the application of displacement. Concerning the applied loading, two subsequent steps were defined. First, the bolts were preloaded and then, the internal stainless plate was pulled. For the quasi-static analysis, the displacements were applied monotonically. To calibrate the dynamic numerical models, the experimental displacement-time curves were applied as a boundary condition, as shown in the example of Fig. 4.2.
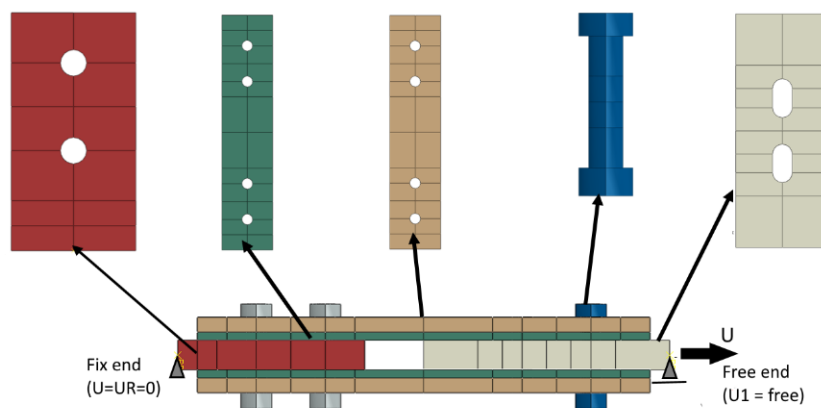
Fig. 4.1. Numerical model of friction damper – Geometry and boundary conditions
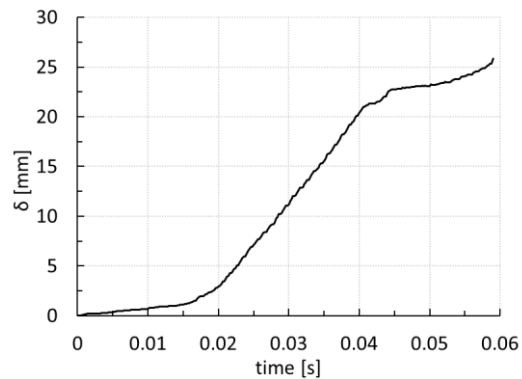
Fig. 4.2. Displacement-time – Impact test T4-M1-FI-30

Solid (or continuum) element type C3D8R (first order reduced integration continuum element) with "Hex" element shape was used in the entire model, allowing for non-linear geometrical and material behaviour. Due to its reduced integration, C3D8R elements reduces the calculation time and provides hourglass behaviour control (this type of element is often used for simulations where high deformations are expected and on impact analyses). Due to the several contact properties, damage modelling of the elements and dynamic analysis, which normally introduce convergence problems, a close mesh had to be used, especially in those elements where high deformations were expected.

a. Slip plate   b. Fix plate   c. Bolt   d. Friction pads
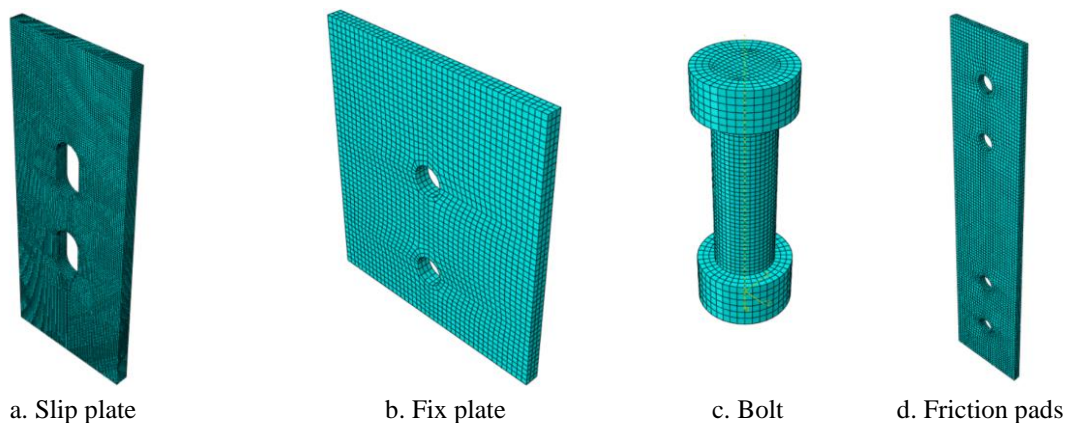
Fig. 4.3. Parts of the FEM model.

4.2.2 Contact conditions and bolt preloading

4.2.2.1 Contact conditions

Normal and tangential contact interactions between all the parts in contact were introduced. Normal contact conditions were introduced with the "*hard-contact*" property allowing for

separation after contact, while for the tangential behaviour, a penalty formulation was assumed with different friction coefficients, depending on the contact surfaces. For the parts that were not in contact with the friction shims a friction coefficient equal to 0.2 was assumed. For the remaining parts, different friction coefficients were assumed, according to the experimental tests (see Table 3.10).

Furthermore, during the experimental campaign, a degradation of the friction resistance was visible during the slip of the damper as well as an increase of this force during the impact tests. Both phenomena were taken into account in the numerical simulations. The degradation of the friction resistance during the slip was modelled as proposed by Uzair [89], degrading the preload force in the bolts according to the degradation factors F_k/F_{slip} found in the experimental tests (Table 3.10). The increase of the initial friction resistance under impact loading was modelled adopting a slip-rate dependence model available with the penalty formulation, taking into account the DF_{frict} reported in Table 3.10.

4.2.2.2   Bolt preloading method

Bolt preloading was introduced with the temperature gradient approach, i.e. by applying a negative temperature to the bolt shank. In this way, a normal force is induced, introducing deformation in the bolt shank. In order to make the bolt shank sensitive to temperature changes, the orthotropic expansion coefficient α for steel was defined in the material properties only in the direction parallel to the bolt shank. The negative temperature was defined in order to produce the same preload as in the experiments (Table 3.1). The change in temperature ΔT can be calculated using simple thermodynamics formulation (Eq.4.1 and 4.2).

$$\Delta T = \frac{\Delta_l}{\alpha \cdot l_{shank}}$$
(4.1)

$$\Delta_l = \delta_{joint} \cdot F_{s,Rd}$$
(4.2)

Where $F_{s.Rd}$ is the bolt preload force, l_{shank} is the length of the bolt shank, α is the expansion coefficient and δ_{joint} is the elastic resilience of joint.

The elastic resilience of the joint, δ_{joint}, has been obtained using the VDI guideline formulation [90], which considered that the elastic resilience of the joint is given by the elastic

resilience of the preloaded bolt δ_{bolt} and the elastic resilience of the clamping package (steel shells + cover-plate + nuts) δ_{cp}

4.2.3 Material modelling

The behaviour of the materials composing of the plates and bolt was introduced in the model using the Von Mises criterion plasticity for isotropic materials. For the plates, the stress-strain curves given by the coupon tests were used, while for the bolts, since no coupon tests were available, it was used the formulation of D'Aniello *et al.* [91] to characterize the tensile behaviour of bolt M20 10.9 (Fig. 4.4). Furthermore, since in the model the nominal diameter of the bolt was used, the stresses were reduced to take into account the reduction in strength coming from the threads.

The stress-strain relationships obtained in the experiments are known as engineering stress $\sigma_{eng.}$ and strains ε_{eng}. In order to implement the stress-strain curves of the materials in the software, they were transformed in true stress σ_{true} – true plastic strain curves ε_{pl}, based on equations 4.3 to 4.5. Additionally, damage was included in both slip plate and the bolt connecting the "slip part" of the damper, using the damage ductile model available on ABAQUS as well as a rate dependence model in impact simulations.

$$\sigma_{true} = \sigma_{eng}(1+\varepsilon_{eng}) \tag{4.3}$$

$$\varepsilon_{true} = ln(1+\varepsilon_{eng}) \tag{4.4}$$

$$\varepsilon_{pl} = \varepsilon_{true} - \sigma_{true}/E_{true} \tag{4.5}$$

a. Plates   b. Bolt
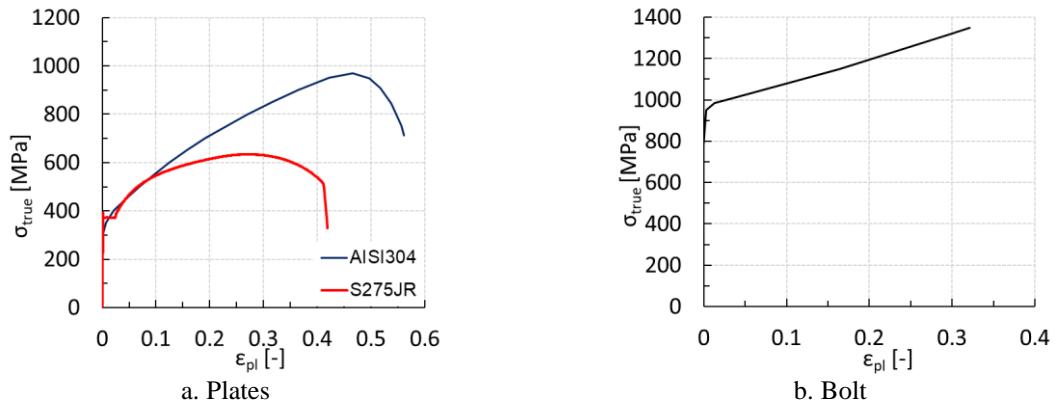
Fig. 4.4. Material laws

4.2.3.1 Damage modelling

The damage ductile model accounts for damage initiation, softening, crack initiation and progression, as shown in Fig. 4.5. The point $D = 0$ corresponds to the damage initiation point, the dashed curve represents the undamaged material response and the continuous line after point $D = 0$ represents the material softening. Therefore, to a correct definition of the material damage, the definition of the undamaged material response curve, damage initiation and damage evolutions laws are required. Damage initiation (D = 0 in Fig. 4.5) begins when the material achieves the plastic equivalent strain at the onset of damage $\bar{\varepsilon}_0^{pl}$. In the adopted damage model, this strain is dependent of triaxiality stresses η and of the strain rate. The triaxiality stresses are given by the ratio between the hydrostatic stress p and the Mises equivalent stress q, Eq.(4.6).

$$\eta = \frac{-p}{q} \tag{4.6}$$
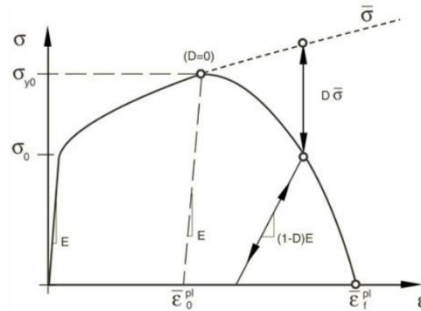
Fig. 4.5. Damage model in Abaqus

The definition of the relationship between the equivalent plastic strain –triaxiality stress was assessed following the work of Pavlovic [92], who developed a procedure to assess the damage parameters of different steel grades, based on experimental and theoretical findings of some others authors: Rice and Tracy [93] and Trattning [94]. Starting from the equation developed by Trattning [94] (Eq.4.7), which relates the equivalent plastic fracture strain $\bar{\varepsilon}_f^{pl}$ with the triaxiality stresses and assuming that the uniaxial fracture strain ε_f^{pl} is given by the same expression with $\eta = 1/3$ (uniaxial tension) for uniaxial strain state, the ratio between $\bar{\varepsilon}_f^{pl} \big/ \varepsilon_f^{pl}$ is obtained from Eq.(4.8).

Finally, assuming that the ratio of equivalent and uniaxial strain at fracture and at the onset of damage are the same, the relationship between the triaxiality stress and the equivalent plastic strain at the onset of damage $\bar{\varepsilon}_0^{pl}$ can be obtained by Eq. (4.9), where ε_n^{pl} is the plastic uniaxial strain at the onset of damage and β a parameter that translates the evolution of the stress-state with void growth. In his work, Pavlovic [92] assumed the value of β obtained by Rice and Tracy [93] ($\beta = 1.5$). However, others authors found different values for this coefficient, as Trattning [94] who assumed a value of β equal to 1.88 for austenitic steels or Chae and Koss [95] who admitted a value of β equal to 2.5 for high strength steel HSLA-100. More recently, Jakse and Moze [96] numerically assessed the evolution of the fracture strain with the triaxiality stresses for bolt bearing, obtaining a curve with the form of Eq.4.7, with a value of α and β equal to 1.16 and 1.89 respectively

$$\bar{\varepsilon}_f^{pl} = \alpha \cdot e^{-\beta \cdot \eta} \tag{4.7}$$

$$\bar{\varepsilon}_f^{pl} / \varepsilon_f^{pl} = e^{-\beta \cdot (\eta - 1/3)} \tag{4.8}$$

$$\bar{\varepsilon}_0^{pl}(\eta) = \varepsilon_n^{pl} \cdot e^{-\beta(\eta - 1/3)} \tag{4.9}$$

The work of Pavlović [92] was also used to define the undamaged material plasticity curve after the onset of the damage and the damage evolution. The former can be obtained by the Eq. (4.10), where $\sigma_{n,eng}$ is the engineering stress at the onset of the damage. The damage at failure is obtained calculating the equivalent displacement at failure $\bar{u}_f^{pl}$, which is obtained multiplying the difference between the plastic equivalent strain at failure ε_f^{pl} and the plastic equivalent strain at the onset of damage ε_n^{pl} by the characteristic length of the element L_E (Eq.4.10). The evolution of the damage up to $\bar{u}_f^{pl}$ can be linear (Eq.4.11) or tabular (Eq.4.12).

$$\sigma_{true,und} = \sigma_{n,eng.} \cdot \left(1 + \varepsilon_{eng.}\right) \tag{4.10}$$

$$\bar{u}_f^{pl} = (\varepsilon_f^{pl} - \varepsilon_n^{pl}) \cdot L_E \tag{4.11}$$

$$\bar{u}_i^{pl} = \bar{u}_f^{pl} \cdot \left(\frac{\varepsilon_i^{pl} - \varepsilon_n^{pl}}{\varepsilon_f^{pl} - \varepsilon_n^{pl}}\right) \tag{4.12}$$

For the slip plate, the damage parameters were calibrated from FEM simulations of the coupon tensile tests described in Chapter 2. In order to define the damage evolution law, the equivalent plastic strain at the onset of damage was considered equal to 47% and a value for β equal to 1.88 was considered according to the work of Trattning [94] for austenitic steel, obtaining the plastic strain- triaxiality stress curve given in Fig. 4.6a. The damage evolution law was considered tabular following the Eq.4.12 (Fig. 4.6b). Since the displacement at failure is dependent on the mesh size, the same size used to model the slip plate was used ($L = 1.5$ mm). Fig. 4.7 compares the FEM true-stress – true plastic strain curve with the experimental curve, showing that the introduced damage parameters can predict with high accuracy the tensile behaviour observed experimentally. In addition, Fig. 4.7 shows the necking zone of the coupon in the FEM model and in the experimental test, where it is possible to conclude that the FEM model gives the exact same deformation as observed in the experimental test.

With reference to the bolts, since there were no coupon tests available, the plastic strain at the onset of damage was considered according to the suggestion of literature and by comparing the deformation between the experiments and numerical models. For the damage initiation, the Eq.4.9 was used with a β equal to 1.5 as in [92] and an equivalent plastic strain at the onset of damage equal to 0.1. The displacement at failure was considered linear and equal to 0.1 mm.

| a. Strain vs Triaxiality stress | b. Damage evolution |
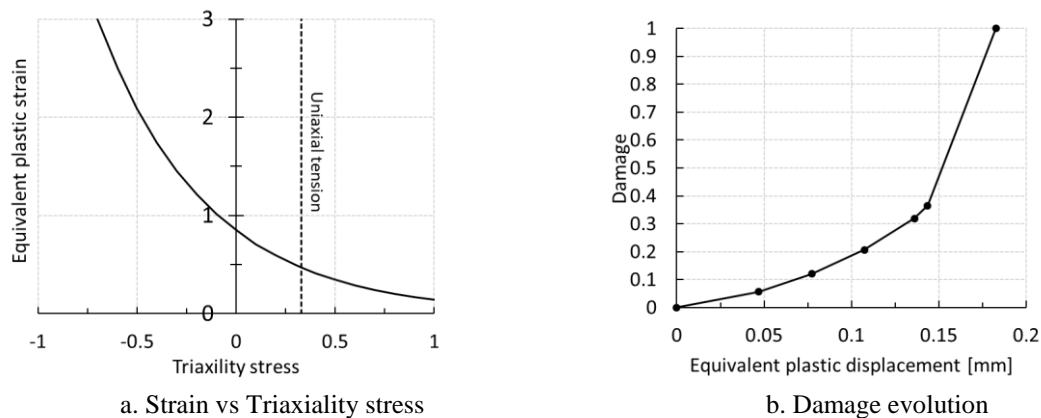
Fig. 4.6. Damage parameters for the slip plate
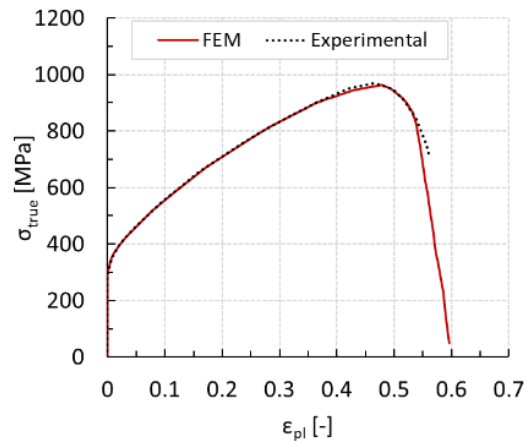
Fig. 4.7. True Stress- true plastic strain curves: Experimental vs fem model
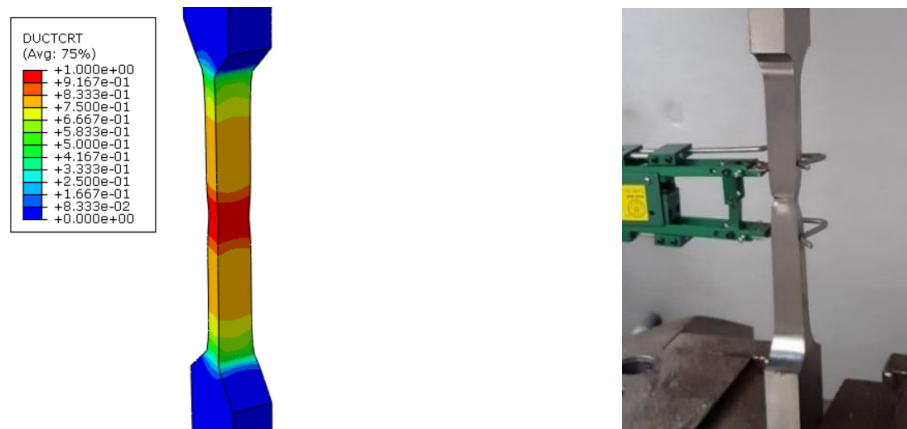
Fig. 4.8. Necking zone at failure: fem mode vs Experimental

4.2.3.2 Rate dependence

The experimental campaign described in the previous section of this work showed that the behaviour of the friction damper is influenced by the strain rates. With reference to the ultimate resistance, the experimental results showed an increase in the resistance when higher strain rates are considered. Besides, the experimental tests also indicated a decrease of the ductility capacity of the damper under high strain rates. In this way, for the simulation of the impact tests, the increase of resistance and the decrease of ductility had to be implemented. The former was implemented with the Johnson-Cook (JC) dependence rate model. This model is described by the Eq.(2.16) reported in section 2.3 and it provides an enhancement of the material stresses by the coefficient *DIF*, requiring the definition of both parameter *C* and the reference strain rate $\dot{\varepsilon}_0$.

With reference to the changes of ductility, they were implemented by changing the ultimate strain in the damage parameters previously described, monitoring the strain and corresponding strain rate and triaxiality stress to which the deformation observed in the experiments was achieved.

4.2.4 Calibration of the numerical model

The validation of the numerical model describing the response of the friction damper is based on the experimental results of Chapter 3. It was chosen to perform this validation against the tests performed with the coating material M1 ("soft material" Tin described in section 2.3.1).

4.2.4.1 Quasi-static response

Fig. 4.9 compares the numerical (Tx-M1-St-Y_FEM) with the experimental response (Tx-M1-St-Y_exp.). For both groups of tests, the numerical model was able to predict satisfactorily all the phases of the response, as shown in Fig. 4.10. As observed in the experimental tests, the behaviour is divided into several phases. At first, no horizontal movement is observed until the friction resistance of the slip part is achieved (Fig. 4.10a). After, there is the slip of the slotted plate up to the end stroke (Fig. 4.10b). The last phase is when the system bolt/plate is in bearing and shear. In this part, the model is also able to predict the slip of the fixed part (2nd slip), as observed in the experiments (Fig. 4.10c).

The initial slippage and the following degradation are predicted with high accuracy. After the slippage, the models predict correctly the ultimate deformation and resistance of the specimen with an error range lower than 10%. With reference to the initial stiffness, in the quasi-static simulations of Group A (Fig. 4.9a), the numerical model after the complete slippage presents a significant higher initial stiffness when compared to the experimental, which is probably due to the bolt modelling which does not take into account the contribution of the threads to the stiffness. On the other hand, the initial quasi-static stiffness in the simulation of the Group C (Fig. 4.9b) is close to the one found in the experiments since, in this case, the behaviour is governed essentially by the slip plate. Concerning the quasi-static design and ultimate resistances, the results show ratios FEM/exp ranging from 0.94 to 1.01, while for the ductility capacity this ratio is equal to 0.94 and 0.92 for Group A and C, respectively.

Finally, the equivalent plastic strain pattern (PEEQ) and activation of the ductile damage criteria (DUCT) is shown in Fig. 4.11. It is visible that, for group A, the plastic pattern is

developed mainly in the bolt, while the plastic strains at the slip plate are not significant. At a load increment before arriving to the maximum strain according to the ductile criteria (DUCT =1), the bolt loses its capacity to sustain additional loads. After this point, the load decreases and the elements at the shear deformation planes starts to be eliminated. Furthermore, from the deformation, it is also clear the development of shear deformation at the planes where the slip plate is in contact with the bolt, as in the experiments. In the simulation of group C, the numerical model shows the different failure mode observed in the experiments, i.e. excessive bearing of the slip plate. Furthermore, it also shows the development of plastic strain at the bolt, which was also observed in the experiments. Concerning the plate, both bearing deformation and necking are visible. However, the complete failure of the steel between holes is not visible because the simulation was stopped when the force started to drop.

| a. T8-M1-st-30 | b. T9-M1-st-30 |
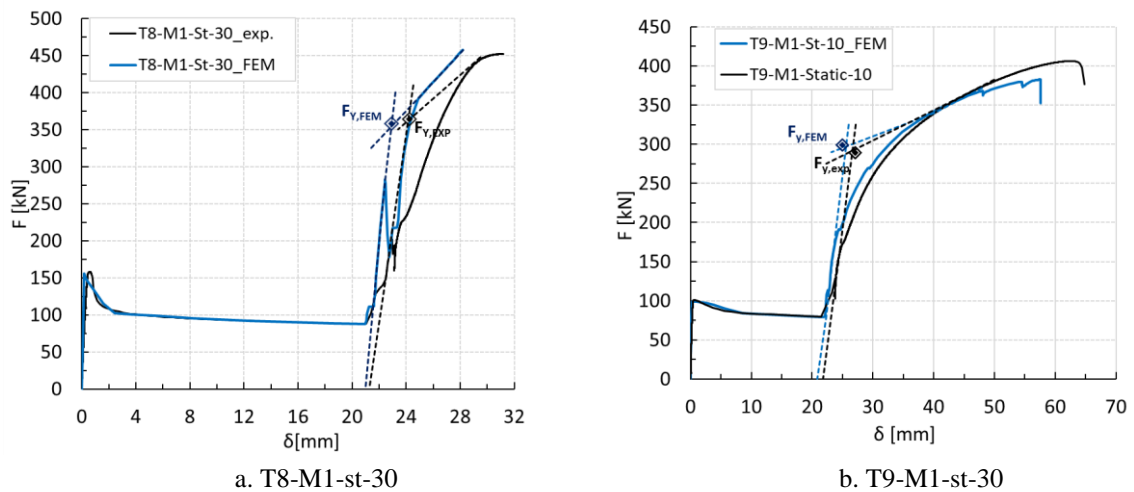
Fig. 4.9. Calibration of the FEM at quasi-static loads

| a. Initial (no movement) | b. Slip of the slotted plate |

c. Behaviour after slip – Left: movement of the fix part (2nd slip); right: deformation of the slip part.
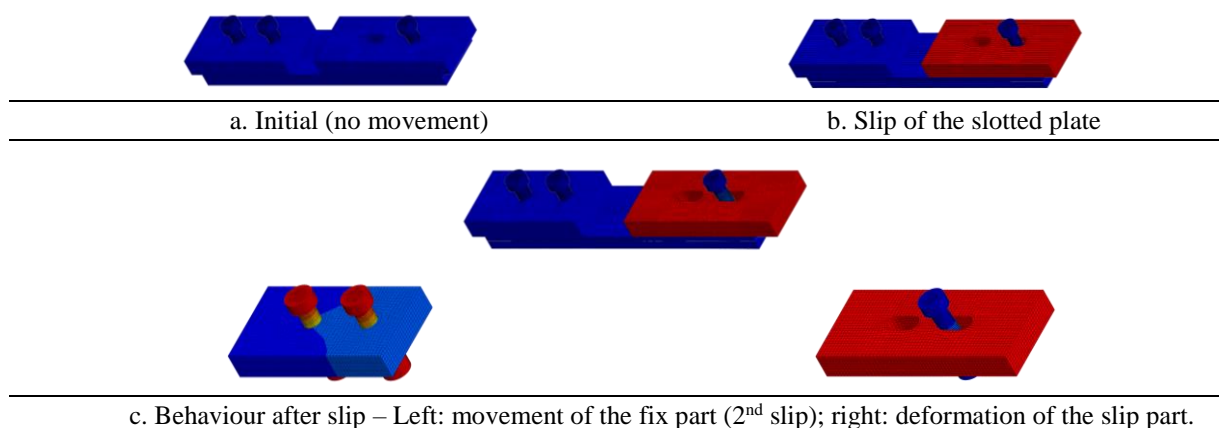
Fig. 4.10. Different phases of the behaviour of the friction damper

T8-M1-St-30 F= 458 kN; δ=28.2 mm	T9-M1-St-10 F= 482.5 kN; δ=57.4 mm
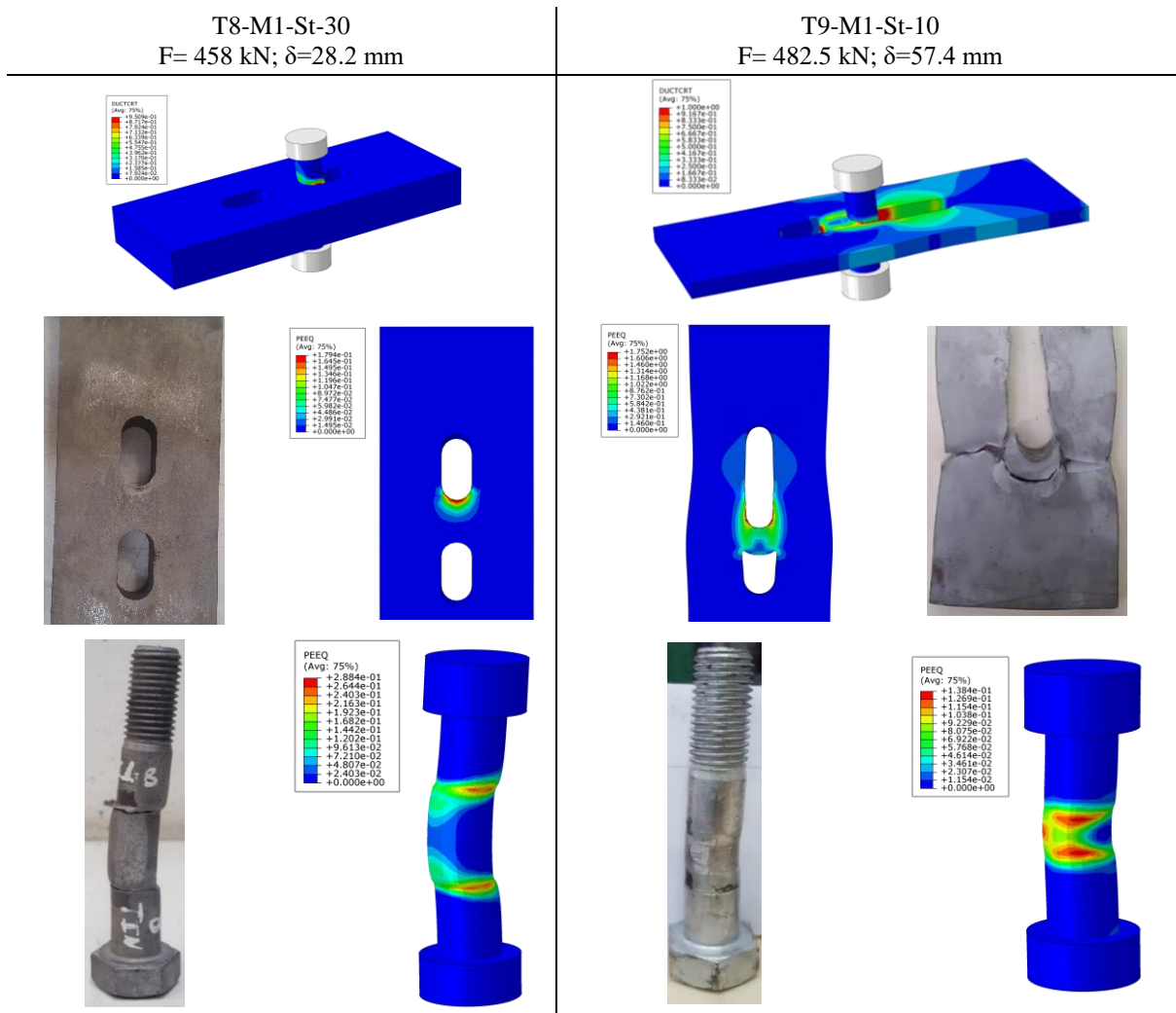
Fig. 4.11. Deformation (U) and plastic strain pattern (PEEQ) at the ultimate load – Group A

4.2.4.2 Impact response

Fig. 4.12 compares the numerical impact simulation (Tx-M1-FI-Y_FEM) with the experimental responses (Tx-M1-FI/SI-Y_exp.). For the full impact of group A (T3-M1-FI-30) the displacement time curve was directly applied. In the case of group C, due to the lack of a full impact test, the maximum displacement found for the quasi-static test was applied linearly considering a total time of 0.06 s in order to have velocity rate around 1 m/s (average velocities of an impact test).

Concerning the friction resistance and slip degradation, the implemented friction model allows prediction of the increase of the initial friction coefficient under impact loads and the degradation of friction resistance observed experimentally.

With respect to the ultimate capacity of the model, it is visible that, by implementing the rate dependence model for the strength and damage of the material described in section 4.2.3, an increase of the elastic stiffness and resistance is observed when compared to the quasi-static simulation, while the ductility at the ultimate load decreases. More specifically, it shows an increase of the stiffness, elastic resistance and ultimate resistance equal to 1.12, 1.10 and 1.06 for Group A and 1.4, 1.23 and 1.1 for group C, respectively. Furthermore, a reduction of the deformation after slip δ_u is observed in both simulations, being this reduction equal to 0.72 and 0.5 for Group A and C, respectively. These values are of the same range as the experimental values.

Finally, Fig. 4.13 shows the FEM and experimental deformation at the end of the tests. For group A, the deformation in shear at the zone of contact of the bolt with the slip plate is clearly visible (Fig. 4.13a), while in Group C, the bearing deformation of the hole as in the experiments is observed.

a. T8-M1-st-30   b. T5-M1-SI-30
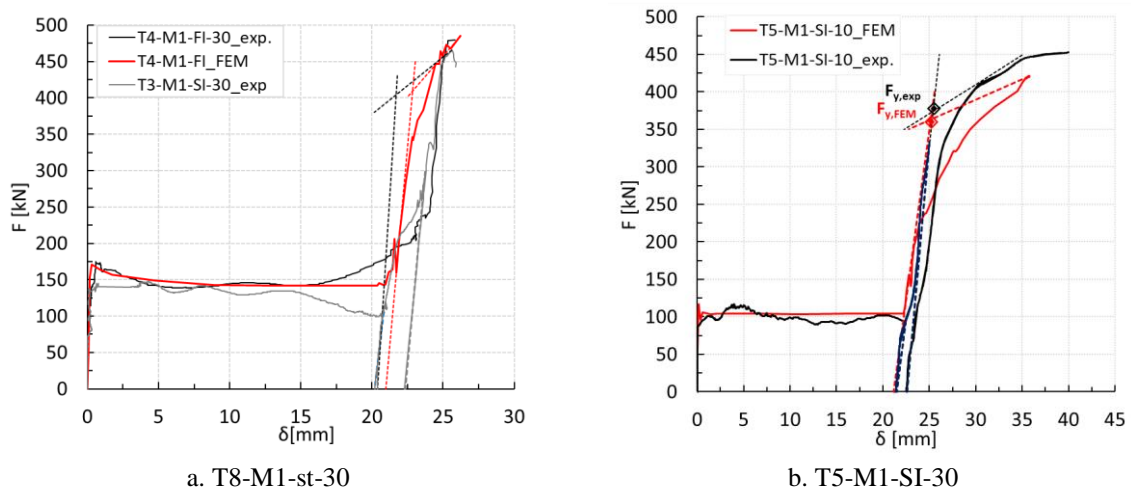
Fig. 4.12. Calibration of the FEM at impact loading

T4-M1-FI-30
F= 485kN; δ=26.2 mm

T5-M1-SI-10
F= 421kN; δ=36 mm
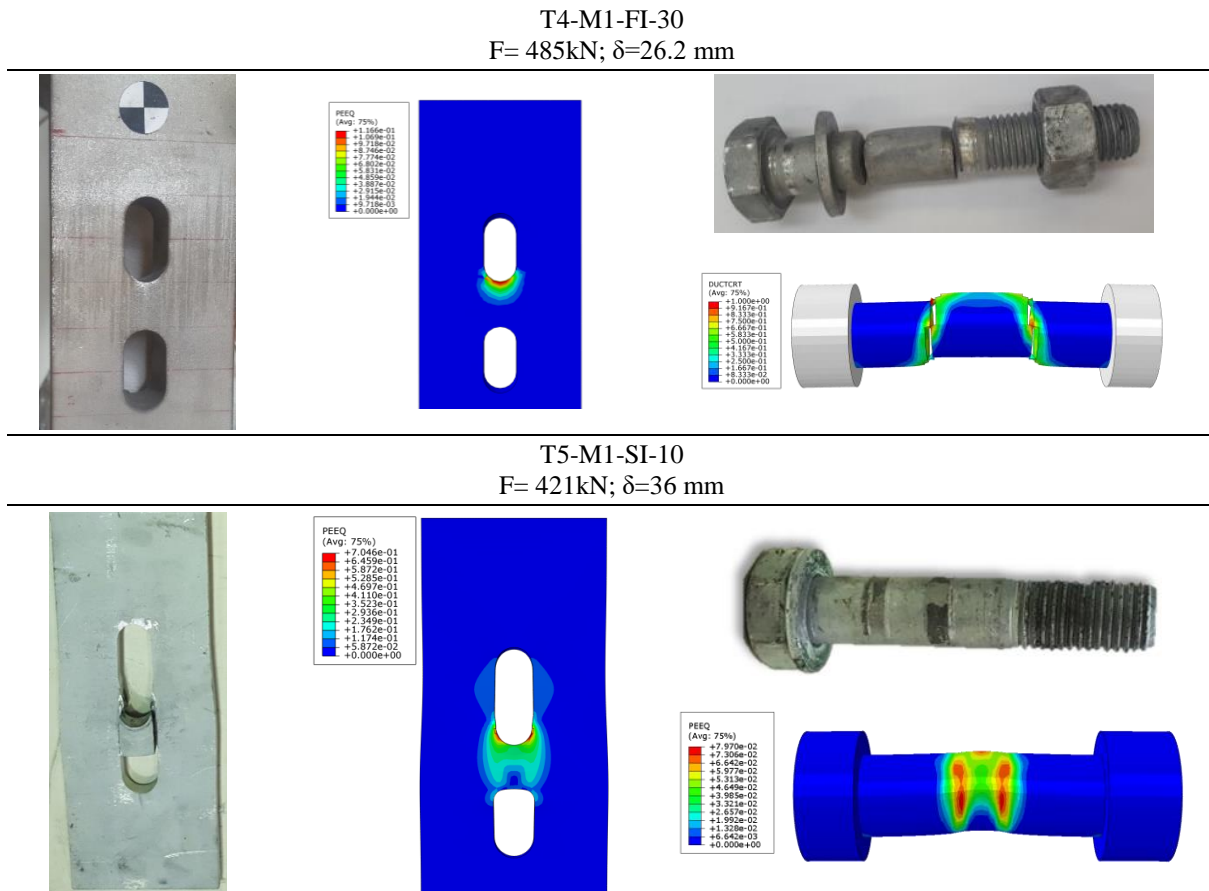
Fig. 4.13. Ductility criteria (DUCT) and plastic strain pattern (PEEQ) at failure – Impact test

4.2.5 Parametric studies

After the validation of the model, parametric studies were carried out in order to check the influence of some parameters on the resistance, failure mode and ductility of the friction damper. Two parameters were chosen for this study, namely: *i*) variation of the internal plate thickness (30 mm, 15 mm, 10 mm and 8 mm) and ii) velocity of the test - 100 mm/s, 600 mm/s and 1000 mm/s.

The same static friction coefficient was implemented in all simulations, corresponding to the minimum average value of the kinematic friction coefficient μ_k calculated from Eq. (4.13). The values of μ_{st}, DF_{frict} and F_k/F_{slip} were taken from Table 3.10 for the coating M1. The bolt preload force was kept constant through the analyses and the experimental preload force was used, i.e. $F_P = 122.5$ kN.

$$\mu_k = \mu_{st} \cdot DF_{fric} \cdot \frac{F_k}{F_{slip}} = \begin{cases} \mu_{k,M1} = 0.42 - static \\ \mu_{k,M1} = 0.44 - impact \end{cases} \tag{4.13}$$

The results from this analysis are reported in Fig. 4.15 and Fig. 4.17 for all the considered geometries and velocities. Fig. 4.15 shows the contribution of the different components to the overall deformation at each deformation rate. The overall deformation of the damper is considered as the sum of the elongation of the internal slotted plate parallel to the application of the load (point DF in Fig. 4.14) and the shear deformation of the bolt (point *AB* in Fig. 4.14).
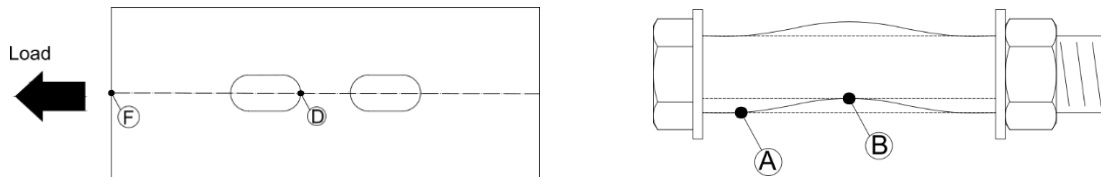
Fig. 4.14. Measurement points of FEM models

First, from the results under quasi-static loading (column *qs* in Fig. 4.15) it is possible to see the different failures modes of the friction damper when different thickness of the plates are used. For the highest plate' thickness (t = 30 mm), the deformation is essentially given by the ultimate deformation of the bolt in shear (see Fig. 4.16 and Fig. 4.15). On contrary, for lowest plate' thickness (t = 8mm), the contribution of the bolt in shear for the deformation of the specimen is minimum (see Fig. 4.16 and Fig. 4.15). For the thickness in between, i.e. t = 15 mm and t = 10 mm, it is visible the transition of a bolt in shear failure modes to a failure mode given by bearing of the plate.

In addition, Fig. 4.15 also shows the increase of the contribution of the most brittle component of the damper, i.e. the bolt in shear, when the specimens are subjected to higher velocities, especially in the specimens where both components contributed significantly for the deformation under quasi-static loading, such as the specimens with thickness equal to 15 and 10 mm. This fact was also visualized by Ribeiro *et al.* [10] and it was explained by the different sensitivity of the materials composing the components. In fact, the plate material is significantly more sensitive to strain rates than the bolt material, which means that when the strain rates at this element increase due to the increase of velocity of the test (Fig. 4.17a), it will show a more pronounced increase of strength than the material composing the bolt. In particular, this is translated by a greater increase of the resistance in the specimens where the failure mode is by the excessive elongation of the plate (specimens with 10 and 8 mm thickness) compared to those failing by bolt in shear, as reported in Fig. 4.17c and d. On the other hand, this sudden increase of strength is also associated with a significant decrease in the ductility, i.e. the material

becomes more brittle. For this reason, for higher velocities, the contribution of this component will significantly decrease, while in the bolt, the decrease of ductility is much lower (Fig. 4.17b), contributing more for the whole deformability of the specimen, as observed in Fig. 4.15. At the limit, it can change completely the failure mode observed under quasi-static loads.

To conclude, the results shown in this analysis highlighted the importance of considering the strain rate effects on the different material composing a connection since it can change drastically their resistance and ductility.
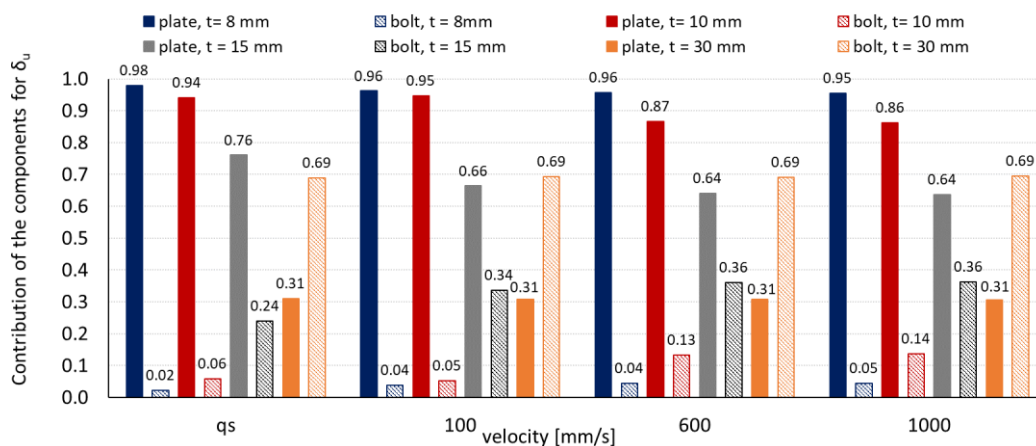
Fig. 4.15. Contribution of the components for the deformation with the velocity of the test

a. t = 30 mm   b. t= 15 mm   c. t= 10 mm   d. t= 8mm
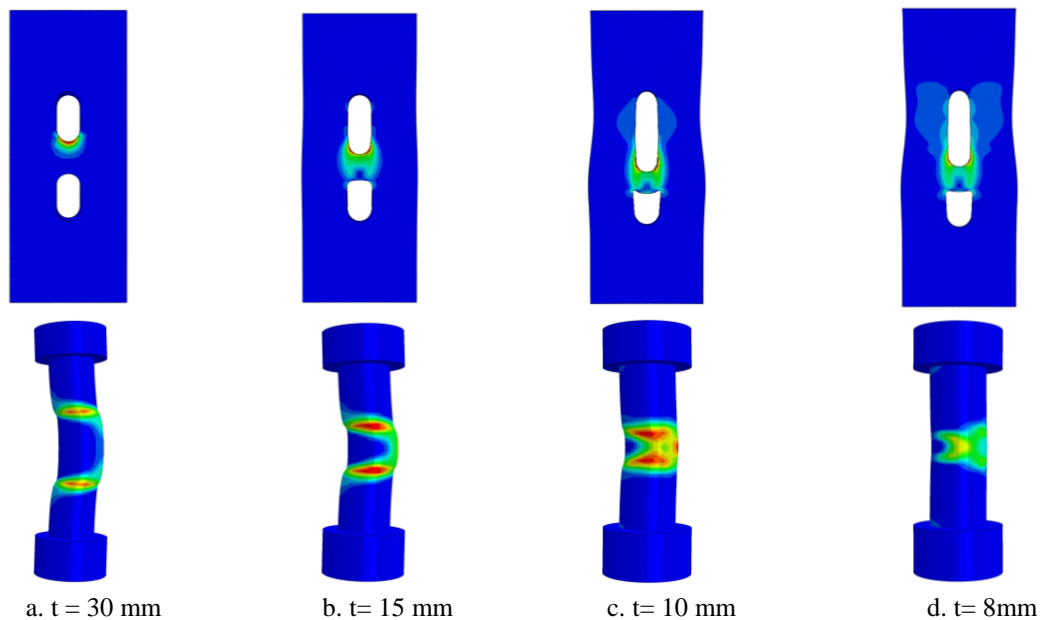
Fig. 4.16. Failure modes – Influence of plate thickness (PEEQ)

a. Strain rate vs velocity

b. Dynamic factors for the ductility capacity, DF_δ

c. Dynamic factor for elastic resistance, DF_y

d. Dynamic factor for ultimate resistance, DF_U
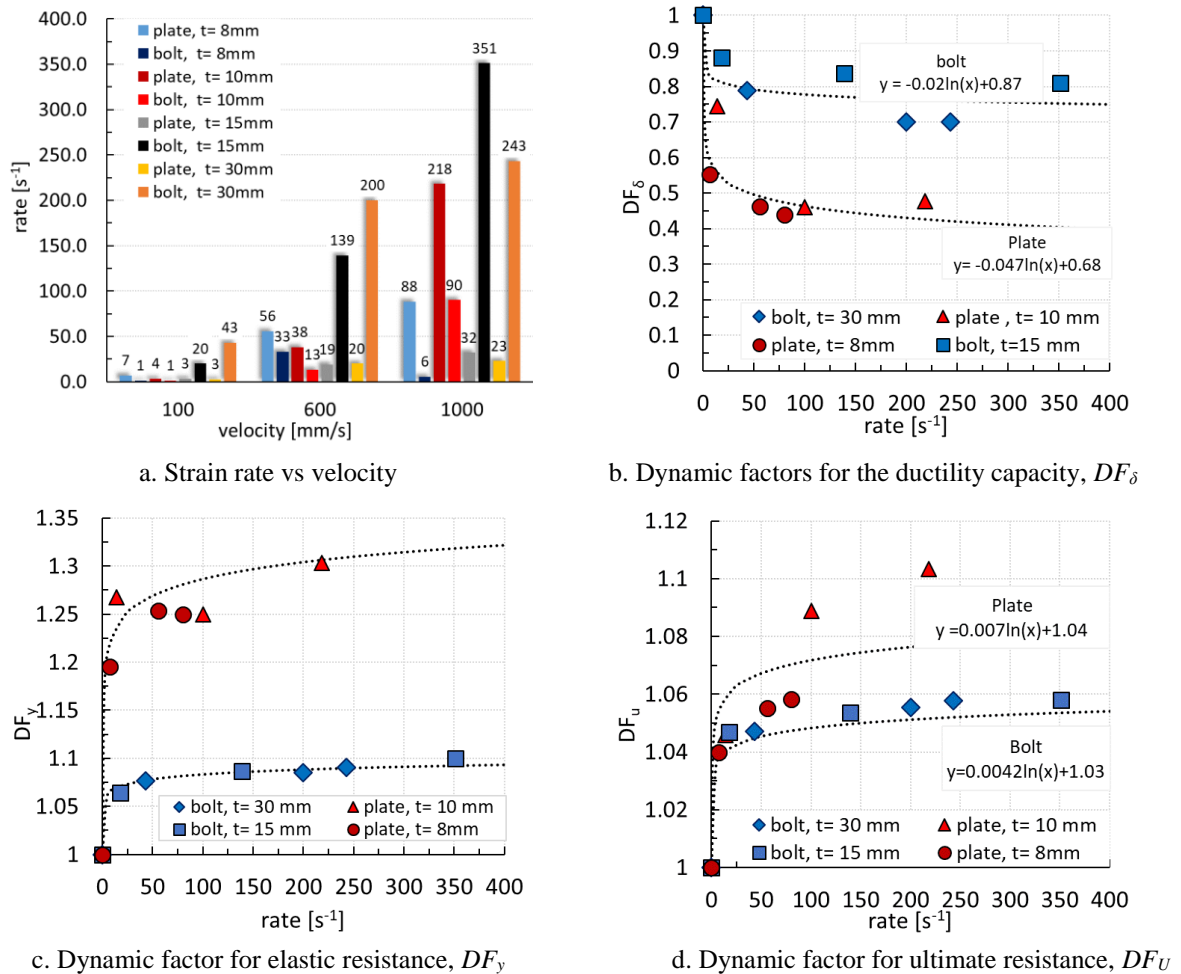
Fig. 4.17. Influence of velocity on the behaviour of the friction damper

4.3 Analytical approach

4.3.1 Previous researches

A connection classified as a bolted lap-shear connection is comprises two different zones: the **bolt area**, where bearing and shear forces in the bolt shank take place and by the holes regions and the plate areas between the holes, where tension forces develop. Therefore, to propose an accurate analytical model able to describe the behaviour of lap shear connection, the force-displacement behaviour of three components have to be properly known, namely: the **bolt in shear**, the **plate/bolt in bearing** and **the plate in tension**.

In the Eurocode 3 Part 1-8 [5] framework, connections subjected mainly to shear loading are considered bearing type connections (Category A) and the three components mentioned above

should be considered in the design. Furthermore, the code considers that these components work in series, thus, the failure mode is the one associated with the weakest component. In this way, the ultimate resistance of a shear lap connection will be the resistance of its weakest component, while its deformation capacity will be the sum of the elastic and plastic deformation of the different components. Table 4.1 presents the formulation suggested by Eurocode 3 Part 1-8 to assess the design resistance and elastic stiffness of the relevant components, for shear connections with one bolt per row (the code considers 2 bolts per row in its formulation).

Table 4.1. Formulation of Eurocode 3 part 1-8 for shear lap joint components

Component	Formulation	
	Elastic Resistance	Elastic Stiffness, S_y [kN/mm]
9 Plate in tension/compression (T)	$F_{y,T} = 0.9 \cdot f_u \cdot A_{net}$	$S_{y,T} = E \cdot A / p$
11 Bolt in shear (s)	$F_{y,s} = n_s \cdot \alpha_v \cdot f_{ub} \cdot A$	$S_{e,s} = 8 \cdot d^2 \cdot n_b \cdot f_{ub} / d_{M16}$
12 Plate in bearing (b)	$F_{y,b} = k_1 \cdot \alpha_b \cdot f_u \cdot d \cdot t$	$S_{e,b} = 12 \cdot n_b \cdot k_b \cdot k_t \cdot d \cdot f_u$

In addition, when there is more than one bolt zone, two additional recommendations are given. The first is related to the resistance of connections with a limited number of bolt zones along the length, while the second is related to long joints:

1. "*The design resistance of a group of fasteners may be taken as the sum of the design bearing resistances of the individual fasteners, F$_{bRd}$, provided that the shear resistance, F$_{v,Rd}$, of each individual fastener is greater than or equal to the design bearing resistance F$_{b,Rd}$. Otherwise, the design resistance of a group of fasteners should be taken as the number of fasteners multiplied by the smallest design resistance of any of the individual fasteners*" (Eurocode 3 Part 1-8: 3.7 [5]);

2. "*The shear resistance should be reduced if the connection length L$_j$ exceeds 15d, using the reduction factor βj (Eq.4.14) to reduce the shear resistance F$_{v,Rd}$ of bolts*" (Eurocode 3 Part 1-8: 3.8 [5])

$$\beta_j = 1 - \frac{L_j - 15d}{200d} \tag{4.14}$$

Following the recommendations of the Eurocode, some authors have already proposed analytical spring models to simulate the capacity of lap shear connections. Wald [97], following the component method, developed an analytical method to predict the force-deformation curve of double cover bolted connections with slotted holes perpendicular to the acting force. The

model was compared with several experiments [98] and showed a satisfactory accuracy in predicting the initial stiffness, but it provided conservative values when considering the ultimate resistance and deformation capacity.

Pietropersa *et al.* [99] proposed a methodology to check the ductility required to achieve a full plastic redistribution of internal forces in shear connections with fit holes and non-preloaded bolts. Later, Henriques *et al.* [14] used the model of Pietropersa *et al.* to derive the equations to obtain the deformation capacity of the bolt zone and they extended the methodology to shear bolted connections with geometrical imperfections. The bolt zone was decomposed into two components, as showed in Fig. 4.18: bolt in shear S_b and plate in bearing $S_{p,b}$. A tri-linear law was used to characterize each component and five parameters were determined, namely: elastic stiffness, elastic resistance, ultimate resistance, post-elastic stiffness and ultimate deformation.
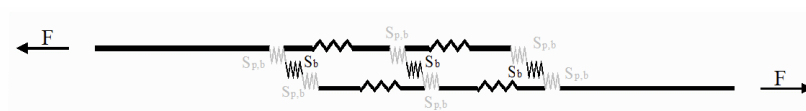
Fig. 4.18. Spring model of the bolt zone [14]

The elastic parameters were obtained through the formulation suggested by Eurocode 3 [5], while the plastic parameters (ultimate resistance and ductility capacity) were assessed considering literature recommendations. For the plate in bearing, the ultimate resistance was considered equal to 1.25 times the bearing elastic resistance [99], while, the ductility capacity was considered 1.1 times the yield deformation, based on the work of Jaspart [85]. The post-elastic stiffness was fixed equal to 0.025 times the elastic stiffness.

Several formulae to predict the ultimate resistance and deformability of the bolt in shear component were derived, depending on the bolt diameter and grade. Both ultimate resistance and deformability of the bolt were represented as a function of its yield resistance and deformability and they were calibrated based on results of experimental tests. Furthermore, the post-elastic stiffness was adjusted to the experimental force-deformation curves. For example, for high strength M20 bolts, it was assumed that the ultimate resistance is 1.44 times the elastic resistance given by the code, while the ultimate deformation is 2.9 times the yield deformation.

Also, Wald [100] assumed a deformation capacity equal to 3 times the yield deformation for this component.

The analytical model described afterwards in this section uses the model of Henriques, with some adaptations. First, a bilinear curve is used instead of a trilinear curve, since a bilinear curve is considered enough to describe the behaviour of components with brittle (bolts) and limited ductility (plate in bearing) [101,102]. For the bolt in shear, the formulae to derive the ultimate resistance and ductility were adapted to the experimental tests on the analysed friction damper (Chapter 3). For the plate in bearing, the ductility capacity was obtained from a formula proposed recently by Moze [103,104] (Eq. 4.15). He carried out an extensive investigation on the ultimate behaviour of shear lap connection failing by bearing and cross-section in tension and he proposed modifications of the Eurocode formulas concerning the bearing resistance. He also made suggestions about the ductility capacity for mild and high strength steel plates.

$$\Delta_{u.80} = \min\left(e_1 - d_0/2; p_1 - d_0/2; d\right)$$ (4.15)

Similarly to Moze, Salih *et al.* [105] also proposed some modifications of the Eurocode equations concerning the bearing resistance and tension resistance of lap shear joints with stainless steel plates. However, no recommendations concerning the deformation capacity currently exist.

4.3.2 Proposed model

The proposed analytical model follows the procedure summarized in the flowchart of Table 4.2 and it is divided into three steps:

1) **Step 1: Identification of the active components.**

Here, the components that contribute to the resistance, stiffness and ductility of the friction damper are identified. According to Eurocode 3 Part 1-8 [5], the friction damper belongs to a Category A joint [5]. Therefore, the following components are considered: *a) Friction resistance; b) Plates in tension (component 9 of EC3 Part 1.8), c) Bolts in shear (component 11 of EC3 Part 1.8), d) Plates in bearing (component 12 of EC3 Part 1.8).*

2) <u>**Step 2: Design of the individual components.**</u>

In this step, the force-deformation curve of each component is obtained. For the bolt in shear and plate in bearing component, a bilinear elastic –plastic curve with hardening is considered (Fig. 4.19a), while for the friction resistance and plate in tension, a bilinear rigid elastic-perfectly plastic curve is used instead (Fig. 4.19b). Furthermore, the influence of the loading rate on the resistance and ductility capacity of each component was also taken into account. Hence, this step is divided into two sub-steps: **(2.1) Evaluation of the strain rate** and **(2.2) Calculation of the bilinear force-deformation curve for the component** i (s for shear, b for bearing and T for tension). In Section 4.3.3 the procedure to assess the behaviour of each individual component is fully explained.

| a. Bolt in shear and plate in bearing | b. Friction resistance |
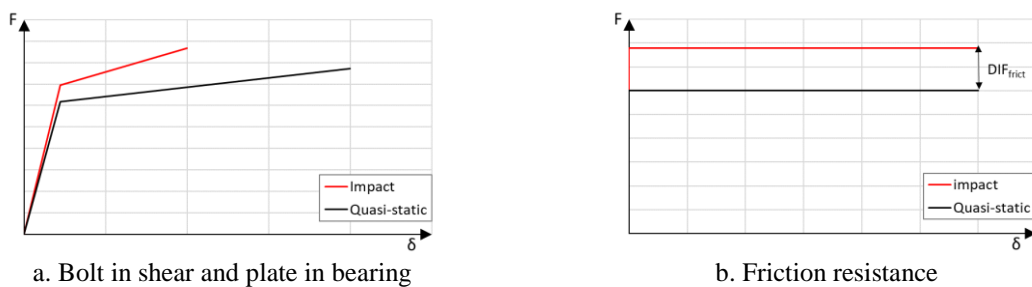
Fig. 4.19. Behaviour law for each individual component

3) <u>**Step 3: Assembly of the components.**</u>

The response of the whole damper is derived by assembling the components as exemplified by the simple mechanical model delivered in Fig. 4.20. At the end of the assembly procedure, the behaviour of the friction connection is defined by an equivalent elastic stiffness S_{eq}, an equivalent elastic resistance R_{eq} and an ultimate displacement capacity of the bolt zone δ_u.

a. Friction damper scheme
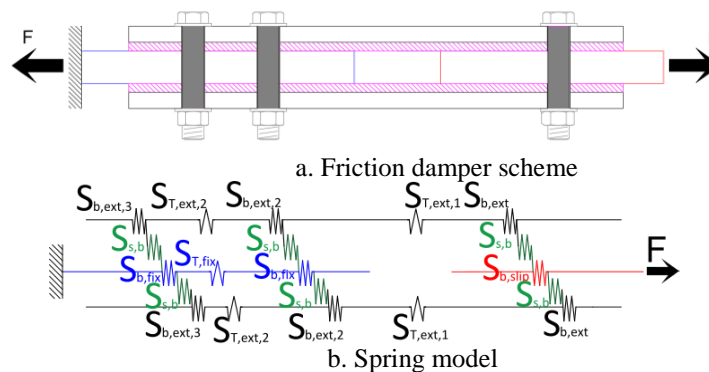
b. Spring model

Fig. 4.20. Mechanical spring model

Table 4.2. Analytical procedure - Flow chart

Step 1) Identification of the active components *i* of the several elements:
Component *i*: shear (*s*), bearing (*b*); tension (*T*), friction resistance (*frict*)
Elements: bolts (*b*), external plates (*ext*), fix plate (*fix*), slip plate (*slip)*
Bolt zone *j* =1,2..

Step 2) Individual characterization of the components *i* (section 4.3.3)		
2.1) Implementation of the strain rate effects:	2.2) Calculation of the parameters of the F-δ bilinear curve for the component *i*	
Possible approximation of the strain rate $\dot{\varepsilon}$: $\dot{\varepsilon}=V_s/\delta_u$, δu – deformation of the friction damper after slip; V_s – shear rate (mm/s)	1.Friction Resistance	2.Plate in bearing, bolt in shear and Plate in tension
Implementation of strain rate on the Resistance $f_{u,dyn}=DF_u\cdot f_{u,st}$, $DF_u=\begin{cases}1,\dot{\varepsilon}\leq\dot{\varepsilon}_0\\1+C\cdot\ln(\dot{\varepsilon}/\dot{\varepsilon}_0),\dot{\varepsilon}\leq\dot{\varepsilon}_0\end{cases}$ Implementation of strain rate on the Friction $F_{frict,dyn}=DF_{frict}\cdot F_{frict,st}$, DF_{frict} - Table 3.10 Implementation of strain rate on the ductility $\delta_{dyn}=DF_\delta\cdot\delta_{st}$, DF_δ - Fig. 4.17	-Friction Resistance, F_{frict} -Slip deformation, δ_{slip}	-Elastic stiffness, $S_{e,i}$ -Elastic Resistance, $F_{e,i}$ -Ultimate Resistance, $F_{u,i}$ -Ultimate Resistance, $\delta_{u,i}$
- $\dot{\varepsilon}_0$ - static reference strain rate (assumed equal to 0.001 s^{-1}) -C – Johnson Cook strain rate constant		

Step 3) Assembly of the components (section 4.3.4)		
A) Equivalent elastic stiffness of the bolt zone, S_{eq}	B) Equivalent elastic resistance of the bolt zone, F_{eq}	C) Deformation capacity of the friction damper, δ_{FD}
$S_{eq}=\dfrac{1}{\dfrac{1}{S_{e,s,b}n_s}+\dfrac{1}{S_{e,b,ext}n_s}+\dfrac{1}{S_{e,b,slip}}}$	$F_{eq}=\min(R_{e,s};R_{e;b})$	$\delta_{FD}=\delta_{slip}+\delta_u$
		δ_u – deformation of the bolt zone (Table 4.4)

4.3.3 Design of the individual components

1) Implementation of the strain rate effects

The effects of the strain rate are implemented in the yield and ultimate strength of the materials composing the components as well as in their ductility capacity. As explained before, the effects of the strain rates on the strength of a material are defined by the coefficient DIF. The definition of this parameter is schematized in the flowchart of Table 4.2. When the strain rates are very small, i.e. less than or equal to the conventional reference strain rate $\dot{\varepsilon}_0$, this parameter is taken as equal to 1. On the other hand, when the strain rates are higher than the

conventional reference strain rate, the value of *DF* will be higher than 1.0. In the case of the bolts and plates, this parameter is defined by the Johnson Cook law, requiring the definition of parameter *C*. Since the formulation used to obtain the resistance and elastic stiffness of the components are based on the ultimate strength of the material, it requires the definition of C_u. The value of this parameter was taken from the trend lines obtained from the parametric numerical studies for the stainless plate and bolt (Fig. 4.17d). For the external plates (carbon S275JR plates), the value 0.039 was used (Table 2.6).

With regard to the variation of ductility capacity, this parameter was changed taking into account the trend line obtained in the parametric numerical studies (Fig. 4.17b).

Finally, concerning the friction resistance, the influence of strain rate was incorporated increasing the static friction coefficient μ by the average values of the DF_{frict} given by the experimental results (Table 3.10).

2) Friction resistance

In the model, in order to simplify the analytical calculations, the friction resistance is considered equal to the kinetic friction resistance F_k and constant through the slip phase. This friction resistance can be obtained considering multiplying the initial friction resistance F_{slip} obtained from Eq. (3.12), by the degradation coefficients F_k/F_{slip}, reported in Table 3.10 of Chapter 3.

3) Bolt in shear, plate in bearing and plate in tension

For the design of the bolt in shear and plate in bearing components, a bilinear force-deformation curve was assumed (Fig. 4.19) and four parameters were defined, namely, (i) elastic stiffness $S_{y,i}$, (ii) limit of Elastic Resistance $F_{e,i}$, (iii) ultimate Resistance $F_{u,i}$ and (iv) ultimate deformation $\delta_{u,i}$.

The equations used to characterize each parameter are summarized in Table 4.3. The elastic stiffness and yield resistance were characterized according to Eurocode 3 Part 1-8 [5] formulations. The ultimate resistance of each component was defined as a function of its yield resistance by a parameter α. For the plate in bearing, this parameter was assumed equal to 1.25, according to [99]. For the bolt in shear, α was defined as the ratio between the yield resistance $F_{y,s}$ obtained from the code and the average value of the experimental ultimate resistance $F_{u,s}$ of the tests with bolt failure (group A).

The ductility capacity of the plate in bearing component was obtained from the formula proposed by Moze [104] (Eq.4.15), while for the bolt in shear, it was defined as a function of its yield deformation by a ductility index φ. This ductility index was calculated from the ratio between the yield deformation $\delta_{e,s}$ and the average value of the ultimate bolt ductility observed in the tests where bolt failure was observed (δ_u in Table 3.9). A coefficient equal to 3.2, very similar to the coefficients proposed by Henriques [14] and Wald [100].

Finally, for the plate in tension, only the elastic parameters were defined using the formulation of the Eurocode since it was considered that this component remains elastic (Table 4.3).

Table 4.3. Elastic and plastic parameters considered in the analytical design

	Bolt in shear	Plate in bearing	Plate in tension
	Quasi-static behaviour		
$F_{y,i}$ [kN]	$F_{y,s} = n_s \cdot \alpha_v \cdot f_{ub} \cdot A$	$F_{y,b} = k_1 \cdot \alpha_b \cdot f_u \cdot d \cdot t$	$F_{y,T} = 0.9 \cdot f_u \cdot A_{net}$
$S_{ini,i}$ [kN/mm]	$S_{ini,s} = 8 \cdot d^2 \cdot f_{ub} / d_{M16}$	$S_{ini,b} = 12 \cdot k_b \cdot k_t \cdot d \cdot f_u$	$S_{ini,T} = E \cdot A / p$
δ_e [mm]	$\delta_e = F_y / S_{ini}$		
$F_{u,i} = \alpha_i F_{y,i}$ [kN]	$\alpha_b = 1.2$	$\alpha_b = 1.25$	-
δ_u [mm]	$\delta_{u,s} = \varphi \delta_{y,s} = 3\,\delta_{y,s}$	$\Delta_{u,80} = \min(e_1 - d_0/2; p_1 - d_0/2; d)$	-
	Impact		
DF_u	$DIF_{u,s} = 1 + 0.0047 \cdot \ln(\dot{\varepsilon}/\dot{\varepsilon}_0)$	$DIF_{u,b,AISI304} = 1 + 0.007 \cdot \ln(\dot{\varepsilon}/\dot{\varepsilon}_0)$ $DIF_{u,b,S275JR} = 1 + 0.039 \cdot \ln(\dot{\varepsilon}/\dot{\varepsilon}_0)$	The same as for the plate in bearing
$S_{ini,i}$ [kN/mm]	$S_{ini,imp,s} = 8 \cdot d^2 \cdot DF_{u,s} \cdot f_{ub} / d_{M16}$	$S_{ini,imp,b} = 12 \cdot k_b \cdot k_t \cdot d \cdot DF_{u,b} \cdot f_u$	$S_{ini,T} = E \cdot A / p$
$F_{y,imp,i}$ [kN]	$F_{y,imp,s} = n_s \cdot \alpha_v \cdot DF_{u,s} \cdot f_{ub} \cdot A$	$F_{y,imp,b} = k_1 \cdot \alpha_b \cdot DF_{u,b} \cdot f_u \cdot d \cdot t$	$F_{y,T} = 0.9 \cdot DF_{u,b} \cdot f_u \cdot A_{net}$
$F_{u,imp,i} = \alpha_i F_{y,imp,i}$ [kN]	$\alpha_s = 1.2$	$\alpha_b = 1.25$	-
$\delta_{u,imp} = DF_\delta\, \delta_{u,st}$ [mm]	$DF_{\delta,s} = -0.02 \ln(\dot{\varepsilon}) + 0.87$	$DF_{\delta,b} = -0.047 \cdot \ln(\dot{\varepsilon}) + 0.68$	-

4.3.4 Assembly of the different components

Elastic equivalent stiffness S_{eq} and Resistance F_{eq}

The components of the bolt zone work in series (Fig. 4.20). In this way, the elastic equivalent stiffness is equal to the reciprocal sum of individual stiffness (Eq.4.16), while the elastic equivalent resistance is the minimum resistance of the individual components (Eq.4.17).

$$S_{eq} = \frac{1}{\dfrac{1}{S_{e,s,b}n_s} + \dfrac{1}{S_{e,b,ext}n_s} + \dfrac{1}{S_{e,b,slip}}} \tag{4.16}$$

$$R_{eq} = \min(R_{e,s}; R_{e;b}) \tag{4.17}$$

Deformation capacity of the bolt zone, δ_u

The deformation of the bolt zone is obtained by summing the deformability of the equivalent bolt rows (sum in series of the deformability of bolt in shear and bolt in bearing). The deformation capacity of the equivalent bolt row was determined by assembling the deformation capacity of each component according to their resistance and deformability, based on the formulations derived by Henriques *et al.* [14].

Table 4.4 reports the generic equations to obtain the ductility capacity of the bolt zone in a double shear lap-joint type. The failure by the bolt in shear and bearing of the internal plate were considered, as well as intermediate cases where the plasticity of the "strongest" component happens. The first two terms of the equations of Table 4.4 are common to all cases and represent the elastic deformation of the equivalent component until reaching the equivalent elastic resistance F_{eq}. In the third term, the deformability of the weakest component is considered. Finally, as the resistance of the equivalent component achieves $\alpha F_{y,i}$ the elastic and/or plastic deformation of the plates/bolt after F_{eq} are taken into account.

Table 4.4. Formulations to determine the deformation capacity of the bolt zone

Case #1 – Weakest component: Plate in bearing + bolt remains elastic	
Cond	$R_{e,s,b} > \alpha_p R_{e,b,slip}$ and $R_{e,b,ext} \geq \alpha_p R_{e,b,slip}$
R_{eq}	$R_{eq} = R_{e,b,slip}$
Def.	$\delta_u = R_{eq}/S_{eq} + (\delta_{u,b,slip} - R_{eq}/S_{e,b,slip}) + ((\alpha_p - 1)R_{eq}/n_s)/S_{e,b,ext} + (\alpha_p - 1)R_{eq}/S_{e,s,b}$

Case #2 – Weakest component: Plate in bearing + Plasticity of the bolt	
Cond.	$\alpha_p R_{e,b,slip} \geq R_{e,s,b}$ and $R_{e,b,ext} \geq \alpha_p R_{e,b,slip}$
R_{eq}	$R_{eq} = R_{e,b,slip}$
Def.	$\delta_u = R_{eq}/S_{eq} + (\delta_{u,b,slip} - R_{eq}/S_{e,b,slip}) + ((\alpha_p - 1)R_{eq}/n_s)/S_{e,b,ext} + (\alpha_p - 1)R_{eq}/S_{e,s,b} + (\alpha_p R_{eq} - R_{e,s,b})/S_{st,s,b}$

Case #3 – Weakest component: Bolt in shear + Plasticity of the internal plate	
Cond	$\alpha_b R_{e,s,b} \geq R_{e,b,slip} \geq R_{e,s,b}$ and $R_{e,b,ext} \geq \alpha_p R_{e,b,slip}$
R_{eq}	$R_{eq} = R_{e,s,b}$
Def.	$\delta_u = R_{eq}/S_{eq} + (\delta_{u,s,b} - R_{eq}/S_{e,s,b}) + ((\alpha_b - 1)R_{eq}/n_s)/S_{e,b,ext} + (R_{e,b,slip} - R_{eq})/S_{e,b,slip} + (\alpha_b R_{eq} - R_{e,b,slip})/S_{st,b,slip}$

Case #4 – Weakest component: Bolt in shear + Plates remain elastic	
Cond	$R_{e,b,slip} > \alpha_b R_{e,s,b}$ and $R_{e,b,ext} \geq \alpha_p R_{e,b,slip}$
R_{eq}	$R_{eq} = R_{e,s,b}$
Def.	$\delta_u = R_{eq}/S_{eq} + (\delta_{u,s,b} - R_{eq}/S_{e,s,b}) + ((\alpha_b - 1)R_{eq}/n_s)/S_{e,b,ext} + (\alpha_b R_{eq} - R_{e,b,slip})/S_{st,b,slip}$

4.3.5 Application of the analytical approach to the analysed friction dampers

The developed analytical model is checked against the numerical simulations previously reported. In order to apply the procedure to the analysed friction dampers, small changes had to be done to account for the 2nd slip visualized in the experimental tests and FEM simulations. These modifications were made at the level of the stiffness and deformation capacity of the bolt zone. For the stiffness, to Eq.(4.16), the stiffness in bearing b and tension T of the external plates Ext corresponding to the "fix" part of the damper was added (Fig. 4.20), Eq.(4.18). In this way, the stiffness obtained from the Eq. (4.16) corresponds to the stiffness after the 1st slip and the stiffness obtained from the Eq. (4.18) to the stiffness after the 2nd slip (Slip_2 in Fig. 3.15). Concerning the deformation capacity of the bolt zone, an additional term corresponding to the elastic path between the end of the slip and the achievement of the friction resistance of the "fix" part was added, $R_{frict.slip\_2}$.

$$S_{aft.slip\_2} = \cfrac{1}{\cfrac{1}{S_{aft.slip\_1}} + \cfrac{1}{S_{e,b,ext,2}n_s} + \cfrac{1}{n_s S_{e,b,ext,3}} + \cfrac{1}{n_s S_{e,T,ext,1}} + \cfrac{1}{n_s S_{e,T,ext,2}}} \qquad (4.18)$$

Finally, to obtain the elastic resistance and stiffness of each component, the ultimate strength f_u found in the coupon tests (Fig. 3.5) was used for the plates, while for the bolt, the nominal value was assumed ($f_{ub} = 1000$ MPa).

4.3.6 Validation under quasi-static loads

Fig. 4.21 compares the analytical F-δ curves with the numerical results. In Table 4.5 the predicted analytical values of the kinetic F_k, elastic resistance F_y, ultimate resistance F_u, initial stiffness after slip S, total ductility of the friction damper δ_{max} and ductility of the bolt zone δ_u are compared with those coming from the FEM simulations, in terms of the ratio Ana/FEM. From the results, it is observed that the analytical procedure provides a rather satisfactory approximation of the F-δ curve of the friction dampers, predicting correctly the changes of failure mode observed in the FEM for the different specimen geometries.

With reference to the friction, elastic and ultimate resistance of the damper, the analytical model gives almost the same resistance as found in the experiments and FEM models, being the ratio ANA/FEM always higher than 0.9. With regards to the ductility capacity, the

procedure can predict very well the ductility capacity of friction dampers failing by bolt shearing without significant plasticity of the plate (t = 30 mm). For the geometries where the deformation of the plate plays an important role for the deformability, the model does not provide the same accuracy, being the ratio ANA/FEM between 0.84 and 0.69. However, the difference is mainly due to the use of formulations to assess the deformation capacity of the plate calibrated for mild steel, which generally has lower ductility than stainless steel.
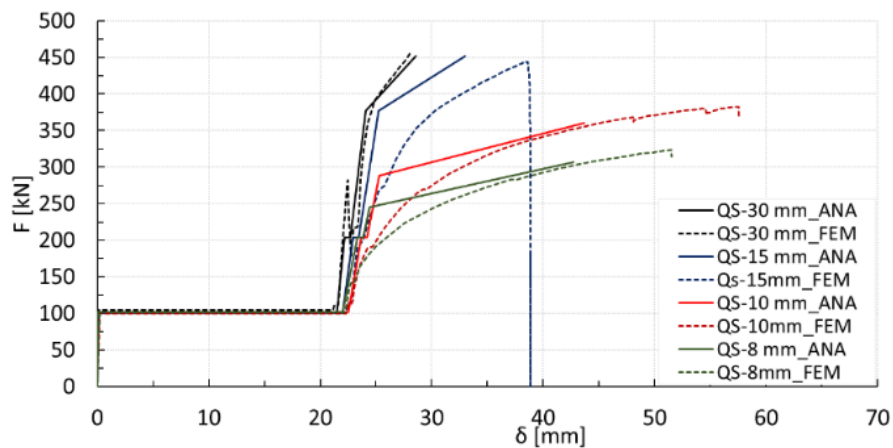
Fig. 4.21. Quasi-static force-deformation curves: Analytical vs Experimental vs Numerical

Table 4.5. Analytical procedure versus Exp. and FEM simulations: Quasi-static tests

	ID	F_k [kN]	S [kN/mm]	F_y [kN]	F_u [kN]	δ_{max} [mm]	δ_u [mm]	Failure mode
t = 30 mm	FEM	105	194	352	458	28.4	6.47	BS
	Analytical	102	145	376.8	452	28.16	6.54	BS
	Ana/FEM	**0.97**	**0.75**	**1.07**	**0.99**	**0.99**	**1.01**	**-**
t = 15 mm	FEM	100	143	357	445	37	15.2	BS + plastic plate
	Analytical	102	107	376	452	30.24	10.5	BS + plastic plate
	Ana/FEM	**1.02**	**0.75**	**1.05**	**1.02**	**0.82**	**0.69**	**-**
t = 10 mm	FEM	99.4	69	294.3	382.5	57.4	24.7	PB + plastic bolt
	Analytical	102	84	300	378.75	43.8	20.7	PB + plastic bolt
	Ana/FEM	**1.03**	**1.22**	**1.02**	**0.99**	**0.76**	**0.84**	**-**
t = 8 mm	FEM	103	50	259	323	51.5	28.14	PB + plastic bolt
	Analytical	102	68.42	242	303	42.64	20.22	PB + elastic bolt
	Ana/FEM	**0.99**	**1.37**	**0.93**	**0.94**	**0.83**	**0.72**	

4.3.7 Validation under impact loads

The parametric numeric studies considering different loading velocities were compared with the analytical model. In order to obtain the parameter DF_u and DF_δ to be applied to the

resistance of the components, the strain rates have to be calculated. The evaluation of the strain rate can be done dividing the velocity of the test by the deformation after the slip δ_u. Therefore, knowing the average maximum deformation after the slip obtained in the quasi-static simulations, the strain rates could be approximately determined.

Fig. 4.22 shows the F-δ curves for each specimen while Table 4.6 gives the ratio between the analytical and FEM in terms of the dynamic factors *DF*. As expected, for an increase of velocity, the friction damper exhibits a more brittle behaviour (an increase of the ultimate resistance and decrease of the ductility capacity). This analysis shows that the analytical model can predict the variation of stiffness, resistance and ductility when subject to different velocities rates with a maximum error of 11%.

a. t = 30 mm

b. t = 15 mm

c. t = 10 mm

d. t = 8mm
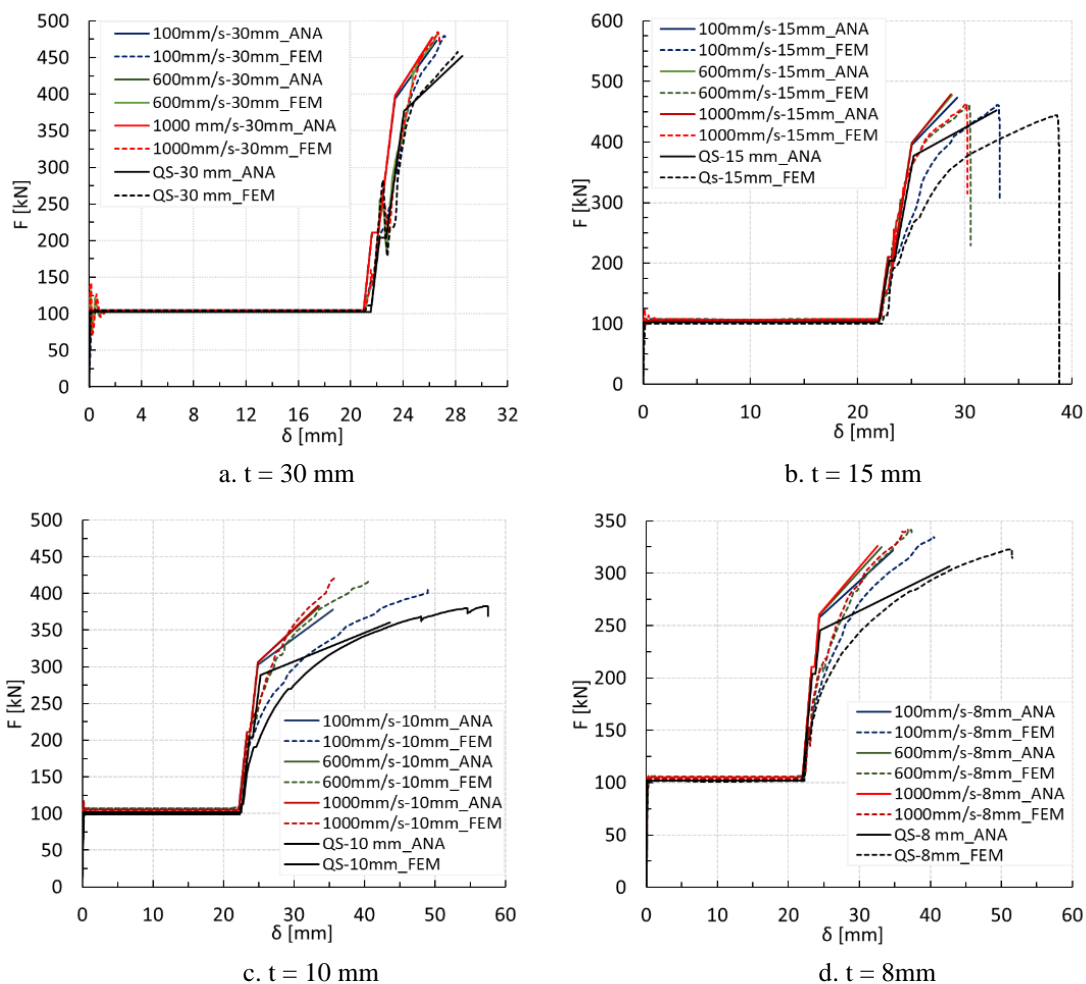
Fig. 4.22. Friction damper under different velocities – FEM vs ANA

Table 4.6. Analytical procedure versus Exp. and FEM simulations: Dynamic factors

		Velocity [mm/s]	100	600	1000
t = 30 mm	DF_S	FEM	1.047	1.072	1.077
		Ana.	1.14	1.167	1.172
		ANA/FEM	**1.09**	**1.09**	**1.09**
	DF_u	FEM	1.047	1.053	1.058
		Ana.	1.046	1.056	1.057
		ANA/FEM	**1.00**	**1.00**	**1.00**
	DF_δ	FEM	0.79	0.7	0.7
		Ana.	0.77	0.73	0.72
		ANA/FEM	**0.97**	**1.04**	**1.03**
t = 15 mm	DF_S	FEM	1.05	1.08	1.08
		Ana.	1.1	1.12	1.12
		ANA/FEM	**1.05**	**1.04**	**1.04**
	DF_u	FEM	1.046	1.053	1.06
		Ana.	1.048	1.056	1.058
		ANA/FEM	**1.00**	**1.00**	**1.00**
	DF_δ	FEM	0.63	0.55	0.53
		Ana.	0.65	0.6	0.59
		ANA/FEM	**1.03**	**1.09**	**1.11**
t= 10 mm	DF_S	FEM	1.186	1.188	1.2
		Ana.	1.081	1.10	1.10
		ANA/FEM	**0.91**	**0.93**	**0.92**
	DF_u	Num	1.059	1.1	1.11
		Ana.	1.048	1.06	1.062
		ANA/FEM	**0.99**	**0.96**	**0.96**
	DF_δ	Num	0.74	0.499	0.53
		Ana.	0.62	0.53	0.52
		ANA/FEM	**0.84**	**1.06**	**0.98**
t= 8 mm	DF_S	FEM	1.09	1.17	1.2
		Ana.	1.08	1.095	1.1
		ANA/FEM	**0.99**	**0.94**	**0.92**
	DF_u	Num	1.04	1.055	1.058
		Ana.	1.049	1.059	1.06
		ANA/FEM	**1.01**	**1.00**	**1.00**
	DF_δ	Num	0.56	0.47	0.45
		Ana.	0.61	0.52	0.5
		ANA/FEM	**1.09**	**1.11**	**1.11**

4.4 Discussion of results

Throughout this chapter, the numerical and analytical work related to the behaviour of the dissipative member of the FREEDAM connection (*friction damper*) was presented.

After calibration of the numerical models with the experimental tests, additional analyses were carried out considering two parameters, namely: i) the loading type (quasi-static or impact

loading) and ii) the thickness of the internal plate. The results showed the activation of different failure modes with the adoption of different plate' thickness and the influence of the loading rate on the ultimate behaviour of the damper for each considered geometry. In all cases, the resistance and ductility are affected by the loading rate although this difference is more significant when the deformation of the plate contributes more to the capacity of the damper.

Finally, an analytical model based on the component method of Eurocode 3 was proposed. The proposed model allows assessing the behaviour of the device. The model predicts correctly the changes in the failure mode when different thickness of the plates are used, similarly to those observed in the FEM and experimental tests. In addition, the implementation of a strain-rate sensitivity model allows the prediction of the changes in the connection behaviour when strain rates are relevant without losing the accuracy showed for quasi-static loads.

The results can provide useful information about the sensitivity of the tested components to the loading speed and can help engineers when dealing with the design of connections with the tested components under short-duration loads. From the results, not considering the strain rate sensitivity of materials can lead to an unsafe design with respect to the ductility capacity of connections and, therefore, the whole structure.

Chapter 5 FREEDAM connection under different loading rates: experimental and numerical characterization

5.1 Introduction

Following the work developed for the friction device, an experimental campaign and numerical studies have been conducted with the final aim to understand how the FREEDAM connection works under different loading rates.

The test rig used for the experimental quasi-static and impact tests was the same as used for testing the friction damper under impact loading.

The numerical simulations were carried out using ABAQUS software and it is divided into two parts: first, the experimental tests were simulated and after, a parametric study on the influence of the loading rate on the behaviour of the connection was performed.

5.2 Experimental campaign

The specimen tested has the geometry shown in Fig. 5.1. This particular geometry was designed from the design rules shown in Section 2.2.2 and considering the limitations of the experimental layouts of both Universities of Coimbra and Liege. It comprises an upper T-stub connecting the upper beam (IPE220) to the column, which is, in this case, the layout column ("flying beam"), by means of M16 10.9 HV bolts. The lower beam flange is bolted to an additional haunch, connected to the column by a system of three angles (L-stubs). A steel plate with a sprayed aluminium (coating material referred to as M4 in section Chapter 3) coating of *300 μm* thickness is located between the haunch flange and the angles, constituting the friction damper. Moreover, in order to have an adequate stroke for the friction damper, the haunch

flange has slotted holes. All the elements are in steel S275JR except for the haunch flange, which is in stainless steel AISI 304. With this geometry, under bending actions, the connection rotates around the upper T-stub. The energy dissipation is provided by the slippage of the haunch flange on the friction pads.

The connection was tested under hogging moment and the experimental campaign comprised a total of four tests and two specimens (Table 5.1): one quasi-static test and three impact tests. The quasi-static test was carried out to know the static behaviour of the connection and to have a reference behaviour to compare with its dynamic one. In this way, this test was carried out prior to the impact. During the impact tests, the impact was applied in a sequential way (only one specimen was used in all the sequences).
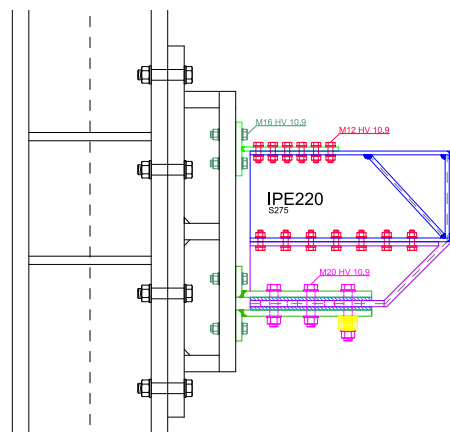
Fig. 5.1: FREEDAM connection tested

Table 5.1. Experimental programme

Test type	Quasi-static	Impact
Loading Scheme	Monotonic:	Sequential Impact:
	displacement control 0.02 mm/s	75 Bar ; 120Bar ; 200Bar

5.2.1 Preliminary design

In order to estimate the resistance of the connection to be tested, the component method described in the Eurocode 3 part 1-8 [5] was used. This method consists in dividing the connection into several active components that contribute to its deformation, to which a bilinear force-deformation curve is given. Afterwards, the components are assembled in series or in parallel and the moment-rotation (M-φ) curve of the connection is obtained.

With reference to the connection under investigation, when subjected to hogging moment (upper T-stub in tension and friction damper in compression), the active components can be

divided into two phases: (i) the phase before the slip of the friction damper and (ii) the phase after the slip. As sketched in Fig. 5.2, before the slip the only active components in tension are the components from the upper T-stub, namely, t-stub in bending (*tsb*), the T-stub bolts in tension *bt* and the T-stub web in tension *twt*, the column web in tension *cwt* and the column flange in bending *cfb*. At the compression zone, the only active components are the column web in shear *cws*, the column web in compression *cwc* and the friction damper FD_{frict}. However, after the complete slip of the friction damper, several other components will start to work at the compression zone, in particular, the bolts in shear *bs* and plates in bearing (*hfB* and *lwB*). At the upper part, also the bolts from the T-stub web will start to work in shear *bs* and the plates in bearing (*twB* and *bwB*) when the bolts from the T-stub web reach their friction resistance tw_{frict}.
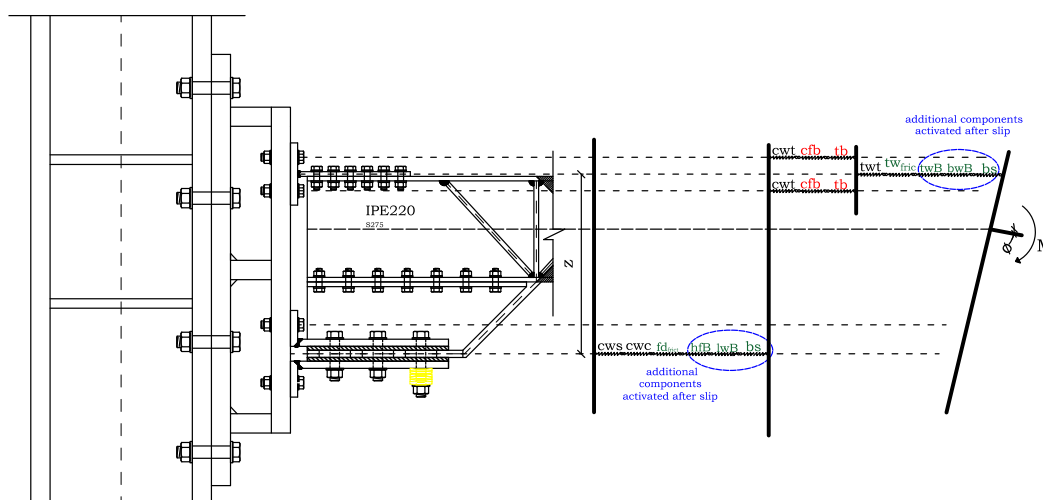
Fig. 5.2. Spring model for hogging moment

From the design rules of Section 2.2.2, a preload force equal to 102 kN should be applied to the connection. It was decided to preload only two of the six bolts of the friction damper with a preload force equal to 50 kN. With this preload force, a minimum and maximum theoretical friction resistance force equal 102 kN and 172 kN, was obtained. Additionally, the bolts of the remaining different parts of the connection (T-stub, L-stubs and connection between the lower beam flange and the haunch) were preloaded with the preload force recommended in the Eurocode 3 part 1-8 [5], as reported in Table 5.2.

Table 5.2. Preload forces applied in each type of bolt

Bolt	M12 HV	M16 HV	M20 HV
Preload force [kN]	59	109	50

After obtaining the friction resistance, the resistance of the other components was calculated considering the formulation of the Eurocode 3 Part 1-8 [5]. The strength average values from the coupon tests were used. Furthermore, for the bolts, an ultimate strength f_{ub} equal to 1050 MPa was considered, according to Cassiano work [91].

Table 5.3 reports the resistance and the stiffness of the connection, while Fig. 5.3 shows the expected quasi-static $M\text{-}\Phi$ curve of the connection. It is then expected that until the achievement of the end stroke of the friction damper, the behaviour of the connection will be governed by the friction resistance of the device, while the other steel components remain elastic. After the total slip of the device, an additional ductility and resistance are provided by the plates and bolts in bearing and shear. The weakest component is expected to be the upper T-stub in bending with collapse mode 2 (bolt failure with yield of the t-stub flange).

Table 5.3. Design of the connection

M_{slip} [kN.m]		Ø [mRad]		$M_{Rd,ana}$ [kN/m]	S_{ini} [kN.m/mRad]	$Ø_{Rd.ana}$ [mRad]
min	max	before slip	end of slip			
41.34	67.86	0.3	57.9	165	48	61.36
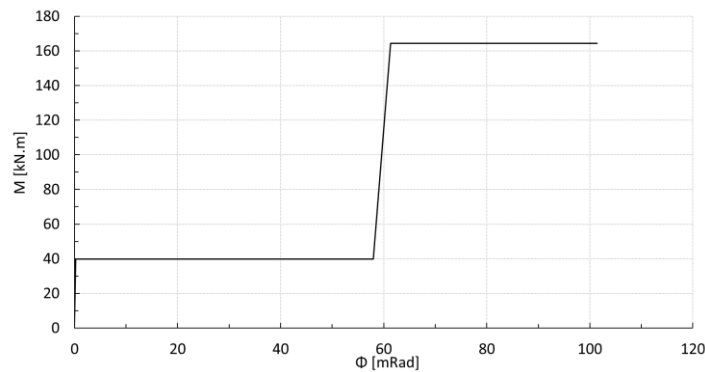
Fig. 5.3. Analytical prediction of the moment-rotation curve of the tested connection under hogging moment

5.2.2 Experimental set up

The experimental set up used for the impact tests on the friction damper was also used here (Fig. 5.4a). However, the boundary conditions of the specimen were changed so that the specimen would be subjected to bending moment. In this way, at one end, the connection was directly bolted to the "flying beam" and, at the other end, it was connected to a support made

from a hollow section, which restrained the vertical movements of the beam but allowed the horizontal sliding (Fig. 5.4b). In addition, to perform the quasi-static test, a hydraulic jack was added to the layout, as showed in Fig. 5.4a.

| a. 3D scheme | b. 2D scheme (top view) |
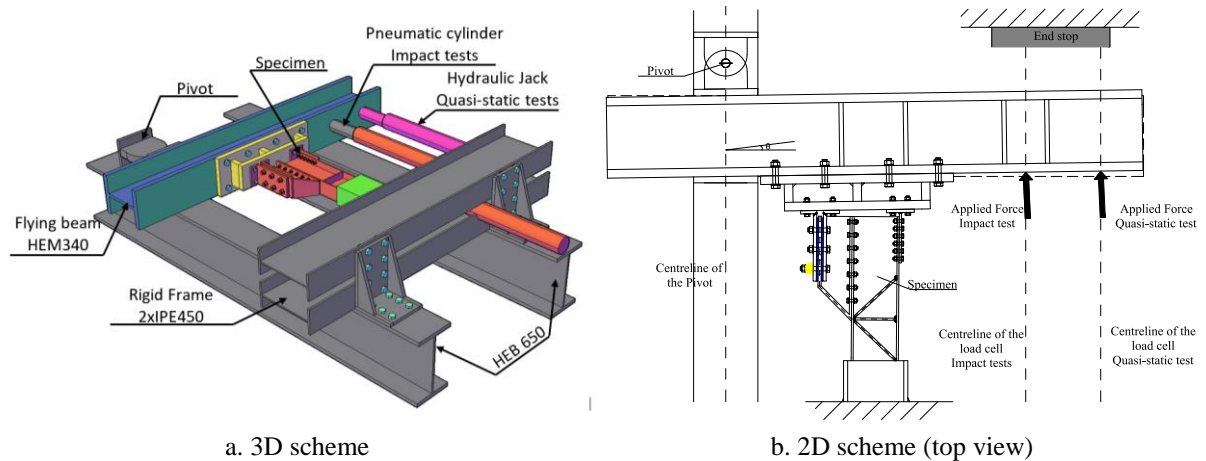
Fig. 5.4. Boundary conditions of the layout – Connection testing

The same type of instrumentation used to capture the behaviour of the friction damper was also used here. In other words, to perform the quasi-static tests, the deformation was capture using LVDT (Fig. 5.5a), while the force was read by two load cells placed at the end of the hydraulic jack (Fig. 5.6).

In Fig. 5.5b is shown the instrumentation system used for the impact tests. Deformations were read by the laser triangulation sensors and additionally by the high-speed camera (Fig. 5.7). Accelerometers were placed at the centre of mass of the beam and at the application load point. Finally, the applied force was read by the load cell already shown in Fig. 3.12a.

| a. Quasi-static test (top view) | b. Impact tests (top view) |
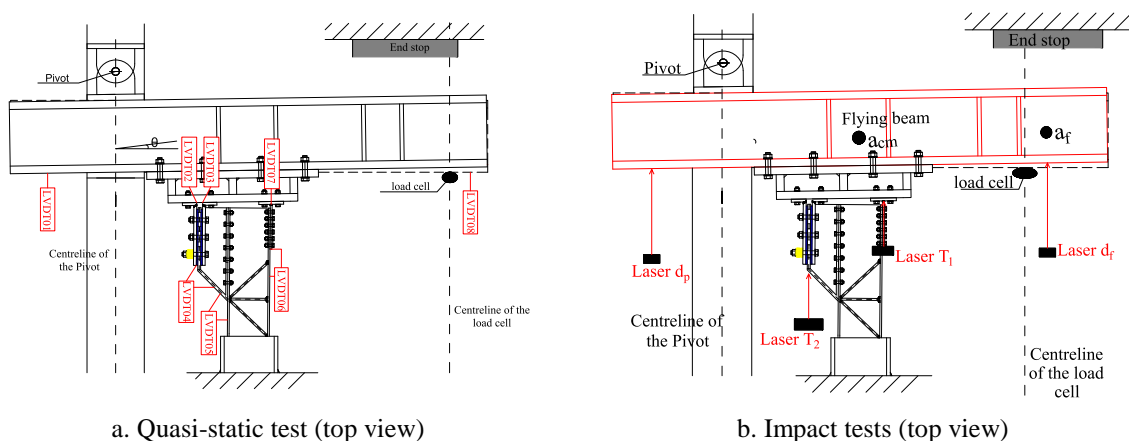
Fig. 5.5. Position of the instrumentation
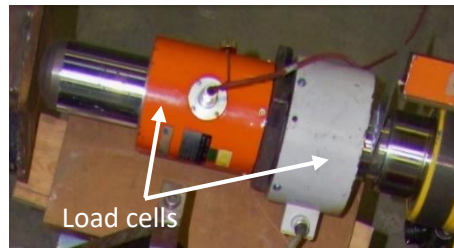
Fig. 5.6. Load cells used in the quasi-static test
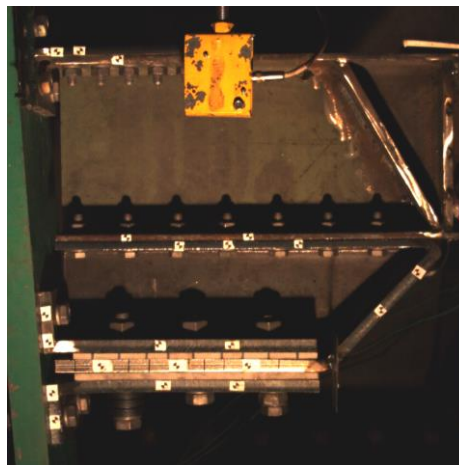
Fig. 5.7. Target points to be read by the high-speed camera

5.2.3 Calculation of the bending moment transmitted to the connection

The bending moment transmitted to the connection during the tests was obtained from the equilibrium of bending moments at the beam-to-column intersection node (Fig. 5.8). From the equilibrium of horizontal forces, it is concluded that the force read at the actuator has the same value of the reaction force at the pivot, Eq.(5.1). In this way, the bending moment transmitted to the column can be obtained from the product between the force on the actuator F_A and the length between the actuator and the pivot, L (Eq. 5.2). When an impact is considered, to Eq. (5.2) the contribution of the inertial forces needs to be added (Eq. 5.3, red forces in Fig. 5.8).

The bending moment at the connection zone M_{con} is obtained by scaling down the bending moment transmitted to the column, considering the slope of the triangular distribution of bending moments along the beam length. Although the beam support is not a perfect hinge, it was assumed that the bending moment at the beam end can be neglected, thus, M_{con} was obtained by Eq. (5.4), where L_{con} is the beam length and L_B is the length between the beam end and the hinge support. The connection rotation Φ is obtained dividing the deformation at the

friction damper by the position of the neutral axis in relation to the centre of compression during the test (Eq.5.5), *NAD*, which is obtained from Eq.(5.6).

In addition, the tension and compression forces can be easily obtained dividing the bending moment by the lever arm of the connection h_t, assuming that the centre of compression is located at the middle axis of the friction device (Fig. 5.9).

$$\sum F_h = 0 \leftrightarrow F_A = F_h \tag{5.1}$$

$$M_{col}(t) = F_A(t) \times (L'_C + L''_C) = F_A(t) \times L \tag{5.2}$$

$$M_{col}(t) = F_A(t) \times (L'_C + L''_C) - I\ddot{\theta}(t) \tag{5.3}$$

$$M_{con}(t) = M_{col}(t) \times L_{con} / L_B \tag{5.4}$$

$$\phi = \delta_{FD} / NAD \times 100 \tag{5.5}$$

$$NAD = \delta_{FD}(t) / \left((\delta_{T-stub}(t) - \delta_{FD}(t)) / h_t \right) \tag{5.6}$$
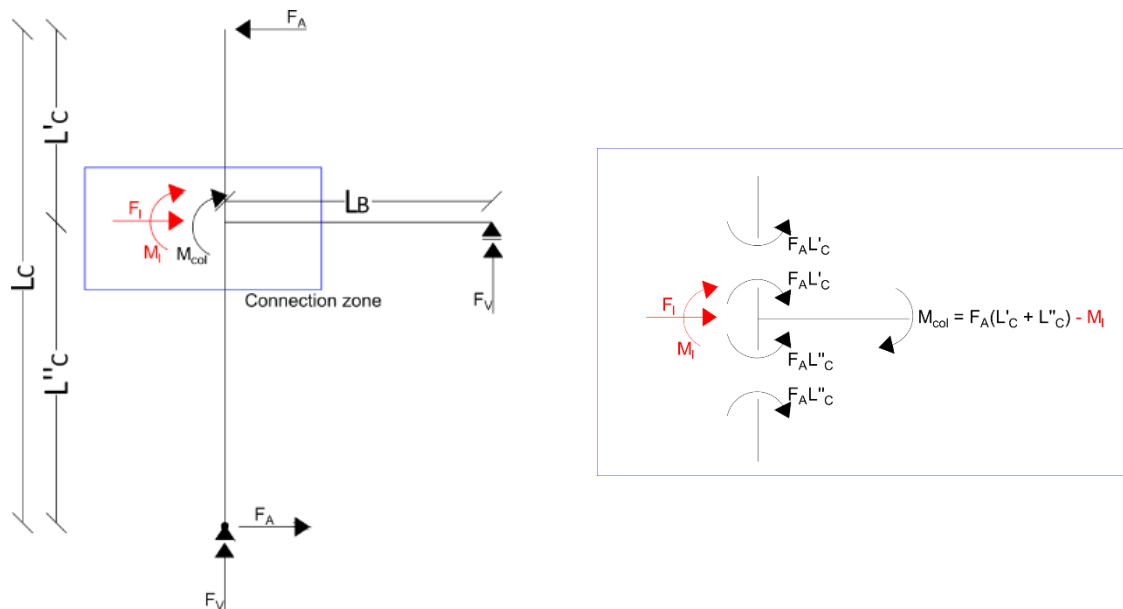
Fig. 5.8. Forces/bending moments of the experimental layout
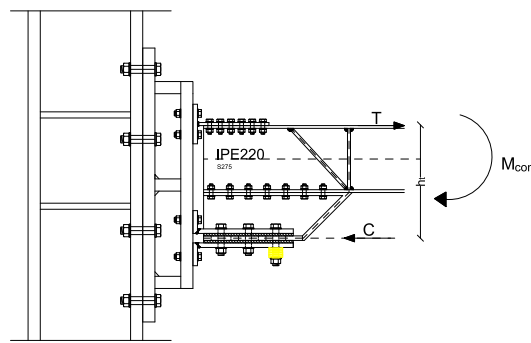
Fig. 5.9. Centre of tension and compression

5.2.4 Experimental results

5.2.4.1 Quasi-static behaviour of the connection

Fig. 5.10 shows the experimental moment-rotation curve at the connection zone up to failure. In addition, also depicted is the predicted analytical curve. Observing the experimental curve, it shows similarities with the behaviour of the friction device reported throughout the previous chapter of this work, which means that, in fact, the connection behaviour is governed by the friction damper behaviour up to the complete slip of the plates. This fact was already shown by Latour *et al.* [41,42,46] (see Chapter 2). The bending friction resistance matches the minimum value predicted by the analytical preliminary design. Furthermore, during the slip, an initial degradation of the force is observed, followed by an increase of this force from the middle of the slip length, which probably happened due to some earlier yielding of the steel parts.

After the complete slip of the friction device, additional components of the joint are activated and some non-dissipative components of the joint start to yield. The experimental resistance bending moment is found by a bilinear approximation of the initial and post-elastic slopes [85]. From the results, a moment resistance 12% higher than the one given by the code was found. Furthermore, a close agreement between the experimental and analytical elastic stiffness was found (Table 5.4).

At the end, the collapse was achieved by the T-stub in bending, as predicted from the analytical design of the Eurocode, with thread stripping failure in the bolts of the T-stub flange (Fig. 5.12). In fact, thread stripping, even though undesired, is the typical failure mode for HV bolts in tension and consequently, in T-stubs with HV bolts when designed to collapse in mode 2 or 3 [26,64,65,91]. An alternative would be using HR bolting assemblies, which are characterized by bolt elongation failure modes (these bolting assemblies have thicker nuts and long thread when compared to the HV bolting systems). However, HV bolting assembling are

more commonly used in steel connections and therefore, these assemblies were chosen for these tests.

Another important measurement is the ductility capacity of the connection, which can be measured by a ductility index φ, given by the ratio between the rotation at the ultimate experimental bending resistance $\phi_{u,exp}$ and the rotation corresponding to the experimental resistance bending moment $\phi_{y,exp}$ [101,106]. According to [101], to ensure a good ductility, the value of the ductility index should be at least equal to 3. In this case, the ductility index is only 1.9, due to the thread stripping, which according to Grimsno *et al.* [24], reduces the rotation capacity of joints in almost 100%.

Plotting the displacements of the LVDT 04 and 07 (Fig. 5.5) versus the tension/ compression force in the connection is possible to plot the curve force vs deformation of the friction damper and T-stub flange up to the ultimate load, as reported in Fig. 5.11 a. and b., respectively. In addition, in Fig. 5.13 is plotted the force vs displacement curve of the relative movement between the beam flange and the T-stub. Additionally, a photo from the web of the T-stub after the test shows some elongation of the holes, especially in the first row.

Finally, in Fig. 5.14 is presented some pictures of the connection after the test. It is possible to observe the complete bending mechanism of the connection (Fig. 5.14a), the failure of the T-stub (Fig. 5.14c) and the yield of the L-stubs (Fig. 5.14b).

Fig. 5.10. M - Φ curve

a. Friction damper   b. Upper T-stub
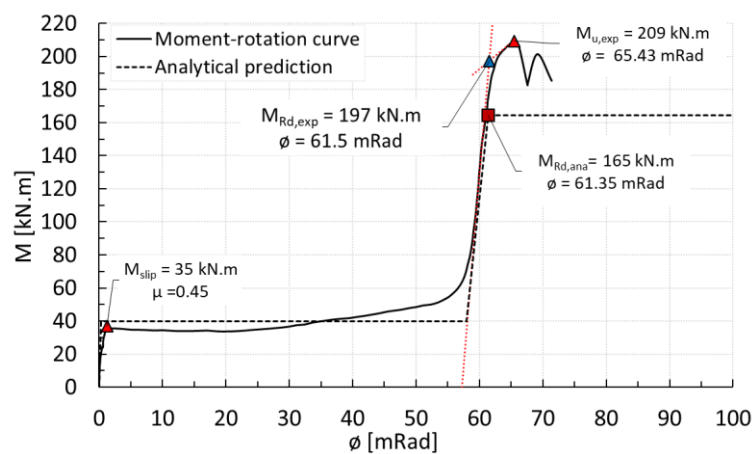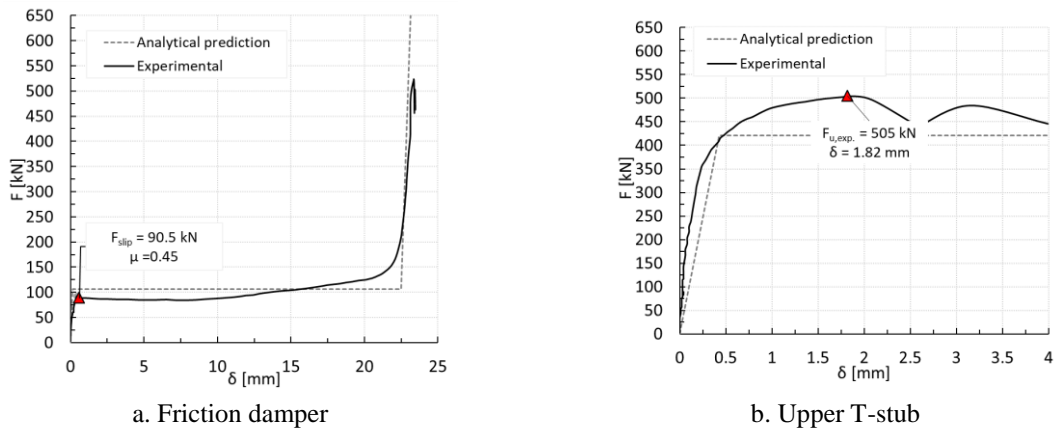
Fig. 5.11. Force-deformation curves of the individual components

Table 5.4: Maximum bending moment, forces and rotation in the connection

	S_{ini} [kN.m/mRad]	M_y [kN.m]	*ϕ_y [mRad]	M_u [kN.m]	*ϕ_u [mRad]	φ	Energy dissipated [kNm.mRad]
Exp.	45.45	197	4.34	210	8.23	1.90	3519
Ana.	48	165	61.35	-	-	-	
Ana/exp	1.06	0.84	1.00	-	-		
*Rotation values after slip							

a. M16 bolts: nut striping failure   b. T-stub: deformation

Fig. 5.12. T-stub and bolts of the T-stub flange after failure

| a. Force-deformation curve | b. Deformation after the test |
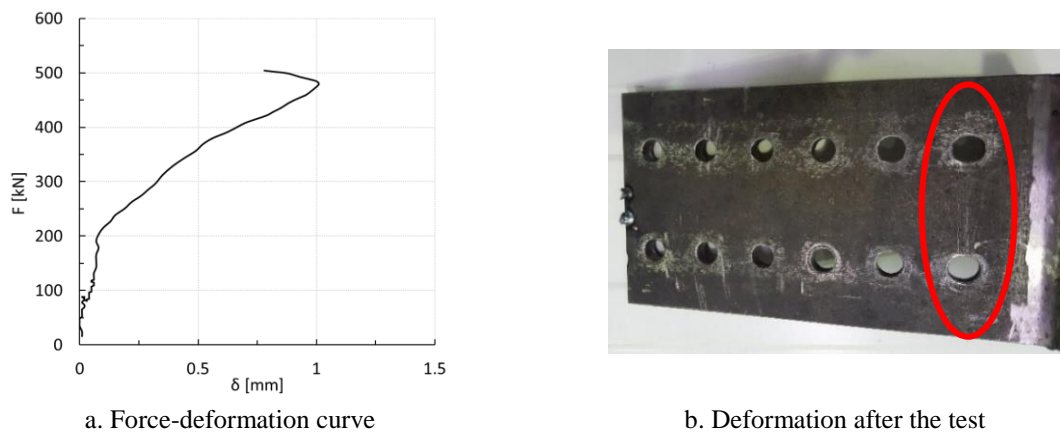
Fig. 5.13. Deformation of the T-stub web

| a. Connection after failure | b. L-stub | c. T-stub in bending + bolt nut stripping |
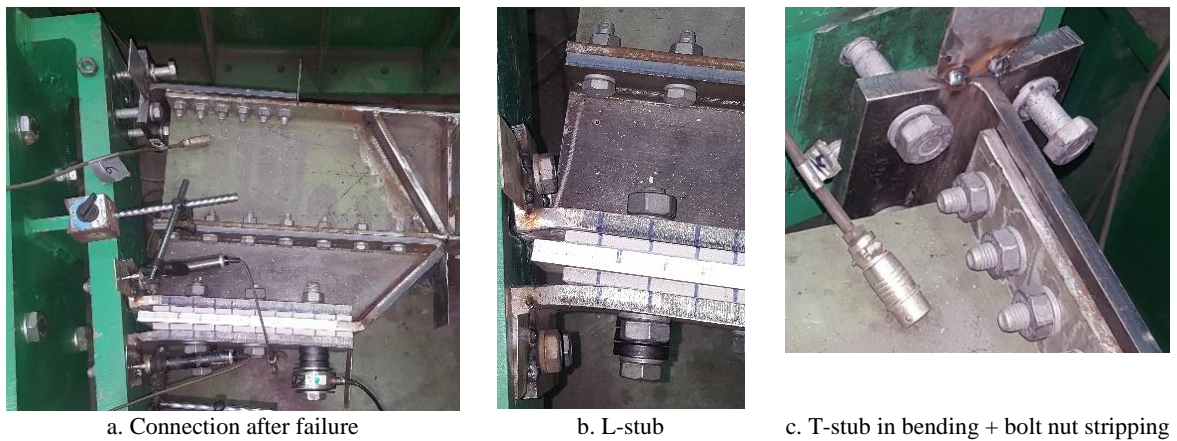
Fig. 5.14. Connection after failure: General view

5.2.4.2   Impact behaviour and comparison with the quasi-static behaviour

Fig. 5.15 shows the experimental bending moment - rotation curves obtained in each sequence of impact (Impact 1, Impact 2 and Impact 3 in Fig. 5.15), as well as the quasi-static curve previously discussed. In the first sequence of impact at a pressure equal to 75 Bar, the slip of the connection was achieved until the bolts reached the end of the slotted holes. From this first curve, some conclusions can be drawn concerning the slip behaviour of the connection under impact loads. In particular, the friction resistance M_{slip} was obtained for a value 1.14 higher than friction resistance at quasi-static loading. This is in agreement with the conclusions from the experimental campaign devoted to the friction damper behaviour presented in Chapter 3. During the slip, an increase of the force is observed. In fact, plotting the velocity of slip versus the rotation of the connection (Fig. 5.16), it is observed an increase of this velocity until almost the end of slip, which can explain the increase of force during the slip.

After the first impact, two additional tests were performed at higher pressures. Unfortunately, these pressures were not enough to induce the failure of the connection. However, it can be observed that after the slip, the impact behaviour tends to follow the static one.
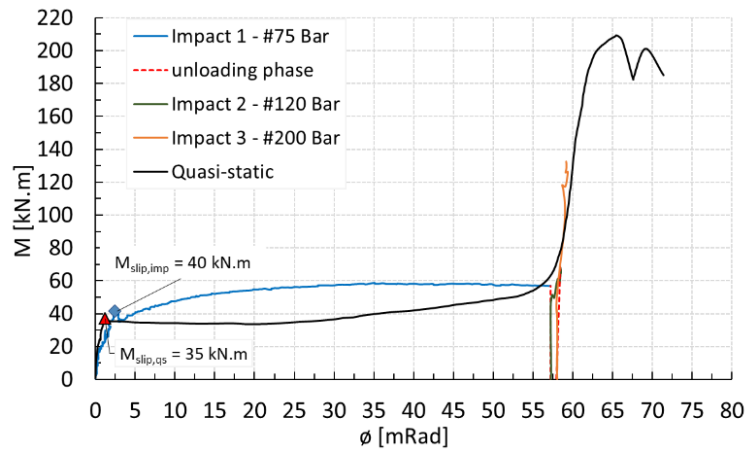
Fig. 5.15. Moment rotation curve: Quasi-static vs Impact tests
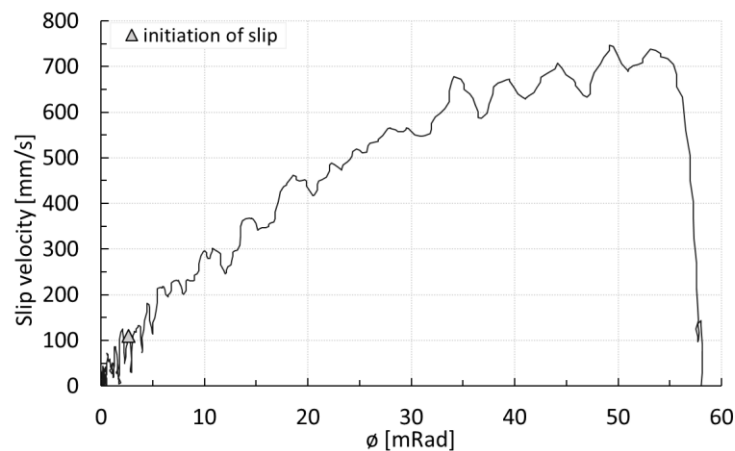
Fig. 5.16. Slip velocity vs rotation – Impact #1

5.3 Numerical study

5.3.1 Model geometry, boundary and loading conditions and model discretization

A numerical evaluation of the response of the tested friction joint has been carried out with ABAQUS software, using the dynamic implicit solver [13]. The quasi-static procedure was

used to capture the quasi-static behaviour of the joint, while the moderate dissipation procedure was used to capture the dynamic behaviour.

In order to decrease the computational time, the experimental layout was simplified. Firstly, since the layout is symmetric in the XX plane, only half of the layout was modelled. Secondly, the reaction frame was omitted. Furthermore, the supports were modelled with reference points, imposing the required constraints in the zones in contact with the supports (pinned constraint and vertical constraint in Fig. 5.17b), while the rod of the actuator was modelled as a solid object in which displacements in time are applied.

In total, fifteen different parts were considered: i) HEM 340 beam "*flying beam*"; ii) the IPE 220 beam; iii) the actuator; iv) the rigid part connecting the connection to the HEM 340 beam and v) all the parts of the FREEDAM connection. Solid (or continuum) element type C3D8R (first order reduced integration continuum element) with "Hex" element shape was used in the entire model, allowing for non-linear geometrical and material behaviour. Due to its reduced integration, C3D8R elements allows to reduce the calculation time, and provide hourglass behaviour control. All bolts were modelled as one single piece of bolt+head+nut. However, for the M16 HV bolts, the transition between the smooth shank and the threads was modelled by reducing the cross-sectional area of the bolt, as suggested by Grimsno *et al.* [8] (Fig. 5.18), to assess more correctly the nut stripping failure observed in the experimental test.

a. Experimental 3D scheme   b. Model
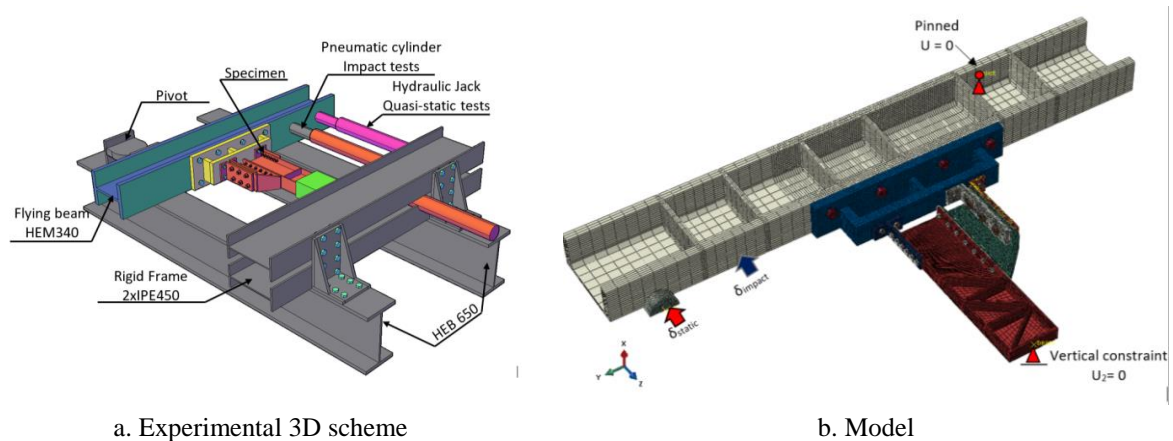
Fig. 5.17. FEM models: Boundary conditions

a. Dimensions (in mm)   b. Mesh
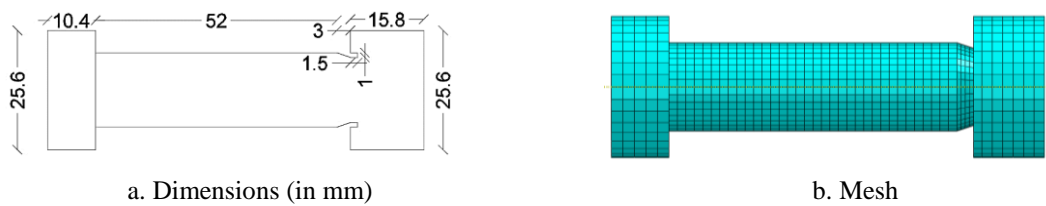
Fig. 5.18. M16 HV Bolt modelling

Contact interactions are assumed for all parts. For the tangential contacts, the "penalty" formulation was used, considering a friction coefficient of 0.2 for all the steel-steel tangential contacts, except for the parts in contact with the friction pads. For these parts, the experimental friction coefficients were used, i.e. 0.45 for a static slip rate (0.002 mm/s) and 0.52 for a slip rate equal 100 mm/s (average value of the experimental slip velocity at the begging of the slip, Fig. 5.16). The normal contact occurrences were modelled with *hard-contact* allowing separation after contact. The bolts were preload using the "bolt load" with adjust length available in ABAQUS.

Concerning the applied loading, two subsequent steps were defined. In a first step, the bolts were preloaded and, in a second step, the column was pushed. For the quasi-static analysis, a displacement controlled loading was applied, whereas to simulate the impact tests, the transient displacement curves measured in the experimental tests were applied as a boundary condition.

The available *dynamic implicit with quasi-static application* algorithm was used for the quasi-static analyses, while the *implicit/dynamic* with *moderate dissipation* was applied in the impact load analysis.

5.3.2 Material modelling

The same approach used in the numerical simulations of the friction damper (Chapter 4) to define the different steel grades composing the components of the device, were also used here. In this way, the results from the coupon tests were used to define the behaviour of all the components, except for the bolts, which were defined by the formulation given by D'Aniello *et al.* [91] (Fig. 5.19). Furthermore, as in the simulations of the friction damper, damage (Fig. 5.20) and strain rate dependence were considered, using the damage ductile model and the Johnson-Cook model together with the strain-hardening model for isotropic materials.
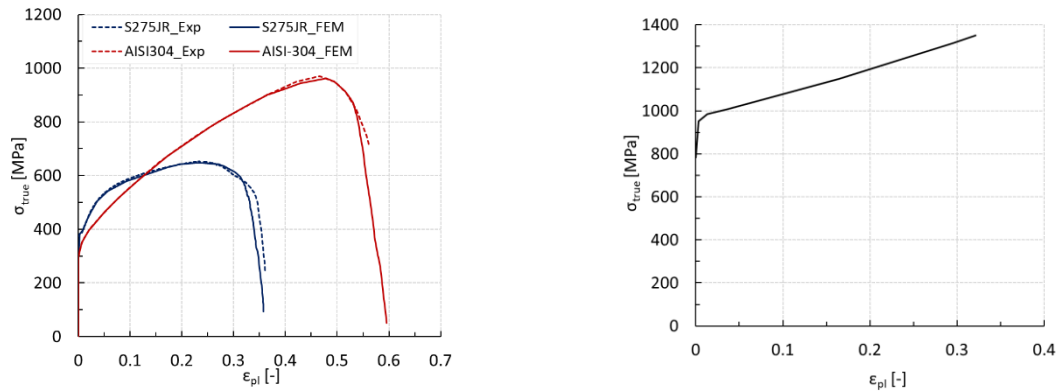
a. Uniaxial coupon tests: True stress-true strain curves   b. stress-strain law for bolts

Fig. 5.19. Stress-strain relationships for plates and bolts
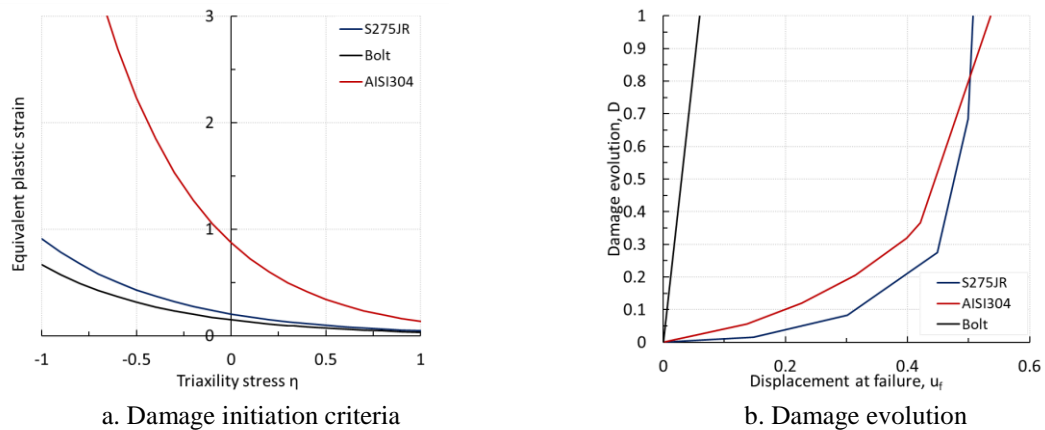
a. Damage initiation criteria   b. Damage evolution

Fig. 5.20. Definition of the damage criteria

5.3.3 Comparison of the results: Experimental vs Numerical

5.3.3.1 Quasi-static response under hogging bending moment

Fig. 5.21 compares the numerical and experimental M-ø curves of the joint, where it is visible that the FEM model can predict correctly the quasi-static behaviour observed in the experimental tests. With reference to the friction resistance ($M_{slip,FEM}$ in Fig. 5.21), the model can predict the exact experimental friction resistance. After the initiation of the slip, the friction resistance decreases slightly following the behaviour observed in the experiments. However, this force starts to increase at the middle of the slip length and earlier than the experiments, achieving at the end of the slip, a higher force. This is probably due to an earlier yielding of the T-stub and L-stubs, as shown in Fig. 5.22a and b at the middle and end of the slip, respectively. After the slip, the force increases until the failure of the bolts of the upper T-stub. The global

deformation of the joint is shown in Fig. 5.22c. As can be seen, the bolt modelling allows an accurate approximation of the ultimate load and rotation capacity of the joint. In addition, Fig. 5.23 compares the force-displacement curves of the friction damper, T-stub flange and T-stub web obtained numerically with those obtained in the experiments, showing that the model can predict the elastic and plastic behaviour of all of these components.

Finally, Fig. 5.24 shows a close up of the failure zone, where it is possible to observe that the bolt elements at the threaded zone achieved the maximum damage (DUCT = 1), indicating that the failure mode happened in the same zone as in the experiments. In addition, the T-stub also shows significant damage, similar to the experimental evidence.

Fig. 5.21. Quasi-static behaviour under hogging moment: M-ø curve, Exp. Vs FEM

a. During the slip ø = 33 mRad   b. End of the slip ø = 59 mRad   c. Ultimate load ø = 64.3 mRad
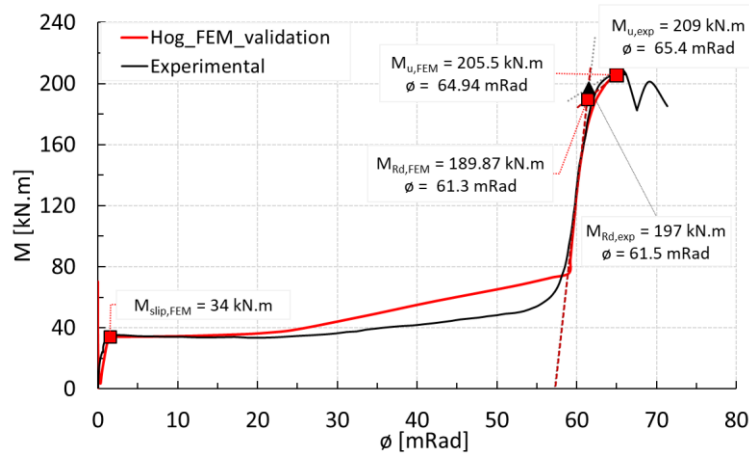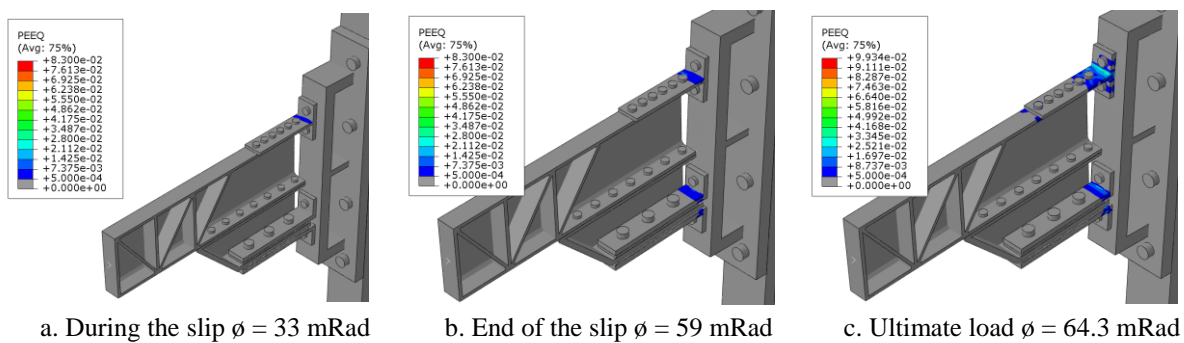
Fig. 5.22. Quasi-static behaviour under hogging moment: plastic equivalent strain during the test (PEEQ)

| a. T-stub flange | b. Friction damper | c. T-stub web |
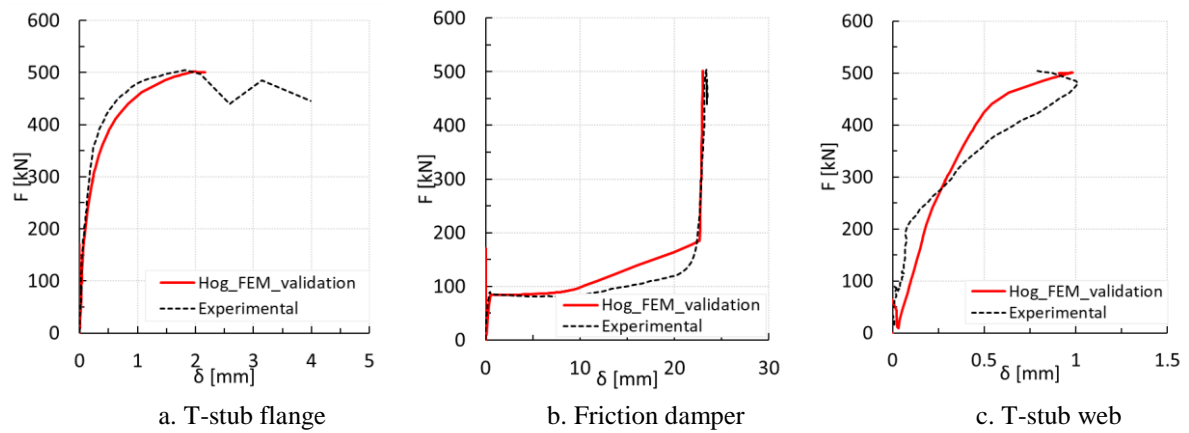
Fig. 5.23. Quasi-static behaviour under hogging moment: F-δ curves, Exp. Vs FEM
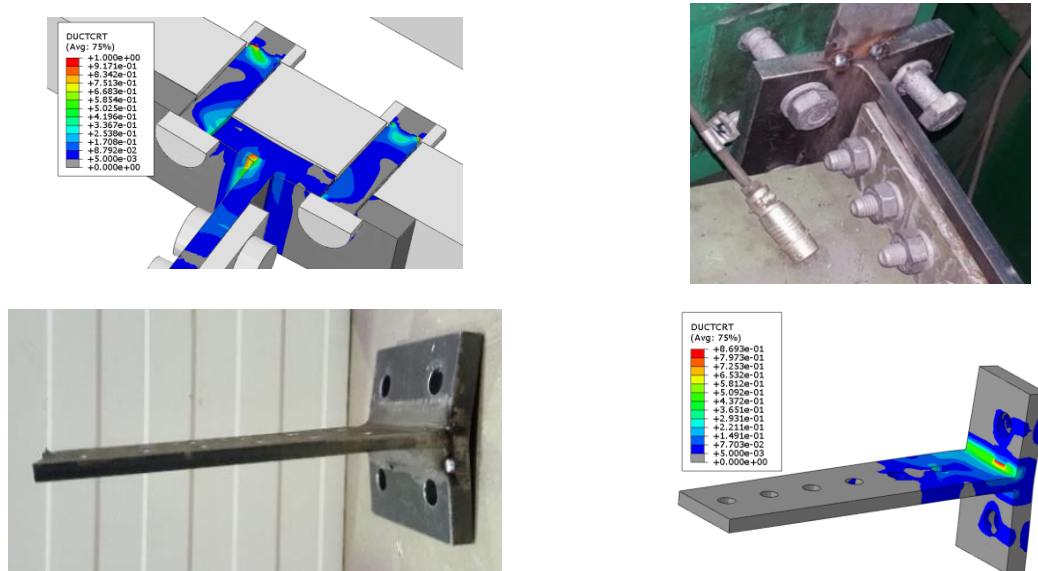
Fig. 5.24. Quasi-static behaviour under hogging moment: T-stub failure – Exp vs FEM

5.3.3.2 Impact response

The dynamic behaviour of the model was verified, implementing the displacement-time curves obtained in the laser closest to the actuator in the model (Fig. 5.25). To assess the bending moment transmitted to the connection, the equations reported in section 5.4.2 that take into consideration the inertial effects of the beam were used.

Fig. 5.26a shows both the numerical and the experimental M-ø curves. Concerning the first impact sequence (Impact 1 - # 75Bar), the model is able to predict correctly the initial friction resistance. In addition, during the slip, the model also presents an increase of the initial forces

in a very similar way as observed in the experiments, which is related to a very similar increase of the slip velocity during the test, as shown in Fig. 5.26b.

Regarding the other two sequences of loading (Impact 2 and 3), the model shows moment-rotation curves similar to those observed in the experiments. Furthermore, at the end of the test, the model presents the same deformation at the global and local level of components as shown in Fig. 5.27 and Fig. 5.28.
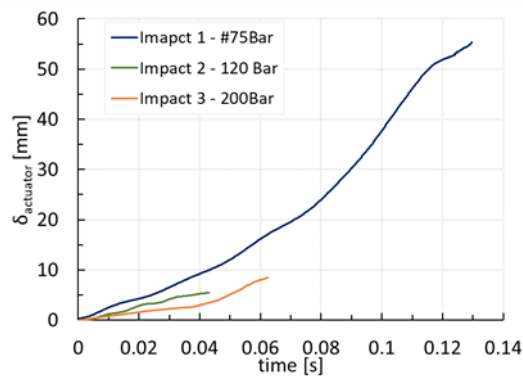
Fig. 5.25. Actuator deformation –time curve – Impact #1 – 75 Bar

a. Moment-rotation curve

b. Slip velocity
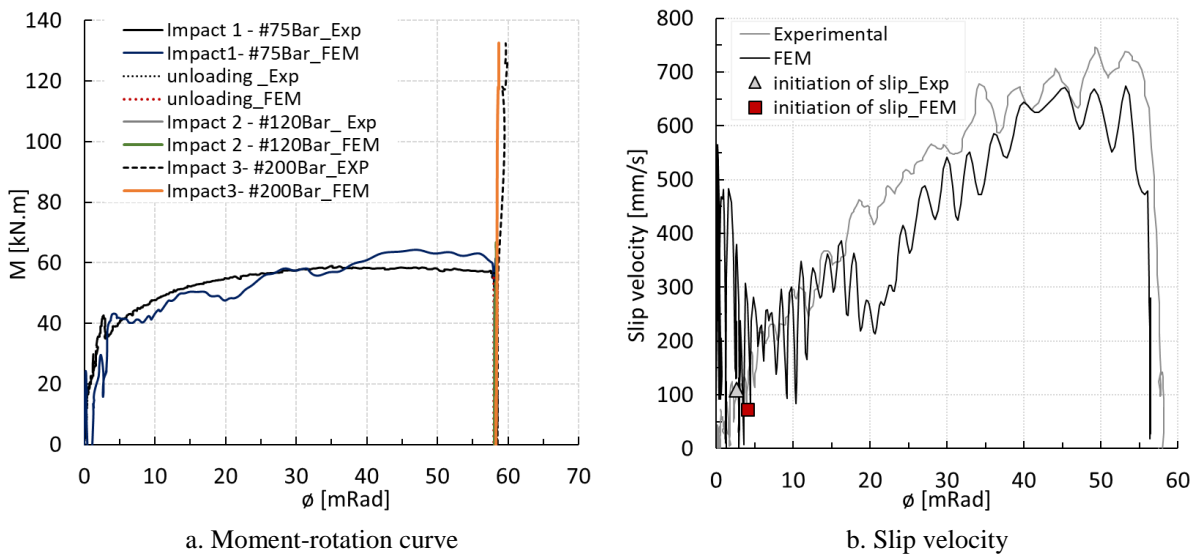
Fig. 5.26. Validation of the FEM model against experimental test – Dynamic behaviour
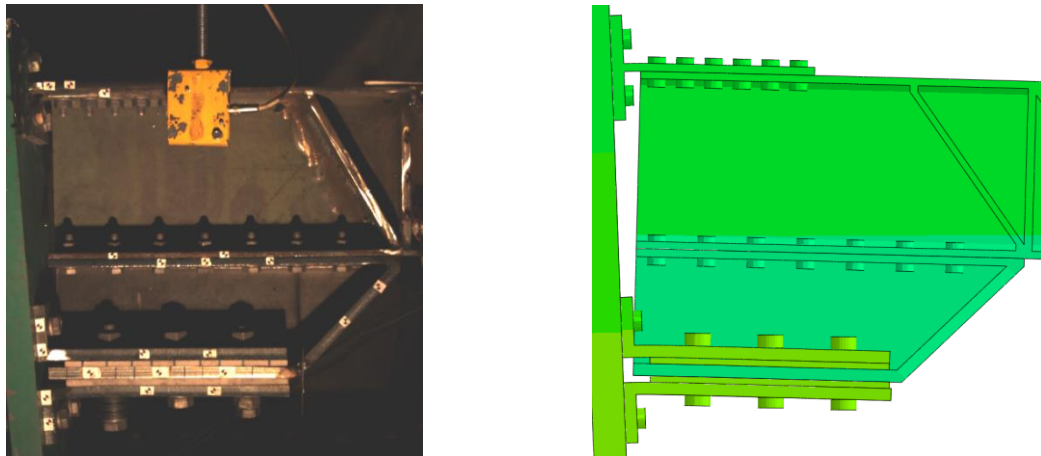
Fig. 5.27. Global deformation of the connection at the end of the test: Exp. Vs FEM
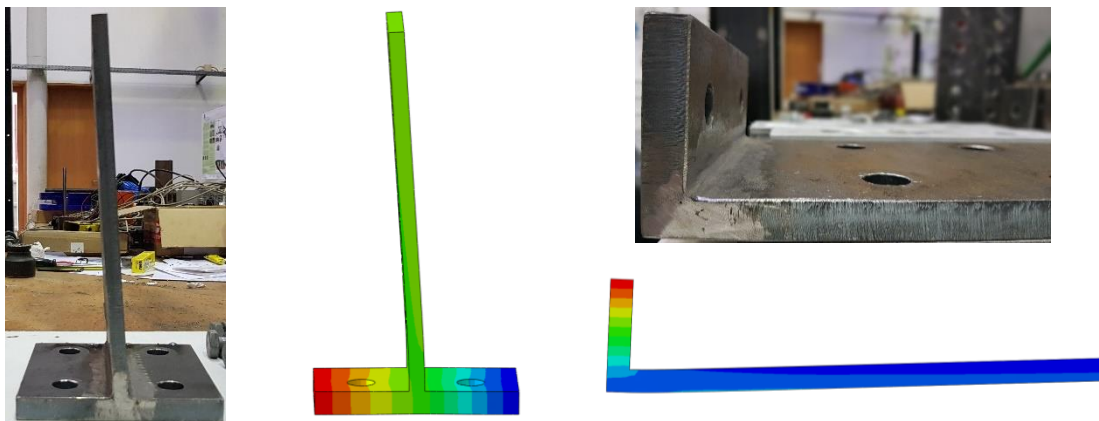
Fig. 5.28. Local deformation of components the connection at the end of the test: Exp. Vs FEM

5.3.4 Parametric studies

After the calibration of the model against the experimental results, parametric studies were carried out to widen the knowledge about the behaviour of the tested connection, which included a prediction of the behaviour under sagging moment as well as the dynamic behaviour considering different loading rates.

5.3.4.1 Behaviour under sagging bending moment

Fig. 5.29 depicts the moment-rotation curve obtained under both hogging and sagging bending moment. Globally, the behaviour of the connection is similar in both situations. In particular, the first part of the curve is also governed by the slip behaviour of the damper, although a lower friction resistance was observed under sagging bending moment (around 25% lower). This lower friction resistance in sagging moment has also observed by Latour *et al.*

[42], and it was justified by the differences in the T-stub and L-stub gap openings under hogging and sagging moment.
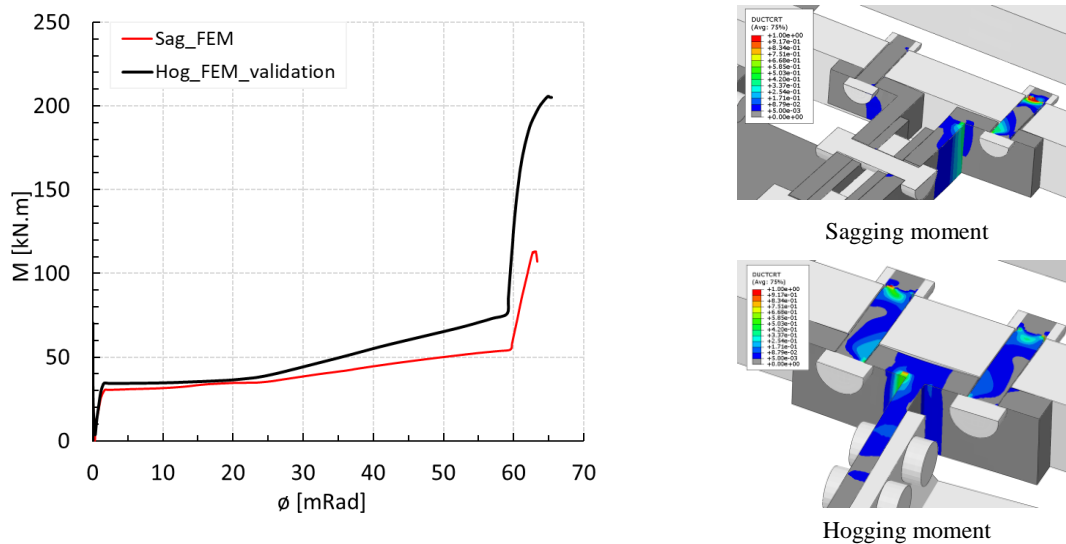
Fig. 5.29. Comparison between the quasi-static behaviour response under sagging and hogging bending moment

After slip, the behaviour of the connection under sagging moment is governed by the L-stubs in bending up to the failure of the bolts of the external L-stubs (Fig. 5.29). Concerning the ultimate resistance under sagging moment, it represents 60% of that obtained under hogging moment (Table 5.6). This difference can be explained mostly by the higher unsymmetrical contribution of the external and internal L-stubs bolt rows for the ultimate resistance when compared to the t-stub' bolt rows, as it is clearly visible in Fig. 5.30a. This figure shows that, at the ultimate load, both T-stub bolts are damaged, while, the damage in the internal L-stub bolt is minimal. In particular, looking at the distances between the middle axes of the L-stubs in relation to the centre of rotation (axis of the T-stub web) showed in Fig. 5.30b, it is observed that the interior L-stubs would contribute only around 40% for the resistance of the specimen. However, the contribution of the internal L-stub to the resistance is only about 20% (Fig. 5.31a), which seems to be related to the deformation of the bolts of the friction damper in shear at the ultimate load, as shown in Fig. 5.31b. As it can be observed, the holes of the L-stubs are not engaged in bearing in the same way, as the bolts do not completely touch the holes of the interior L-stub. This particularity seems to explain the lower tension forces observed in the interior L-stub and it happens due to the high rotations associated with the slip of the connection.

In addition, the behaviour under sagging moment shows a lower initial stiffness after the complete slip of the damper (S_{ini} in Table 5.6) since it is mainly governed by the stiffness of the L-stubs. In addition, the ductility index is 40% lower than the values observed under hogging moment (φ in Table 5.6). For these reasons, a significantly lower energy dissipation capacity is also observed (E_{diss} in Table 5.6).
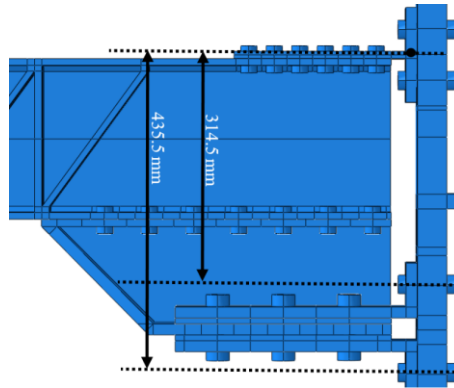
Fig. 5.30. Lever arms and centre of rotation under sagging moment

External L-stub   Internal L-stub   t-stub

a. Forces at the tee elements at the ultimate load

b. Deformation of the bolts in shear
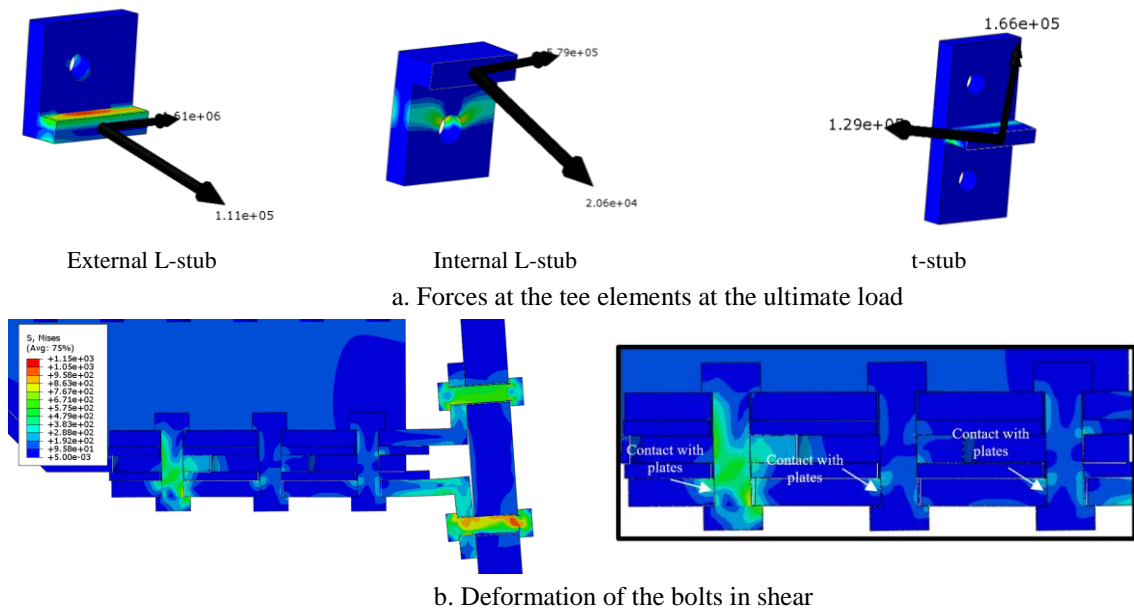
Fig. 5.31. Forces at the tee elements and deformation of the friction damper at the ultimate load

5.3.4.2 Effect of bolt ductility

Considering the results of the previous section, an additional study was carried out to better understand what are the factors that influence the balance between the contributions of the L-stubs under sagging moment. In particular, one parameter that seems to have a great influence

on the ultimate behaviour of the connection is the ductility of the bolts, which in this case is very limited due to the adoption of bolts failing due to thread stripping. Although this failure mode is the most common in HV bolt assemblies, in this case, it is also the most undesired, because it affects significantly the resistance and ductility of the whole connection [24]. The recent work of Cassiano [52] clearly shows the difference between the ductility of a 10.9 HV bolt failing by thread stripping or by shank necking if two nuts are adopted (Table 5.5). For bolts M16, this difference is around 3. In order to understand the influence of the bolt ductility over the connection response, the ductility of the bolts was fictitiously increased by changing its displacement at failure of the ductile damage parameters, simulating the adoption of HV bolts with two nuts.

Table 5.5. Average bolt assembly ductility and failure modes [52]

Nominal bolt diameter [mm]	Bolt class [-]	Bolt type [-]	Number of nuts [-]	Failure mode [-]	Ductility d_d/d_y [-]
16	8.8	SB	1	Shank necking	13.6
16	10.9	HR	1	Shank necking	6.4
16	10.9	HV	1	Thread stripping	2.0
16	10.9	HV	2	Shank necking	5.5
20	8.8	SB	1	Shank necking	11.0
20	10.9	HR	1	Shank necking	5.6
20	10.9	HV	1	Thread stripping	1.8
20	10.9	HV	2	Shank necking	4.6
24	8.8	SB	1	Shank necking	9.5
24	10.9	HR	1	Shank necking	5.5
24	10.9	HV	1	Thread stripping	2.1
24	10.9	HV	2	Shank necking	5.2
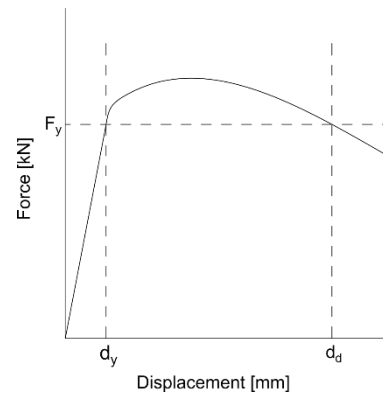
The results from this analysis are reported in Fig. 5.32 and in Table 5.6. Increasing the bolt ductility, increased 32% the ultimate resistance and the ductility index of the connection in 54%. Furthermore, at failure, the contribution of the interior L-stub also increases, from the previous 20 % to 31 % (Fig. 5.33). In the previous model, the lower contribution of the interior L-stub was thought to be related to the deformation of the damper bolts in shear at the ultimate load. In fact, comparing the deformation of the bolts in shear in both models (Fig. 5.34), it is observed that, in this case, the shape gets closer from what was expected, i.e. two bolts are in contact with both L-stubs webs.

With reference to the failure mode, increasing the bolt ductility switched the thread failure to failure at the shank part (Fig. 5.35). It is also noticed more bending and shear deformation at the bolts at the time of failure.

The reported results showed why the earlier failure by thread stripping should be avoided as much as possible since it can significantly change the behaviour of connections designed to fail in the tee elements by mode 2 or mode 3 of Eurocode [5].
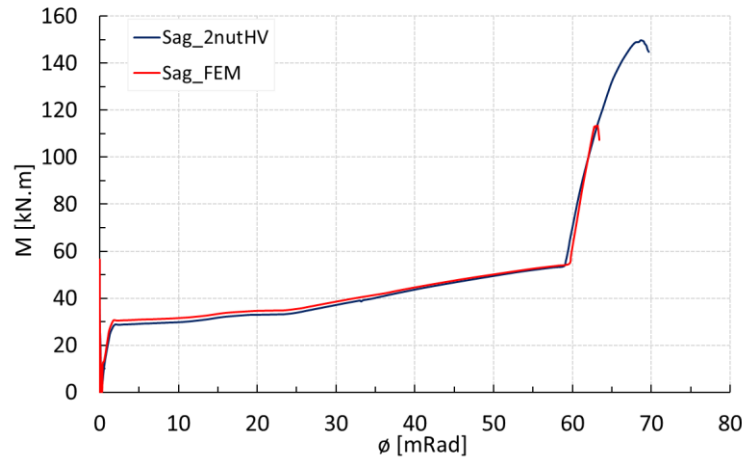
Fig. 5.32. Quasi-static behaviour response under sagging moment – effect of bolt ductility
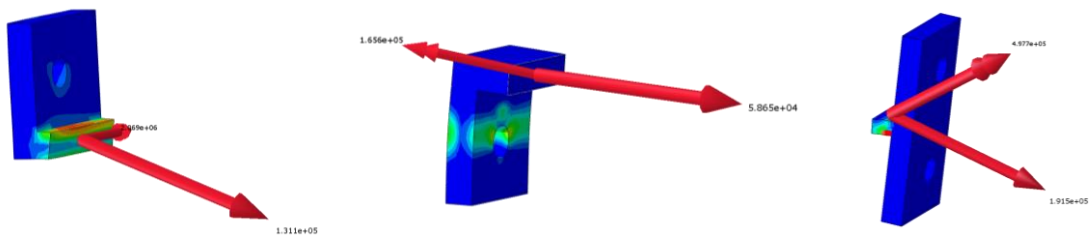
Fig. 5.33. Forces at the tee elements and failure mode – effect of bolt ductility

a. Thread stripping   b. Shank necking
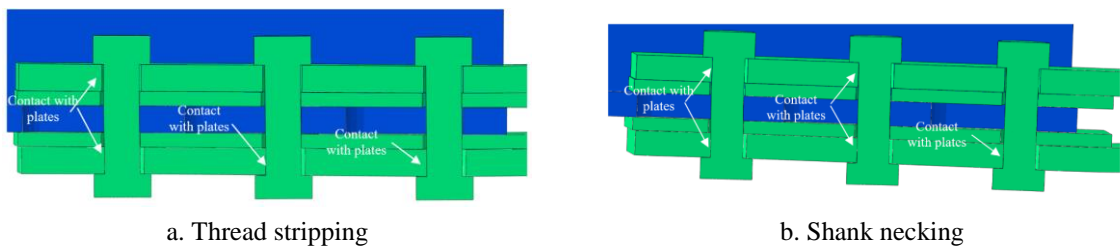
Fig. 5.34. Deformation of the bolts in shear at the ultimate load – effect of bolt ductility

External bolt Internal bolt

a. Shank necking

External bolt Internal bolt
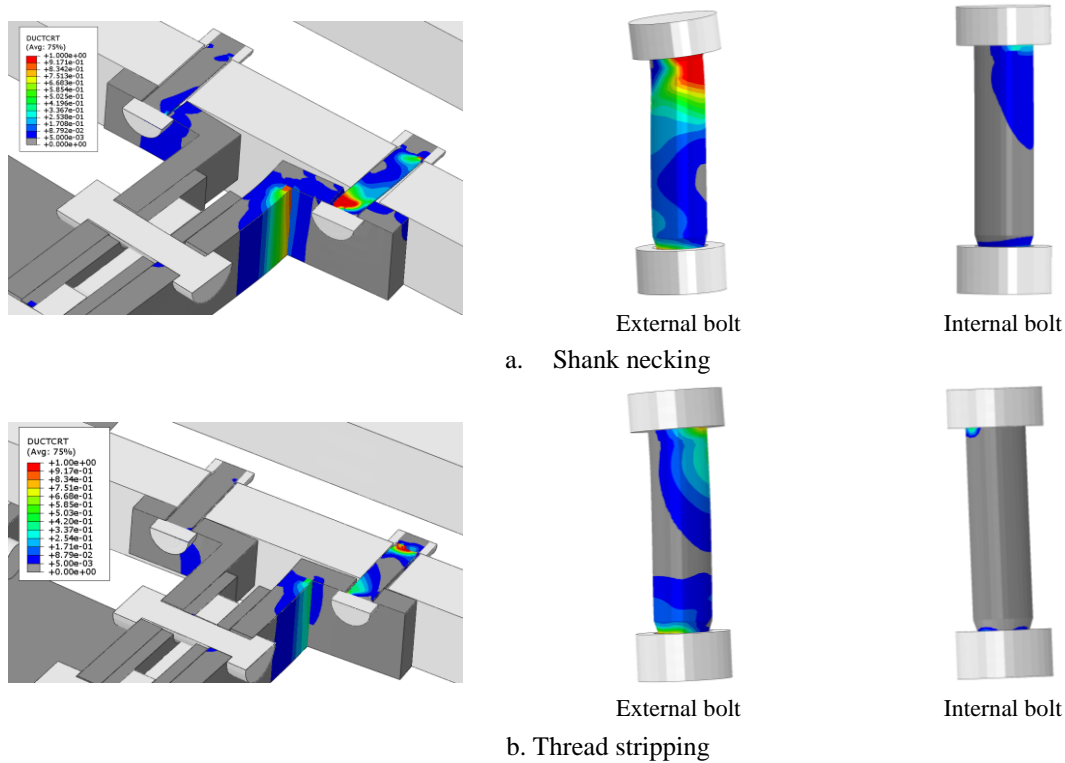
b. Thread stripping

Fig. 5.35. Failure modes – Effect of bolt ductility

Due to the benefits in avoiding the thread stripping failure observed under sagging moment, an additional simulation under hogging moment was carried out. The results are reported in Fig. 5.36 and in Table 5.6, in terms of moment-rotation curve and local deformation of the T-stub. Similarly to what was observed under sagging bending moment, a higher resistance is observed. However, this increase in the resistance is, in this case, is lower than the value observed under sagging moment (7%), since the asymmetry of the bolt rows is not very significant. In addition, an increase of ductility capacity is observed (an increase of 59%). Concerning the failure mode, a larger elongation of the bolts is observed, being the failure localized at the transition between the thread and unthreaded zones, as depicted in Fig. 5.37.

a. Moment rotation curve

b. F-δ of T-stub
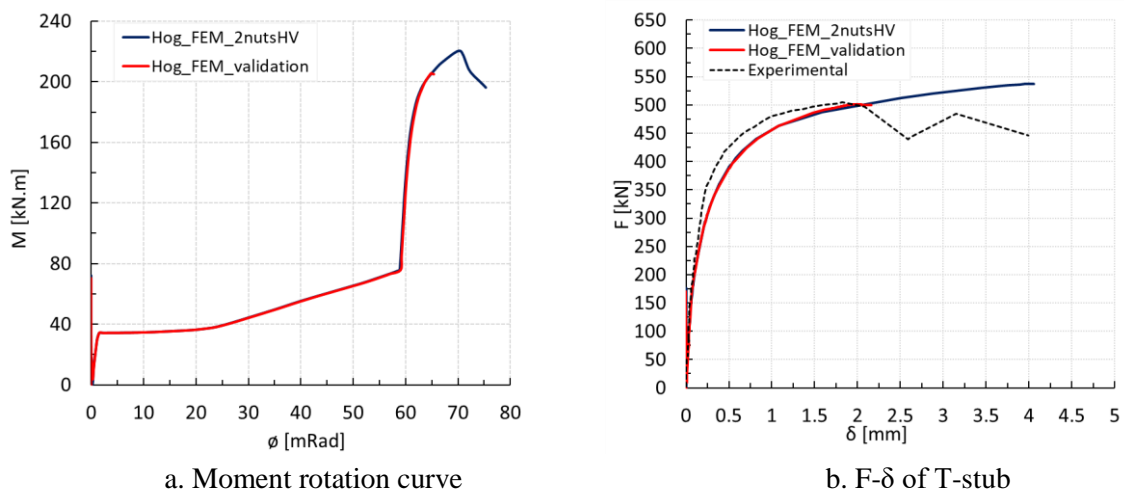
Fig. 5.36. Effect of bolt ductility under hogging moment – M-ø and F-δ curves

a. Shank necking

b. Thread stripping
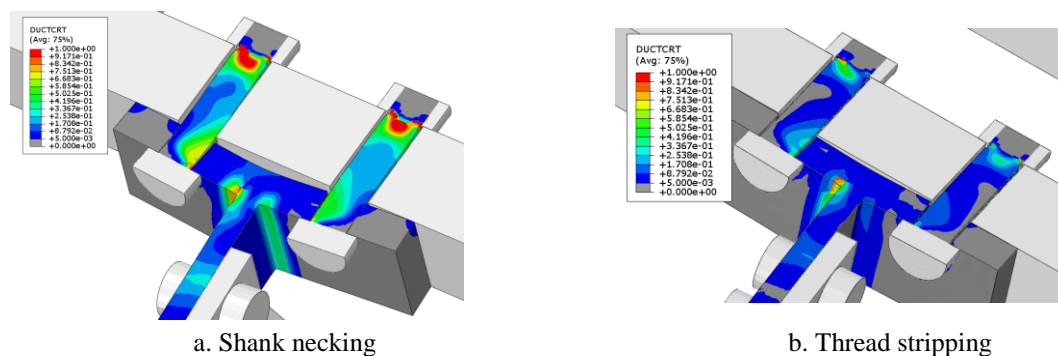
Fig. 5.37. Failure mode under hogging moment – Effect of bolt ductility

Table 5.6. FEM results under quasi-static loading

Bending direction	Hogging		Sagging	
Model ID	Hog_FEM_validation	Hog_FEM_2nutsHV	Sagging	Sag_2nutsHV
M_{slip} [kN.m]	35	35	28.8	28.82
S_{ini} [kN.m/mRad]	47.37	47.37	20.83	19.23
M_{Rd} [kN.m]	189.87	202	111.83	138.10
*ϕ_{Rd} [mRad]	4.01	4.27	5.37	7.18
M_u [kN.m]	205.58	220	113.27	149.76
*ϕ_u [mRad]	7.63	12.91	6.11	12.56
Ductility index φ	1.9	3.03	1.14	1.75
E_{diss} [kNm.mRad]	3804.64	4956.87	2684.59	34126.97
*Rotations value only after slip				

149

5.3.4.3 Behaviour under different velocities

The influence of the velocity of the application of the load on the connection behaviour was tested, under both hogging and sagging moment, for the velocities 100 mm/s, 600 mm/s and 1m/s. In Table 5.7 the "*dynamic factors*" (*DF)* for some behavioural parameters of the connection are reported, namely: (i) friction resistance M_{slip}, (ii) initial stiffness after slip S_{ini}, (iii) ultimate resistance M_u, (iv) ductility capacity after slip ϕ_u and (v) dissipated energy E. These factors are obtained from the ratio between the dynamic behaviour of the connection and its reference static behaviour.

From the curves provided in Fig. 5.38 it is observed that the connection behaves in the same way as observed under quasi-static loading. At the beginning of the analysis, the behaviour is controlled by the friction behaviour of the connection, with an increase of the bending moment at the beginning of the slip M_{slip}. After slip, it is observed an increase of resistance, while the ductility capacity slightly decreases. It is also noticed that the variation of resistance is more significant under hogging moment, which is probably related to the strain rates developed in the failing components as it is depicted in Fig. 5.39 for the ultimate load. In fact, under hogging moment, the strain rates induced at the failing component (external bolts) are slightly higher. However, this would not lead to a significant increase in the dynamic increase factor of the materials (DIF) according to the Johnson Cook law (Eq.2.). In this way, it seems that the difference in the increase of resistance is more related to the different strain rates activated in the internal bolts, which are significantly higher in the T-stub under hogging moment. This difference is related to the different contribution of the bolt rows of the L-stubs, as explained through this Chapter.

With reference to the initial stiffness after slip S_{ini}, a significant change of this parameter was not noticed. This seems to be in agreement with the conclusions of Ribeiro *et al.* [10] for T-stub components.

Additionally, it is always noticed that an increase of the energy dissipation capacity of the connection occurs, except for the velocity of 1000mm/s under hogging moment in which the energy dissipation capacity is equal to the value under quasi-static loading. The increase of the energy dissipation capacity is related to the increase of resistance of the connection for higher velocities. However, under hogging moment, at 1000 mm/s the reduction of ductility is more significant than under 600 mm/s, while the increase of resistance is similar. For this reason, the energy dissipation capacity decreases.

Table 5.7. Behaviour of the connection - FEM results

Velocity [mm/s]		Hogging				Sagging		
	QS	100	600	1000	QS	100	600	1000
M_{slip} [kN.m]	35.0	35.9	36.4	40	28.82	28.85	29.85	29.94
S_{ini} [kN.m]	47.37	47.14	47.62	47.771	19.23	19.231	19.231	19.231
M_{Rd} [kN.m]	202.00	222.18	229.65	231.33	138.10	148.41	161.67	152.93
M_u [kN.m]	220.00	240.97	244.80	246.86	149.75	157.34	161.10	163.00
ϕ_u [mRad]	12.91	13.21	12.55	11.40	12.56	12.43	12.46	12.24
E [kNm.mRad]	4956.87	5241.27	5223.92	4937.06	3426.97	3451.72	3521.44	3531.36
DF	M_{slip}	-	1.02	1.04	1.14	-	1.00	1.04	1.04
	S_{ini}		1.00	1.01	1.01		1.00	1.00	1.00
	M_{Rd}		1.10	1.14	1.15		1.07	1.10	1.11
	M_u		1.10	1.11	1.12		1.05	1.08	1.09
	ϕ_u		1.02	0.97	0.88		0.99	0.99	0.97
	E		1.06	1.05	1.00		1.01	1.03	1.03

a. Hogging moment   b. Sagging moment
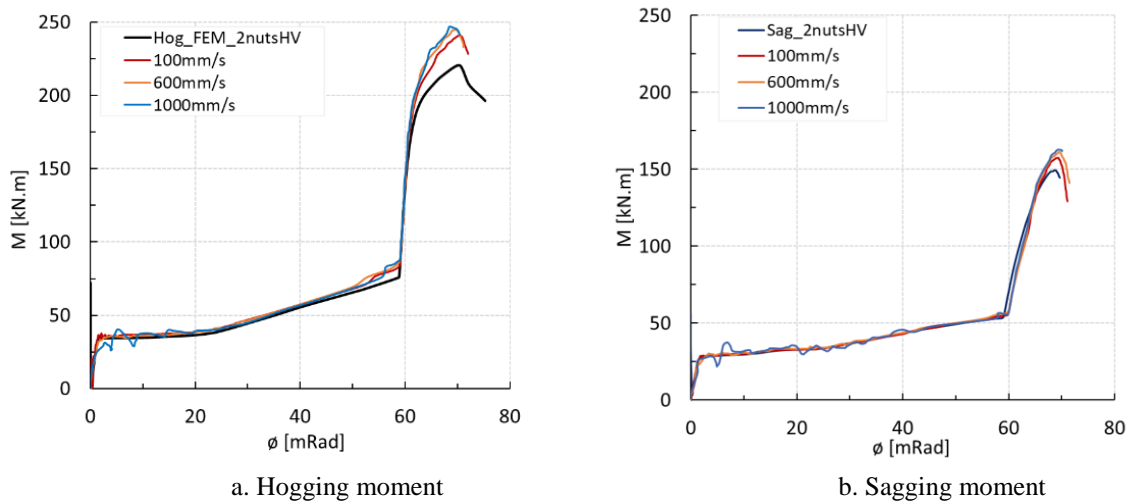
Fig. 5.38. Parametric study: behaviour under different velocities – Moment –rotation curves

a. Hogging moment
b. Sagging moment
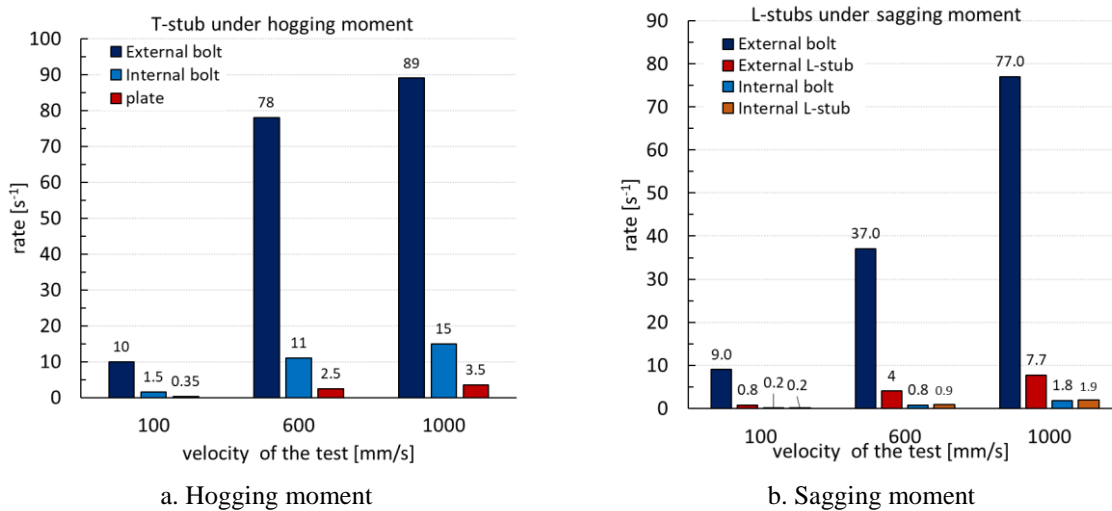
Fig. 5.39. Parametric study: behaviour under different velocities – Strain rates at ultimate load

5.4 Discussion of results

Throughout this chapter, the work related to the behaviour of the FREEDAM connection was reported. This work consisted of an experimental campaign and numerical studies through the development of a 3D finite element. The influence of the loading rate to the connection behaviour was investigated considering both hogging and sagging bending moment.

The experimental tests under hogging moment have shown that the connection behaves according to the design assumptions in both static and dynamic tests, i.e. up to the edge of the slotted holes the behaviour is governed by the friction properties of the friction damper. Secondly, after slip, the ultimate resistance is provided by the T-stub in tension, following the collapse mode 2 of the Eurocode 3 Part 1-8 [5]. However, the rotation capacity of the connection was affected by the earlier bolt failure by nut thread stripping, due to the use of high strength bolts class 10.9 HV.

Under impact loadings, an increase of the friction resistance of the connection was observed, which is in agreement with the conclusions drawn in Chapter 3 concerning the behaviour of the friction damper under impact loading. After slip, a significant difference in the initial stiffness was not observed. The collapse was not achieved due to limitations of the experimental layout.

The numerical study showed that the connection behaviour under hogging and sagging bending moment is not symmetric. This asymmetry up to the slip was already proved by the experimental and numerical work carried out by Latour *et al.* [42] and it has been related to the higher opening of the L-stub when compared to the T-stub opening under hogging moment.

After slip, the asymmetric behaviour is due to the different contribution of the upper and lower L-stubs. In particular, this asymmetry even though predictable due to the lever arms of the L-stubs in relation to the centre of rotation, was significantly greater than expected. This was mainly due to the deformation of the friction damper bolts in shear and at the ultimate load, which were not all in contact with both L-stubs webs. It was demonstrated through FE that this behaviour could be improved by avoiding the brittle nut thread stripping failure of the tee elements bolts.

With reference to the dynamic behaviour of the connection, in general, it is observed that an increase of the initial friction resistance occurs with the speed of the tests as well as an increase of the elastic and ultimate resistance. Conversely, the ductility capacity decreases although not significantly. In addition, no significant changes were observed in the initial stiffness of the specimens.

Chapter 6   Component-based method to assess the behaviour of FREEDAM connections under different loading rates

6.1 Introduction

The real behaviour of steel connections is difficult to assess analytically since it is characterized by complex multi-phenomena such as material and geometrical nonlinearity, nonlinear contact between the several elements and residual stresses. The first efforts to characterized steel connections by means of analytical procedures were focused on resistance and elastic stiffness [85] and their findings are adopted in the Eurocode 3 part-1-8 [5] by the component method. This method provides to break up the joint into elementary components, which are individually characterized and then assembled into a single rotational spring representing the moment-rotation response of the connection.

In general, the individual response of the components can be represented in terms of force versus displacement curves through four parameters, namely: the elastic resistance and stiffness, the post-elastic stiffness and the ultimate resistance or ductility. The first two are addressed in Eurocode 3 part 1-8 [5], while for the others, no formulations are available. Recent researches, focused on the post-elastic response of typical components used in steel connections, have found that the post-elastic stiffness generally ranges from the 1% to the 5% of its elastic stiffness [106,107]. Concerning the ductility capacity δ_u, this is generally expressed as a function of its deformation at yielding δ_y by a ductility index φ [106], Eq.(6.1).

$$\varphi = \frac{\delta_u}{\delta_y} \tag{6.1}$$

According to the proposal of Kulhman *et al*. [101], each component can be defined as belonging to one of three categories of ductility: high ductility, limited ductility and brittle

components. Later, Simões da Silva *et al*. [106] suggested values of ductility index limits for each class of ductility. For the components with high ductility (such as column web in tension, column web in shear) a value higher than twenty was suggested ($\varphi > 20$), while for components with limited ductility (plate in bearing, T-stub in bending, plates in tension) a value between 3 to 20 was recommended. For brittle components, the authors indicated a ductility index lower than three, but, they recommended that, in the design, these components ductility should be taken equal to 1.0 [106].

In the cases where strain rates are relevant, besides the parameters previously mentioned, the influence of the strain rates on the strength (yield and ultimate strengths) and ductility capacity of each component must be also defined. On this matter, the codes do not provide any information whereas, in literature, only the models developed by Stoddart *et al*. [11] and Ribeiro *et al*. [10] described in Chapter 2 were found.

In this chapter, a component-based analytical approach for the FREEDAM connection studied under quasi-static and dynamic loads is presented. Both the behaviour for hogging and sagging bending moment is analysed.

6.2 Modelling of the individual components

According to the component method codified in Eurocode 3 Part 1-8, under hogging and sagging moment, the connection is composed by the components reported in Fig. 6.1. Each component is modelled with an axial spring characterised by a non-linear force-displacement curve (F-δ) characterized by resistance, stiffness and displacement capacity. In terms of design, the components can be divided into three groups, namely:

1-   Column components (black coloured in Fig. 6.1), namely the components column web in shear *cws*, column web in tension *cwt* and compression *cwc*.

2-   Components design as T-stub components (red coloured in Fig. 6.1), which include the tee elements in bending and the column flange in bending. The non-linear behaviour of these elements is obtained with the model developed by Francavilla *et al*. [15].

Components design as shear lap joints (Green coloured in Fig. 6.1), which include the components of the friction damper and the upper T-stub web. The force-displacement up to failure of these elements are obtained applying the model presented in Chapter 4 for the friction damper.

a. Hogging moment

b. Sagging moment
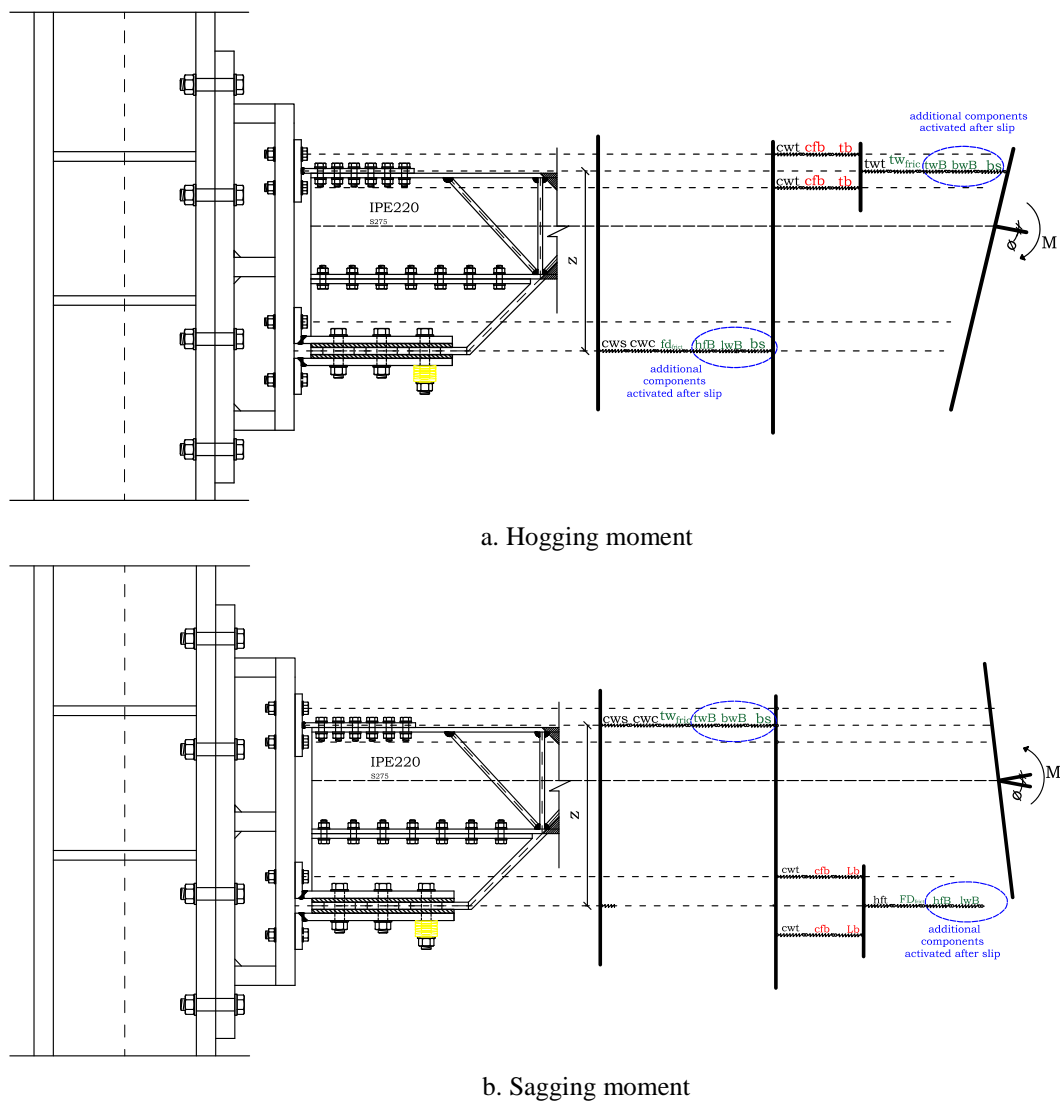
Fig. 6.1. Active components under bending moment

As observed in the FEM simulations carried out in the previous chapter, the connection behaviour is asymmetric and so, the spring model to be developed had to describe correctly this asymmetry. In this way, four springs were used (Fig. 6.2) namely a top spring representing the T-stub components, a couple of lower springs representing the behaviour of the exterior and interior L-stubs and the last one placed in series with the L-stubs' springs, representing the friction damper behaviour. This assumption is acceptable for the T-stub bolt rows because they are close enough and symmetric with respect to the T-stub web. Each spring was implemented adopting a nonlinear force-displacement F-δ response considering in each component the

influence of the strain rate (see Annex B). The values introduced in the FEM model for the plates and bolts were also used here.

The analytical model previously described was implemented in ABAQUS. The model was built, using the one-dimensional elements B31 for column and beam and axial springs to represent the components of the connection (Fig. 6.2). As in the previously presented 3D FEM model, in order to simulate the impact on the connection, a monotonic displacement or velocity was imposed at the tip of the column. Conversely, the column and the beam were restrained at the end according to the laboratory scheme.
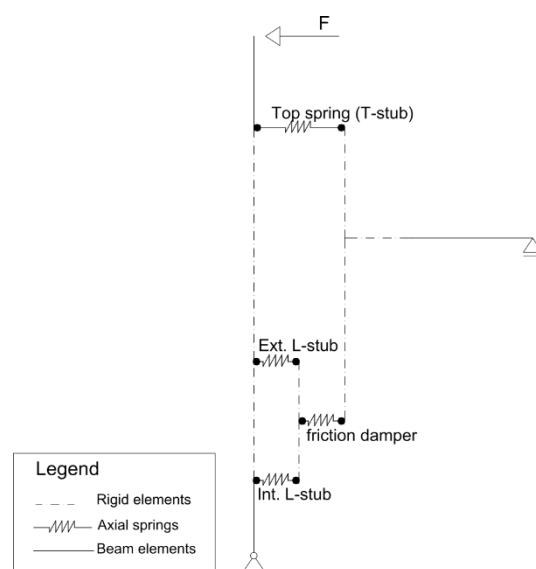
Fig. 6.2. Spring model in ABAQUS

6.2.1 Column components

These elements are designed considering a bilinear force-displacement curve, where the elastic parameters are designed according to the formulation of the Eurocode 3, while for the post-elastic stiffness and ductility capacity, the suggestions of [101,106] were followed (Table 6.1).

Table 6.1. Column components - Formulation

Component	Formulation			
	Elastic Resistance [kN]	Elastic Stiffness, k^e [mm]	Post-limit stiffness[106]	Ductility index φ
1 Column web in shear (cws)	$V_{wp,Rd} = \dfrac{0.9 \cdot f_{y,wc} \cdot A_{vc}}{\sqrt{3} \cdot \gamma_{M0}}$	$k_1 = \dfrac{0.38 \cdot A_{vc}}{\beta \cdot z}$	4.6% k_1	$\varphi_{min} = 20$
2 Column web in compression (cwc)	$F_{c,wc,Rd} = \dfrac{w \cdot b_{eff,c,wc} \cdot t_{wc} \cdot f_{y,wc}}{\gamma_{M0}}$ but $F_{c,wc,Rd} \leq \dfrac{w \cdot \rho \cdot b_{eff,c,wc} \cdot t_{wc} \cdot f_{y,wc}}{\gamma_{M1}}$	$k_2 = \dfrac{0.7 \cdot b_{eff,c,wc} \cdot t_{wc}}{d_c}$	2.3% k_2	3-5 [106]
3 Column web in tension (cwt)	$F_{t,wc,Rd} = \dfrac{w \cdot b_{eff,c,wc} \cdot t_{wc} \cdot f_{y,wc}}{\gamma_{M0}}$	$k_3 = \dfrac{0.7 \cdot b_{eff,t,wc} \cdot t_{wc}}{d_c}$	1.7% k_3	$\varphi_{min} = 20$

6.2.2 Components designed as tee elements

The analytical procedure of Francavilla *et al.* [15] was chosen to describe the behaviour of the components of the connection modelled as tee elements. This model allows the definition of the T-stub response up to failure by defining the geometry of the elements, boundary conditions and the non-linear behaviour of T-stub components, i.e. plate and bolts, and it is in line with the methodology of the Eurocode 3 Part 1-8 [5].

The flange of the T-stub is modelled as a simplified beam (Fig. 6.3a) where the distance *m* and *n* are defined according to Eurocode 3, i.e, *m* is the distance between the bolt line and the plastic hinge at T-stub stem and is equal to *d-0.8r,* while *n* represents the distance between the bolt line and the end of the plate. The bolt forces are uniformly spread under the bolt head over a length equal to the washer diameter, d_w (Fig. 6.3b), while the bolt shank is modelled as a translational spring allowing to check the resistance of the bolt and to evaluate the compatibility condition between the elongation of the bolt and the deformation of the plate. Due to symmetry condition, the beam comprising the T-stub flange is assumed to be constrained with a bi-pendulum, in correspondence to the stem. The contact zone is modelled with prying forces applied in a point located between the tip of the plate and the edge of the bolt head, whose position is determined evaluating the compatibility of the vertical displacements of the plate in order to respect the horizontal symmetry condition (*Q* in Fig. 6.3b).

a. Geometric discretization of the T-stub   b. Mechanical model
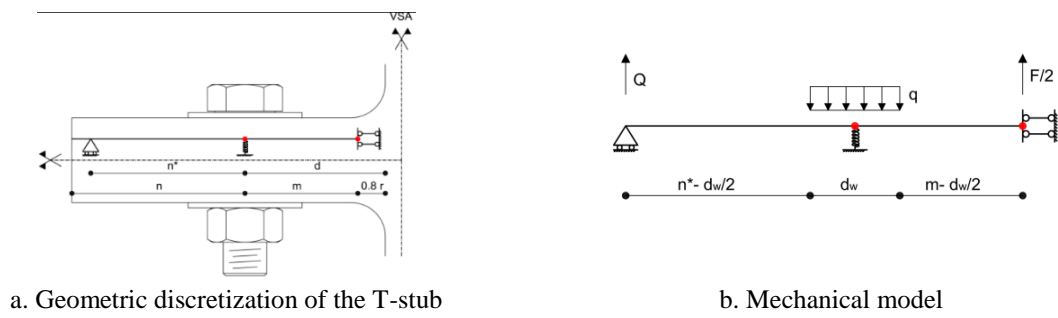
Fig. 6.3. T-stub model [15]

a. Plate   b. Bolt
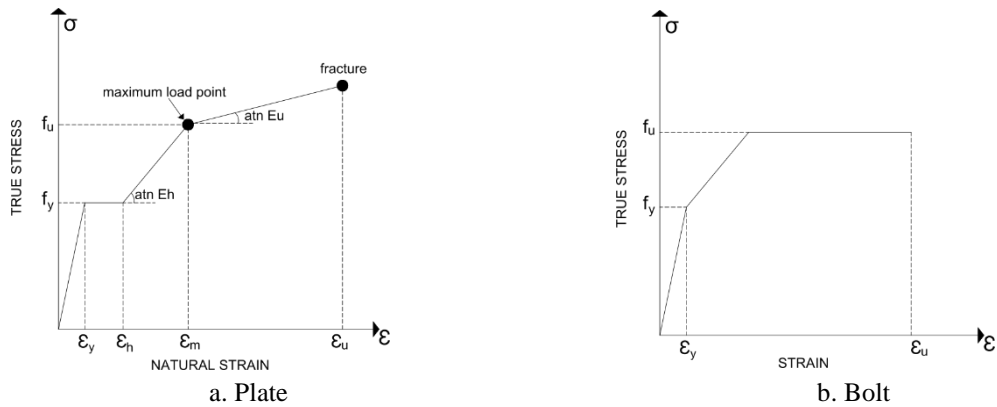
Fig. 6.4. Stress-strain material law of the components composing the t-stub[15]

The behaviour of the plate is defined with a lumped plasticity approach by means of nonlinear plastic hinges located at the T-stub web and bolt line (Fig. 6.3), whose characteristics are derived starting from the moment-curvature diagram of the cross-section representing the plate, according to the approach presented by Piluso *et al*. [108]. For the bolt, the nonlinear spring representing the bolt shank is characterized from the knowledge of the stress-strain law of the basic material (Fig. 6.4). The failure of the elements is modelled by checking the ultimate condition of the stress-strain laws of the materials (Fig. 6.4). Particularly, the failure of the plastic hinges of the plate is identified when the plastic rotation leading to the attainment ultimate strain is achieved at the most external fibre, while the failure of the bolt is identified in correspondence to the uplift value leading to the fracture elongation of the material composing the bolt. All the procedure to assess the behaviour of both bolts and plates is detailed explained in [15]. The assembly of the subcomponents in order to get the whole force-deformation of the T-stub up to failure is made according to the bending distribution and the kinematic failure mechanism depicted in Fig. 6.5a and b, which are solved incrementally by means of the algorithm reported Fig. 6.5c.

The model was compared with experimental tests on T-stubs in tension and the model showed satisfactory results on the safe side with average ratios analytical/experimental higher than 0.9 for the resistance and deformation capacity [15].

Although this model was only calibrated for static loads, here it is adopted to characterize the dynamic behaviour of these components also under impact, which was done modifying the material stress-strain curves of the plates and bolts in the same way as done in the FEM modelling. In Annex B, the curves obtained for each T-stub elements are provided.

a. Kinematic failure mechanism   b. Cantilever scheme for evaluating the plastic rotations
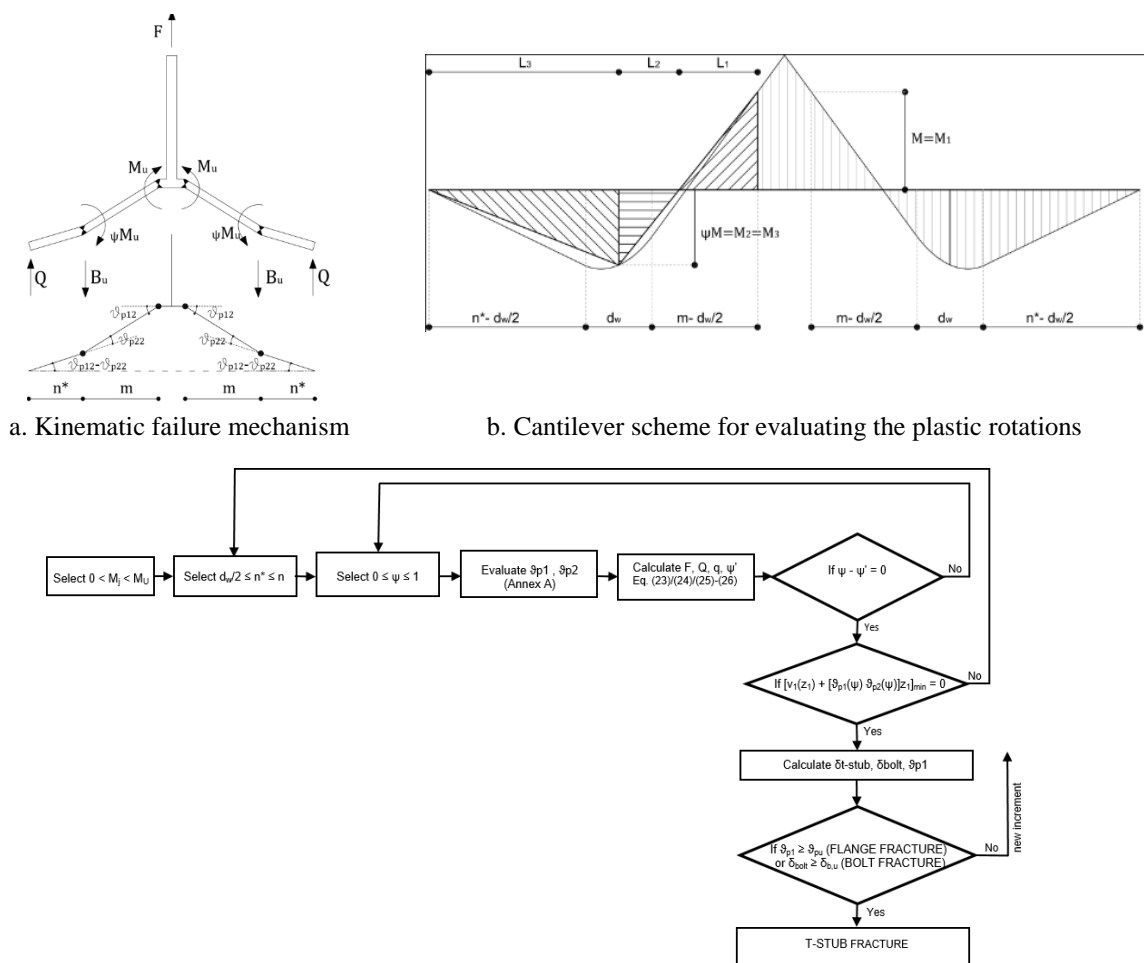
c. Flow chart for solving the equation system

Fig. 6.5. Assembly procedure [15]

6.3 Validation of the analytical approach

The validation of the described analytical approach is done comparing the analytical moment-rotation curves and force-deformation of the components in tension with the

correspondent FEM curves showed in the previous chapter. Since in the FEM models the column is considered rigid, the column components were neglected in the analytical approach.

6.3.1 Validation under quasi-static loads

The validation of the analytical model was done comparing the analytical quasi-static moment-rotation curves and force-deformation of the components in tension with the FEM curves showed previously (Fig. 6.6).

With reference to the behaviour under hogging moment, the model can predict the overall behaviour of the connection, being the error range lower than 10% all behavioural parameter, except for the energy dissipation capacity where the error around 20% (Table 6.2). This higher difference is due to the increase of the force observed in the FEM model during the slip, which was not modelled in the analytical model. Furthermore, the local force-deformation of the T-stub is also accurately predicted (Fig. 6.6b).

Under sagging moment, the spring model can also predict the behaviour of the connection observed in the FEM models accurately, being able to capture the differences observed between hogging and sagging behaviour. In this case, the ultimate resistance and ductility are also predicted accurately as for hogging moment while the initial stiffness is overestimated compared to the one predicted by the FEM models.

Table 6.2. FEM vs analytical model – Quasi-static values

Bending direction	Hogging			Sagging		
Model ID	ANA	FEM	ANA/FEM	ANA	FEM	ANA/FEM
M_{slip} [kN.m]	37	35	1.06	28	28.82	0.97
S_{ini} [kN.m/mRad]	50	47.37	1.06	32	19.23	1.66
M_u [kN.m]	197	220	0.90	135.09	149.76	0.90
*ϕ_u [mRad]	12.38	12.91	0.96	10.56	11.42	0.92
E_{diss} [kNm.mRad]	4042.98	4956.87	0.82	2745.61	3372.90	0.81
*Rotations value only after slip						

Moment-rotation

Tension force vs T-stub deformation

a. Hogging moment

Moment-rotation

Tension force vs L-stubs deformation

b. Sagging moment
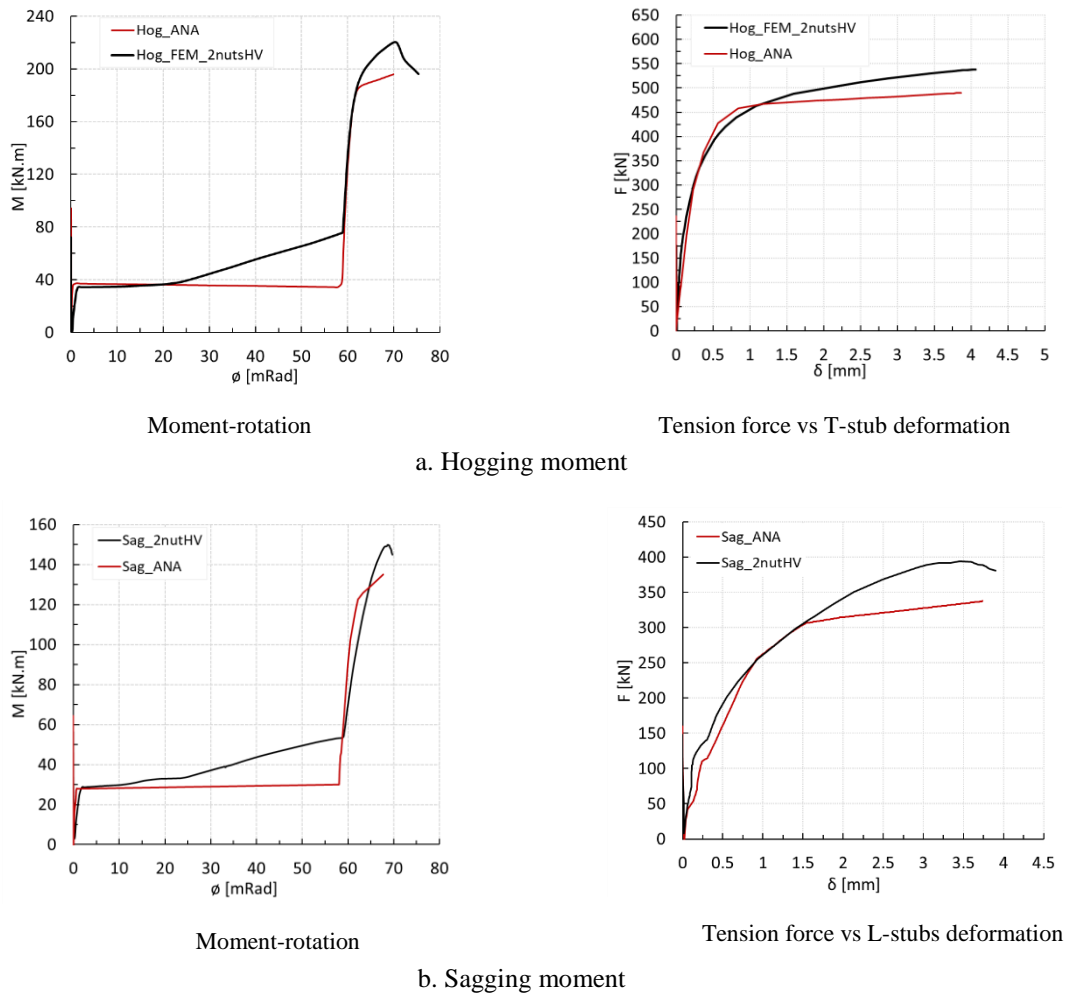
Fig. 6.6. Validation of the analytical model under quasi-static loading

6.3.2 Validation under different loading velocities

The model was tested against the same three velocities used in the 3D FEM models, being the results from this analysis depicted in Fig. 6.7 in terms of moment-rotation curves and in Table 6.3, where the dynamic factors are reported. From the results, it is possible to conclude that the analytical model can predict with enough accuracy (ratio ANA/FEM lower than 10%) the increase or decrease of the selected behavioural parameters. In particular, the increase of resistance of the connection for the considered velocities is very similar to the values obtained in the FEM models. With reference to the ductility capacity, the analytical model shows conservative values in comparison to those observed in the numerical models. However, it should be noted that to assess the force-displacement curves of the components for different strain rates, a constant value was given, which is an approximation of the real behaviour since,

as reported in Fig. 5.39, each element has its own deformation rate which continuously changes during the test. For instance, in Fig. 5.39a, the external bolt of the T-stub has always a higher deformation rate at the ultimate load, followed by the internal bolt and T-stub flange. This approximation can explain the conservativism generally observed in the analytical model.

In addition, the model shows accurate values for the variation of the energy dissipation capacity of the connection.

a. Hogging moment   b. Sagging moment
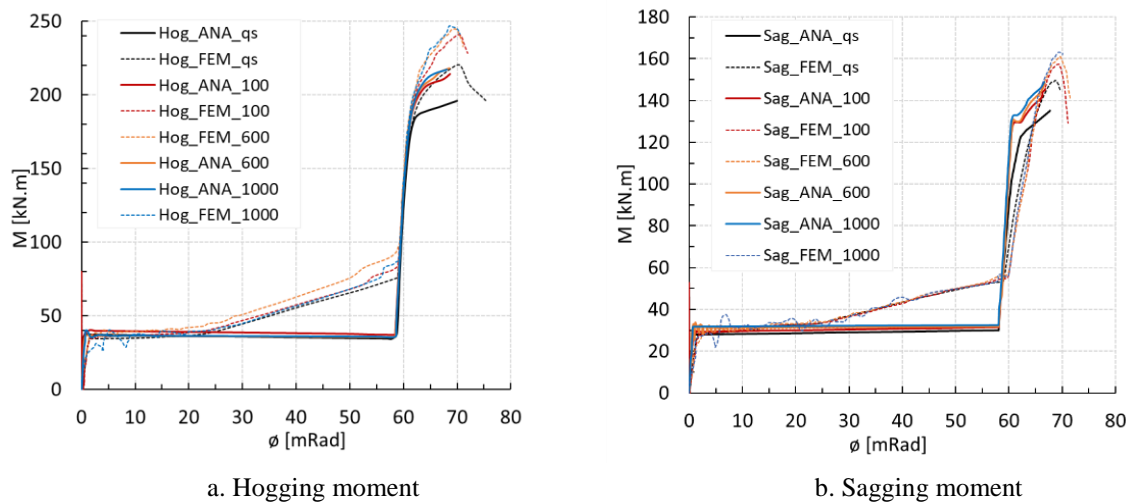
Fig. 6.7. Validation of the analytical model under dynamic loading

Table 6.3. FEM and analytical results – Dynamic factors (DF)

Velocity [mm/s]		Hogging			Sagging		
		100	600	1000	100	600	1000
DF_{Mslip}	FEM	1.02	1.04	1.14	1.00	1.04	1.04
	ANA	1.02	1.08	1.09	1.02	1.04	1.09
	ANA/FEM	**1.00**	**1.03**	**0.95**	**1.02**	**1.00**	**1.05**
DF_{Sini}	FEM	1.00	1.01	1.01	1.00	1.00	1.00
	ANA	1.00	1.00	1.00	1.00	1.00	1.00
	ANA/FEM	**1.00**	**0.99**	**0.99**	**1.00**	**1.00**	**1.00**
DF_{Mu}	FEM	1.10	1.11	1.12	1.05	1.08	1.09
	ANA	1.10	1.11	1.11	1.08	1.10	1.10
	ANA/FEM	**1.00**	**1.00**	**0.99**	**1.03**	**1.02**	**1.01**
$DF_{øu}$	FEM	1.02	0.97	0.88	0.99	0.99	0.97
	ANA	0.92	0.90	0.86	0.93	0.91	0.90
	ANA/FEM	**0.90**	**0.93**	**0.98**	**0.94**	**0.92**	**0.93**
DF_E	FEM	1.06	1.05	1.00	1.01	1.03	1.03
	ANA	1.03	1.06	0.95	1.02	1.04	1.06
	ANA/FEM	**0.97**	**1.01**	**0.95**	**1.01**	**1.01**	**1.03**

6.4 Discussion of results

Throughout this chapter, an analytical approach to assess the behaviour of the FREEDAM connection when subjected to both quasi-static and dynamic loading was described.

The presented approach is based on the component method codified in Eurocode 3 Part 1.8 and it allows assessing both the elastic and post-elastic behaviour under static and impact loading conditions.

The analytical model was compared with the numerical simulations reported in Chapter 5, and satisfactory results were found. However, it should be noted that, in the analytical model, the strain rate was considered constant during the impact and equal for all the components composing the connection, while in an impact scenario, the strain rate changes continuously and each component has its own deformation rate. Nevertheless, it is also useful to observe that the effect of strain rates could be easily accounted for in the mechanical model of the connection, component by component, obtaining a variation of the behavioural parameters of the connection very similar to those observed in the experiments and numerical studies. The proposed analytical model is useful, in general, to model the behaviour of moment resisting frames, including the response of connections, into an impact loading scenario, as shown in the next Chapter of this thesis.

Chapter 7   Robustness of steel frames

7.1 Introduction

In this chapter, the robustness of 2D steel frames is investigated. The purpose is to evaluate the robustness of a steel frame with the connection under study in this thesis, i.e the FREEDAM connection, when subjected to an impact on one of its external columns. In addition, the behaviour of the frame is compared with the response of the same frame with a more traditional typology of connection. For this purpose, the dog-bone shape connection was chosen.

In this study, two approaches were considered: (i) removal of the support external column (column loss scenario) and (ii) lateral impact by a vehicle, in order to check the differences in the structure behaviour when the impact event is explicitly considered.

In the first approach, two types of analyses were considered, namely, a preliminary nonlinear static pushdown analysis, which allowed a first estimation of the robustness of the analysed structures and a "sudden" column loss dynamic analysis. The comparison between these two analyses highlighted the importance of considering the dynamic effects on the robustness of frames.

Finally, in the second approach, a lateral impact from a vehicle in one external column is considered. The vehicle and the impact velocities were modelled as recommended in Eurocode 1 part 1-7 [16].

7.2 Design of the frame and connection typologies

The frame used is the same as used in Francavilla's PhD thesis [109] (Fig. 7.1), used in her thesis to perform IDA seismic analysis as well as nonlinear static pushdown analysis considering the loss of the middle ground floor column. The frame is assumed to be a perimeter

frame from a building and it is composed of four bays and six storeys. The interstorey heights are equal to 3.20 m except for the first storey whose height is equal to 3.50 m. The bay span L_t is equal to 6 m.

The beams were designed to withstand vertical loads assuming a design maximum beam plastic moment approximately equal to $qL^2/8$ (even though this distribution of bending moments does not corresponds to the exact bending moment distribution of the structure due to the connections adopted, it is a conservative value for the beam design). Therefore, an S275 steel IPE270 profile was adopted. The column sections were selected adopting the theory of plastic mechanism control design procedure (TPCM), developed by Mazzolani and Piluso [111] and improved by Montuori *et al*. [112]. This design method is based on a rigid-plastic analysis and on the kinematic theorem of plastic collapse, extended to the concept of the equilibrium curve mechanism, and it assures that, under seismic actions, a global collapse mechanism is achieved. In other words, it assures that a mechanism involving all the dissipative zones of the frame is achieved. The method has already been employed in several works where its reliability under seismic actions is proven [113].

Regarding the design loads, a uniform dead load g_k=4.00 kN/m^2 and a uniform live load q_k=2 kN/m^2 have been considered. Since the analysed frame is a perimeter frame, a uniform dead load G_k=$gk·L_t/2$=12.00 kN/m and a uniform live load Q_k=$q_k·L_t/2$= 6 kN/m were obtained. The accidental load combination according to Eurocode [110] was considered to determine the vertical load distribution, i.e. q= $G_k + Q_k$= 18.00 kN/m.

In the robustness analyses, two connection typologies were considered. The first connection (FREEDAM-CYC01) have the same geometric details as the connection studied in Chapter 5 and 6 of this thesis, but in a bigger scale, as shown in the drawing of Fig. 7.2a. The second connection presented in Fig. 7.2b (EEP-DB-CYC 03) is a rigid bolted endplate connection with the particularity of having a cut at the beam-end. The cut has a bone shape and this region is designed as the dissipative member of the connection. For this reason, these connections are known as dog bone connection.
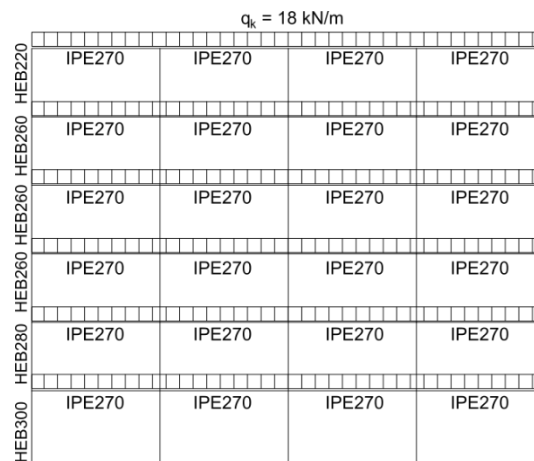
Fig. 7.1. Analysed Frame [109]
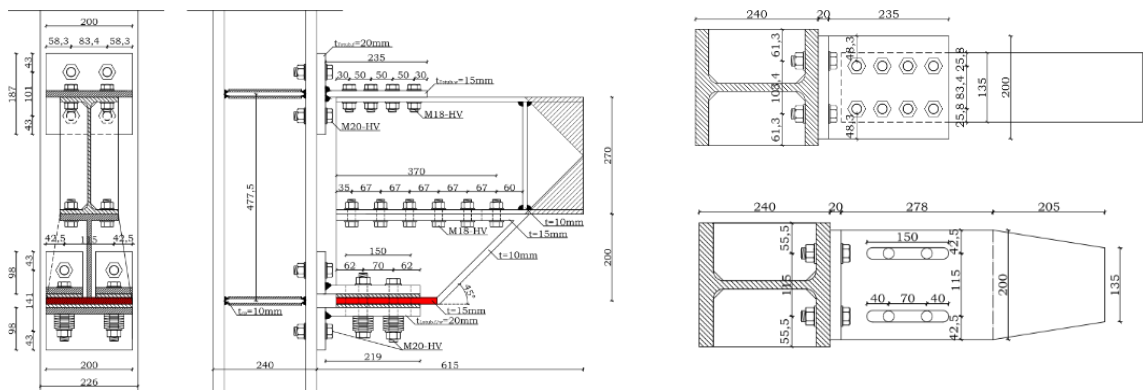
a. Freedam CYC 01
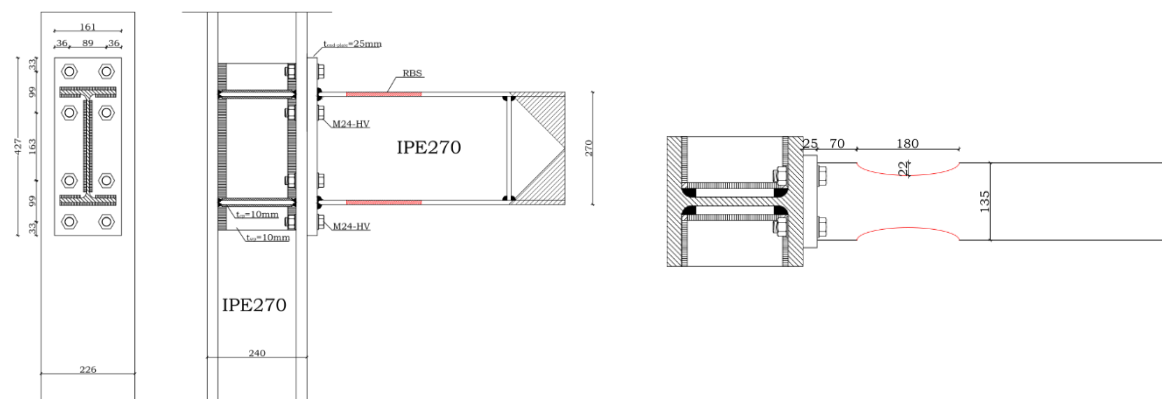
b. Rigid connection - EEP-DB-CYC 03

Fig. 7.2. Connections used in robustness analyses [109]

7.3 Connection and frame modelling

The structure was modelled in ABAQUS/Standard software [13]. Both beam and columns elements were modelled using linear B31 beam element. The use of these elements allows to decrease the computation time and still get accurate results [22]. The quadrilinear curve of Fig. 6.4a was used to characterize the stress-strain curves of these elements, using the values indicated by Francavilla [109] (Table 7.1). Furthermore, the dynamic behaviour of the column and beams elements was considered introducing the dynamic increase factor (*DIF*) and damage parameters, as described in the previous chapters of this thesis.

Table 7.1. Mechanical parameters beam/columns [109].

Element	f_y [MPa]	f_u [MPa]	E [MPa]	$\varepsilon_h / \varepsilon_y$	E / E_h	ε_u	E / E_u
beam	405	546	210000	9.8	48.2	0.8	632.8
column	430	523	210000	9.8	48.2	0.8	632.8

The beam-to-column connections were modelled as described in the previous Chapter, i.e. with axial connectors available in ABAQUS library, connected with rigid beam elements (rigid elements in Fig. 7.3). More specifically, for modelling the FREEDAM the T-stub bolt rows were modelled with an equivalent spring, while the lower part, composed by the L-stubs and the friction damper, was modelled with three individual springs (Fig. 7.3a). In the case of the Dogbone connection, the bolt rows of the upper and lower T-stubs were modelled with two equivalent springs (Fig. 7.3b).

The force-displacement curves introduced in each spring were obtained using the analytical model described in Chapter 6, considering both static and dynamic behaviour, as well as the influence of the column size. All these curves are reported in Annex C. The mechanical properties of the end-plate of the dog-bone connection is given in Table 7.2. These values were taken from the PhD thesis of Francavilla [109]. Furthermore, in the case of the Dog-bone connection (EEP-DB-CYC 03), a reduced cross-section was used in the zone of the reduction section (Fig. 7.3b).

In addition, in the dynamic analyses, masses were applied to the connectors starting from the uniform distributed loads. The columns were considered fixed at the base.

a. Freedam CYC 01   b. Rigid connection - EEP-DB-CYC 03
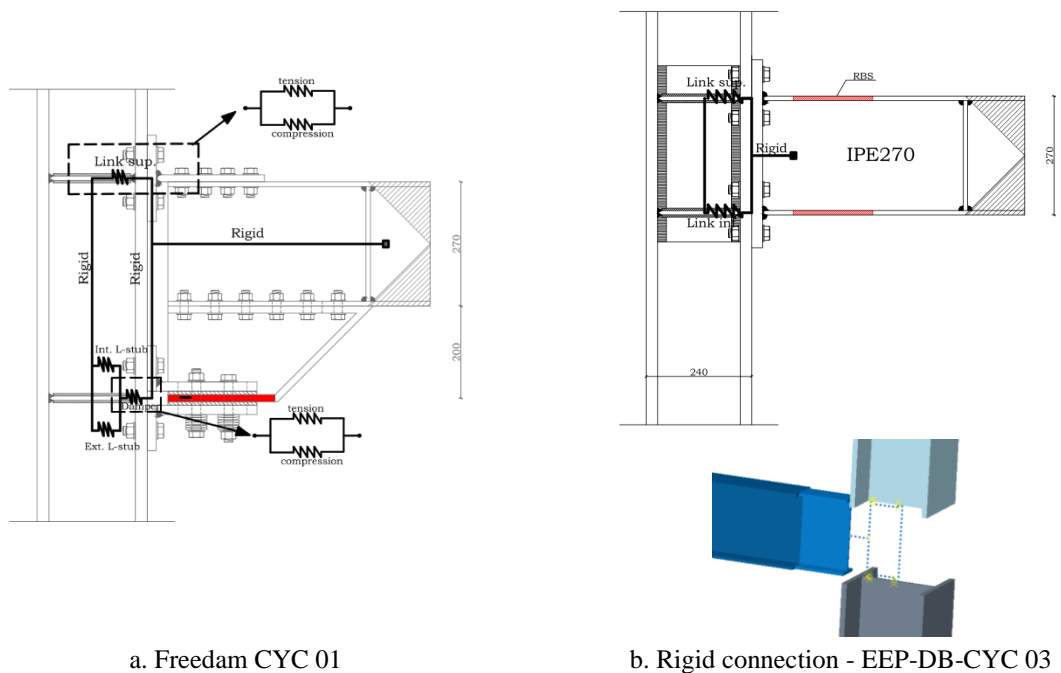
Fig. 7.3. Beam-to-column connection modelling in robustness frame analyses

Table 7.2. End plate mechanical parameters [109]

f_y [MPa]	f_u [MPa]	E [MPa]	ε_h / ε_y	ε_u / ε_y	E / E_h	E / E_u
290	493.7	207288	11.3	589	86.5	632.8

7.4 Column loss scenario analyses

In this subsection, the robustness assessment of the frames is investigated, performing column loss analyses. The removal of the corner column was considered since it is the column that most likely will be impacted by a vehicle. Furthermore, in a frame, the loss of a corner column is more critical than the loss of an interior column, since there are fewer members to redistribute the load after the loss of the column. Two types of column loss analyses were considered, namely: i) Energy balance nonlinear static pushdown analysis (PD) and ii) nonlinear dynamic analysis (NDA).

7.4.1 Analysis procedure

7.4.1.1 Push down analyses

The removal of the columns in the pushdown analysis was simulated with the following procedure. At first, a static analysis on the undamaged frame considering only the vertical loads was performed. From this analysis, the reactions at the column removal were determined. The

column was then removed and its effect was simulated by its reactions forces obtained in the static analysis. Finally, the column removal was simulated by pushing down the node to which the column reactions forces were applied, generating the vertical force-displacement pushdown curve (Fig. 7.4a).

There are several parameters to measure the robustness of structures, which can be divided into local and global robustness measures. The local measures type considered local demand-to-capacity ratios to measure robustness, whereas, in the global type, the robustness is measured through ratios between the load capacity of the damaged structure and the one coming from the gravity load analysis [114]. Here, the deterministic global Residual Strength Ratio (RSR) measurement (Eq. 7.1) was used to evaluate the system.

$$RSR = \frac{F_{u,damaged}}{F_{dyn,damaged}} \tag{7.1}$$

Where $F_{u,damaged}$ is the ultimate capacity of the system after the column removal and $F_{dyn,damaged}$ is the force for which the system reaches the equilibrium in the damaged state (Fig. 7.4a), which is obtained through the energy zero balance method suggested by Izzudin et $al.$ [23] (Fig. 7.4b). This method assumes that the equilibrium in the damaged state is reached when the work done W_{ext} (corresponding to the axial force in the column prior to removal times the total vertical displacement at each step of the analysis, Eq.7.2) equals the internal energy W_{int} (given by the integral of the force-displacement curve of the system, Eq.7.3). The minimum RSR value that a structure can have is 1.0, corresponding to the case when the force for which $F_{dyn,damaged}$ is equal to the ultimate capacity of the structural system in the damaged configuration $F_{u,damaged}$. For cases in which the energy balance is not reached, equilibrium is not reached and the RSR is taken as zero, indicating zero residual strength.

a.Force displacement curve   b. Energy balance method
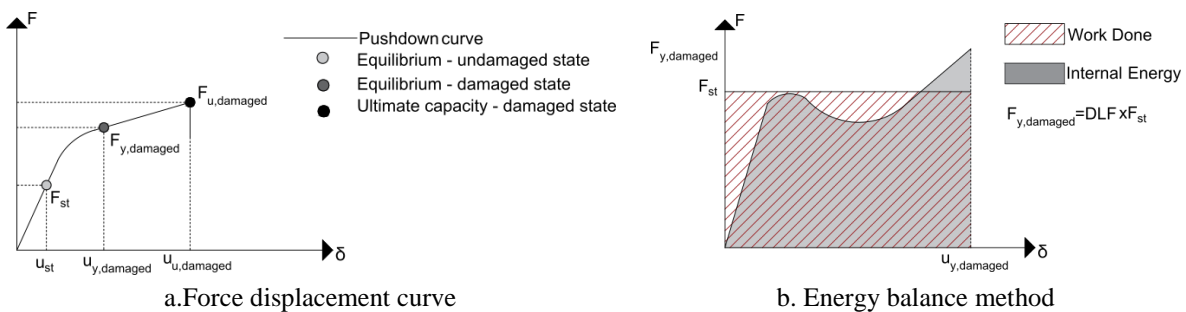
Fig. 7.4: Pushdown analysis – energy balance

$$W_{ext} = F_{st} \cdot u_i \tag{7.2}$$

$$W_{int} = \int_0^{u_i} F(u) \cdot du \tag{7.3}$$

Another important aspect is the capacity of a system to respond to a column loss in the plastic range, taking advantage of the global ductility of the system. This can be measured by calculating the Dynamic Load Factor (DLF), which is given by the Eq.(7.4). In the case where this value is equal to 2, the structure response is completely linear, while a DLF equal to 1 means a rigid-plastic response. If the collapse of the structure is achieved this parameter is equal to zero.

$$DLF = \frac{F_{dyn,damaged}}{F_{st}} \tag{7.4}$$

Finally, the ductility capacity in the damaged state was assessed using the residual ductility ratio (RDR) given by Eq. (7.5), which should always be higher than 1.

$$RDR = \frac{u_{u,damaged}}{u_{dyn,daamged}} \tag{7.5}$$

7.4.1.2 Nonlinear dynamic analysis

For the nonlinear dynamic analysis (NDA), an instantaneous column removal was considered. In the same way as in the pushdown analysis, the structure is slowly loaded considering only the gravity loads, with the equivalent reactions force at the node where the column used to be (Fig. 7.5). Afterwards, the column removal was simulated by decreasing the reactions forces at the node during a time interval t_r (Fig. 7.5). GSA guidelines [50] recommends that this time interval should be equal or lower than 1/10 of the natural vibration period of the structural response mode for the vertical element removal. A frequency analysis was carried out and a natural period equal to 2s has been found and, consequently, a time interval equal to 0.2s according to GSA [50]. However, a sensitivity study on column removal action time interval was performed to verify the applicability of GSA recommendation. In this analysis, the maximum vertical displacement for which equilibrium is reached in the damages configuration was checked.
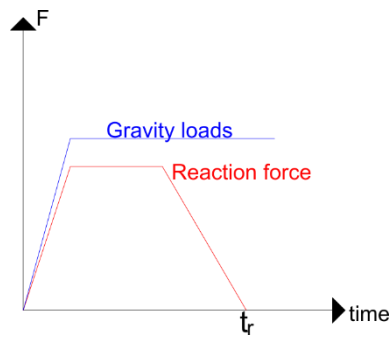
Fig. 7.5. Column loss time history for NDA analysis

7.4.2 Results from pushdown analyses

The response curves obtained from the pushdown analyses are plotted in Fig. 7.6 while Table 7.3 reports the robustness evaluation parameters. In both cases, the structures can find equilibrium in the damaged stage (RSR > 1), showing that both structures have the ability to transmit the forces associated with the loss of the bearing member to the adjacent members, avoiding the progressive collapse. However, the frames show very different behaviour. The frame with dog bone rigid connection achieves the equilibrium with plastification of the beam-ends at the dog bone cut zone as these elements are the dissipative member of the connection (Fig. 7.7), while both columns and connections remain elastic (Fig. 7.8). Conversely, the frame with the FREEDAM connection achieves the equilibrium during the slip phase of the connections (rectangular points in Fig. 7.8), keeping the remaining elastic components of the connections as well as the beam and columns elements. For this reason, there are no plastic strains at the beams/columns as well as at the others components of the connections when the equilibrium in the damaged state is reached (Fig. 7.7). This observation leads to the conclusion that the connections can fulfil their design purposes, i.e. free from damage structures up to the end of the slots.

After reaching the equilibrium, the frames were continually pushed until the attainment of their ultimate load in order to estimate their residual strength (RSR) and ductility (RDR). Both frames have residual strength, being this parameter higher for the frame with the FREEDAM connection, which is also due to the slip path of the connections. As already mentioned, until the achievement of the edge of the slots, the beam/columns adjacent to the connection as well as the remaining components of the connection remain in their elastic range. In this way, the yield of these elements is delayed, reason why a higher residual strength is obtained. In terms of residual ductility, both frames also show good results. However, the frame with the dog-bone

rigid connection has a higher residual ductility, which was expected due to the higher ductility of the beam elements when compared to the ductility of the tee elements and bolts composing the FREEDAM connection. The ultimate resistance was achieved for the dog bone zone of the beams above the removed column and at the upper T-stub for the frame with the dog-bone connection and FREEDAM connection, respectively.

Table 7.3. Robustness parameters from the pushdown analysis

Frame	F_{stat} [kN]	$F_{dyn,damg}$ [kN]	$u_{dyn,damg}$ [mm]	F_u [kN]	u_u [mm]	DLF	RSR	RDR	Failure mode
DB	300	425.4	615	468.7	1164.9	1.42	1.10	1.89	Beam
FREEDAM	279	338.6	376.6	477.3	521.4	1.21	1.41	1.38	Upper T-stub
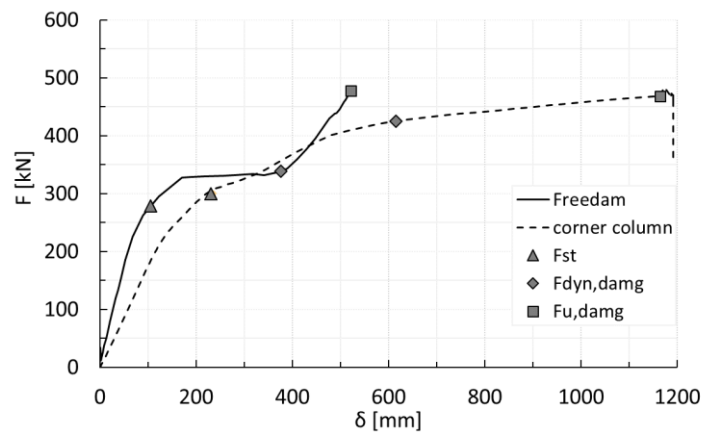
Fig. 7.6. Pushdown curves

Fig. 7.7. Plastic strains at the beams/columns

Localization

Dog bone connection   **FREEDAM connection**
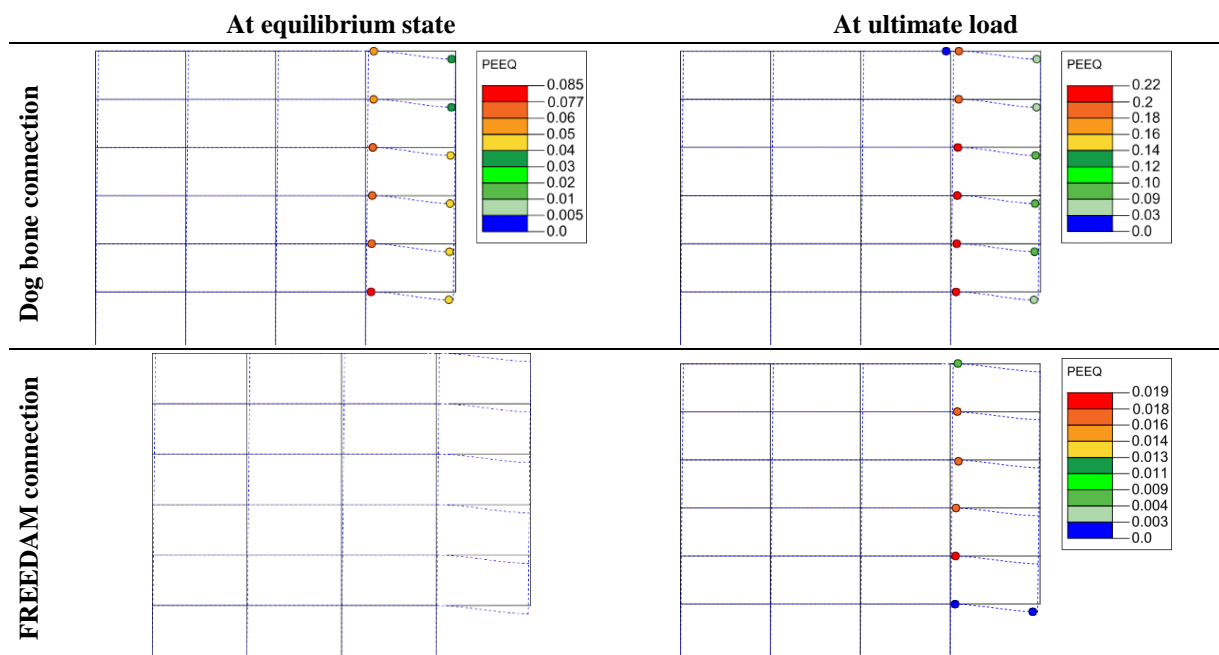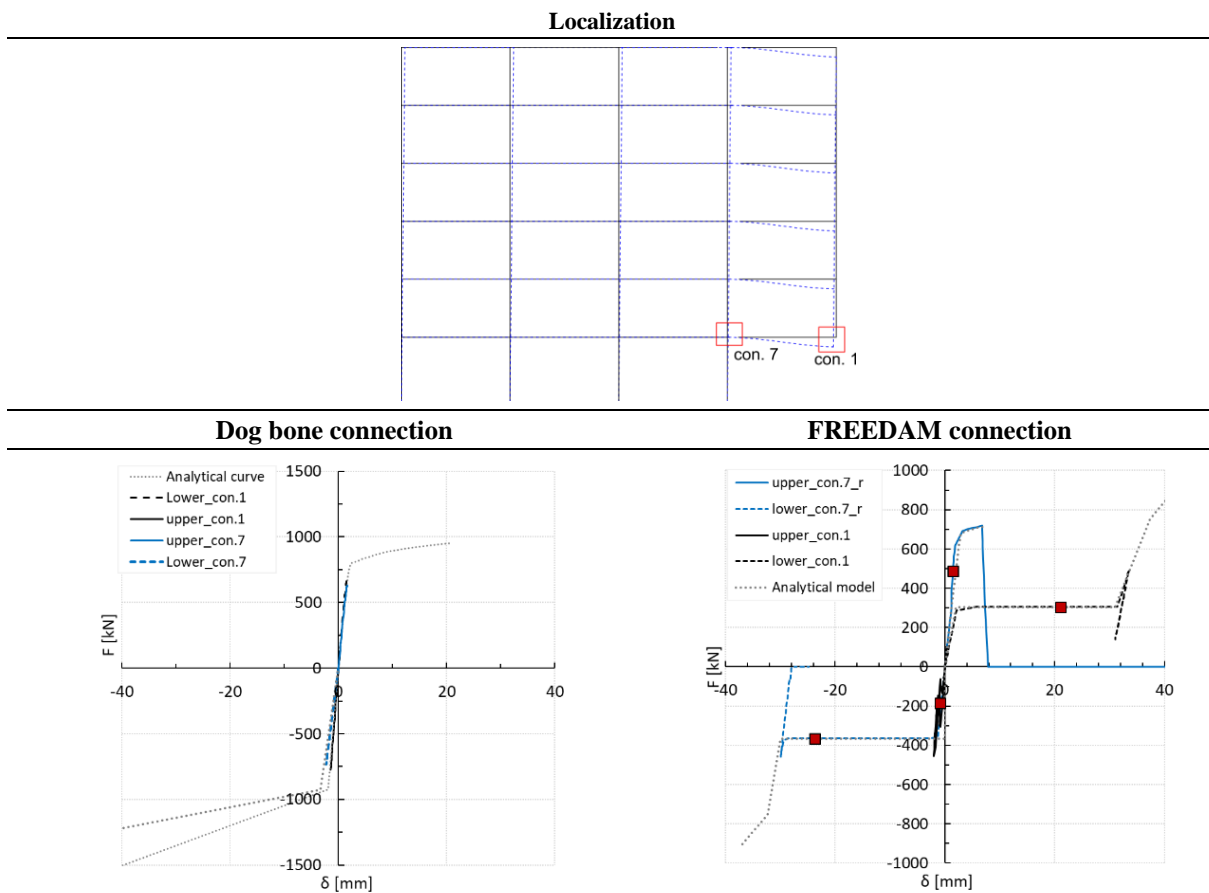
Fig. 7.8. Beam-to-column connections

7.4.3 Results from dynamic sudden column loss analyses

Fig. 7.9 shows the results from the sensitivity analysis performed to check the influence of removal column time. For this analysis, removal times ranging from 1s to 0.01s were considered. From the displacement-time curves, it is clearly visible the effect of the removal column time in both frames. For faster column removal times, the amplification of the vertical displacements is higher and it is achieved within a shorter time interval. However, for times lower than the minimum time recommended by the GSA guideline (t_r = 0.2s), the maximum vertical displacement does not change significantly, providing the accuracy of this suggestion.

The importance in considering the dynamic effects and a correct column time removal in column loss analyses can be understood from the ratio between the vertical displacement to which the equilibrium at damaged configuration is achieved in the pushdown analysis $u_{dyn,damaged}$, with the maximum vertical displacement achieved in the NDA analyses $u_{max,NDA}$ (Table 7.4). As it may be observed, nonlinear analysis induces smaller maximum displacements

in the frame, which is due to the dynamic effects of the analysis and some activation of the strain rate effects at the connections and beam/column elements. However, this difference is higher for the frame with the FREEDAM connections, which is due to the increase of friction resistance due to the dynamic analysis. In the frame with dog bone connections, there is a slight increase in the strength of the beams due to dynamic loading, but not significant.

Comparing both frame solutions, the frame with the FREEDAM connections achieves the equilibrium in its damaged state for a lower maximum vertical displacement (Table 7.4). This was also observed in the preliminary static pushdown analysis, and it is related with the slip mechanism of these connections, i.e. due to the high dissipative properties of the friction dampers, a lower rotation is required to dissipate the same amount of energy and reach equilibrium. In addition, as in the preliminary static pushdown analysis, the frame with the FREEDAM connection does not present any plastic strain at the beam elements nor in the connection components, the damage being localized only at the friction pads. Nevertheless, in both solutions, the progressive collapse is not likely to happen since both frames can achieve equilibrium in their damaged state.

a. Frame with dog bone connection

b. Frame with FREEDAM connection
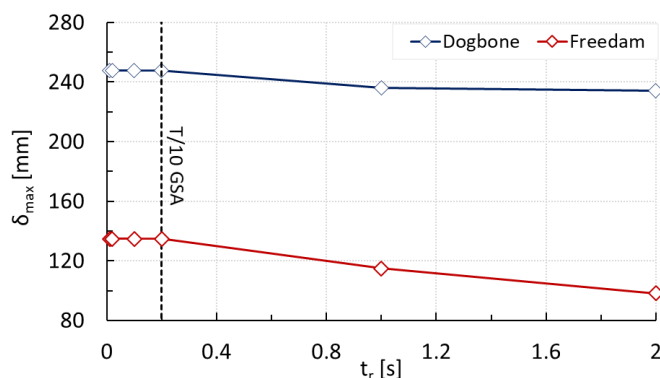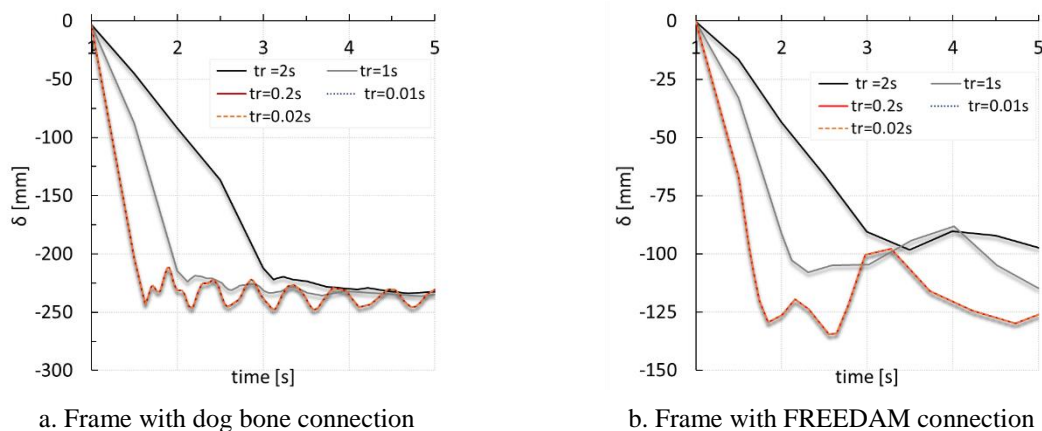
c. Effect of the time removal on the maximum vertical displacement at the damage state

Fig. 7.9. Vertical displacement as a function of the removal time t_r

Table 7.4. Pushdown vs NDA analysis

Connection	$u_{dyn,damg}$[mm]	$u_{max,NDA}$ [mm]	$u_{dyn,damg}$/ $u_{max,NDA}$	Max damage	Max PEEQ	Max ER beams
Dog bone	615	247.9	2.48	Dog bone section	0.026	0.0011
FREEDAM	376.6	134.7	2.80	Friction pads	0	0.0015

7.5 Vehicle impact on external column

7.5.1 Analysis procedure

The simulation has been subdivided into three steps: the first step (static analysis) involves the application of all static loads on the structure. In the second step, the vehicle is accelerated with the required velocity and finally, in the third step, the actual impact is applied. The Abaqus/Standard solver has been adopted for the analysis. For the first two steps, a Static General analysis has been used while for the impact analysis, a Dynamic implicit analysis was used instead.

The chosen impact velocities are those recommended in table C.1 of the Eurocode 1 Part 1.7 [16] (Table 2.5) for urban areas (50 km/h) and highways (80 km/h).

7.5.2 Vehicle modelling

Following the recommendations of Eurocode 1 part 1-7 [16] for the definition of a lateral impact from a lorry vehicle provided in Table 2.5 and Fig. 2.15, the vehicle the vehicle was represented by a rectangular rigid body of 0.5m (height) x 0.3m (width of HEB 300 column) x 1 m (arbitrary dimension) with 10 ton (Fig. 7.10b). The vehicle hits the column at 1 m height (Fig. 7.10a). Furthermore, the front part of the vehicle has a curve shape to facilitate the contact interactions between the vehicle and the impact column.

a. Close up of the impact zone   b. Dimensions of the vehicle (in m)
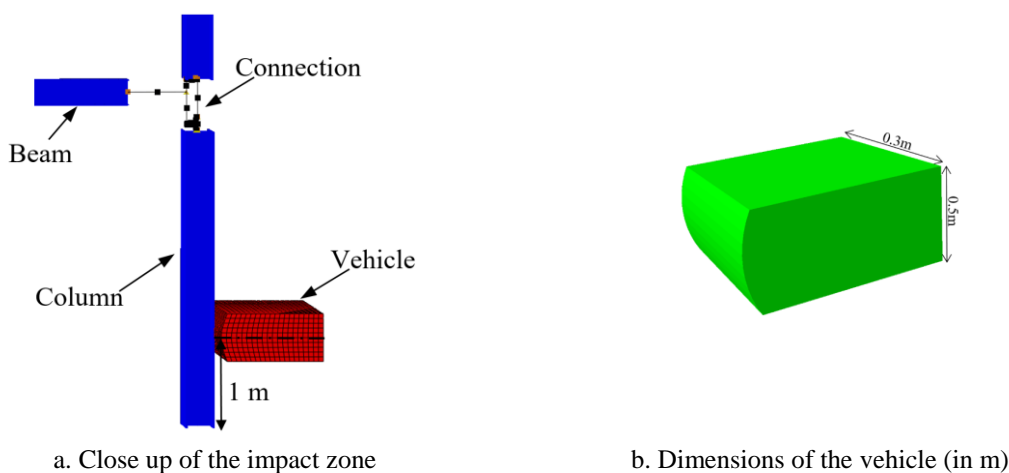
Fig. 7.10. Vehicle model for impact analysis

7.5.3 Results

The results from the impact analyses are reported in terms of vertical displacement time history, final damage configuration of the frames and the force-displacement curves of the more stressed connections.

At 50 km/h, the corner column sustains severe damage in both frames at the impact zone and at the support, as depicted in Fig. 7.11a. However, this velocity was not enough to reach the collapse of the structures and the structures found their equilibrium just in a few milliseconds after the impact (Fig. 7.12a).

For the frame with FREEDAM connections, connection failure was not observed. Concerning the behaviour of the connection at the first storey (con. 1 and 7, see Fig. 7.8), they show a quite different behaviour than in the analyses under column loss. In the column loss analyses, the connections were subjected to tension and compression forces, which means that the forces transmitted to the frame at the achievement of its equilibrium, were mainly done by bending actions (flexural mechanism). However, in the impact analysis, at the equilibrium state, only compression forces are transmitted to these connections. This means that the beam is not transmitting the forces from the impact actions by flexural actions, but mainly by axial actions, in this particular case, by compression actions (Fig. 7.13a).

In the case of the frame with dog-bone connections, no failure was observed at the beam ends. The same observations concerning the action mechanisms observed in the frame with FREEDAM connections were also observed here. Furthermore, as in the column loss analyses,

the frame with dog-bone connections requires a higher deformation to achieve the equilibrium at the damage state than the frame with the FREEDAM connections.

At speed velocity of 80 km/h, the impact column fails, pulling down the external bay (Fig. 7.11b.). In the frame with the FREEDAM connections, the connections at the first storey of the external bay failed for the bolts of the friction damper in shear under compression (Fig. 7.13b). The failure happened for forces equal to 1464 kN for the connection right above the impact column (con.1) and equal to 1263 kN for the connection in the opposite side of the beam (con.7), to which are associated strain rates at failure higher than 1000 s^{-1} and approximately of 30 s^{-1}, respectively. The failure observed here is different from those observed under column loss (upper T-stub in tension in con.7, Fig. 7.8), due to the different mechanism undertaken by the beam to resist the progressive collapse. In addition, plastic strains appeared also at the beams and columns of the external bay.

In the frame with dog-bone connections, the failure happened at the dog-bone section above the impacted column. In addition, moderate levels of plasticity at the other beams of the external bay occurred as well as some light damage at the adjacent interior bay.

From the results, it looks that the main advantage of using FREEDAM connections in moment resisting frames is that, with these connections, structures need fewer plasticity levels at the beams and columns to achieve the equilibrium in their damaged state, when compared to the traditional dog-bone connection. In particular, in the analysis under 80 km/h, it was observed that the end of the slip in most of the remaining beam-to-column connections of the frame was not achieved at the end of the analysis. Nevertheless, in both solutions, at least the first storey of the external bay should be replaced.

Finally, comparing the maximum vertical displacements obtained here with those obtained in the dynamic nonlinear analyses, it is clear that these displacements are significantly higher in the impact analyses, which is due to the different deformations that the structures are subjected to in these two analyses. While dynamic nonlinear analyses involve only the vertical vibration generated by sudden column removal, in the impact analyses, besides the vertical deformation, a significant deformation along the impact direction also occurs along. The combination of these two deformations results in quite different responses of the structures when compared to those coming from the alternate path approach.
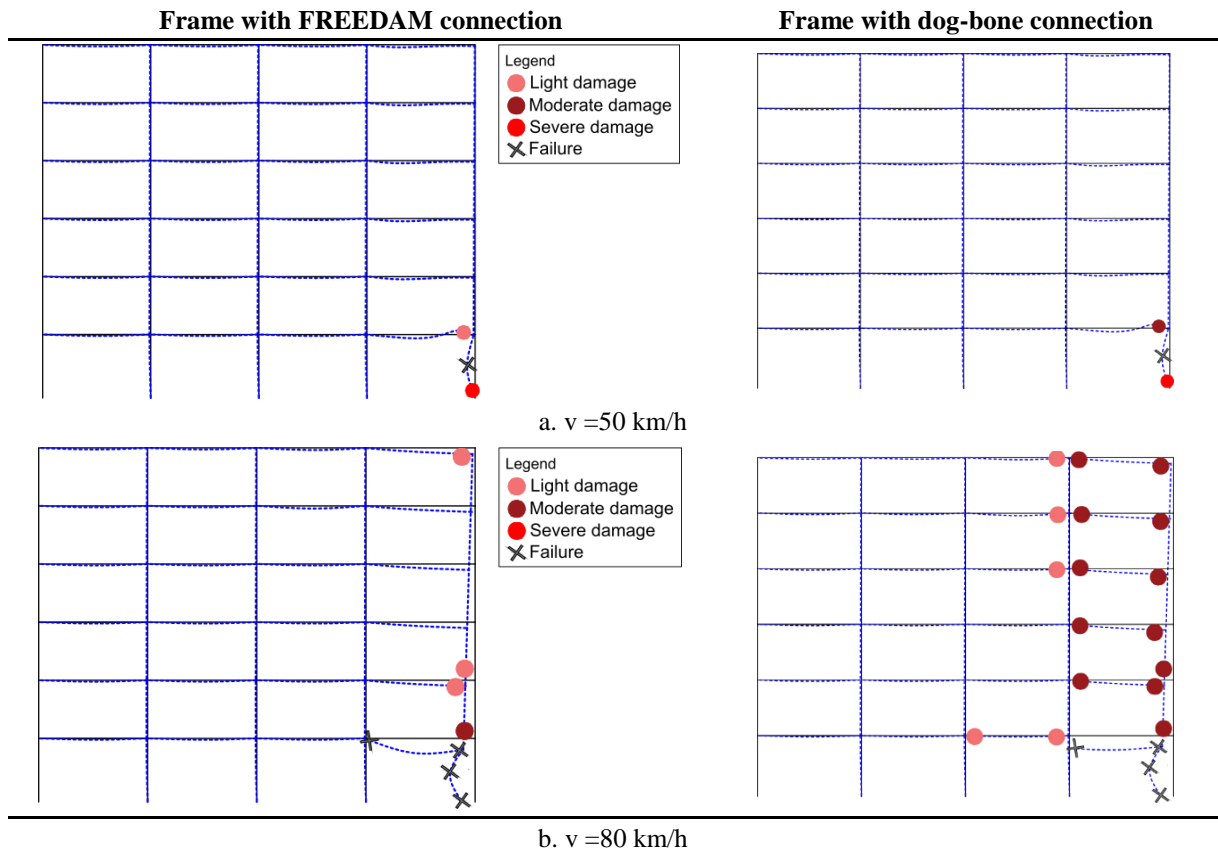
Frame with FREEDAM connection   **Frame with dog-bone connection**

a. v =50 km/h

b. v =80 km/h

Fig. 7.11. Frames deformation

a. v = 50 km/h   b. v = 80 km/h
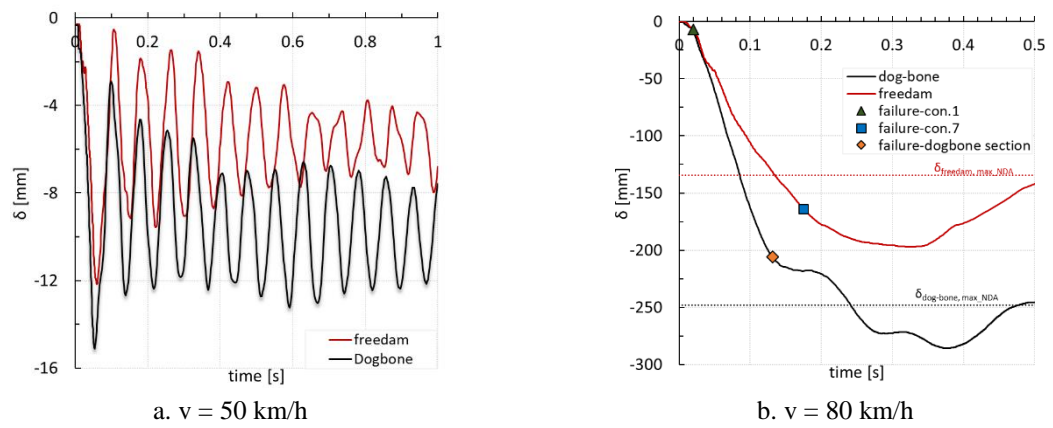
Fig. 7.12. Vertical displacement time history

a. v = 50 km/h   b. v = 80 km/h
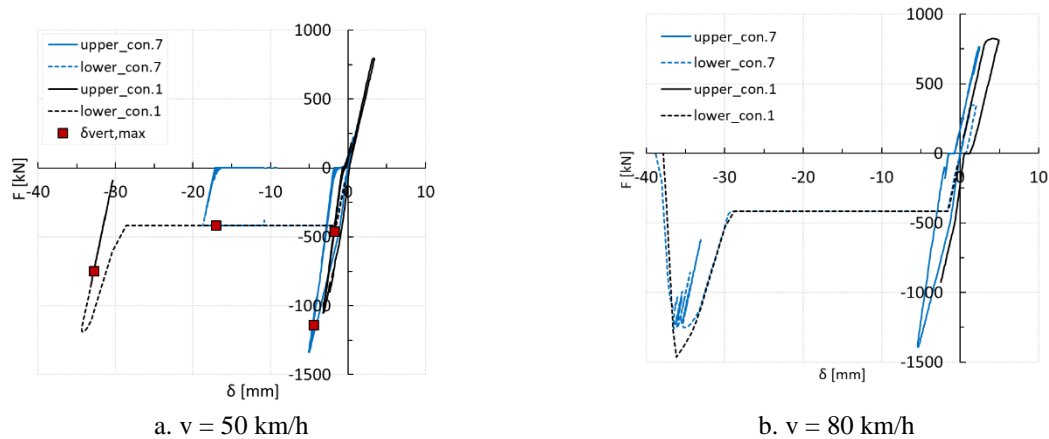
Fig. 7.13. Bem-to-column connections – Frame with FREEDAM connections

7.6 Discussion of results

In this chapter, the robustness evaluation of frames was performed in order to assess if the progressive collapse of the structures were likely to happen. This study was carried out in two frames with exactly the same geometry but with different typologies of the beam-to-column connections. With reference to the beam-to-column connections, a rigid dog-bone connection and a FREEDAM connection was used, with the purpose of comparing the robustness performance of the frame with these two types of connections.

The final objective of this study was to assess the robustness of the frames when subjected to a lateral impact coming from a vehicle. However, before performing the impact analyses, a static pushdown analysis and a nonlinear dynamic analysis (NDA) were carried out, considering the loss of the corner column.

From the column loss analyses, some observations could be drawn regarding the robustness of the analysed frames. The static pushdown analysis showed that progressive collapse is not likely to happen when the corner column is removed since both frames were able to find the equilibrium in their damaged state. The frame with the FREEDAM connections shows an initial stiffer behaviour due to the friction resistance of the friction pads. In addition, at the equilibrium state, no plastic strain at the beams/columns was observed, being the energy dissipated only by the slip of the friction dampers. On the contrary, the frame with the dog-bone connection shows a significant amount of damage at the dog bone beam section (dissipative member). By continuously pulling the frames up to the achievement of their ultimate load, it was observed that both frames have good residual strength and ductility properties.

182

The NDA column loss analysis, showed the importance of considering the dynamic effects and the column removal time in the analyses since it leads to vertical displacements at equilibrium in the damage state significantly lower from those observed in the static pushdown analysis.

Finally, the frames were subjected to a lateral impact from a vehicle. Two velocities were chosen, namely, 50 km/h and 80 km/h. Under 50 km/h, both frames remained stable. However, at an impact speed of 80 km/h, the structures were severely damaged, leading to the failure of beams and/or connections above the impact column and damage in the remaining elements of the external bay. However, both frames seem to find equilibrium after failure.

The different type of analyses highlighted that, for higher impact velocities, using alternate-load path methods to check the robustness of a structure cannot be enough since it leads to a quite different structural response than those coming from the impact analyses.

Concerning the adoption of tested different connection typologies, in all the analyses it was showed that the main difference of using the FREEDAM connection instead of the rigid dogbone connection, is the "delayed" yielding of the beam and columns elements due to the slip mechanism of these connections. In this way, for events where the dissipation of energy is mainly done by the friction dampers, the structure can be reused after the event.

Chapter 8   General conclusions and perspectives

8.1 Conclusions

The present thesis reflects the author's work on the European FREEDAM project, which was developed at both the University of Coimbra and the University of Salerno. This thesis follows the tasks of the project related to the robustness under exceptional actions. Therefore, it is divided into three main parts.

The first part of the work dealt with the behaviour of the dissipative component subjected to tension loads, considering both quasi-static and impact loads. For this study, experimental and numerical modelling was carried out. The friction dampers tested have a geometry similar to a bolted shear lap connection with two additional steel plates coated by means of thermal sprayed. In addition, the internal plate is slotted to allow the slip between plates. It was considered the variation of the thickness of the plates, the bolt class and friction coating material. During the experimental tests, a variation of the resistance and ductility of the specimens was observed, depending on the velocity of loading. In general, a higher resistance and a lower ductility were observed when impact loads were considered, due to the higher strain rates induced by this type of loading. In addition, an increase in the initial stiffness was also observed, which is related to the increase of the material ultimate strength under higher strain rates. The FEM studies were able to show a similar variation of resistance, ductility and initial stiffness than those observed in the experimental tests. The parametric FEM analyses showed the activation of different failures modes than those observed experimentally and to evidence more clearly the effects of the strain rates on the component's ductility capacity and resistance.

The effects of the strain rates in each individual component of the friction damper were introduced in an existent spring analytical model based on the component method of Eurocode

3 Part 1-8 to assess the behaviour of shear lap connections [14]. The analytical model was compared to the experimental and numerical results and satisfactory results were found.

After the complete characterization of the dissipative component, the entire connection was extensively studied by means of experimental and FEM analyses. The experimental tests were carried out considering the connection subjected to hogging bending moment. The experimental results showed that the moment-rotation curve of the connection could be divided into two parts: the first part is related to the slip behaviour of the friction damper, which gives an additional rotational capacity to the connection without significant plasticity of the other connection' components. After the end of the slip, the steel parts start to yield up to the attainment of failure. For the specimen studied, the upper T-stub failed in bending showing a collapse mode 2 (Eurocode 3 Part 1-8). However, this collapse was achieved earlier than expected due to the use of HV bolt assemblies with only one nut. The impact tests showed that the friction resistance of the connection depends on the velocity of the test, which is in agreement with the observations made for the friction damper.

The developed 3D FEM models were able to predict accurately the behaviour of the connection observed in the experimental tests. Additional parametric analyses were performed considering the variation of the direction of the bending moment (sagging bending moment), the effect bolt ductility and the velocity of the application of the load. The numerical study highlighted the asymmetrical connection behaviour. This asymmetry up to the end of the slip is related to the higher opening of the L-stub when compared to the T-stub opening under hogging moment [42]. After slip, the asymmetric behaviour is due to the different contribution of the upper and lower L-stubs. In particular, this asymmetry, even though predictable due to the lever arms of the L-stubs in relation to the centre of rotation, was significantly greater than expected. This was mainly due to the deformation of the friction damper bolts in shear at the ultimate load, which were not all in contact with both L-stubs webs. It was demonstrated through FE that this behaviour could be improved by avoiding the brittle nut thread stripping failure of the tee elements bolts.

With reference to the dynamic behaviour of the connection, in general, it is observed an increase of the initial friction resistance with the speed of the tests as well as an increase of the elastic and ultimate resistance. On the contrary, the ductility capacity decreases although not significantly. In addition, and contrarily to the observations made on the behaviour of the individual friction dampers, no significant changes were observed in the initial stiffness of the

specimens. This is related to the different components governing the ultimate behaviour of the specimens. While in the case of the friction damper, the stiffness of the components governing the resistance and ductility capacity is dependent on their material strength [5], in the case of the connection this is no longer true since, for the analysed specimen, the ultimate behaviour is governed by T-stubs or L-stubs in bending, whose stiffness only depends on their geometrical properties [5].

The component method codified in EC3 Part 1.8 was used to develop an analytical model to capture the behaviour of the connection when subjected to quasi-static and impact loads. Both elastic and post-elastic behaviour of each component contributing to the deformation and resistance of the connection was considered as well as the influence of strain rates on their resistance and ductility. The model previously developed for the friction damper was used to characterize this component. The results provided by this model showed that by considering the effect of strain rates component by component, a variation of the behavioural parameters of the connection very similar to those observed in the experiments and numerical studies was observed.

Finally, in the last chapter, the robustness of a 2D frame equipped with the connection under study when subjected to a lateral impact was evaluated. In addition, in terms of comparison, the robustness of the same 2D frame equipped with beam-to-column connections more commonly used was also evaluated. A rigid dog-bone connection was chosen for this matter. The beam-to-column connections were modelled as axial springs and their force-displacement behaviour was assessed using the developed analytical model. The model could also be used to characterize the rigid dog-bone connection since the active components are of the same kind, namely the T-stub in bending and the column components in shear, tension and compression.

Prior to the impact analyses, alternate load path analysis considering the loss of the corner column were performed by means of a preliminary static push down analysis and nonlinear dynamic analysis (NDA). These analyses showed that both frames can achieve the equilibrium in their damaged state. Furthermore, the frame with the FREEDAM connection shows lower levels of plasticity at the beam level because the dissipation of energy is done mainly by the slip of the friction dampers. For this reason, it also requires lower rotation levels to achieve the equilibrium in the damaged state.

In the impact analyses, not only the vertical deformation of the structure was observed but also a significant deformation in the direction of the impact load. This different deformation

leads to a structural response very different from those observed in the column loss analyses. For this reason, the evaluation of the robustness only by alternate path load analyses (column loss scenarios) could not be enough to characterize correctly the robustness of frames under impact from vehicles under high velocities. However, these analyses are useful to have a first estimation about the robustness properties of a structure to a loss of a member, because these analyses are much easier and less time consuming than complete impact analyses.

8.2 Contributions

The main contributions of this investigation are the following:

i) Additional information about the influence of strain rates due to impact loads on steel components commonly used in steel connections, such as bolts in shear, plates in bearing and tee elements in bending;

ii) The behaviour of a new beam-to-column connection with great energy dissipative capacity under impact loads. In this thesis, it was shown that this connection has great dissipative properties even under extreme loads. In fact, the amount of energy dissipated during the slip of the connection increases for loads rapidly applied, since the friction resistance increases for higher velocities. Even after slip, the dissipative energy tends to increase due to the increase of resistance.

iii) Analytical approaches to design shear lap connections with preloaded bolts and the FREEDAM connection taking into consideration not only the full behaviour of each component contributing for the deformation and resistance of the connections but also the effects of strain rates in each component. Although these approaches were used for the particular cases under study, they can also be used for other types of connections using some of the same components studied here.

iv) Contribution to robustness analysis of steel frames with different beam-to-column connections. In most of the literature works, in robustness analyses, the beam-to-column connections are considered as rigid or pinned. Here it was showed an easy way to model the right behaviour of beam-to-column connections, without increasing too much the complexity of the model. In addition, a "revision" on different types of robustness analyses have been made, showing their advantages and disadvantages.

8.3 Publications

8.3.1 Journal publications

During the development of this PhD thesis, the following papers were published in International journals:

- Santos, A. F., Santiago, A., Latour, M. and Rizzano, G. "*Analytical assessment of friction dampers under different loading rates*", Journal of Constructional steel research, vol. 158, pp.443-459, July 2019;

- Santos, A. F., Santiago, A. and Rizzano, G. "*Experimental response of friction dampers under different loading rates*", International Journal of Impact Engineering, vol. 132, October 2019;

- Santos, A. F., Santiago, A., Latour, M., Rizzano, G. and Simões da Silva, L. "*Response of friction joints under different velocity rates*", Journal of Constructional steel research, 168, May 2020 (accepted on February 24th 2020)

8.3.2 Conference proceedings

The work developed in this PhD thesis was presented at the following conferences:

- Santos, A.F, Santiago, A., Simões da Silva, L., Latour, M., Rizzano, G., "*Experimental assessment of friction dampers under impact loads*", EUROSTEEL 2017, 13-15 September, Copenhagen, Denmark.

- Santos A.F., Santiago A., Latour, M. Rizzano G., and Simões da Silva, L., "*Robustness of steel structures with friction joints – numerical study*", IRFF Conference, Lisboa, July 2018.

- Santos A.F., Santiago A. and Rizzano G., "*Dissipative beam-to-column connections for offshore structures*", CMN Conference, Guimarães, Portugal, July 2019.

- Santos A.F., Santiago A., Latour, M. and Rizzano G., "*Assessment of the response of friction dampers subjected to high strain rates*", ISCAS Conference, Bradford, UK, July 2019.

- Santos A.F., Santiago A., Latour, M., Rizzano G. and Simões da Silva, L. "*Behaviour of a beam-to-column steel friction connection under quasi-static and impact loading*", ConFab Conference, London, UK, September 2019.

- Santos A.F., Santiago A., Latour, M., Rizzano G. and Simões da Silva, L. "*Behaviour of a friction joints under different deformation rates*", XII Congresso de Construção Metálica e Mista, Coimbra, Portugal, November 2019.

8.3.3 Presentations in meetings and workshops

During the development of this PhD thesis, the author participated in the following meetings and workshop related to the FREEDAM project:

- 2nd FREEDAM Meeting, FIP Industriale – Servazzano (PD), 28-29 January 2016;

- 3rd FREEDAM Meeting, Universidade de Coimbra, 7-8 July 2016;

- 4th FREEDAM Meeting, Liège University (Belgium), 6-7 February 2017;

- 6th FREEDAM Meeting, Università degli studi di Salerno, 24 January 2018;

- FREEDAM workshop - *"Frames with friction connections: results of FREEDAM project"*, Università degli Studi di Salerno, 10 July 2018

8.4 Open questions and further research interests

The work presented in this thesis deals with the behaviour of an innovative beam-to-column connection under extreme loading (impact loads). In the course of the research, several topics are identified as requiring further examination:

i)   High-speed coupon tests on the different materials composing the components of the connection. In this work, the characterization of the materials was carried out only for quasi-static strain rates, while, the effects of the strain rates on the material strength and ductility was taken by literature suggestions. Although the use of these suggestions in the FEM models lead to similar results when compared to those observed experimentally, the existence of material testing under different strain rates would have made it easier to obtain precise results, especially concerning the differences in the ultimate and fracture strains at high strain rates;

ii)   Experimental connection testing under sagging bending moment. The FEM models have shown that the connection response under sagging moment is quite different from the correspondent response under hogging moment. In particular, this difference was related not only to the lever arms of the L-stubs in relation to the centre of rotation of

the connection but also due to the position of the bolts in shear of the friction damper at the ultimate load, which did not touch both L-stubs webs. This "problem" was improved in the FEM models by avoiding the nut stripping failure of the bolts. However, this parameter deserves a more detailed study, which should involve experimental testing;

iii)   The influence of strain rates in the ductility of column components. There is no available literature concerning it and since in the experiments and FEM the column has been considered rigid, these components were not studied. However, they are important when introducing the connection behaviour in moment resisting frames;

iv)   The effect of the slab on the connection behaviour. The additional inertia due to the slab can sometimes change the failure mode of connections, as shown by Grimsno *et al.* [8].

v)   The evaluation of the robustness considering the vehicle impact in different columns. In this work, only the impact of the corner column has been considered. Although this is most critical in the majority of the times, it would be interesting to investigate the robustness considering the impact in one interior column, to check if the resistance beam mechanisms and following failure modes would be the same;

vi)   Still, in the robustness analyses, the importance of the slab should be also investigated. The consideration of the slab generally improves the robustness of structures [22].

REFERENCES

References

[1]   B.R. Ellingwood, R. Smilowitz, D.O. Dusenberry, D. Duthinh, H.S. Lew, N.J. Carino, Best practices for reducing the potential for progressive collapse in buildings (NISTIR 7396), U.S. Natl. Inst. Stand. Technol. (NIST). (2007) 216.

[2]   D.A. Nethercot, Design of building structures to improve their resistance to progressive collapse, Procedia Eng. 14 (2011) 1–13.

[3]   Q. Fu, B. Yang, Y. Hu, G. Xiong, S. Nie, W. Zhang, G. Dai, Dynamic analyses of bolted-angle steel joints against progressive collapse based on component-based model, J. Constr. Steel Res. 117 (2016) 161–174.

[4]   B. Yang, K.H. Tan, Numerical analyses of steel beam-column joints subjected to catenary action, J. Constr. Steel Res. 70 (2012) 1–11.

[5]   Eurocode 3, Design of steel structures. Part 1.8: Design of joints, Brussels, Belgium, 2010.

[6]   P. Barata, A. Santiago, J.P. C. Rodrigues, C. Rigueiro, Experimental behaviour of beam-to-column steel joints subjected to impact loading, in: Eighth Int. Conf. Adv. Steel Struct., Lisbon, July, 2015.

[7]   J. Ribeiro, A. Santiago, C. Rigueiro, P. Barata, M. Veljkovic, Numerical assessment of T-stub component subjected to impact loading, Eng. Struct. 106 (2016) 450–460.

[8]   E.L. Grimsmo, A.H. Clausen, A. Aalberg, M. Langseth, A numerical study of beam-to-column joints subjected to impact, Eng. Struct. 120 (2016) 103–115.

[9]   R. Rahbari, A. Tyas, J. Buick Davison, E.P. Stoddart, Web shear failure of angle-cleat connections loaded at high rates, J. Constr. Steel Res. 103 (2014) 37–48.

[10]   J. Ribeiro, A. Santiago, C. Rigueiro, L.S. Da Silva, Analytical model for the response of

T-stub joint component under impact loading, J. Constr. Steel Res. 106 (2015) 23–34.

[11] E.P. Stoddart, M.P. Byfield, J.B. Davison, A. Tyas, Strain rate dependent component based connection modelling for use in non-linear dynamic progressive collapse analysis, Eng. Struct. 55 (2013) 35–43.

[12] P. Barata, A. Santiago, J.P.C. Rodrigues, C. Rigueiro, Development of an experimental system to apply high rates of loading, Int. J. Struct. Integr. 7 (2016) 291–304.

[13] Abaqus, Abaqus Theory Manual, 2011.

[14] J. Henriques, J.P. Jaspart, L.S. da Silva, Ductility requirements for the design of bolted lap shear connections in bearing, Adv. Steel Constr. 10 (2014) 33–52.

[15] A.B. Francavilla, M. Latour, V. Piluso, G. Rizzano, Bolted T-stubs: A refined model for flange and bolt fracture modes, Steel Compos. Struct. 20 (2016) 267–293. https://doi.org/10.12989/scs.2016.20.2.267.

[16] Eurocode 1, Actions on structures - Part 1-7: General actions - Accidental actions, 2006.

[17] T. Ngo, P. Mendis, A. Gupta, J. Ramsay, Blast Loading and Blast Effects on Structures – An Overview, Electron. J. Struct. Eng. (2007).

[18] H. Kang, J. Kim, Progressive Collapse of Steel Moment Frames Subjected to Vehicle Impact, J. Perform. Constr. Facil. (2014).

[19] J. Demonceau, Steel and composite building frames: sway response under conventional loading and development of membrane effects in the beams further to an exceptional action., 2008.

[20] C. Huevelle, V.-L. Hoang, J. Jaspart, J. Demonceau, Complete analytical procedure to assess the response of a frame submitted to a column loss., Eng. Struct. 86 (2015) 33–42.

[21] S. Jeyarajan, J.Y.R. Liew, C.G. Koh, Analysis of Steel-Concrete Composite Buildings for Blast Induced Progressive Collapse, Int. J. Prot. Struct. 6 (2015) 457–485. https://doi.org/10.1260/2041-4196.6.3.457.

[22] S. Jeyarajan, J.Y.R. Liew, Robustness analysis of 3D Composite buildings with semi-rigid joints and floor slab, 6 (2016) 20–29. https://doi.org/10.1016/j.istruc.2016.01.005.

[23] B.A. Izzuddin, A.G. Vlassis, A.Y. Elghazouli, D.A. Nethercot, Progressive collapse of

multi-storey buildings due to sudden column loss - Part I: Simplified assessment framework, Eng. Struct. 30 (2008) 1308–1318. https://doi.org/10.1016/j.engstruct.2007.07.011.

[24] E.L. Grimsmo, A.H. Clausen, M. Langseth, A. Aalberg, An experimental study of static and dynamic behaviour of bolted end-plate joints of steel, Int. J. Impact Eng. 85 (2015) 132–145.

[25] J.B. Davison, Investigation the Robustness of Steel Beam-to-column connections, in: 10th Int. Conf. Steel, Sp. Compos. Struct., North Cyprus, May, 2011.

[26] G. Culache, M.P. Byfield, N.S. Ferguson, A. Tyas, Robustness of Beam-to-Column End-Plate Moment Connections with Stainless Steel Bolts Subjected to High Rates of Loading, J. Struct. Eng. 143 (2017). https://doi.org/10.1061/(ASCE)ST.1943-541X.0001707.

[27] A. Al-rifaie, Z.W. Guan, S.W. Jones, Q. Wang, Lateral impact response of end-plate beam-column connections, Eng. Struct. 151 (2017) 221–234. https://doi.org/10.1016/j.engstruct.2017.08.026.

[28] B. Yang, K.H. Tan, Experimental tests of different types of bolted steel beam-column joints under a central-column-removal scenario, Eng. Struct. 54 (2013) 112–130.

[29] B. Yang, K.H. Tan, G. Xiong, Behaviour of composite beam–column joints under a middle-column-removal scenario: Component-based modelling, J. Constr. Steel Res. 104 (2015) 137–154.

[30] B. Yang, K.H. Tan, Behaviour of composite beam-column joints in a middle-column-removal scenario: Experimental tests, J. Struct. Eng. 140 (2014).

[31] H.Z. Jahromi, B.A. Izzuddin, D.A. Nethercot, S. Donahue, M. Hadjioannou, E.B. Williamson, M. Engelhardt, D. Stevens, K. Marchand, M. Waggoner, Robustness Assessment of Building Structures under Explosion, (2012) 497–518. https://doi.org/10.3390/buildings2040497.

[32] A.G. Vlassis, B.A. Izzuddin, A.Y. Elghazouli, D.A. Nethercot, Progressive collapse of multi-storey buildings due to failed floor impact, Eng. Struct. 31 (2009) 1522–1534. https://doi.org/10.1016/j.engstruct.2009.02.009.

[33] H. Wang, B. Yang, H. Wang, B. Yang, X. Zhou, S. Kang, Numerical analyses on steel

beams with fin- plate connections subjected to impact loads to impact loads, J. Constr. Steel Res. 124 (2016) 101–112. https://doi.org/10.1016/j.jcsr.2016.05.016.

[34] G.S. Urgessa, T. Arciszewski, Blast response comparison of multiple steel frame connections, Finite Elem. Anal. Des. 47 (2011) 668–675. https://doi.org/10.1016/j.finel.2011.01.009.

[35] D. Grecea, F. Dinu, D. Dubina, Performance criteria for MR steel frames in seismic zones, J. Constr. Steel Res. 60 (2004) 739–49.

[36] F. Iannone, M. Latour, G. Rizzano, Experimental Analysis of Bolted Steel Beam-to-column Connections: Component identification., J. Earthq. Eng. 15 (2011) 214–44.

[37] K. Inoue, K. Suita, I. Takeuchi, P. Chusilp, M. Nakashima, F. Zhou, Seismic-Resistant Weld-Free Steel Frame Buildings with Mechanical Joints and Hysteretic Dampers, J. Struct. Eng. 132 (2006) 864–872. https://doi.org/10.1061/(ASCE)0733-9445(2006)132:6(864).

[38] A. kishiki, S., Yamada, S., Suzuki, K., Saeki, E., Wada, New Ductile Moment-Resisting Connections Limiting Damage To Specific Elements At the Bottom Flange, Construction. (2006).

[39] S.-H. Oh, Y.-J. Kim, H.-S. Ryu, Seismic performance of steel structures with slit dampers, Eng. Struct. 31 (2009) 1997–2008.

[40] G.A. MacRae, G.C. Clifton, H. Mackinven, N. Mago, J. Butterworth, S. Pampanin, The sliding hinge joint moment connection, Bull. New Zeal. Soc. Earthq. Eng. 43 (2010) 202–212.

[41] M. Latour, V. Piluso, G. Rizzano, Free from damage beam-to-column joints: Testing and design of DST connections with friction pads, Eng. Struct. 85 (2015) 219–233.

[42] M. Latour, M. D'Aniello, M. Zimbru, G. Rizzano, V. Piluso, R. Landolfo, Removable friction dampers for low-damage steel beam-to-column joints, Soil Dyn. Earthq. Eng. 115 (2018) 66–81. https://doi.org/10.1016/j.soildyn.2018.08.002.

[43] N. Milovanović, Innovative joint configuration for structures subjected to high seismic actions and to exceptional events – Development of aspring model reflecting the joint behaviour in case of a column loss., University of Liege, 2017.

[44] F.P. Bowden, D. Tabor, Friction and lubrication, Methuen co, LTD, 1950.

[45]   M.A. Chowdhury, D.M. Nuruzzaman, B.K. Roy, P.K. Dey, M.G. Mostafa, M.S. Islam, M.R. Mia, Experimental Investigation on Friction and Wear of Stainless Steel 304 Sliding Against Different Pin Materials, World Appl. Sci. J. 22 (2013) 1702–1710.

[46]   M. Latour, V. Piluso, G. Rizzano, Experimental analysis of beam-to-column joints equipped with sprayed aluminium friction dampers, J. Constr. Steel Res. 146 (2018) 33–48. https://doi.org/10.1016/j.jcsr.2018.03.014.

[47]   G.F. Cavallaro, A. Francavilla, M. Latour, V. Piluso, G. Rizzano, Experimental behaviour of innovative thermal spray coating materials for FREEDAM joints, Compos. Part B Eng. 115 (2016) 289–299.

[48]   G.F. Cavallaro, A. Bianca, M. Latour, V. Piluso, G. Rizzano, Cyclic behaviour of friction materials for FREEDAM connections, in: Eighth Eur. Conf. Steel Compos. Struct., Copenhagen, September, 2017.

[49]   University of Salerno, University of Coimbra, FIP Industriale, University of Liege, University of Naples, O Feliz Metalomecanica, FREEDAM, FREE from DAMage Steel Connections, Mid-term Report, 2017.

[50]   General Services Administration (GSA), Progressive Collapse Analysis and Design Guidelines for New Federal Office Buildings and Major Modernization Projects, 2003.

[51]   Department of Defense (DOD), DESIGN OF BUILDINGS TO RESIST PROGRESSIVE COLLAPSE, 2016.

[52]   D. Cassiano, Post seismic structural robustness in moment resisting frame steel buildings, University of Coimbra, 2017.

[53]   M. Byfield, W. Mudalige, C. Morison, E. Stoddart, A review of progressive collapse research and regulations, in: Struct. Build., 2014.

[54]   S. Gerasimidis, C.C. Baniotopoulos, Steel moment frames column loss analysis: The influence of the time step size, J. Constr. Steel Res. 67 (2011) 557–564.

[55]   S.M. Marjanishvili, Progressive Analysis Procedure for Progressive Collapse, J. Perform. Constr. Facil. 8 (2004).

[56]   Arup, Review of international research on structural robustness and disproportionate collapse, Department for Communities and Local Government, 2011.

[57] L.J. Malvar, J.E. Crawford, DYNAMIC INCREASE FACTORS FOR STEEL REINFORCING BARS L, in: Twenty-Eighth DDESB Semin., Orlando, n.d. https://doi.org/10.1061/(ASCE)CF.1943-5509.0000971.

[58] K. Vedantam, D. Bajaj, N.S. Brar, S. Hill, Johnson - Cook strength models for mild and DP 590 steels, AIP Conf. Proc. 845 I (2006) 775–778.

[59] E. Saraiva, Variação das propriedades mecânicas do aço relacionadas com problemas de impacto em estruturas., University of Coimbra, 2012.

[60] J. GR, W. Cook, A constitutive model and data for metals subjected to large strains, high strain rates and high temperatures, in: Proc. 7th Int. Symp. Ballist., The Hague, The Netherlands, 1983: pp. 541–7.

[61] C. ALBERTINI, M. MONTAGNANI, DYNAMIC UNIAXIAL AND BIAXIAL STRESS-STRAIN RELATIONSHIPS FOR AUSTENITIC STAINLESS STEELS, Nucl. Eng. Des. 57 (1980) 107–123.

[62] W.-S. Lee, C.-F. Lin, Impact properties and microstructure evolution of 304L stainless steel, Mater. Sci. Eng. A. 308 (2001) 124–135.

[63] W.E. Luecke, J.D. McColskey, C.N. McCowan, S.W. Banovic, R.J. Fields, T. Foecke, T.A. Siewert, F.W. Gayle, Mechanical Properties of Structural Steels, Federal Building and Fire Safety Investigation of the World Trade Center Disaster, NIST NCSTAR 1-3D;, 2005.

[64] E. Munoz Garcia, J.. Davidson, A. Tyas, Analysis of the response of structural bolts subjected to rapid rates of loading, in: 4th Eur. Conf. Steel Compos. Struct. - EUROSTEEL, Mastricht, The Netherlands, n.d.

[65] H. Fransplass, M. Langseth, O.S. Hopperstad, Tensile behaviour of threaded steel fasteners at elevated rates of strain, Int. J. Mech. Sci. 53 (2011) 946–57. https://doi.org/10.1016/j.ijimpeng.2012.10.009.

[66] J.S. Kim, H. Huh, T.S. Kwon, Characterization of dynamic tensile and shear strength of safety bolts in light collision safety devices of a train, 64 (2009) 81–92.

[67] H. Couque, R. Boulanger, F. Bornet, A modified Johnson-Cook model for strain rates ranging from 10 -3 to 10 5 s -1, J. Appl. Phys. 134 (2006) 87–93. https://doi.org/10.1051/jp4:2006134015.

[68] A.A. Dehkharghani, Tuning Johnson-Cook Material Model Parameters for Impact of High Velocity , Micron Scale Aluminum Particles, (2016).

[69] A. Manes, L. Peroni, M. Scapin, M. Giglio, Analysis of strain rate behavior of an Al 6061 T6 alloy, Procedia Eng. 10 (2011) 3477–3482. https://doi.org/10.1016/j.proeng.2011.04.573.

[70] T. Sabuwala, D. Linzell, T. Krauthammer, Finite element analysis of steel beam to column connections subjected to blast loads, Int. J. Impact Eng. 31 (2005) 861–876.

[71] TM5-1300, Strutuctures to resist the effects of accidental explosions, 1990.

[72] A. Tyas, J.A. Warren, E.P. Stoddart, J.B. Davison, S.J. Tait, Y. Huang, A Methodology for Combined Rotation-Extension Testing of Simple Steel Beam to Column Joints at High Rates of Loading, Exp. Mech. 52 (2012) 1097–1109.

[73] E.P. Stoddart, M.P. Byfield, A. Tyas, Blast Modeling of Steel Frames with Simple Connections, J. Struct. Eng. 140 (2014) 04013027.

[74] M. Sarraj, The behaviour of steel fin plate connections in fire, (2007). http://etheses.whiterose.ac.uk/3035/.

[75] Eurocode 3, Design of steel structures. Part 1.1: General rules and rules for buildings, 2002.

[76] P. Barata, A. Santiago, J.P. C. Rodrigues, C. Rigueiro, Experimental Analysis of a T-Stub Component Subjected, in: Eurosteel (Ed.), Naples, Italy, 2014.

[77] J. Ribeiro, A. Santiago, C. Rigueiro, Análise dinâmica não linear de ligações viga-pilar aparafusadas com placa de extremidade, in: IX Congr. Construção Metálica e Mista, 1991. https://doi.org/10.1016/S0304-4017(13)00104-0.

[78] H. Yu, I.W. Burgess, J.B. Davison, R.J. Plank, Development of a yield-line model for endplate connections in fire, J. Constr. Steel Res. 65 (2009) 1279–1289. https://doi.org/10.1016/j.jcsr.2008.12.001.

[79] E.L. Grimsmo, A.H. Clausen, M. Langseth, A. Aalberg, An experimental study of static and dynamic behaviour of bolted end-plate joints of steel, Int. J. Impact Eng. 85 (2015) 132–145. https://doi.org/10.1016/j.ijimpeng.2015.07.001.

[80] ROBUSTNESS - Robust structures by joint ductility. Final report, 2009.

[81] L. Hẚi, Structural response of steel and composite building frames further to an impact leading to the loss of a column., University of Liege, 2009.

[82] H. Kang, J. Shin, J. Kim, Analysis of Steel Moment Frames subjected to Vehicle Impact, in: APCOM ISCM, Singapore, 2013.

[83] ISO 6892-1, "Metalic Metallic materials - Tensile testing - Part 1: Method of test at room temperature," 2009 (2009).

[84] Eurocode 3, Design of steel structures . Part 1.4: General rules -Supplementary rules for stainless steels, Brussels, Belgium, 2006.

[85] J.-P. Jaspart, Etude de La semi-rigidite des noeuds poutre-colonne et son influence sue la resistance et la stabilite des ossatures en acier, 1991.

[86] G.H. Sterling, J.J. Wallaert, J.W. Fisher., What happen TO BOLT TENSION IN LARGE JOINTS ?, 20 (1965).

[87] J.J. Wallaert, J.W. Fisher, Shear strength of high-strength bolts, (1964).

[88] H. Block, H. Blok, Fundamental mechanical aspects of boundary lubrication, S.A.E.J. 46 (1940) 54–68.

[89] U. Maqbool, Numerical Assessment of Friction Dampers Under Quasi-Static and Impact Loading, 2018.

[90] V.-H. Konstruktion, V. GmbH, VDI Guideline - Part I, Systematic calculation of high duty bolted joints – Joints with one cylindrical bolt, 2003.

[91] M.D. Aniello, D. Cassiano, R. Landolfo, Monotonic and cyclic inelastic tensile response of European preloadable gr10 . 9 bolt assemblies, JCSR. 124 (2016) 77–90. https://doi.org/10.1016/j.jcsr.2016.05.017.

[92] M.S. Pavlović, Resistance of Bolted Shear Connectors, (2013) 1–10.

[93] J. Rice, D. Tracey, On the Ductile Enlargement of Voids in Triaxial Stress Fields, J. Mech. Phys. Solids. 17 (1969) 201–17.

[94] G. Trattnig, T. Antretter, R. Pippan, Fracture of austenitic steel subject to a wide range of stress triaxiality ratios and crack deformation modes., Eng. Fract. Mech. 75 (2008) 223–235.

[95] D. Chae, D.A. Koss, Damage accumulation and failure of HSLA-100 steel, Mater. Sci.

Eng. A. 366 (2004) 299–309.

[96] B. Jakse, P. Može, Different approaches towards numerical modelling of bolt bearing, in: Eurosteel, Copenhagen, Denmark, September, 2017.

[97] F. Wald, Z. Sokol, M. Moal, V. Mazura, C. Republic, Component Method for Cover Plate Connections, Int. Colloq. Stab. Ductility Steel Struct. (2002) 1–8.

[98] F. Wald, V. Mazura, M. Moal, Z. Sokol, Experiments of Bolted Cover Plate Connections With Slotted Holes, Praha, 2002.

[99] C. Pietrapertosa, E. Piraprez, J. Jaspart, Ductility requirements in shear bolted connections, Proc. Fifth Int. Work. Connect. Steel Struct. V. (2004) 335–346.

[100] F. Wald, J. Kabeláč, M. Kuříková, O. Perháč, P. Ryjáček, O. Minor, M.B.F. Pazmiño, L. Šabatka, D. Kolaja, Advanced procedures for design of bolted connections, IOP Conf. Ser. Mater. Sci. Eng. 419 (2018) 012044. https://doi.org/10.1088/1757-899X/419/1/012044.

[101] K. U, D. JB, K. M., Structural systems and rotation capacity., in: COST Conf. Liege, Belgium, n.d.

[102] C. Fang, B.A. Izzuddin, A.Y. Elghazouli, D.A. Nethercot, Robustness of multi-storey car parks under localised fire - Towards practical design recommendations, J. Constr. Steel Res. 90 (2013) 193–208.

[103] P. Može, D. Beg, A complete study of bearing stress in single bolt connections, J. Constr. Steel Res. 95 (2014) 126–140. https://doi.org/10.1016/j.jcsr.2013.12.002.

[104] P. Može, DEFORMATION CAPACITY , STIFFNESS AND BEARING STRENGTH AT, in: 8th Int. Work. Connect. Steel Struct., Boston, Massachusetts, USA, 2016: pp. 69–78.

[105] E.L. Salih, L. Gardner, D.A. Nethercot, Bearing failure in stainless steel bolted connections, Eng. Struct. 33 (2011) 549–562.

[106] L. Simões Da Silva, A. Santiago, P. Vila Real, Post-limit stiffness and ductility of end-plate beam-to-column steel joints, Comput. Struct. 80 (2002) 515–531.

[107] L.R.O. de Lima, P.C.G. da S. Vellasco, J.G.S. da Silva, L.A.C. Borges, L. da Silva, Post-limit stiffiness prediction of semi-rigid joints using genetic algorithms, Lat. Am. J. Solids

Struct. 2 (2005) 305–320.

[108] Vincenzo Piluso, C. Faella, G. Rizzano, Ultimate Behavior of Bolted T-Stubs. I: Theoretical Model, J. Struct. Eng. 127 (2001) 686–693.

[109] Antonella Francavilla, Robustness and seismic behaviour of structures equipped with traditional and innovative beam-to-column connections, University of Salerno, 2016.

[110] Eurocode, Basis of structural design, European Committee for Standardization, 2005.

[111] F.M. Mazzolani, V. Piluso, PLASTIC DESIGN OF SEISMIC RESISTANT STEEL FRAMES, Earthq. Eng. Struct. Dyn. 26 (1997) 167–91.

[112] R. Montuori, E. Nastri, V. Piluso, Advances in theory of plastic mechanism control: closed form solution for MR-Frames, Earthq. Eng. Struct. Dyn. 44 (2015) 1035–54.

[113] V. Piluso, R. Montuori, M. Troisi, Innovative structural details in MR-frames for free from damage structures, Mech. Res. Commun. 58 (2014) 146–156. https://doi.org/10.1016/j.mechrescom.2014.04.002.

[114] S. El-Tawil, H. Li, S. Kunnath, Computational Simulation of Gravity- Induced Progressive Collapse of Steel-Frame Buildings: Current Trends and Future Research Needs, Spec. Issue Comput. Simul. Struct. Eng. A2513001. (2014).

Annex A – Dynamic experimental response of friction dampers under different loading rates

In this annex is presented the force-displacement curves of the impact tests that were not showed in the main document. The sequential and full impact tests corresponding to the same coating material are plotted together as well as the correspondent quasi-static test.

A.1 Results: Group A

A.1.1 Coating material M4 (sprayed aluminium)

In Fig.A.1 is showed the force-displacement curve of the sequential test performed with the coating material M4 (ID: T3-M4-SI-30) and one of the corresponding quasi-static tests (ID: T10-M4-St.-30). Table A.1 reports the main behavioural parameters that describe the behaviour of the specimens. The results are in agreement with what was discussed in the main document, i.e. under impact loading, the friction damper behaviour becomes stiffer and brittle. There is a general increase of all the behavioural parameters when the device is tested under impact loads, except for the ductility.
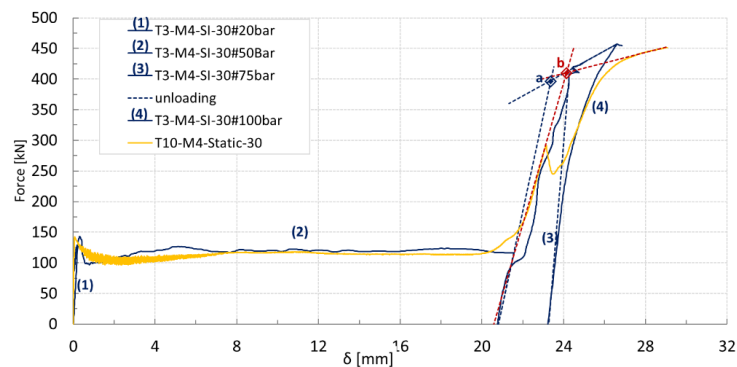

Fig. A.1. Force-displacement curves: T10-M4-St.-30 vs T3-M4-SI.-30

Table A.1. Behavioural parameters: Specimens with coating material M4, Group A

Parameter Test Type	μ	F_k/F_{slip}	S [kN/mm]	F_y [kN]	F_u [kN]	δ_u [mm]
Static	0.58	0.8	106	371.9	452	5.4
Impact	0.58	0.84	159	380.5	457	4.6
DF	**1**	**-**	**1.5**	**1.02**	**1.02**	**0.85**

A.1.2 Coating material M6 (METCO-70NS)

In Fig.A.2 is showed the force-displacement curves of both sequential and full impact test performed with the coating material M6 (ID: T3-M6-SI-30 and T4-M6-FI-30) and the corresponding quasi-static tests (ID: T8-M6-St.-30). In Table A.2 is reported the main behavioural parameters that describe the behaviour of the specimens.

The results show that the increase in both design and ultimate resistance are of the same value. Furthermore, an increase of 47% of the initial stiffness and a decrease of 30% of the ductility capacity is reported.

Concerning the friction resistance, also an increase of the static friction coefficient is observed in the full impact test. Furthermore, in the sequential test, a different sliding behaviour is observed: first, after the initiation of the slip, the damper stops, requiring a higher force to reinitiate the movement. Secondly, after a constant path, the friction resistance increases until the end of the slip, contrarily to the other materials. This particular behaviour was also visualized in the cyclic tests, in both low and high velocities, where this material was characterized with significant sticks-slip phenomena, an increase of the friction coefficient during the cyclic and significant noise. For all these reasons, this material was discarded.

Table A.2. Behavioural parameters: Specimens with coating material M6, Group A

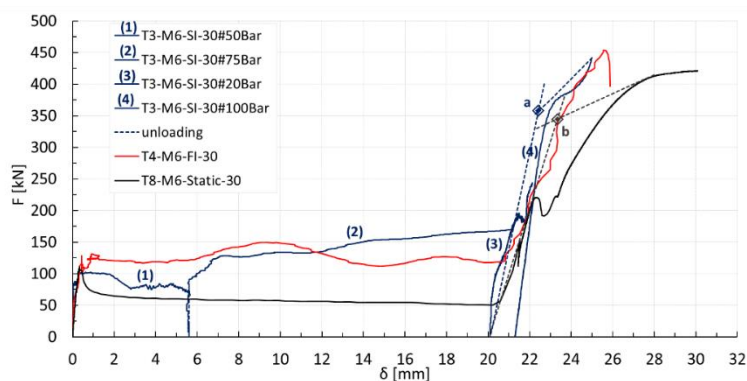| Parameter Test Type		μ	F_k/F_{slip}	S [kN/mm]	F_y [kN]	F_u [kN]	δ_u [mm]
Static		0.45	0.5	105	345	421	6.3
Impact	SI	0.42	1.37	154	356.7	441	4
	FI	0.53	0.84	-	-	456	4.5
	Mean	0.49	1.15	154	356.7	449	4.3
DF		**1.09**	**-**	**1.47**	**1.04**	**1.07**	**0.68**

Fig. A.2. Force-displacement curves: T8-M6-St.-30 vs T3-M6-SI.-30 and T4-M6-FI-30

A.2 Results: Group B

A.2.1 Coating material M6 (METCO-70NS)

In Fig.A.3 is showed the force-displacement curve of the sequential impact test of the group B performed with the coating material M6 (ID: T1-M6-SI-30). In Table A.3 is reported the main behavioural parameters that describe the behaviour of the specimens.

The results show an increase in the ultimate resistance of about 7%. Furthermore, an increase of 30% of the initial stiffness and a decrease of almost 50% of the ductility capacity is reported. In this case, the increase of the kinetic friction resistance and the stick-slip phenomena was not visualized, probably due to the lower preload force applied.
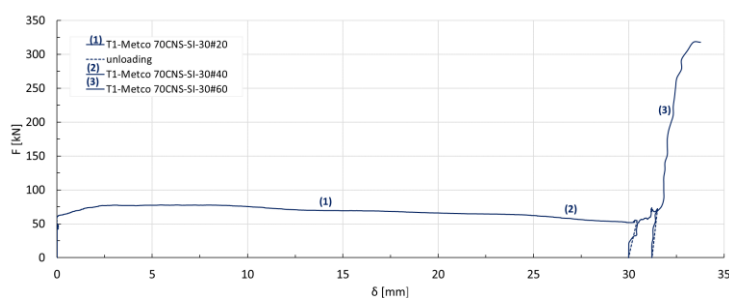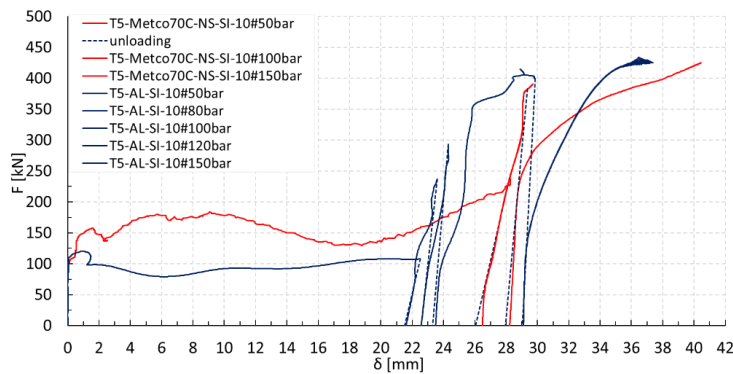

Fig. A.3. Force-displacement curve of the test T1-M6-SI.-30

Table A.3. Behavioural parameters: Specimens with coating material M6, Group B

Parameter Test Type		μ	F_k/F_{slip}	S [kN/mm]	F_y [kN]	F_u [kN]	δ_u [mm]
Static		0.38	0.67	92.8	242.6	297	7
Impact	SI	0.39	0.83	121	-	318	3.4
DF		**1.03**	**-**	**1.3**	**-**	**1.07**	**0.48**

A.3 Results: Group C

In Fig.A.4 is showed the force-displacement curves of the sequential impact tests of the group C performed with the coating material M4 and M6 (ID: T5-M4-SI-10 and T5-M6-SI-10, respectively). In Table A.4 is reported the main behavioural parameters that describe the behaviour of the specimens.

Concerning the slip path, the specimens show a similar behaviour than those previously reported. After slip, is observed a significant higher ductility, since, in these cases, the behaviour is governed by the ductility of the slip plate. However, as mentioned in the main document, no failure was observed, only a high bearing deformation.

Fig. A.4. Force-displacement curve of the tests T5-M6-SI.-10 and T5-M4-SI.-10

Table A.4. Behavioural parameters: Specimens with coating material M6 and M4, Group C

Parameter Test Type		μ	F_k/F_{slip}	S [kN/mm]	F_y [kN]	F_u [kN]	δ_u [mm]
Impact	M4	0.5	0.89	107	-	433	39.17
	M6	0.6	1	111	-	427	42.55

Annex B – Component-based method to assess the behaviour of friction joints under different deformation rates

B.1. Force-displacement curves of components design as T-stubs

The theoretical model of Francavilla *et al.* was used to assess the force-displacement curves of the T-stubs and L-stubs in bending. The model requires the definition of the geometrical properties as in Eurocode 3 Part 1-8 and of the material stress-strain law of bolts and plates. The geometrical and material properties are provided in Table B.1 and Table B.2 and the obtained curves in Fig. B.1. In order to assess the curves for other strain rates than the quasi-static curve, the strength of the materials was increased using the Johnson Cook equation ($C_y = C_u = 0.039$ for plates and $C_y = 0.0072$ and $C_u = 0.0047$ for bolts), and the ultimate strain was decreased considering the equations of Table 4.3.

Table B.1. Material properties – static properties

Component	f_y [MPa]	f_u [MPa]	E [MPa]	E_h [MPa]	E_u [MPa]	ε_h [%]	ε_u [%]
T-stub/ L-stubs	275	650	150000	3504.7	667.0	2.017	37
Bolt	900	1050	210000	-	-	-	4

Table B.2. Geometry of the T-stubs

Component	d_b [mm]	d_{bh} [mm]	d_w [mm]	t_{bh} [mm]	t_n [mm]	t_f [mm]	m [mm]	n [mm]	b [mm]	L_b [mm]
T-stub	16	25.6	30	10	13	15	30	30	65	47.5
Exterior L -stub	16	25.6	30	10	13	15	37.5	30	80	47.5
Interior L -stub	16	25.6	30	10	13	15	37.5	30	65	47.5

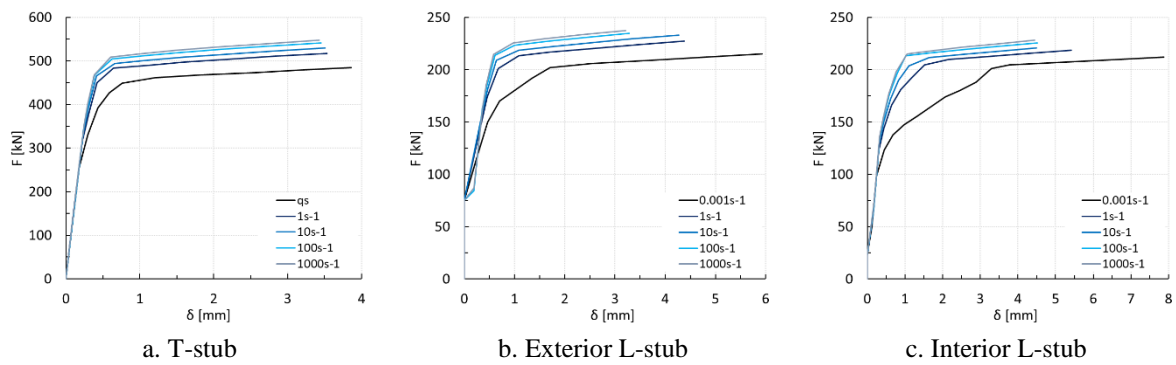| a. T-stub | b. Exterior L-stub | c. Interior L-stub |

Fig.B.1. Force-displacement curve of components designed as T-stubs

B.2. Force-displacement curves of components design as shear lap connections

The analytical approach developed in chapter 4 was used to obtain the force-displacement curves of these elements. It requires the definition of the material properties of plates and bolts (Table B.3), the friction properties (Table B.4) and the geometry of the plates as in Eurocode 3 Part 1-8 (Table B.5). The formulation to assess the static and dynamic curves showed in Fig.B.2 are detailed explained in chapter 4 of this document.

Table B.3. Material properties – static properties

Component		Internal Plate	External Plate	Bolt
Fricton damper	Material	*AISI 304*	S275 JR	10.9 HV
	f_y [MPa]	278	275	-
	f_u [MPa]	615	507	1000
T-stub web	Material	S275 JR	S275 JR	10.9 HV
	f_y [MPa]	355	275	-
	f_u [MPa]	510	507	1000

Table B.4. Friction properties

Component		Friction damper	T-stub web
n_b		2	12
n_s		2	1
$F_{P,C}$ [kN]		50	69
μ		0.47	0.3
$F_{slip,st}$ [kN]	Hogging	90	315
	Sagging	75	
DF_{frict}		1.05	1.05

Table B.5. Plates Geometry

Component	Friction damper		T-stub web	
	External Plate	Internal Plate	External Plate	Internal Plate
d_0 [mm]	21	21	13	13
t [mm]	23 (15 + 8 friction pads)	15	9.2	10
e_1 [mm]	62	62	20	20
e_2 [mm]	42.5	42.5	32.5	25.3
$p_{1,1}$ [mm]	70	70	35	35
$p_{1,2}$ [mm]	-	-	60	60
$e_{1,2}$ [mm]	40	40	40	30
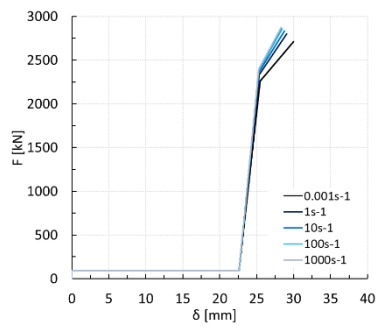
a. Friction damper (hogging moment)　　　　　b. T-stub web
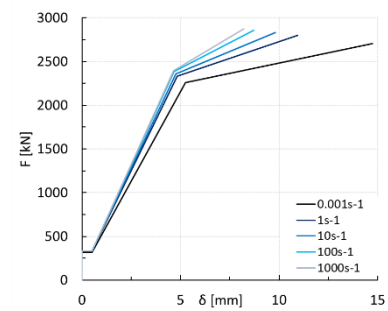
Fig.B.2. Force-displacement curve of components designed as shear lap connections

ANNEX C – Robustness of steel frames

C.1. Freedam connection

The process and the required considerations to analytical assess the behaviour of a freedam connection was already detailed explained. The only difference between the freedam connection analysed in chapter 5 and 6 and the one used in the frame are the dimensions of the components, as shown in the drawings below (Fig. C.1). In addition, since the analysed frame is characterized by the columns whose size decreases in height, the springs modelling the beam-to-column behaviour have to be properly detailed for each subassembly, as well as for both external and internal joints. These several curves are shown in the next figures.
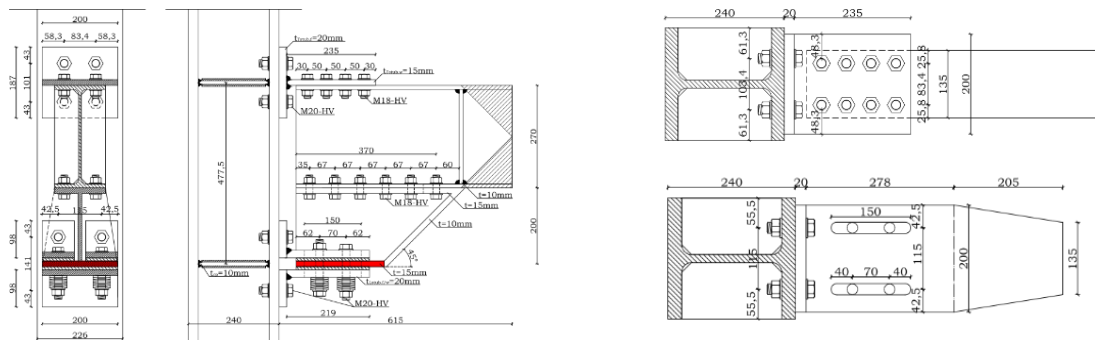
Fig. C.1. Geometry of the freedam connection used in robustness analyses [109]
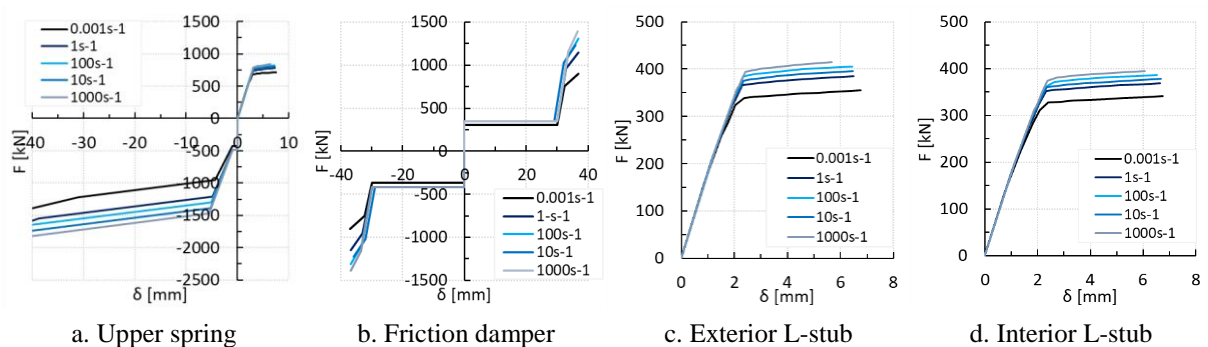
a. Upper spring   b. Friction damper   c. Exterior L-stub   d. Interior L-stub

Fig.C.2. Freedam connection: HEB300- IPE270 – Exterior/ Interior connections

a. Upper spring   b. Friction damper   c. Exterior L-stub   d. Interior L-stub
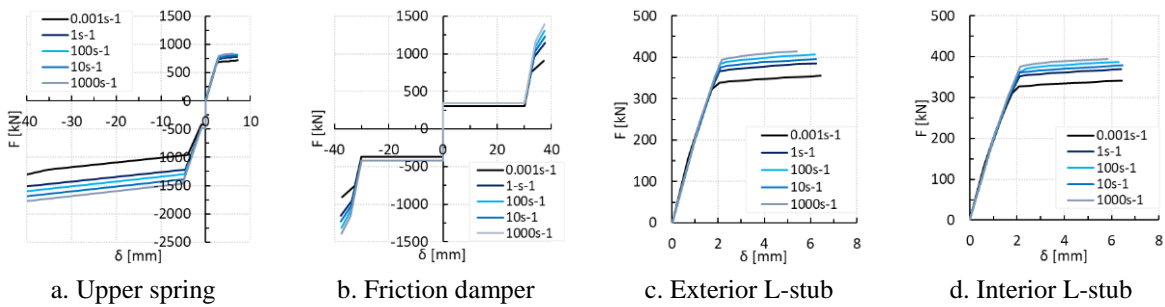
Fig.C.3. Freedam connection: HEB280- IPE270 – Exterior/ Interior connections

a. Upper spring   b. Friction damper   c. Exterior L-stub   d. Interior L-stub
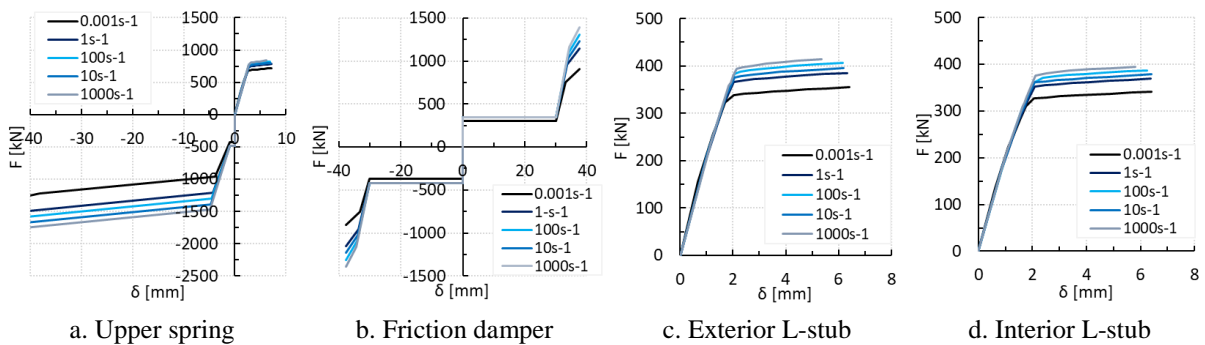
Fig.C.4. Freedam connection: HEB260- IPE270 – Exterior/ Interior connections

a. Upper spring   b. Friction damper   c. Exterior L-stub   d. Interior L-stub
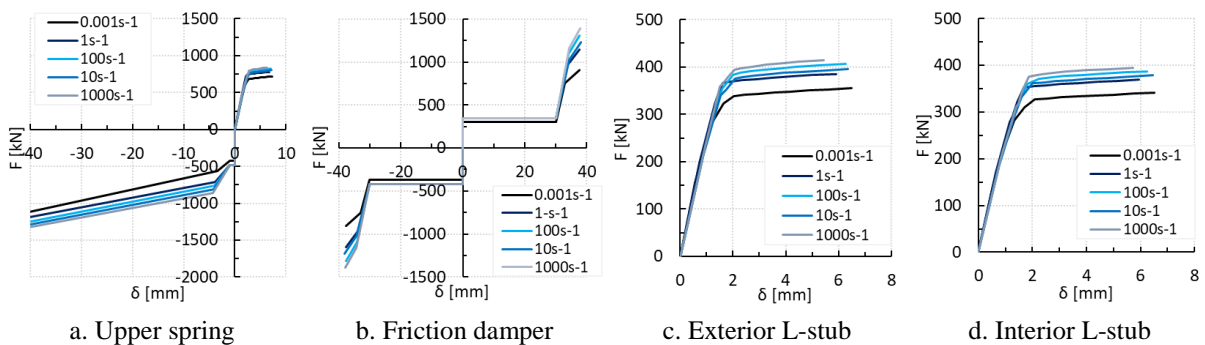
Fig.C.5. Freedam connection: HEB220- IPE270 – Exterior/ Interior connections

C.2. Dog-bone connection

With reference to the prediction of the response of bolted extended endplate connections, when subjected to both sagging and hogging moment, the following components have to be taken into account in order to evaluate the stiffness and the resistance of the whole joint:

- column web in shear (*cws*);
- column web in compression (*cwc*);
- beam flange and web in compression (*bfc*);
- column web in tension (*cwt*);

- column flange in bending (*cfb*);

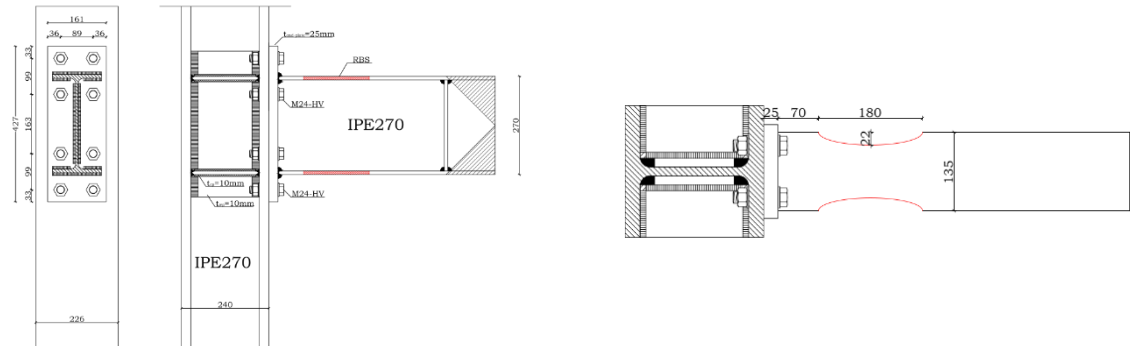- endplate in bending (*epb*);

- beam web in tension (bwt).

Fig. C.6. Connections used in robustness analyses [109]

As for the freedam connection, the springs modelling of the beam-to-column behaviour take into consideration the column size in height, the influence of the velocity and the differences between external and internal joints. These several curves are shown in the next figures.
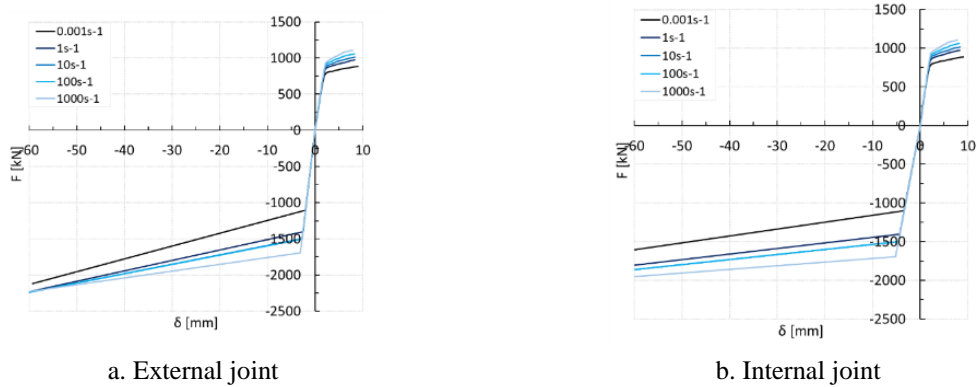

a. External joint

b. Internal joint

Fig.C.7. Dog bone connection: HEB300- IPE270

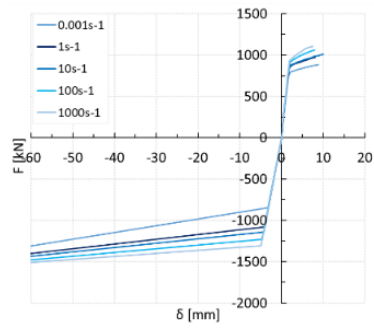a. External joint
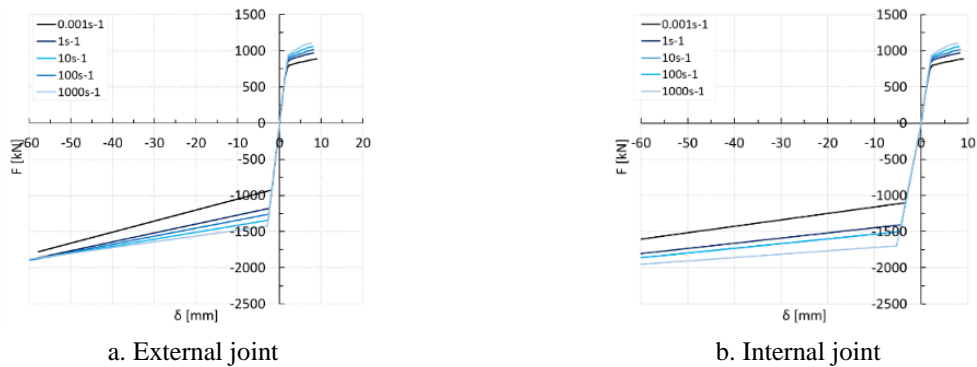
b. Internal joint

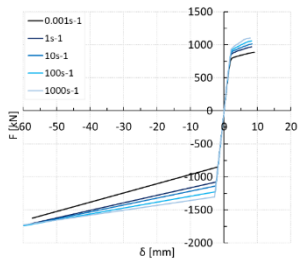Fig.C.8. Dog bone connection: HEB280- IPE270
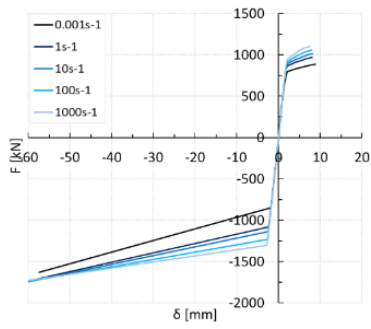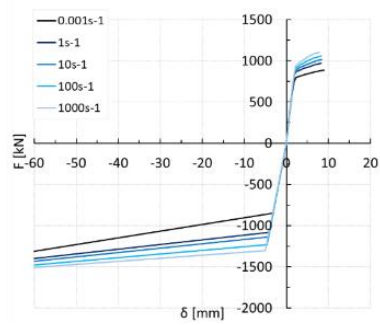
a. External joint

b. Internal joint

Fig.C.9. Dog bone connection: HEB260- IPE270

a. External joint

b. Internal joint

Fig.C.10. Dog bone connection: HEB220- IPE270